Impact of Fast Ions on Microturbulence in Fusion Plasmas

Samuele Mazzi

Aix*Marseille université
Socialement engagée

NNT/NL : 2021AIXM0470/059ED352

THÈSE DE DOCTORAT

Soutenue à Aix-Marseille Université
le 23 novembre 2021 par

Samuele MAZZI

Impact of Fast Ions on Microturbulence in Fusion Plasmas

Discipline
Physique et Sciences de la Matière

Spécialité
Energie, Rayonnement et Plasma

École doctorale
ED 352

Laboratoire/Partenaires de recherche
Physique des Intéractions Ioniques et Moléculaires (PIIM)—AMU–CNRS, UMR7345

IRFM—CEA Cadarache, 13108 Saint-Paul-Lez-Durance, France

Composition du jury

Paola MANTICA CNR Milano	Rapporteuse
Olivier SAUTER EPFL, SPC	Rapporteur
Pascale HENNEQUIN CNRS, Ecole Polytechnique	Présidente du jury
Alberto LOARTE ITER Organization	Examinateur
Carlos HIDALGO CIEMAT	Examinateur
Sadruddin BENKADDA CNRS, AMU	Directeur de thèse
Jeronimo GARCIA CEA Cadarache	Encadrant
David ZARZOSO CNRS, AMU	Encadrant
Gerardo GIRUZZI CEA Cadarache	Invité

cea

Affidavit

Je soussigné, Samuele Mazzi, déclare par la présente que le travail présenté dans ce manuscrit est mon propre travail, réalisé sous la direction scientifique de Sadruddin Benkadda, dans le respect des principes d'honnêteté, d'intégrité et de responsabilité inhérents à la mission de recherche. Les travaux de recherche et la rédaction de ce manuscrit ont été réalisés dans le respect à la fois de la charte nationale de déontologie des métiers de la recherche et de la charte d'Aix-Marseille Université relative à la lutte contre le plagiat.

Ce travail n'a pas été précédemment soumis en France ou à l'étranger dans une version identique ou similaire à un organisme examinateur.

Fait à Marseille le 23/09/2021

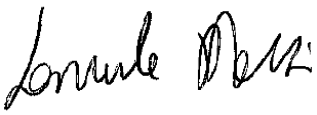

to Mariarosa

Acknowledgements

It has been a long, very long, journey. But despite this, it has been simply special, for real.

I believe I can say, without any doubt, that some unexpected stuff has happened lately. In the whole world, I mean. I like to think, however, that all of this has helped me to grow: sometimes when there is darkness you just need the courage to endure. But thankfully, along this journey, I've had brilliant people, friends, mentors by my side who have illuminated this darkness. Some have done it from very close, and some from further, but all of you must know that I have always felt your light clearly shining. Yet, listing a series of names is brutal and pointless, because three years are long and the brilliant people many. Thus, I would rather like to address only those who have shone with brighter on this path, hoping not to wrong anyone.

I would certainly like to start by thanking Jeronimo and David, two superlative supervisors and two admirable guys. Jeronimo, I still remember the morning, more than four years ago, when you welcomed me in Cadarache. I never imagined that I would end up writing these sentences. Thank you so much for betting on me, for trusting me, for all the time you have dedicated to me, for all the teachings, for all the efforts you have spent for me, and for all your incredible ardor and passion in what you do, which I hope I've made mine during these years. I don't think many people are lucky enough to have a supervisor, colleague, and friend like you. And a huge thank goes to David as well. You have been one of the best teachers I have ever met, a complete mentor, talented and clever, always positive and so genuinely full of ideas. I hope I have repaid you as I should have and as you deserve. Many thanks truly to both of you for making this possible. This work is as mine as yours.

I think now is the time to thank a special person, who really introduced me first to this community, who has always believed in me, has always protected me, has always cared, and guided me towards the future, advising me wisely. Thank you very much Gerri. I've been told once that I shouldn't thank you because at your time there were someone doing the same for you. But actually, I think it's really rare to find a colleague and a friend who cares for you the way you have done for me. So, thank you really again. I hope that I can really play your role in the future and not break this chain.

I would also like to thank Sadri, who made this trip possible and for giving me even more than I perhaps deserved over these three years. And how could I not thank Yann? Despite all your commitments, despite that I was not your student,

you always found time for me, to help me and to answer all my questions, even the most stupid and naive ones. Thank you very much indeed Yann for your kindness and your availability, I hope I can bother you again soon. And then Tobias, a fantastic person and a researcher so good to make envy. Thank you so much again for the two weeks of training in Garching and for all the times you answered comprehensively my mails. If I have learned something about GENE, I owe much − or almost everything − to you. Thanks again Tobias.

An important thank also go to Yevgen and Jef. The core of the work presented in this thesis is the result of a vast collaboration and project, in which the main minds and hands were you. Thank you for putting your trust in me, and thank you for struggling along my side during this last year. I'm figuring out how to get that box of *prosecco* to you, I swear.

I would also like to dedicate a few words to the members of the jury who, despite the difficult situation we are in, made the effort to come to Marseille to participate in the defense of the thesis. I would also like to thank them for bringing questions to the table that enriched the value of this thesis. In particular, Carlos, thank you very much for all the interest you have shown in my work, I am really proud and honoured to think that I have collaborated with a researcher of your stature.

A big thank also goes out to my office mates, Neeraj and Mun. Two generous, funny, and wonderful friends. And of course, thank also to all the other students and researchers, new and old, from the groups I was part of, both at PIIM and IRFM. Special thanks go to Myriam, for helping me deeply during my first year despite my shameful French, to Surabhi for always making me feel funny, to the Pirate for being so genuinely himself and to Virgi and Vale for all the *tisane*. Thank you very much also to Bettina and Alejandro, a super couple that I feel somewhat guilty of. And thanks also to Luca and Vero, two wonderful folks I'd never want to lose sight of. Thanks to Nuzzi, JD and Galaxy, for letting me sit at your table without even having earned it, thanks again. And then a special thanks goes to Tatalo and Nespo, two guys so incredibly different to be almost inseparable in my memories. However, a special thank also goes to Michael, Dwight, Creed and everyone else in The Office, you've helped me through so many difficult times. I'm sure I'll be laughing with all of you again in the future.

An infinite thank goes to my dearest and oldest friends, the *Ussaniani*, with whom we laughed, laugh and will always laugh. And to the *Grilli* as well, first mates of this adventure. Although oceans may separate us in the future, you must know that I will not fail to cross them to come to you and to feel Home again.

I would like to give an exceptional thanks to those points of reference that everyone has, not only in their careers, but also in their lives. Giacomino, Giorgione and Albi you have been and I think you will be forever mine. I thank you for being my true mentors, for pouring in me that passion that I hope will burn for a long time, for making me the person I am now in these last years, and for being such wonderful friends.

I would also like to thank my family, my brother Ludovico, my sister Melania

and the two wonderful *monelli* Nico and Fede. Thank you for your most genuine support and for the esteem that perhaps I don't even deserve. There are also thanks that might seem redundant, but they are not in reality: thank you for being the real authors of all this work, for being my first supporters, thank you for always protecting me, for all your sacrifices just to grant me the best, and, above all, thank you for your deep love. I hope I have made you proud of me, because you know that your approval is the main reason that moves my ambitions. Grazie mamma, grazie papà.

The sweetest thank, however, goes to the brightest light of all. They have been intense years, certainly complicated, but always and still amazing. Thank you for being by my side in every step of this way, and for simply being what I need, always. Grazie *scisc*iola.

Abstract

The exploitation of magnetically confined fusion plasmas as a sustainable and clean energy source is limited by the radially outward turbulent transport. Such transport is mainly induced by microinstabilities, arising due to the steep gradients. Among those, the ion temperature gradient (ITG) instability is one of the most relevant. Moreover, next-generation fusion devices, such as ITER, will be mainly heated by the alpha particles born from the nuclear fusion reactions between Deuterium (D) and Tritium (T). Alpha particles, with larger energy than the thermal part of the plasma (3.5 MeV vs. $\sim$10 keV), must be well confined in order to transfer their energy to the bulk ions. However, very little knowledge is available regarding the interaction between alpha particles and microturbulence, since very few DT experiments were performed in the past. Thus, unexpected turbulence and transport regimes may lead to further detrimental effects on the performance of future alpha-heated devices. Recently, externally generated fast ions, at higher energies with respect to the bulk ions, have been revealed to constitute a potential way to control turbulence in fusion plasmas. Fast ions can indeed trigger a complex multi-scale mechanism leading to an increased bulk-ion confinement. Yet, some crucial questions remain open, and thereby the main objective of this thesis is to extend the frontiers of the current knowledge on the interaction between fast ions and microturbulent transport.

The study of a tokamak scenario which can mimic the experimental conditions expected in future devices is hence crucial. This has been carried out by numerically investigating the impact of fast ions in the MeV energy range on the ITG-driven turbulent transport. A recently developed scenario at the Joint European Torus (JET) provides a suitable test-bed case to analyze this topic. A substantial population of fast ions at very high energy was generated through the efficient combination of external heating systems. Such fast ions can thus effectively reproduce the conditions of a burning plasma core, in which alpha particle dynamics dominate. Alfvén Eigenmodes (AEs) are destabilized by the highly energetic ions through a wave-particle interaction in the experiments at JET. With complex simulations, it is shown that a suppression of the ion-scale turbulent transport is achieved in conditions of strong Alfvén activity. AEs are shown to play an essential role in the multi-scale mechanism for the transport suppression. Multi-mode analyses demonstrate the spatio-temporal interaction between the fast-ion-driven AEs and the zonal components of the electrostatic potential. The nonlinear effects of the zonal flows on the ITG-driven transport are then analyzed.

Plasmas in fusion devices can be dominated by turbulence regimes different from ITG. In such scenarios, the effectiveness of the turbulence stabilization by fast ions is not guaranteed. Thus, the emphasis is put on the trapped electron mode (TEM) dominated turbulence. TEMs are a major instability in fusion plasmas, found to characterize the turbulent dynamics in various present tokamaks, and expected also in future devices. Numerical investigations of TEM-dominated plasmas in the presence of fast ions are carried out. It is shown that the TEM-induced transport, in a plasma of the Japanese tokamak JT-60U, is mildly affected by the fast ions. The weak role of zonal flows on the TEM turbulence is conjectured to be the missing ingredient to recover the beneficial effect. Instead, a significant reduction of the ion-scale transport is obtained in the presence of AEs destabilized by highly energetic ions, similarly to the ITG-dominated plasmas. This latter TEM-dominated system, suitably tailored for the purpose, is inspired from a particular pulse of the TCV tokamak. Deep analyses further highlight the possibility to recognize hallmarks of the ion-scale transport reduction, regardless the dominant turbulent regime.

Keywords: tokamak, microturbulence, fast ions

Résumé

L'exploitation des plasmas de fusion magnétiquement confinés en tant que source d'énergie propre est limitée par le transport turbulent. Ce transport est principalement induit par des micro-instabilités, dues à des gradients élevés. Parmi celles-ci, le gradient de température ionique (ITG) est à l'origine d'une forte instabilité dans le cœur des tokamaks. En outre, les futurs réacteurs, comme ITER, seront principalement chauffés par les particules alpha produites par les réactions de fusion nucléaire entre le deutérium (D) et le tritium (T). Les particules alpha, dont l'énergie est supérieure à celle de la partie thermique du plasma (3,5 MeV vs. $\sim$10 keV), doivent être bien confinées afin de transférer leur énergie aux ions thermique. Cependant, on a aujourd'hui trés peu de connaissances sur l'interaction entre les particules alpha et la microturbulence, car très peu d'expériences en DT ont été réalisées. Récemment, on a découvert que les ions rapides générés de l'extérieur, à des énergies plus élevées que les ions thermique, constituent un moyen potentiel de contrôler la turbulence dans les plasmas de fusion. Ceux-ci peuvent déclencher un mécanisme complexe conduisant à un confinement amélioré des ions thermique. Cependant, certaines questions cruciales restent ouvertes. L'objectif de cette thèse est d'étendre les frontières des connaissances actuelles sur l'interaction entre les ions rapides et le transport microturbulent.

L'étude d'un scénario de tokamak qui peut imiter les conditions expérimentales attendues dans les futurs réacteurs a été réalisé en analysant au moyen de simulations numériques, l'impact des ions rapides dans la gamme d'énergie MeV sur le transport turbulent provoqué par l'ITG. Un scénario récemment développé au tokamak JET, où des ions rapides à très haute énergie a été générée par la combinaison efficace des systèmes de chauffage externes, fournit un banc d'essai approprié. Une telle population peut ainsi reproduire efficacement les conditions d'un noyau de plasma de fusion, dans lequel la dynamique des particules alpha domine. Dans les expériences du JET, des modes d'Alfvén (AE) sont déstabilisés par l'interaction onde-ions rapide. Il est ainsi démontré qu'une suppression du transport turbulent à l'échelle des ions thermiques est obtenue dans des conditions de forte activité Alfvénique. En particulier, il est démontré que les AEs jouent un rôle essentiel dans le mécanisme multi-échelle qui conduit à la suppression du transport. Des analyses multi-modes montrent l'interaction spatio-temporelle entre les AEs et les composantes zonales du potentiel électrostatique. Les effets des flux zonaux sur le transport induit par l'ITG sont ensuite analysés en detail.

Les plasmas dans les tokamaks peuvent être dominés par des régimes de turbulence différents de l'ITG. Dans de tels scénarios, l'efficacité de la stabilisation de la turbulence induite par les ions rapides n'est pas garantie. Donc, l'accent est mis sur la turbulence dominée par le mode électrons piégés (TEM). Les TEMs sont une instabilité qui est fréquent dans les tokamaks actuels, et sont attendus aussi dans les futurs réacteurs. Ainsi, des études numériques des plasmas dominés par les TEMs en présence des ions rapides sont réalisées. Il est démontré que les ions rapides ont un effet négligeable sur le transport induit par les TEMs, dans un plasma du tokamak JT-60U. Le faible rôle des flux zonaux sur le flux du TEMs est supposé être l'ingrédient manquant pour l'effet bénéfique des ions rapides. Au contraire, une réduction significative du transport est obtenue en présence d'AEs déstabilisés par des ions fortement énergétiques, de manière similaire aux plasmas sur JET. Ce dernier système dominé par les TEMs est inspiré d'un scenario du tokamak TCV. Des analyses approfondies mettent en évidence la possibilité de reconnaître des caractéristiques distinctifs de la réduction du transport par les ions rapides, quel que soit le régime turbulent dominant.

Mots clés: tokamak, microturbulence, ions rapides

Résumé (Version étendue)

L'exploitation des plasmas de fusion magnétiquement confinés en tant que source d'énergie propre est limitée par le transport turbulent radial. Ce transport est principalement induit par des micro-instabilités, dues à des forts gradients existants dans ces plasmas. Parmi ceux-ci, le gradient de température ionique (ITG) est à l'origine de l'existence d'une forte instabilité dans la région dite de cœur des tokamaks. Le tokamak est le concept de machine à fusion le plus prometteur en termes de performances. En outre, les futurs tokamaks de la prochaine génération, comme ITER, seront principalement chauffés par les particules alpha produites par les réactions de fusion nucléaire entre les noyaux légers du deutérium (D) et tritium (T). Les particules alpha, dont l'énergie est supérieure à celle de la partie thermique du plasma (3,5 MeV vs. 10 keV), doivent être bien confinées afin de transférer leur énergie aux ions thermiques. Cependant, on a aujourd'hui très peu de connaissances sur l'interaction entre les particules alpha et la micro-turbulence, car très peu d'expériences en DT ont été réalisées. Ainsi, des régimes de turbulence et de transport inattendus pourraient avoir des effets délétères sur les performances des futurs réacteurs. Récemment, on a découvert que les ions rapides générés de l'extérieur, à des énergies plus élevées que les ions thermiques, constituent un moyen potentiel de contrôler la turbulence dans les plasmas de fusion. Ceux-ci peuvent déclencher un mécanisme complexe conduisant à un confinement amélioré des ions thermiques. Cependant, certaines questions cruciales sur ce sujet restent ouvertes. L'objectif de cette thèse est d'explorer l'interaction multi-échelles entre le transport micro-turbulent et les ions rapides afin de comprendre l'impact de ces derniers sur le confinement.

Dans ce qui suit, on donnera un bref résumé de ce manuscrit, en introduisant d'abord quelques concepts importants pour sa compréhension, puis en montrant les principaux résultats du travail décrit dans cette thèse.

La première partie de la thèse est consacrée à l'introduction des concepts physiques fondamentaux, qui sont utiles pour bien comprendre le sujet de la thèse. En fait, dans ce travail, on a fait appel à un modèle réduit, qui est largement utilisé dans le contexte de l'analyse des plasmas magnétisés pour la fusion. Ce modèle mathématique vise à résoudre la fonction de distribution des particules en réduisant à 5 les 6 dimensions utilisées dans l'approche cinétique. Elle exploite la séparation des échelles, tant temporelles que spatiales, qui est inhérente à la trajectoire d'une particule chargée immergée dans un champ magnétique. En fait, le mouvement circulaire (dû à la force de Lorentz) que la particule effectue autour des lignes de force, appelé mouvement giratoire, est beaucoup

plus rapide que le mouvement qu'elle effectue dans une direction parallèle. Par conséquent, une transformation des coordonnées vers un système gyrocentré est d'abord effectuée, puis la dépendance du mouvement rapide autour des lignes magnétiques est négligée. Ce modèle mathématique est appelé théorie gyrocinétique. Ce sujet est traité en détail dans la section 1.2.

La théorie gyrocinétique est largement utilisée dans l'analyse de la stabilité d'un plasma magnétisé dans une machine à fusion. En effet, comme on l'a déjà mentionné, de forts gradients de pression et de courant sont créés à l'intérieur des tokamaks afin de confiner le plasma. Ces gradients provoquent donc le développement d'instabilités dans le plasma du tokamak, qui est alors un système nécessairement hors équilibre. Ces instabilités, présentées dans la section 1.3, peuvent être différenciées en fonction de différents paramètres. Dans cette thèse, on traitera principalement des instabilités qui se développent au niveau microscopique (c'est-à-dire dans l'ordre de grandeur du gyrocentre des ions thermiques), mais aussi des instabilités plus particulières qui sont excitées par les ions rapides. Les ions rapides sont nécessairement présents dans un plasma de fusion. Ils sont produits par les réactions de fusion, c'est-à-dire les particules alpha, mais peuvent aussi être introduits par les systèmes de chauffage additionnels. Les particules rapides doivent être bien confinées dans le plasma afin qu'elles aient le temps d'échanger leur énergie avec le plasma thermique. La dynamique caractéristique des ions rapides peut être corrélée avec les fréquences des instabilités de type Alfvénique. Ainsi, les ions rapides peuvent facilement exciter les modes Alfvéniques, par le mécanisme fondamental de l'interaction onde-particule, qui implique un échange d'énergie entre les ondes (qui sont les instabilités) et les particules. Ces instabilités sont souvent associées à des effets négatifs sur les performances des tokamaks, car elles provoquent un fort transport d'ions rapides, mais réduisent également le confinement thermique du plasma.

Un autre concept important, introduit dans la section 1.4.1 de cette thèse, est la turbulence, qui se développe dans le régime non linéaire, lorsque ces instabilités peuvent interagir les unes avec les autres. Le transport turbulent, qui s'est révélé être la principale source de transport diffusif vers l'extérieur et donc le principal responsable de la perte de confinement dans les plasmas de fusion, est généré par l'interaction non linéaire multi échelles des instabilités mentionnées précédemment. Dans ce contexte, il existe une interaction particulière entre les micro-instabilités et/ou les modes Alfvéniques, qui se développent à différentes échelles spatiales, avec les fluctuations axisymétriques du potentiel électrostatique. Ces dernières fluctuations à grandes échelles sont généralement appelées flux zonaux, et constituent un phénomène fréquemment observé dans la nature, dont l'exemple le plus caractéristique sont les flux azimutaux dans l'atmosphère de Jupiter, clairement visibles dans les photos de cette planète. Les flux zonaux ont un effet favorable sur les micro-instabilités de type ITG, car ils peuvent décorreler les structures turbulentes qui sont créées et aider à dissiper l'énergie à petites échelles. Ainsi, une forte activité zonale est considérée comme bénéfique pour le confinement des ions. La dynamique non linéaire des plasmas magnétisés pour

la fusion thermocontrôlée est discutée dans la section 1.4.

Ainsi, comme nous l'avons vu, le plasma confiné par les champs magnétiques dans la région dite de cœur des tokamaks constitue un système complexe. Dans le cadre de la théorie gyrocinétique on essaie de caractériser la dynamique sous-jacente à ce système complexe et de comprendre les effets physiques qui s'y produisent. En pratique cela se fait, en résolvant de manière cohérente les variations de la fonction de distribution, pour les espèces considérées, et les fluctuations des champs électromagnétiques, le niveau de transport turbulent peut être établi. Malgré la réduction de la taille du système en passant d'une approche purement cinétique à une gyrocinétique la résolution de ce type de problème reste un défi très exigeant, notamment du point de vue du temps de calcul. Pour cette raison, une approximation supplémentaire est souvent exploitée dans les codes numériques utilisés pour ce type d'étude. Fondamentalement, le domaine radial du plasma est réduit à un tube de flux centré autour d'une surface de flux magnétique spécifique. De cette façon, seulement la dynamique locale du système est prise en compte et résolue. Cette approche, normalement appelée locale ou "flux-tube", est utilisée de manière extensive dans cette thèse pour étudier la stabilité des plasmas dans la région de cœur des machines à fusion, comme cela sera présenté dans ce qui suit. Plus de détails sur l'approche gyrocinétique locale et sur le code numérique GENE utilisé dans ce travail, sont développés dans le chapitre 2.

A présent, discutons les principaux résultats obtenus dans le cadre de cette thèse. Comme déjà mentionné, l'objectif de ce travail était d'étudier l'interaction entre les ions rapides et la turbulence induite par les micro-instabilités au sein des plasmas de fusion afin d'obtenir des prédictions fiables pour les réacteurs de prochaine génération, tels qu'ITER. Un résumé bref mais complet sur ce sujet particulier est donné dans la section 1.5. Plus précisément, ce travail est consacré à répondre à deux questions cruciales, qui sont encore sans réponse. Tout d'abord, bien que l'effet bénéfique des ions rapides sur le transport turbulent causé par les instabilités de type ITG soit maintenant établi à la fois expérimentalement et théoriquement, cela se limite aux ions rapides générés par des systèmes de chauffage externes. Celles-ci sont donc normalement introduites dans le système à une énergie bien inférieure (généralement d'un ordre de grandeur inferieur) à celle des particules alpha produites par les réactions de fusion. Ainsi, l'impact des particules alpha sur la microturbulence et sur le transport induit peut s'avérer inattendu et entraîner des effets négatifs sur le confinement. Certaines études pionnières ont été réalisées sur des plasmas chauffés par des particules alpha dans des scénarios prédictifs d'ITER, et donc uniquement dans des conditions non encore vérifiables expérimentalement. Il est donc nécessaire de développer des scénarios dans les tokamaks actuels qui puissent reproduire les conditions attendues dans ITER, et ainsi de vérifier ces simulations et de les comparer aux résultats expérimentaux. En outre, dans les tokamaks actuels, mais aussi dans les futurs, des régimes de turbulence autres que l'ITG peuvent être atteints. Jusqu'à présent, les études sur l'interaction entre les ions rapides et la microturbulence n'ont concerné que le transport induit par les insta-

bilités de type ITG. Ainsi, il n'est pas garanti que l'effet bénéfique décrit ci-dessus puisse également être obtenu dans des régimes de transport autres que l'ITG. Ces deux directions seront essentiellement explorées au cours de la thèse comme on verra ci-dessous.

Afin de répondre à la première question posée, c'est-à-dire la validation de l'effet bénéfique des ions rapides de type alpha sur le transport induit par l'ITG, une étude numérique complexe est rapportée en détail au Chapitre 3. Cette étude s'est concentrée sur l'analyse d'un scénario récemment développé au tokamak européen JET, le plus grand tokamak opérationnel actuellement. JET a la particularité de pouvoir confiner de manière adéquate des particules de très haute énergie, comme les particules alpha. En effet, dans le scénario développé au JET, une population importante de deutérium est efficacement accélérée à des températures de l'ordre du MeV. Cela a été rendu possible par l'application du système de chauffage dit "three-ion scheme". Cette méthode repose sur l'introduction de trois espèces dans le plasma, l'une de ces espèces jouant le rôle d'un efficace absorbeur d'énergie. De plus amples détails sur l'application du "three-ion scheme" sont donnés dans la section 3.1.1 de cette thèse. Avant de commencer à discuter des analyses numériques il est nécessaire de montrer quelques observations expérimentales qui ont justifié l'importance de l'étude. En effet, la présence de ces ions dans le range du MeV a des effets clairs sur les propriétés globales du scénario. Tout d'abord, la présence de ces ions rapides à une énergie beaucoup élevée implique un échange d'énergie par collision avec les électrons plus important qu'avec les ions thermiques. De ce fait, ces ions très rapides entraînent un fort réchauffement électronique dans le cœur du JET. Cependant, il faut se rappeler que ce sont les ions qui réagissent pour produire l'énergie de fusion, de sorte que le chauffage des électrons n'est pas toujours recherché dans les plasmas de tokamak. En second lieu, ces ions rapides donnent lieu à une forte activité Alfvénique comme indiqué dans la section 3.1.3. Ces deux propriétés sont considérées comme nocives pour le confinement thermique des ions dans les tokamaks, mais étonnamment dans ce scenario, une amélioration de la température des ions au-delà des attentes a été systématiquement mesurée. Cela a conduit à la suggestion qu'un mécanisme physique lié à la présence d'ions rapides était en jeu, et des analyses gyrocinétiques détaillées ont donc été effectuées pour découvrir le possible mécanisme.

Ainsi, des simulations gyrocinétiques très couteuses (du point de vue du calcul) et très complexes ont été réalisées et les principaux résultats de celles-ci, et de leur comparaison avec les données expérimentales sont décrits à partir de la section 3.3. Tout d'abord, une étude linéaire a été réalisée pour vérifier la stabilité du système aux différentes échelles spatiales considérées. En fait, les ions rapides, dont la dynamique se déroule à de grandes échelles spatio-temporelles, et les particules thermiques ont été simulés de manière cohérente. On a constaté que l'effet des ions rapides dans le régime linéaire sur les instabilités de type ITG, qui sont dominantes dans le spectre linéaire est très faible. Cependant, si le gradient de pression des ions rapides est augmenté au-delà d'un certain seuil, une déstabilisation du mode à grande échelle se produit. La

fréquence de ces instabilités est similaire à celle mesurée expérimentalement pour des modes Alfvéniques particuliers, le Toroidal Alfven Eigenmode (ou TAE), systématiquement observé dans le scénario étudié. Une analyse plus détaillée de l'instabilité à grande échelle et à haute fréquence a permis d'identifier ces instabilités comme précisément des TAEs (voir section 3.3.3), excités par le mécanisme de résonance avec le mouvement caractéristique des ions rapides piégés le long de la direction toroïdale du tokamak.

Dans le régime non linéaire cependant, l'effet des ions rapides devient beaucoup plus clair. En effet, en laissant le système évoluer de façon non linéaire et donc en permettant l'interaction entre les différentes échelles du système on observe clairement que la déstabilisation des TAEs dans le régime non linéaire conduit à la suppression du transport radial des ions thermiques dû aux fluctuations du champ électrostatique. Pour être exhaustif, la dépendance de la diffusivité thermique des ions due aux fluctuations électrostatiques sur la déstabilisation des TAEs est montrée dans la figure 1 ci-dessous. En effet, pour des valeurs du gradient de pression des ions rapides $R/L_{p_{FD}} > 10.7$, les TAEs sont déstabilisés et, en fort accord avec les données expérimentales on observe une réduction de plus de 95% du transport électrostatique des ions. Pour mieux comprendre la forte réduction du transport thermique des ions, des analyses détaillées ont été réalisées. En effet, il a été noté que lorsque les TAE sont déstabilisés les composantes zonales du potentiel électrostatique sont fortement dominantes. Cela indique que les flux zonaux, dont l'effet bénéfique sur le transport induit par les ITG a déjà été expliqué précédemment sont largement augmentés lors de la déstabilisation des TAEs. Ceci suggère une corrélation entre les deux échelles, c'est-à-dire celle du TAE et celle des flux zonaux. Afin de démontrer cette corrélation, des analyses dites bispectrales ont été réalisées. Ces dernières étudient le couplage non linéaire possible entre les différents modes considérées dans la simulation numérique. En se concentrant donc sur les modes d'intérêt pour cette étude il a été démontré qu'il existe une forte corrélation entre les TAEs et les flux zonaux, ce qui suggère qu'un transfert net d'énergie peut se produire des TAE aux flux zonaux. Ainsi, l'augmentation de l'activité zonale peut supprimer le transport radial des ions thermiques, ce qui induit une augmentation de l'intensité de l'activité zonale. Plus de détails sur ces analyses sont donnés dans la section 3.4.4 de cette thèse.

Dans les autres sections du chapitre 3 de cette thèse, d'autres particularités de ces simulations numérique sont analysées qui d'une part corroborent les résultats obtenus en les comparant avec des preuves expérimentales et d'autre part ouvrent la voie à de nouvelles confirmations à rechercher directement dans les expériences. A cet égard il est conseillé de lire les sections 3.4.5 et 3.4.6 respectivement, qui analysent la déstabilisation des modes basse fréquence qui semblent avoir été mesurés également de manière expérimentale et l'effet des ions rapides sur la phase croisée.

Un autre aspect important analysé dans cette thèse est que, contrairement aux études numériques gyrocinétiques précédentes le transport électronique induit par les fluctuations du champ magnétique n'est pas radicalement augmenté dans

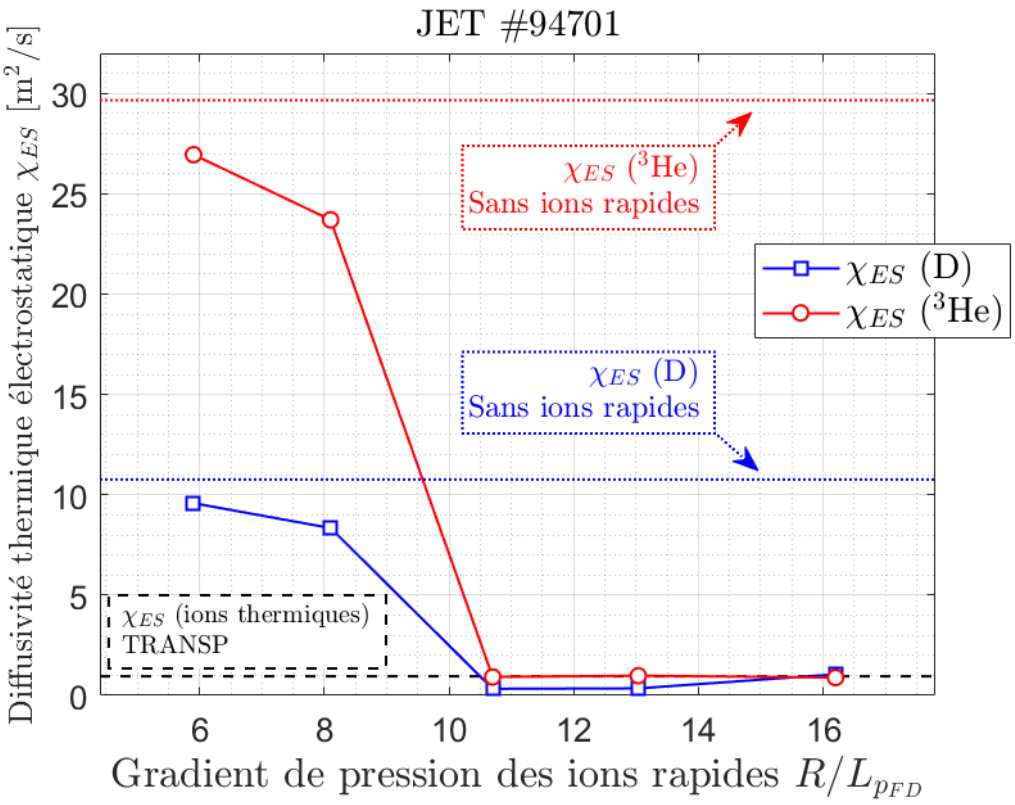

Figure 1: *La diffusivité thermique électrostatique des ions thermiques est représentée en fonction du gradient de pression des ions rapides à partir des simulations* GENE *de la décharge du JET #94701 pour une position radiale spécifique dans le cœur. Les lignes horizontales en pointillés font référence aux diffusivités thermique des simulations sans ions rapides. La ligne horizontale noire en pointillés représent la diffusivité thermique des ions thermiques à partir des bilans de puissance. Voir la figure 3.16 et la section 3.4.1 pour plus de détails.*

des conditions avec les TAEs instables. Parallèlement à cette observation importante, qui corrobore la validité des résultats de la simulation, une augmentation significative des composantes zonales des fluctuations du potentiel magnétique a également été mesurée dans les simulations avec une forte activité Alfvénique. Même si l'effet des flux zonaux, c'est-à-dire les fluctuations zonales du potentiel magnétique sur le transport électromagnétique n'est toujours pas clair, il faut reconnaître que l'énergie qui s'écoule vers les échelles zonales n'implique pas ensuite de transport radial, et pourrait donc contribuer à l'atténuation du transport des électrons. En ce sens, les flux zonaux peuvent agir comme une réserve d'énergie libre et améliorer ainsi le confinement thermique du plasma.

Pour conclure ce chapitre, une étape supplémentaire a été franchie pour comprendre les effets des ions rapides dans le scénario développé à JET. En fait, les simulations numériques discutées précédemment ont été réalisées avec une configuration de champ magnétique où la pente du facteur de sécurité q, un

paramètre très important dans les tokamaks, était positive. Ce paramètre qui définit la pente du profil radial de q est appelé cisaillement magnétique. Dans ces conditions, il y a donc une suppression du transport turbulent des ions thermiques lorsque les TAE sont instables, mais au même temps un fort transport radial d'ions rapides est également mesuré (voir section 3.4.2). En pratique, cela signifie que si le confinement des ions thermiques s'est amélioré celui des ions rapides s'est détérioré. Cependant, dans le scénario du JET, on note également la déstabilisation de modes Alfvéniques particuliers (le Reversed Shear Alfven Eigenmodes, ou RSAEs) qui certifient que, pour une certaine région du plasma cœur, il y a une inversion du cisaillement magnétique. Par conséquent, d'autres simulations gyrocinétiques ont été effectuées avec la même configuration numérique à l'exception de la modification du cisaillement magnétique, qui est maintenant négatif. Les résultats de ces simulations sont présentés dans la section 3.7. Il a ainsi été démontré que l'inversion de la pente du profil radial de q dans le cœur du plasma a un effet bénéfique supplémentaire sur le confinement, réduisant le transport turbulent des ions rapides d'un ordre de grandeur, mais laissant la situation inchangée pour les ions thermiques. Des analyses détaillées montrent que l'inversion du cisaillement magnétique conduit à une modification des résonances onde-particule dans l'espace des phases qui excitent les TAEs. Ainsi, cette modification induit une diminution de l'intensité des TAEs, et donc une moindre amplitude des fluctuations du champ électromagnétique et donc du transport radial des ions rapides.

Ainsi, l'effet bénéfique des ions rapides sur le transport turbulent induit par l'ITG a été démontré dans le "three-ion scheme" scénario développé à JET avec une forte activité Alfvénique. Cela pourrait donc suggérer que des conditions similaires peuvent également être obtenues dans des plasmas chauffés par des particules alpha, comme dans la phase D-T d'ITER.

Dans le Chapitre 4 de la thèse, cependant, , une tentative a été faite pour répondre à la deuxième question posée au début de ce résumé. Autrement dit, l'effet bénéfique des ions rapides est-il indépendant du régime de turbulence dominant dans le plasma ? Ou est-il possible que pour autres régimes de microturbulence, les ions rapides n'aient aucun effet sur la microturbulence, ou même un effet délétère ?

Pour répondre à ces questions, on a analysé une décharge particulière riche en ions rapides du tokamak japonais JT-60U, qui a été mis hors service pendant plus de dix ans. Il a d'abord été démontré que ce plasma particulier était dominé par une autre instabilité différente de l'instabilité ITG. Cette instabilité est appelée "trapped electron mode ou TEM". Elle est essentiellement due à une résonance onde-particule avec le mouvement de précession "toroïdal des électrons piégés". Cette instabilité est très présente dans les tokamaks actuels et devrait également être présenté dans les futurs réacteurs de fusion dans des régimes de densité particuliers. Ainsi, l'étude décrite au chapitre 4 est certainement importante non seulement pour la gestion des tokamaks actuellement en exploitation, mais aussi pour la prévision du comportement des futurs tokamaks. Tout d'abord, de plus amples informations ont été données sur l'expérience réalisée dans le tokamak

JT-60U dans la section 4.1, qui sera analysée en profondeur dans le chapitre 4. Il est important de noter que dans cette décharge de plasma du JT-60U, contrairement au scénario du JET, les ions rapides sont injectés dans le plasma à des températures beaucoup plus basses que les particules alpha (environ un ordre de grandeur plus bas). Ensuite, le même flux de travail a été suivi que dans le chapitre 4, c'est-à-dire l'utilisation du code gyrocinétique local GENE pour analyser les effets des ions rapides sur le transport induit par l'instabilité TEM. Ainsi, une étude de stabilité linéaire a été réalisée et il a été noté que le spectre linéaire montrait une situation plus complexe, où trois instabilités différentes ont pu être identifiées. Cependant, l'instabilité dominante est TEM, déstabilisée aux échelles ioniques, tandis qu'une instabilité à haute fréquence (proche des fréquences Alfvénique) est mesurée aux grandes échelles liées aux ions rapides. Cette instabilité à haute fréquence sera importante dans ce qui suit. En fait, comme nous essayons de valider les simulations gyrocinétiques avec des données expérimentales il est important de noter qu'aucune instabilité à haute fréquence n'a été observées expérimentalement dans cette décharge particulière du JT-60U. Par conséquent ces modes instables, qui ont été identifiés comme des modes Alfvéniques particuliers, des AITG et des BAE, doivent être stabilisés. Afin de stabiliser ces instabilités la configuration des paramètres numériques a été modifiée notamment les paramètres physiques de la partie thermique du plasma. Essentiellement, on a modifié les gradients de température des ions thermiques et la densité des particules de ces derniers dans une barre d'erreur supposées être d'environ 20%. Cependant, dans le cas de la configuration des particules rapides, il a été nécessaire de modifier de plus de 20% les valeurs calculées par la modélisation intégrée. De plus amples détails sur ces changements sont donnés dans la section 4.5.1.

Une autre raison pour laquelle la stabilisation des modes Alfvéniques à haute fréquence s'est avérée nécessaire concerne le niveau de transport turbulent dans le régime non linéaire lorsque ces instabilités sont présentes. En effet, lorsque ces modes sont linéairement instables, une forte augmentation du transport à toutes les échelles est mesurée par le code gyrocinétique. Les valeurs obtenues du flux thermique radial sont incompatibles avec les résultats des bilans de puissance. C'est une preuve supplémentaire que les instabilités à grande échelle doivent être stabilisées afin de valider les résultats de la simulation. Ces effets sont décrits dans la section 4.4.1 de cette thèse.

Ainsi, une fois que les modes à haute fréquence ont été stabilisés en ajustant les paramètres locaux d'input, il est démontré que l'instabilité de type TEM est le principal drive du transport turbulent radial. Cela permet d'évaluer l'effet des ions rapides sur la micro-turbulence induite par les TEMs et de le valider ensuite par rapport aux résultats expérimentaux (principalement le niveau de transport calculé avec les bilans de puissance). Ceci a été rapporté de manière très détaillée dans la section 4.5, et la figure 2 significative du résultat obtenu à partir de l'analyse numérique est également présentée ci-après. Dans cette figure, les flux de chaleur électrostatique des électrons et des ions sont présentés en fonction du temps (a) et du nombre d'onde binormal (b) pour trois cas différents : le cas où

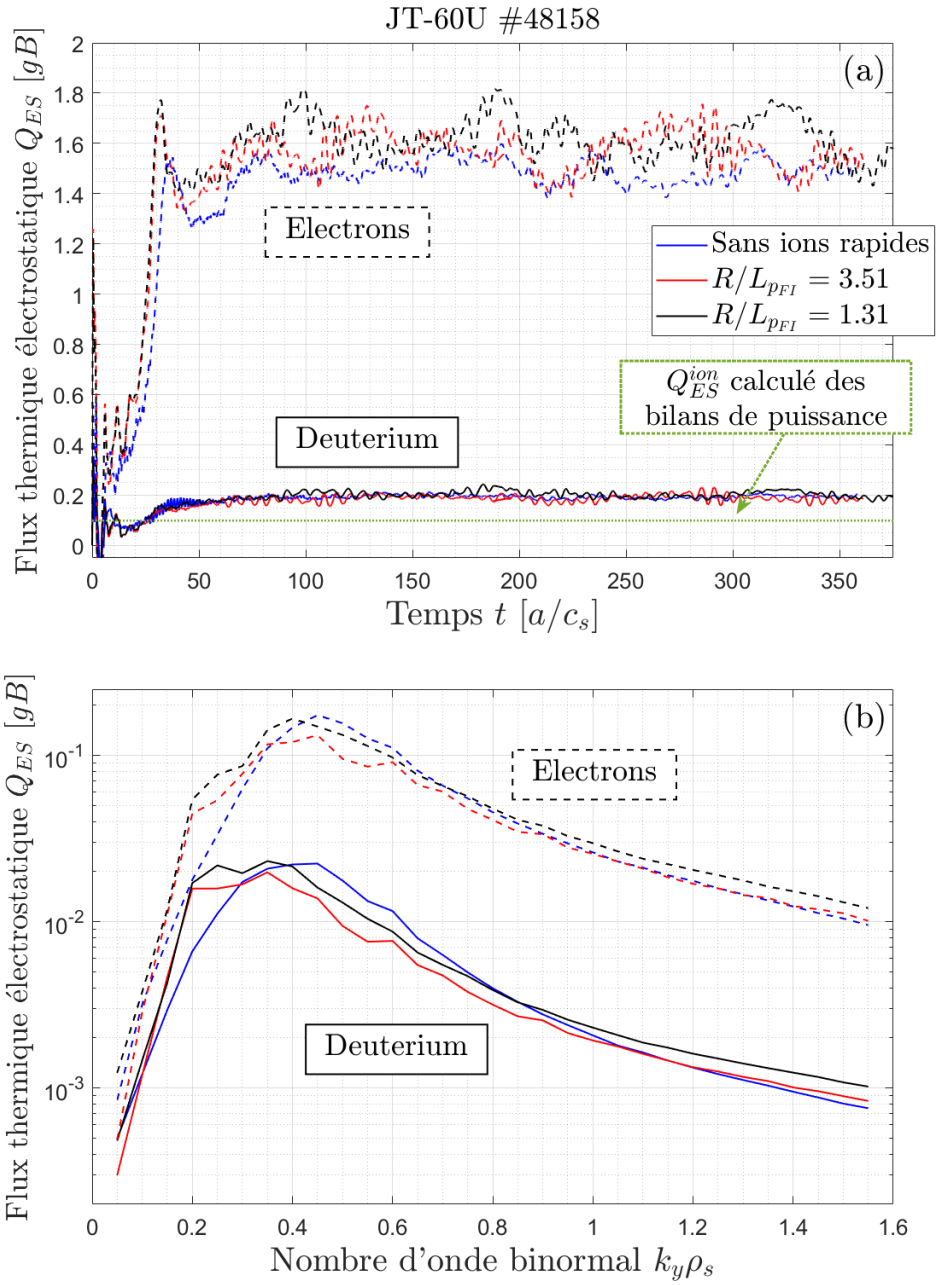

Figure 2: *Dans (a), les traces temporelles du flux thermique électrostatique des électrons (lignes pointillés) et des ions thermiques (lignes pleines) sont présentées pour le cas sans ions rapides et pour deux configurations différentes du gradient de pression des ions rapides dans le setup numérique modifié, qui est dominé par le TEMs. La ligne pointillée horizontale verte représente la valeur du flux thermique des ions à partir des bilans de puissance expérimentaux. Dans (b), les spectres de flux de chaleur au lieu des traces temporelles sont montrés pour les mêmes cas. Voir la figure 4.20 et la section 4.5 pour plus de détails.*

les ions rapides ne sont pas considérée dans le système, et deux configurations différentes du gradient de pression des ions rapides. Dans les deux panels, on peut voir que l'effet des ions rapides sur le transport turbulent induit par les TEM est absolument négligeable. Suite à ce résultat différent de celui obtenu précédemment concernant le transport déterminé par l'ITG (Chapitre 3), on a supposé que l'ingrédient manquant pour compléter la recette était l'effet des flux zonaux sur l'instabilité de type TEM. En fait, plusieurs études ont prouvé que les flux zonaux ne sont pas un mécanisme efficace pour saturer la turbulence induite par les TEMs. Plus de détails sont donnés dans la section 4.5.4, où la corrélation entre les TEMs et les flux zonaux a été analysée en utilisant également l'outil de l'analyse bispectrale.

Ainsi, il a été démontré que l'effet des ions rapides sur le transport turbulent induit par les instabilités de type TEM dans la décharge particulière du tokamak japonais JT-60U est en fait négligeable. Cependant, un autre cas a été présenté inspiré cette fois par une décharge (#58375) récente du tokamak suisse TCV. Dans cette décharge le cœur du plasma est dominé par l'instabilité de type TEM, qui est essentiellement due à une température électronique élevée (par rapport à la température ionique) et à un fort gradient de température électronique. Pour éviter que les modes de type ITG ne soient instables, le gradient de température des ions a été réduit et la présence d'impuretés a également été négligée. En ce sens, on n'a donc pas cherché à valider les résultats obtenus par les simulations, mais on a plutôt pensé à une expérience numérique. Ceci peut donc être considéré comme la première étape d'une étude prédictive visant à la validation expérimentale. Dans cette décharge du TCV, il y a notamment une population importante d'ions rapides, qui sont injectés à l'extérieur à des températures plus élevées que les électrons. Il faut noter que la rapport entre la température des ions rapides et celle des électrons dans cette décharge du TCV est plus proche de celui de la décharge du JET analysée au chapitre 3 que de celui de la décharge du JT-60U analysée au chapitre 4. En plus de cette similitude, le régime de confinement du plasma de cette décharge du TCV est également plus proche de celui du JET que de celui du JT-60U. Un paramètre important pour cette comparaison est le rapport entre la pression thermodynamique du plasma et la pression magnétique. Ainsi, une fois de plus, la version locale du code gyrocinétique GENE a été utilisée. Les simulations non linéaires de ce système ont donné des résultats conformes à ceux obtenus au JET. En effet, bien que le système soit dominé par des instabilités de type TEM, une forte activité zonale est mesurées lors de la déstabilisation des instabilités induites par la présence des ions rapides, et une réduction significative du transport d'électrons a été mesurées. A noter que dans ce cas, on ne peut pas parler de suppression, car la réduction du transport turbulent est moins prononcée que celle observée dans le cas du JET. Toutefois, la section 4.7 est entièrement consacrée à cette étude préliminaire. De manière significative, certains signes distinctifs de la forte réduction du transport turbulent aux échelles ioniques, qui ont également été observés dans le cas étudié et rapporté dans le chapitre 3, ont été notés aussi dans ce cas. Ceux-ci sont analysés en détail.

Enfin, le chapitre 5 de cette thèse présente les conclusions et un bref résumé des principaux résultats. Malgré cela, il reste de nombreuses questions ouvertes, qui sont également présentées à la fin de cette thèse.

Contents

List of Figures

List of Tables

Chapter 1

Introduction to plasma physics related to microinstabilities, fast-ion-driven modes and self-regulation mechanisms

Contents

The first part of this thesis is dedicated to providing the basic concepts useful for the comprehension of the following matters. Therefore, after a brief introduction to the nuclear fusion is given, the fundamentals of the plasma physics related to the fast ions, microturbulent transport and fast-ion-driven modes in the specific magnetized plasmas confined in tokamak devices will be the principal focus of the first chapter.

1.1 Nuclear fusion

Controlled thermonuclear fusion energy represents one suitable candidate to satisfy the future energy needs, providing all the characteristics of a sustainable, clean CO_2-free civil energy source. Such an energy source crucially relies on the nuclear fusion process of light nuclei. Indeed, when two light nuclei, up to the iron element ($\mathrm{A} = 56$, with A the number of nucleons) fuse together, the binding energy per nucleon is increased, and the kinetic energy is released under different forms, depending on the reaction, consistently with the Einstein's law. The reaction yielding the most advantageous energy balance at the lowest temperatures is the fusion between two hydrogen isotopes, the deuterium (D) and the tritium (T):

$$ {}^{2}_{1}\mathrm{D} \; + \; {}^{3}_{1}\mathrm{T} \implies {}^{4}_{2}\mathrm{He}\,(3.5\,\mathrm{MeV}) + \; {}^{1}_{0}\mathrm{n}\,(14.1\,\mathrm{MeV}) \tag{1.1} $$

in which the ^{4}He nucleus are also generally called alpha particles. Nevertheless, for such a reaction to occur, the reactant positively charged nuclei must overcome the Coulomb electrostatic barrier through quantum tunneling, thus temperatures of the order of 10 keV ($\sim 10^8$ K) are required. At this level of energies, the matter is present only under the form of fully ionized gas with a behaviour dominated by collisionless, long-range and collective effects of the electromagnetic fields. Such a state is commonly called *plasma*.

In order for the controlled thermonuclear fusion to be a valid contribution to the energy mix, the power balance between the total power generated by the fusion reactions P_F and the injected power P_H in the system must be positive. The amplification factor Q is an important figure of merit, commonly used to measure the performance of the fusion reaction:

$$ Q = \frac{P_F}{P_H} \tag{1.2} $$

Therefore, in order to reach the ignition condition, at which the internal heating provided by the fusion-born alpha particles is sufficient to compensate for the energy losses, the maximization of the three following parameters must be pursued: the temperature of the reacting ions T_i, the plasma particle density n and the energy confinement time τ_E, which is basically the confinement time of the plasma stored energy in the absence of external input energy. Combining these three factors in a single relation, the Lawson criterion [1] is obtained:

$$nT_i\tau_E > 3 \times 10^{21} \frac{\text{keV s}}{\text{m}^3} \tag{1.3}$$

Beyond the unfeasible gravitational confinement achieved only in the stars, to reach the Lawson criterion on Earth for very hot plasmas ($T_i \sim 10$ keV) two main different paths can be taken. The inertial confinement aims at concentrate very dense plasmas ($n \sim 10^{31}$ m^{-3}) for very short confinement times ($\tau_E \sim 10^{-11}$ s) by means of high-power laser beams, whereas the magnetic confinement's goal is to achieve in low-density ($n \sim 10^{20}$ m^{-3}) plasmas energy confinement times of the order of the second ($\tau_E \sim 1$ s). Although the inertial confinement is significantly progressing in the last years [2], the magnetic confinement concept [3] is likely the most promising for the controlled thermonuclear fusion to fully obtain the status of a profitable and reliable source of clean and durable energy.

1.1.1 Magnetically confined plasmas

Since the plasma system at the ignition conditions should reach envisaged temperatures that any of the presently available wall material can resist to, in order to confine the charged particles it is possible to exploit the nature of the plasmas. Indeed, the charged particles follow the intense magnetic field lines due to the Lorentz force, without coming in contact with the containing wall surfaces. Various configurations of the magnetic topology have been exploited during the last decades, but the most efficient are the ones enforcing the magnetic field lines on bounded surfaces, called magnetic flux surfaces. Among these configurations, *stellarators* and *tokamaks* are two of the most pursued solutions. The next generation magnetically confined fusion device, to be built in southern France, is ITER. Based on the tokamak concept, ITER aims at demonstrating the feasibility of magnetically confined plasmas as an energy source. This thesis is therefore devoted to studying the tokamak plasmas, although stellarators have recently shown an impressive potential (see e.g. [4, 5]).

In tokamaks, the total confining magnetic field is provided by the superposition of two components, namely the toroidal B_φ and the poloidal B_θ. Whereas the former is generated by a current flowing in the external coils wrapped around the toroidal chamber of the tokamak, the latter is induced by the plasma current flowing within the chamber in the toroidal direction. The poloidal magnetic field is essential for balancing the pressure forces generated by the confined plasma pressure. The principle of the transformer is used to generate the plasma toroidal current I_p, with the plasma acting as the secondary circuit while the magnetic flux in the central coils is varied. Yet, in current tokamak devices, as well as in ITER, other coils mainly delegated to the control of the plasma shape and position are present. In Figure 1.1, the vertical coils generates the additional vertical magnetic field component B_v for such a purpose. For a schematic view of the tokamak device see Figure 1.1.

In the following, a brief overview of the tokamak devices whose plasmas are analyzed in this thesis is given.

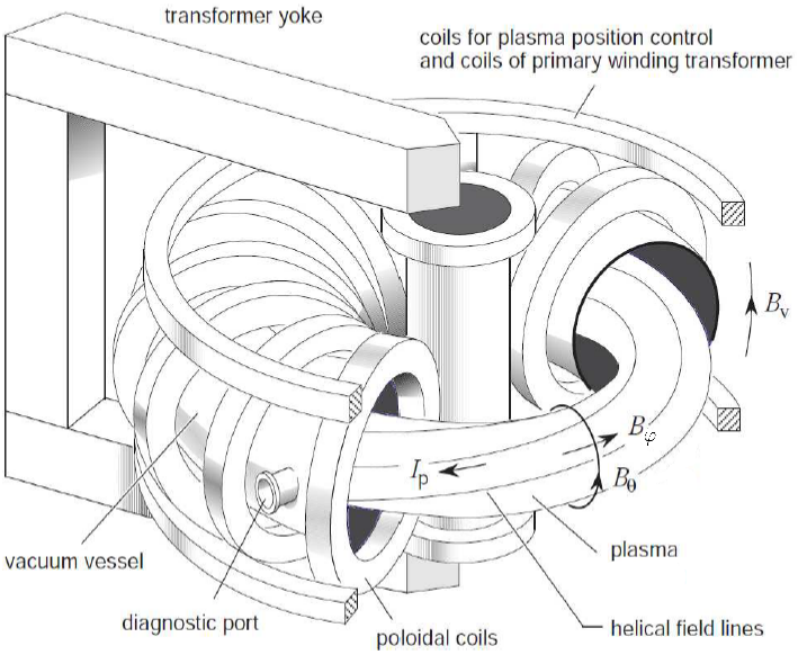

Figure 1.1: *Schematic representation of a tokamak device. The plasma is represented by the inner torus, in which the plasma current I_p, generating the poloidal component of the magnetic field (B_θ), is shown. The vacuum vessel is surrounded by poloidal coils, generating the toroidal component of the magnetic field (B_φ). Additional coils generate the vertical component B_v, necessary for the plasma position control. The resulting magnetic field lines are highlighted, illustrating their helical form. This figure has been adapted from Ref. [6].*

- **Joint European Torus** (**JET**): The JET device, located at Culham (England), is to date the largest operating tokamak in the world. It was the second machine to operate in D-T mixture, in the '90s [7], and since then a tremendous improvement of the diagnostic capabilities as well as the component material has been introduced. Due to its great size and large power of the external heating systems, this device is unique for the study of the impact of highly energetic ions on the plasma stability, which is the main scope of this thesis. Moreover, JET is the only operating machine that can use Tritium as fuel. The second D-T JET experimental campaign, and the first one in the new millennium for all the fusion device, is currently undergoing (September 2021);

- **Japan Torus-60 Upgrade** (**JT-60U**): The JT-60U device was the japanese tokamak device, operating between the 1991 until 2008, upgraded from the previous JT-60 tokamak. Built in Naka (Japan), it has now been further upgraded to a fully superconducting tokamak, which is now called JT-60 Super Advanced (JT-60SA) device. With its external heating capabilities, JT-60U holds the record for the highest triple product 1.3 ever achieved in a

magnetically confined fusion device.

- **Tokamak à Configuration Variable** (**TCV**): The TCV tokamak is currently operating at Lausanne (Switzerland). It is a unique device thanks to the configuration of the magnetic coils which permits to highly modify the magnetic geometry. Recent development of the external heating systems allows the generation of a substantial population of suprathermal particles, fundamental for the study carried out in this thesis.

1.2 Basic introduction to tokamak plasma description

In this section, the physical fundamentals for the description of the magnetized plasma behaviour are given. Much more comprehensive details on the following models and equations can be found in well-known manuals about magnetized plasma physics and tokamak devices, such as [8, 9, 10, 11] and references therein.

1.2.1 The magnetic equilibrium in tokamaks

It is now briefly introduced the magnetic field equilibrium in a tokamak device and the coordinates that define it. Being the magnetic field in a tokamak a continuous vector field, it is possible to determine the set of tangent vectors, which are usually called magnetic field lines. In order for the charged particles in a plasma to be confined by the field lines, those must lie on a closed surface, which are termed as magnetic or flux surfaces. In a tokamak, a magnetic surface is topologically a torus, and therefore a convenient set of coordinates to describe this geometry is the toroidal coordinates $\mathbf{x} = (\rho, \theta, \varphi)$, where ρ is the label of the magnetic surface, whereas θ and φ are respectively the poloidal and toroidal (axisymmetric) angles. Actually, as it is described later, the magnetic field lines must have both a toroidal and a poloidal components in order for the charged particles to be confined. A schematic view of a circular cross-section toroidal geometry is illustrated in Figure 1.2.

Being the tokamak configuration axisymmetric around the vertical central axis, the equilibrium magnetic field can be written as:

$$\mathbf{B}_{\text{eq}} = \boldsymbol{\nabla}\psi \times \boldsymbol{\nabla}\varphi + I(\psi)\boldsymbol{\nabla}\varphi \tag{1.4}$$

with $I(\psi) = R^2\mathbf{B}_{\text{eq}} \cdot \boldsymbol{\nabla}\varphi$ a flux function of the poloidal magnetic flux ψ. The poloidal flux ψ can also be used to label the magnetic flux surfaces, and hence can represent a sort of radial location in the plasma cross-section. Likewise, the toroidal magnetic flux Φ_{tor} can be used instead of ψ as a radial-relevant coordinate. Their respective definitions are the following:

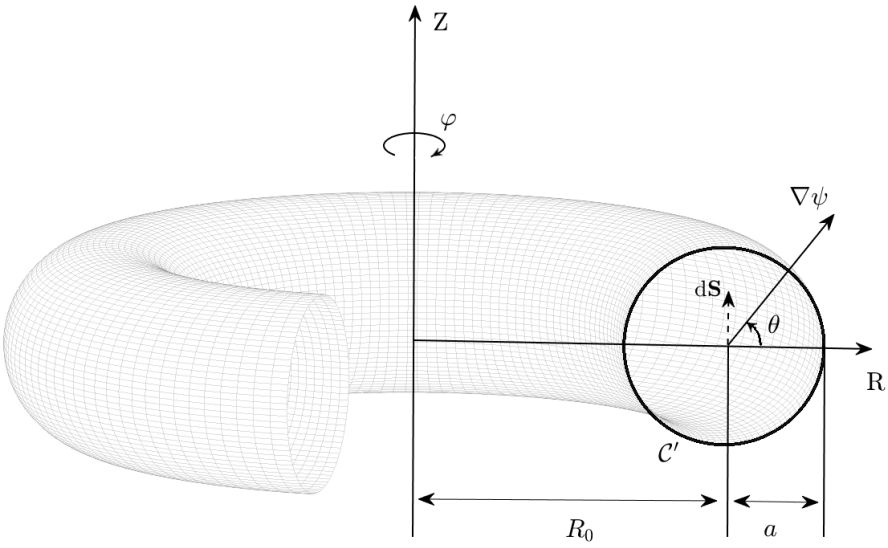

Figure 1.2: *Schematic view of the coordinate system for tokamak magnetic fields. Toroidal coordinates (R, Z, φ) are represented together with the poloidal angle θ, the poloidal magnetic flux ψ with $\mathrm{d}S$ the surface element perpendicular to $\mathcal{C}$ (not represented here), and $\mathcal{C}'$ the surface lying at a constant toroidal angle φ. The major and minor radius of the torus are represented by R_0 and a respectively.*

$$\psi = \frac{1}{2\pi}\int_{\mathcal{C}} \mathbf{B}_{\mathrm{eq}} \cdot \mathrm{d}\mathbf{S} \tag{1.5}$$

$$\Phi_{tor} = \frac{1}{2\pi}\int_{\mathcal{C}'} \mathbf{B}_{\mathrm{eq}} \cdot \mathrm{d}\mathbf{S}' \tag{1.6}$$

where the surface $\mathcal{C}$ is a curve lying on a toroidal cross-section as shown in Figure 1.2 and $\mathrm{d}\mathbf{S}$ is the surface element perpendicular to $\mathcal{C}$, and $\mathcal{C}'$ the surface at a constant poloidal angle symmetric to the torus internal axis with $\mathrm{d}\mathbf{S}'$ the surface element perpendicular to $\mathcal{C}'$. In the remainder of the thesis, the normalized square root of the toroidal magnetic flux $\rho_{tor} = \sqrt{\Phi_{tor}/B_0}$ is often exploited to identify the magnetic flux surface of reference, as well as a meaningful radial coordinate. And so, in the following definitions, it will be preferred to the poloidal magnetic flux ψ, even if they are interchangeable.

Moreover, such a magnetic configuration described by Relation 1.4 determines a helical form of the magnetic field lines in the equilibrium field wrapped up on the flux surfaces. The helicity of the magnetic field lines at each flux surface can be quantified by the well-known parameter of merit the safety factor q, which is defined as:

$$q(\rho_{tor}) = \frac{\mathbf{B}_{\mathrm{eq}} \cdot \boldsymbol{\nabla}\varphi}{\mathbf{B}_{\mathrm{eq}} \cdot \boldsymbol{\nabla}\theta} \tag{1.7}$$

Basically, the q parameter determines the number of toroidal per poloidal revolutions covered by a magnetic field line, and it depends on the flux surface. In case q is a rational number, the magnetic field line close on itself. This does not happen for irrational q, the magnetic field line thereby covering the entire flux surface. Therefore, for each flux surface is possible to calculate the value of q, building thus the q-profile. Another relevant parameter is related to the radial derivative of the safety factor, the so-called magnetic shear, and has the following definition:

$$\hat{s}(\rho_{tor}) = \frac{\rho_{tor}}{q}\frac{\mathrm{d}q}{\mathrm{d}\rho_{tor}} \tag{1.8}$$

All the relations that have been provided above are valid whatever the shape of the magnetic flux surfaces is, although Figure 1.2 illustrates, for the sake of simplicity, a toroidal configuration of the magnetic field with circular and concentric flux surfaces. In such a case, the equilibrium magnetic field admits the following simplified analytic expression:

$$\mathbf{B}_{\mathrm{eq}} = \frac{B_0 R_0}{R}\left(\mathbf{e}_\varphi + \frac{r}{qR_0}\mathbf{e}_\theta\right) \tag{1.9}$$

where $R = R_0 + r\cos(\theta)$ is the major radius and r is the minor radius, $\mathbf{e}_\varphi = R^2\nabla\varphi$ and $\mathbf{e}_\theta = r^2\nabla\theta$. Note that in this case, the magnetic flux used to label the flux surfaces and to describe thereby the radial coordinate has been replaced by the minor radius r.

On the other hand, for realistic configurations in present tokamak devices, the magnetic topology of the flux surfaces presents crucial differences. The first one to be observed is the toroidal expansion of the flux surfaces outward due to the plasma pressure. This leads to have non-concentric flux surfaces, and to an outward radial shift of the center of each flux surface which is generally called the Shafranov shift. In the remainder of the thesis, the symbol α_{S} is used to represent the Shafranov shift. Another important difference concerns the shape of the single flux surface, which departs from a circumference. A schematic view of a non-circular shaped poloidal cross section is reported in Figure 1.3 in which for illustrative purposes the lengths a, b, c and d have been clearly identified. It is thus possible to describe the shape of the magnetic flux surface with the additional parameters κ and δ, respectively referred to as elongation and triangularity, whose definitions are:

$$\kappa = \frac{b}{a} \tag{1.10}$$

$$\delta = \frac{c+d}{2a} \tag{1.11}$$

It is worthy to note that the effects of the plasma shape on the global performance

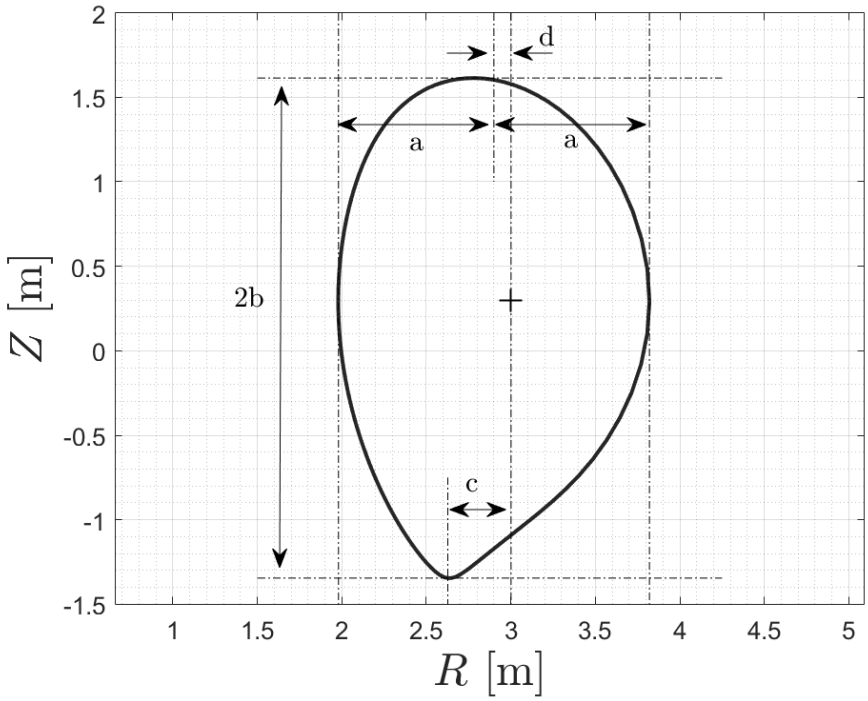

Figure 1.3: *Schematic representation of a flux surface in a non-circular tokamak section, with the definition of dimension parameters useful to describe the plasma shape.*

of the tokamaks have been evidenced in the past. Whereas the high-triangularity regimes have been found to be beneficial for the density confinement both in the plasma core and in the edge [12], more recent experimental findings pointed at better confinement in negative-triangularity regimes [13, 14, 15].

In this context, for the analytical description of the magnetic topology, the well-established Miller parametric model [16] can accurately describe the magnetic configuration with nine parameters, among which the elongation, the triangularity, the local values of q and of the magnetic shear are listed. The Miller parametrization will be used in Chapter 3 to describe the local topology of the equilibrium magnetic field in the numerical modeling.

1.2.2 Modeling of magnetized plasmas towards the δf approach

In order to model the magnetized plasmas, the particle dynamics and the time evolution of the electromagnetic fields must be solved self-consistently. Indeed, particles and fluctuations of the fields interact in a complex system. The collective effects of the particles on the electromagnetic fields are well described by the Maxwell equations [17]:

$$\nabla \cdot \mathbf{D} = \rho \tag{1.12a}$$
$$\nabla \cdot \mathbf{B} = 0 \tag{1.12b}$$
$$\nabla \times \mathbf{E} = -\frac{\partial \mathbf{B}}{\partial t} \tag{1.12c}$$
$$\nabla \times \mathbf{H} = \mathbf{j} + \frac{\partial \mathbf{D}}{\partial t} \tag{1.12d}$$

with $\mathbf{D}$ the displacement electric field, $\mathbf{B}$ the magnetic induction, ρ the charge density, $\mathbf{E}$ the electric field, $\mathbf{H}$ the magnetic field and $\mathbf{j}$ the current density. This set of equations is usually termed as Maxwell macroscopic equations, referring to the dynamics of the electromagnetic fields in a medium, with the following relations:

$$\mathbf{D} = \epsilon_0 \mathbf{E} + \mathbf{P} \tag{1.13}$$
$$\mathbf{B} = \mu_0 \mathbf{H} + \mathbf{M} \tag{1.14}$$

where $\mathbf{P}$ is the polarization field, $\mathbf{M}$ the magnetization field and ϵ_0 and μ_0 the vacuum permittivity and permeability, respectively. For the sake of simplicity, the magnetic field $\mathbf{H}$ will be intentionally confused with the magnetic induction $\mathbf{B}$ in the remainder of thesis, and will be referred to by the symbol $\mathbf{B}$.

It is thus clear that each of the particle dynamics affect the electromagnetic field time evolution by continuously modifying the charge ϱ and current $\mathbf{j}$ density, such as:

$$\varrho(\mathbf{x}, t) = \sum_i e Z_i \delta(\mathbf{x} - \mathbf{x}_i(t)) \tag{1.15a}$$
$$\mathbf{j} = \sum_i e Z_i \mathbf{v}_i \tag{1.15b}$$

where δ is the Dirac delta distribution, e the elementary charge, Z_i the atomic number and $\mathbf{x}_i$ and $\mathbf{v}_j$ the position, respectively, in the spatial and velocity domain of the particle i. As can be seen, to evaluate the charge and density current the information about the whole set of particle trajectories is needed. This can be provided by the integration of the motion's equation together with the expression of the Lorentz force, which are reported in the following:

$$\mathbf{v}_i = \frac{\mathrm{d}\mathbf{x}_i}{\mathrm{d}t} \tag{1.16}$$
$$m_i \frac{\mathrm{d}^2 \mathbf{x}_i}{\mathrm{d}t^2} = e Z_i (\mathbf{E} + \mathbf{v}_i \times \mathbf{B}) \tag{1.17}$$

with m_i the mass of the particle i. Eventually, combining all those relations leads to the possible evaluation of the phase space density for the entire set of particles, i.e.:

$$N(\mathbf{x}, \mathbf{v}, t) = \sum_i \delta(\mathbf{x} - \mathbf{x}_i)\delta(\mathbf{v} - \mathbf{v}_i) \tag{1.18}$$

It should be noted that Equation 1.18 could be written for each species of the considered system. In this first step, the subscript s is avoided for the sake of simplicity.

It is easily understandable that solving the system of partial differential equations, constituted by Relations 1.12, 1.16 and 1.17, for all the particles to obtain the phase space density N would be extremely demanding and even nonessential because of the impossibility of an experimental validation. For this reason, it reveals much more convenient the use of a statistical approach, which consists in measuring the probability distribution function F by integrating the phase space density Relation 1.18 over a volume element $\Delta\mathcal{P} = \Delta\mathbf{x}\Delta\mathbf{v}$. This latter volume element $\Delta\mathcal{P}$ must contain a sufficiently large number of particles for ensuring the statistical property, but must be smaller than the Debye length $\lambda_\mathrm{D} = (\epsilon_0 T_e / n_0 e^2)^{1/2}$. Thus the distribution function is obtained:

$$F(\mathbf{x}, \mathbf{v}, t) = \frac{1}{\Delta\mathcal{P}'} \int_{\Delta\mathcal{P}'} N(\mathbf{x}, \mathbf{v}, t)\mathrm{d}\mathcal{P}' \tag{1.19}$$

with $\mathcal{P}' = (\mathbf{x}, \mathbf{v})$, i.e. the spatial and velocity spaces.

In the absence of particle interactions, like collisions, the Liouville theorem provides that the distribution function F is constant along the trajectories of the total phase space, which implies that the total phase space density is conserved in the time interval Δt. Thus in the collisionless limit, the probability distribution function over the particle trajectory in the whole phase space $\mathcal{P} = (\mathbf{x}, \mathbf{v}, t)$ is conserved. Such a relation is usually known as Vlasov or *kinetic* equation:

$$\begin{aligned} \frac{\mathrm{d}F}{\mathrm{d}\mathcal{P}} &= \frac{\partial F}{\partial t} + \frac{\partial}{\partial \mathbf{x}}(F\mathbf{v}) + \frac{\partial}{\partial \mathbf{v}}(F\mathbf{a}) = \\ &= \frac{\partial F}{\partial t} + \mathbf{v}\cdot\nabla F + \frac{\mathbf{F}}{m}\cdot\nabla_\mathbf{v} F = \\ &= \frac{\partial F}{\partial t} + \mathbf{v}\cdot\nabla F + \frac{eZ}{m}(\mathbf{E} + \mathbf{v}\times\mathbf{B})\cdot\nabla_\mathbf{v} F = 0 \end{aligned} \tag{1.20}$$

where the assumption $\nabla_\mathbf{v}\cdot\mathbf{a} = 0$ is valid only in the absence of collisions, and the force $\mathbf{F}$ acting on the particles is thereby the non-collisional Lorentz force 1.17. In Equation 1.20, only the *collective* effects in the plasma system are retained, which are generated by the particle ensemble.

Those latter effects can be opposed to the *collisional* effects that indeed involve only discrete interactions among the particles and lead to sharp modifications of

the individual particle trajectories in the phase space. Although diverse considerations on the collisions in tokamak plasmas establish that the collisional frequency is somehow negligible with respect to the collective effects (normally associated to the plasma frequency ω_p), it is crucial to retain the collisional effect in the plasma modeling for multiple reasons. First of all, the fusion-born alpha particles mainly heat electrons by Coulomb collisions [18], which then thermalize via collisions with the bulk ion species and allow the self-sustenance of the whole fusion process. Moreover, collisions play a crucial role in the transport dynamics by modifying the particle phase space and thereby the drivers of the possible instabilities arising in the system (see e.g. the following section 1.3). Eventually, without discussing any further the collisions term, the form of the *kinetic* equation with retaining collisional effects is:

$$\frac{\partial F}{\partial t} + \mathbf{v} \cdot \nabla F + \frac{eZ}{m}(\mathbf{E} + \mathbf{v} \times \mathbf{B}) \cdot \nabla_{\mathbf{v}} F = \left(\frac{\partial F}{\partial t}\right)_c \tag{1.21}$$

where in the right-hand side of Equation 1.20, it has been added the term $(\partial F/\partial t)_c$ accounting for the modification of the particle distribution function F due to collisions. It is to be noted that the collisional term in Equation 1.20, as it is reported, defines a collective behaviour, since the whole distribution function F is considered. Such a collisional term may have different interpretations and formulations, with the Fokker-Planck as one of the most commonly used. Because of this, Equation 1.21 is generally referred to as Fokker-Planck equation.

Therefore, the coupling between the Maxwell equations 1.12 and Equation 1.21 allows the statistical self-consistent description of the plasma system, including both particle and field dynamics. Nevertheless, no other assumption has been made on the dimensionality of the phase space, which still considers three spatial and three velocity dimensions. The kinetic set of equations must be hence solved in 6-D for each species considered in the system, leading thus to computationally very demanding efforts. For this reason, additional simplifications are made to reduce the complexity and also the number of degrees of freedom of the system. The former simplification is generally called δf-splitting, whereas the latter dimensionality reduction will be treated in the following section 1.2.5. The δf-splitting relies on the separation of the perturbed distribution function δf (the δ symbol will be dropped out for the sake of simplicity) and the static background counterpart, reported in the following as F_0. This relation can be visualized as $F = F_0 + f$, where it must be stressed that $\langle f \rangle = 0$ with the brackets representing an average over the phase space and the time. A clear distinction on the mathematical ordering of the two terms can be outlined, since the background distribution function F_0 is of order $\mathcal{O}(1)$, while the perturbation is of lower order (precisely $\rho^* = \rho_{ref}/a$, with $\rho_{ref} = m\mathbf{v}_\perp/(eZB)$ the gyroradius). Such an approximation it is widely exploited in the modeling of fusion plasmas (see e.g. Refs. [19, 20, 21, 22]). Moreover, there is experimental evidence that the fluctuations of the electromagnetic fields, as well as of the particle observables such as density and pressure, are much smaller than those of the quasi-static background counterpart. In the δf approach, hence, the background distribution function F_0

does not evolve, and with that also the plasma current. Because of this, the magnetic equilibrium is kept fixed, and thus only the phenomena with a characteristic time smaller than the magnetic field geometry evolution can be described. Yet, as it will be addressed in the remainder of the thesis, such a constraint does not strongly limit the physical relevance of the results obtained in this work.

1.2.3 Fluid moments

In general, the particle distribution function F is not experimentally measurable. Even if F is computed and its expression obtained, an experimental comparison is almost impossible in tokamak plasmas, where the density of the particles is too large to allow such measurements. For this reason, the large amount of information carried by the distribution function can be condensed in more useful expressions by integrating over the velocity space. In this way, the so-called fluid moments of the probability distribution function are computed. In the following, the subscript s indicating the considered species is retained after having been dropped out in the description of the kinetic equations.

The general form of the moment of order k is:

$$\mathcal{M}_s^{(k)}(\mathbf{x},t) = \int \mathbf{v}^k F_s(\mathbf{x},\mathbf{v},t)\mathrm{d}\mathbf{v} \tag{1.22}$$

where the integral is calculated over the entire velocity space and $\mathbf{v}^k$ is defined as the tensor product applied on the velocity space $\mathbf{v}$ k^{th} times. As can be seen, the order of the moment is therefore given by the highest power of the variable $\mathbf{v}$ in the integral. Thus, the first fluid momentum (of order $k = 0$) is the particle density:

$$n_s(\mathbf{x},t) = \int F_s(\mathbf{x},\mathbf{v},t)\mathrm{d}\mathbf{v} \tag{1.23}$$

Whereas, the fluid velocity (second moment of order $k = 1$) is defined as:

$$\mathbf{U}_s(\mathbf{x},t) = \frac{1}{n_s(\mathbf{x},t)} \int \mathbf{v} F_s(\mathbf{x},\mathbf{v},t)\mathrm{d}\mathbf{v} \tag{1.24}$$

From Equations 1.23 and 1.24, it is possible to define also a couple of related moments. Nonetheless, before it is useful to introduce the velocity $\mathbf{u}_s = \mathbf{v} - \mathbf{U}_s$. Thus, the particle charge and current densities are respectively:

$$\varrho_s(\mathbf{x},t) = eZ_s \int F_s(\mathbf{x},\mathbf{v},t)\mathrm{d}\mathbf{v} = eZ_s n_s(\mathbf{x},t) \tag{1.25}$$

$$\mathbf{j}_s(\mathbf{x},t) = eZ_s \int \mathbf{u}_s F_s(\mathbf{x},\mathbf{v},t)\mathrm{d}\mathbf{v} \tag{1.26}$$

To compute the higher order moments, i.e. the pressure and the heat flux tensors (as well as the temperature), the velocity $\mathbf{u}_s$ is also used. Then, the elements p_s^{ij} of the pressure tensor P_s of rank $k = 2$ is defined as:

$$p_s^{ij}(\mathbf{x},t) = \int m_s \mathrm{u}_s^i \mathrm{u}_s^j F_s(\mathbf{x},\mathbf{v},t)\mathrm{d}\mathbf{v} \tag{1.27}$$

where a matrix formulation with i and $j \in 1,2,3$ indicating the position in the pressure tensor has been employed. The velocity components are also indicated by the superscripts i and $j \in 1,2,3$. This formulation enables to decompose easily the pressure tensor P_s in two sub-terms, i.e. the scalar pressure p_s and the traceless stress tensor Π_s, as:

$$P_s = p_s \cdot \mathbb{I} + \Pi_s \tag{1.28}$$

where $\mathbb{I}$ is the unit matrix, and

$$\begin{aligned} p_s(\mathbf{x},t) &= \frac{m_s}{3}\int |\mathbf{u}_s|^2 F_s(\mathbf{x},\mathbf{v},t)\mathrm{d}\mathbf{v} \\ \Pi_s^{ij}(\mathbf{x},t) &= m_s \int \left(\mathrm{u}_s^i \mathrm{u}_s^j - \frac{|\mathbf{u}_s|^2}{3}\delta^{ij}\right) F_s(\mathbf{x},\mathbf{v},t)\mathrm{d}\mathbf{v} \end{aligned} \tag{1.29}$$

with δ^{ij} the Kronecker symbol. Relation 1.29 can be directly related to the definition of the kinetic temperature by remembering the theorem of equipartition of energy for an ideal gas, which states that each of the three degrees of freedom in a translational motion has a third of the total energy, namely $(k_\mathrm{B}T_s)/2$, with k_B the Boltzmann constant. Hence, the temperature can be defined as:

$$\frac{3}{2}n_s(\mathbf{x},t)T_s(\mathbf{x},t) = \frac{m_s}{2}\int |\mathbf{u}_s|^2 F_s(\mathbf{x},\mathbf{v},t)\mathrm{d}\mathbf{v} = \frac{3}{2}p_s(\mathbf{x},t) \tag{1.30}$$

where the Boltzmann constant k_B has been absorbed into the variable temperature T_s for the sake of simplicity.

Finally, the heat flux is defined as:

$$\mathbf{Q}_s(\mathbf{x},t) = \frac{m_s}{2}\int |\mathbf{u}_s|^2 \mathbf{u}_s F_s(\mathbf{x},\mathbf{v},t)\mathrm{d}\mathbf{v} \tag{1.31}$$

The moments $\mathcal{M}_s^{(k)}$ of the probability distribution function F are sometimes referred to as macroscopic quantities, since they describe the plasma as a fluid system.

1.2.4 Wave-particle interaction

In this section, the fundamental mechanism of the resonant interaction between waves and particles, ubiquitous in nature, is presented. Such an interaction constitutes the principal resonant mechanism in a magnetized plasma through which

the instabilities of the resonant kinetic type are excited. Also, some specific external heating systems make advantage of the wave-particle interaction for depositing energy specifically to ions (Ion Cyclotron Resonance Heating, or ICRH) and electrons (Electron Cyclotron Resonance Heating, or ECRH), or to both (Lower Hybrid Current Drive, or LHCD). It is therefore a key aspect to be described for the remainder of the thesis. Yet, it must be stressed that the description of the wave-particle interaction requires a kinetic approach to the problem. In fact, one of the *collective* effects of the charged particles moving in a magnetized plasma is to generate waves. Such waves can thereby interact with the charged particles when particular resonant conditions, taking place in the velocity phase space, are fulfilled. As it has been shown, the fluid moments, through which the fluid equations are derived, lose on purpose the information on the velocity of the particle distribution. Therefore, the fluid approach cannot reflect the wave-particle interaction.

In order to clearly grasp the concept of the wave-particle mechanism, it is useful to calculate the exact solution of the linearized Vlasov Equation 1.20. Reminding the δf-splitting explained at the end of section 1.2.2, the perturbed distribution function is separated from the static background counterpart, with the ordering $f \ll F_0$. As a first step, the Vlasov equation is linearized, reading:

$$\frac{\partial f}{\partial t} + \mathbf{v} \cdot \left(\frac{\partial F_0}{\partial \mathbf{x}} + \frac{\partial f}{\partial \mathbf{x}} \right) + \frac{eZ}{m} \frac{\partial \phi}{\partial \mathbf{x}} \cdot \frac{\partial F_0}{\partial \mathbf{v}} = 0 \tag{1.32}$$

where for the sake of simplicity the magnetic field is neglected ($\mathbf{B} = 0$) and the electric field $\mathbf{E} = -\partial\phi/\partial\mathbf{x}$ (with ϕ the electrostatic potential) is considered as the same order of the perturbed distribution function ($\mathbf{E} = \mathcal{O}(f)$). In Equation 1.32, the second order term $\partial_{\mathbf{x}}\phi \cdot \partial_{\mathbf{v}} f$ has been neglected, and the time derivative of the background distribution function are null since F_0 depends only on the spatial and velocity space.

Once the Vlasov equation has been linearized, it is possible to find the eigenvectors of the perturbed distribution function and of the electrostatic potential ϕ. Those eigenvectors are plane waves of the form $\hat{A}\mathrm{e}^{i(\mathbf{k}\cdot\mathbf{x}-\omega t)}$, with $\mathbf{k}$ and ω the wavevector and the frequency respectively. A brief digression is needed to observe that such plane waves are infinitely extended in time, carrying therefore an infinite energy. From a physical point of view, however, the wave cannot propagate in negative times ($t \to \infty$) and therefore the choice of these eigenvectors is justified. Thus, Equation 1.32 can be rewritten as:

$$0 = -i\omega\hat{f} + i(\mathbf{k}\cdot\mathbf{v})\hat{f} + \mathbf{v} \cdot \frac{\partial F_0}{\partial \mathbf{x}} + i\mathbf{k}\frac{eZ}{m}\hat{\phi} \cdot \frac{\partial F_0}{\partial \mathbf{v}} \tag{1.33}$$

$$= (\omega - \mathbf{k}\cdot\mathbf{v})\hat{f} + \mathbf{v} \cdot \frac{\partial F_0}{\partial \mathbf{x}} + \mathbf{k}\frac{eZ}{m}\hat{\phi} \cdot \frac{\partial \hat{F}_0}{\partial \mathbf{v}} \tag{1.34}$$

from which it is possible to obtain the exact solution as:

$$\hat{f} = -\frac{\frac{eZ}{m}\hat{\phi}\mathbf{k}\cdot\frac{\partial F_0}{\partial \mathbf{v}} + \mathbf{v}\cdot\frac{\partial F_0}{\partial \mathbf{x}}}{\omega - \mathbf{k}\cdot\mathbf{v}} \tag{1.35}$$

The latter relation is useful to highlight the fundamental physical mechanism of the wave-particle resonance. In fact, coupling this relation to the Poisson equation:

$$\begin{aligned}\nabla^2\hat{\phi} &= -eZ\int \hat{f}\mathrm{d}\mathbf{v}\ (+\text{non-resonant terms})\\ &= eZ\int \frac{\frac{eZ}{m}\hat{\phi}\mathbf{k}\cdot\frac{\partial F_0}{\partial \mathbf{v}} + \mathbf{v}\cdot\frac{\partial F_0}{\partial \mathbf{x}}}{\omega - \mathbf{k}\cdot\mathbf{v}}\mathrm{d}\mathbf{v}\ (+\text{non-resonant terms})\end{aligned} \tag{1.36}$$

it is possible to describe the interaction between the electromagnetic field fluctuations and the particle dynamics. It is worthy to notice that Relation 1.36 has been explicitly written for only a single species in the system, not explicating the non-resonant terms of the complete relation. This is consistent with the assumption of the non-overlapping dynamics among the different species, such as electrons and ions. Indeed, as an example, if one singular wave is resonating with a characteristic electron frequency, it is likely not interacting with the ion dynamics.

The concept of the wave-particle interaction is fully represented by the denominator of Relation 1.36, namely the terms $\omega - \mathbf{k}\cdot\mathbf{v}$, which correlates the particle dynamics (the particle velocity $\mathbf{v}$) and the wave parameters (ω and $\mathbf{k}$). It is also important to stress the fact that for the wave-particle interaction to occur, the condition $\omega \sim \mathbf{k}\cdot\mathbf{v}$ is to be fulfilled, and not the exact $\omega = \mathbf{k}\cdot\mathbf{v}$. This is because at the precise point in the phase space where $\omega = \mathbf{k}\cdot\mathbf{v}$, the wave is traveling at the same velocity of the particles and thereby cannot receive or give energy to the particles themselves.

From a physical point of view, therefore, the wave-particle resonant condition is governed by the derivative of the background distribution function in both the spatial and velocity phase spaces, appearing at the numerator of the integrand in Relation 1.36. Such gradients determine the direction of the net energy transfer, either from the wave to the particle or from the particle to the wave. It is now worthy to provide a heuristic illustration of the effect of the spatial and velocity gradients of the equilibrium distribution function. Focusing on the term $\partial_{\mathbf{x}}F_0$, it can be exemplified by the temperature radial gradient of the particle distribution, which is generally negative going from the core to the plasma edge. Considering a narrow plasma region around the flux surface at which the interaction takes place, it is direct to notice that the number of particles with higher temperature is larger than the one with lower temperature, due to the negative slope of the distribution ($\partial_{\mathbf{x}}F_0 < 0$). Therefore, the net energy transfer from the particles to the wave is positive, and the instability grows. In the case of a positive slope of the radial distribution ($\partial_{\mathbf{x}}F_0 > 0$), the opposite occurs: the particles receive energy from the wave which is thereby damped. If now the focus is put on the term $\partial_{\mathbf{v}}F_0$, the conclusions are reversed. Indeed, for a positive slope in the velocity

phase space ($\partial_{\mathbf{v}} F_0 > 0$), there are more particles giving energy to the wave than the ones receiving it. The instabilities is thus driven by the positive gradient of the equilibrium distribution in the velocity space.

1.2.5 Gyrokinetic theory

As already stated, the statistical kinetic description of the particle trajectories in a magnetized plasma is extremely expensive for the present computational resources. Nevertheless, the resonant mechanisms taking place in the velocity space must be taken into account in order to retain the relevant physics for studying the tokamak plasma core, and in particular the results reported in this thesis. For this reason, a well-established theoretical framework is now briefly introduced, which allows to reduce the 6-D system of equations of the kinetic approach to five dimensions. Such a framework is the gyrokinetic approach [23], which will be described in the following. Yet, there could be other interesting solutions to the problem, which rely on the so-called hybrid approach. These are based on the fluid description of the thermal background plasma, while describing a selected species with a fully kinetic model. An example of a numerical code adopting this modeling framework is JOREK [24, 25, 26].

The gyrokinetic theory is based on the adiabatic limit. To fully comprehend the adiabatic limit, it is important firstly to briefly introduce the motion of a charged particle embedded in a magnetic field. Due to the Lorentz force 1.17, the charged particles are constrained to follow the magnetic field lines describing helical trajectories around it. Projecting this trajectory on a plane perpendicular to the magnetic field line, the motion can be seen as a superposition of a guiding-center motion and a gyromotion. Basically, while it is moving along the field line, the particle is rotating around the field line at the so-called cyclotron frequency $\omega_c = |qB/m|$ with a circular trajectory whose radius is the Larmor radius $\boldsymbol{\rho}_{\mathrm{L}} = m\mathbf{v}_\perp/(qB)$. The motion variables can then be written as:

$$\begin{aligned} \mathbf{x}(t) &= \mathbf{X}(t) + \boldsymbol{\rho}_{\mathrm{L}}(\mathbf{X}, \mathbf{v}_\perp, \varphi_c, t) \\ \mathbf{v}(t) &= \mathrm{v}_\parallel \mathbf{b}(\mathbf{X}, t) + \mathbf{v}_\perp(\mathbf{X}, \varphi_c, t) \end{aligned} \tag{1.37}$$

with the term $\mathbf{X}$ representing the guiding center position in space and φ_c the gyrophase. It is relevant now to determine that the characteristic time of the gyromotion and the spatial extension of the ion Larmor radius are much smaller than the characteristic time and spatial scales of the electromagnetic field variations in the whole plasma domain. These conditions can be summarized as:

$$\omega_{EF} \equiv \left| \frac{\partial \log B}{\partial t} \right| \approx \left| \frac{\partial \log E}{\partial t} \right| \ll \omega_c \tag{1.38}$$

$$\left| \frac{\nabla B}{B} \right| \ll \frac{1}{\rho_{\mathrm{L}}} \tag{1.39}$$

with ω_{EF} the characteristic frequency of the electromagnetic field variations. The normalized gradient of the magnetic field, i.e. $\nabla B/B$, can be roughly approximated with the major radius R_0 of the tokamak. It has therefore been set an upper bound to the considered frequencies and a lower bound to the spatial scales in this framework. Any characteristic frequency retained in the gyrokinetic approximation indeed is lower than the cyclotron frequency and the spatial scales of the described phenomena larger than the Larmor radius. These considerations allow the definition of two reference *small* parameters:

$$\epsilon_\rho = \frac{\rho_{\mathrm{L}}}{a} = \rho^* \ll 1 \tag{1.40}$$

$$\epsilon_\omega = \frac{\omega_{EF}}{\omega_c} \sim \rho^* \ll 1 \tag{1.41}$$

In the above described adiabatic framework, the dimensionality of the Vlasov Equation 1.20 (and more in general the Fokker-Planck Equation 1.21) can be reduced from 6-D to 5-D by moving from the particle position to the guding-center set of coordinates. Therefore also the electromagnetic fields must be evaluated at the guiding center position, and to do so a gyroaverage operation is applied. The gyroaverage operator $\mathcal{J}_0(\cdot)$ represents an average over the fast gyromotion around the magnetic field line, which can be expressed as:

$$\mathcal{J}_0(\mathcal{A}) \equiv \frac{1}{2\pi} \oint_{\rho_{\mathrm{L}}=cst} \mathcal{A} \mathrm{d}\varphi_c \tag{1.42}$$

Hence, the distribution function is not anymore dependent on the particle phase space $(\mathbf{x}, \mathbf{v}, t)$, but it is reported as $\bar{F}(\mathbf{X}, \mathrm{v}_\parallel, \mu, t)$, with $\mathrm{v}_\parallel$ the parallel velocity along the magnetic field line and $\mu = mv_\perp^2/(2B)$ the magnetic moment of the particle. Then, the Fokker-Planck equation in the gyrokinetic approximation reads:

$$\frac{\partial \bar{F}}{\partial t} + \mathrm{v}_\parallel \cdot \nabla_\parallel \bar{F} + \mathbf{v}_\perp \cdot \boldsymbol{\nabla}_\perp \bar{F} + \dot{\mathbf{v}} \frac{\partial \bar{F}}{\partial \mathbf{v}_\parallel} = \left(\frac{\partial \bar{F}}{\partial t} \right)_c \tag{1.43}$$

with the operators $\nabla_\parallel$ and $\boldsymbol{\nabla}_\perp$ representing the parallel and perpendicular (to the magnetic field lines) gradients.

After presenting the theoretical bases of the gyrokinetic approximation which have led to a dimensionality reduction of the kinetic Vlasov-Maxwell system of equations and thereby to a more affordable model from a computational point of view, it should be stressed the relevance of such an approach in present modeling frameworks for tokamak plasmas. In fact, the kinetic model allows to explore an extremely wide range of spatial and temporal scales, up to phenomena not of prime interest for the the goal of the present study. It is pertinent to stress again the conditions 1.38 and 1.39, which limit the spatio-temporal scales of the phenomena describable through the gyrokinetic theory. In order to analyze still with a great confidence the cross-field transport in tokamak plasmas, indeed, the gyrokinetic approximation is widely employed and leads to notable results. It must

be stressed however that this approach is limited both spatially and temporally. The physical phenomena of the order of the Larmor radius and of the cyclotron frequency are indeed not retained.

It could be also anticipated that the structures induced by the fluctuations of the electromagnetic fields are strongly anisotropic, preferentially elongated along the parallel direction. In fact, the parallel correlation length is much larger than the perpendicular one, $k_\parallel/k_\perp \sim \epsilon_\rho \ll 1$, meaning that the turbulent structures are moving mainly along the magnetic field lines before experiencing a perpendicular shift. This consideration reveals crucial for the choice of the coordinate system which best exploit such a turbulent feature, and it will be explained in section 2.1.

1.2.6 Orbits of charged particles in toroidal plasmas

In this section, the orbits of charged particles in magnetized toroidal plasmas will be addressed within the already introduced adiabatic limit theory. The particle orbits are considered in the guiding-center coordinates. In the axisymmetric toroidal configuration and neglecting the perturbations of the electromagnetic fields, which excludes the turbulent regimes, it is possible to show that the particle motion can be described by three invariants along the trajectory of the particles. The three invariants of the motion of a charged particle plunged in a static electromagnetic field, within the adiabatic approximation, are the total energy $\mathcal{E}$, the magnetic moment μ and the toroidal kinetic momentum P_φ.

As it is explained in section 1.2.1, the strength of the magnetic field varies with the major radius R of the tokamak as $B \sim 1/R$. Moreover, the magnetic field line lies on the magnetic field surface, and therefore explores the whole poloidal angle in turning around the torus. The same does the charged particle confined by this magnetic field, which hence experiences the variation of the magnetic field in its trajectory, namely the peak and the wells of the magnetic field. The total energy of the particle, in the absence of electrostatic potential is $\mathcal{E} = m_s v^2/2$. The velocity in this latter relation can be decomposed in parallel and perpendicular directions and rewritten in terms of the magnetic moment as $\mathcal{E} = m_s v_\parallel^2/2 + \mu B$. Making explicit the parallel velocity:

$$v_\parallel = \pm\sqrt{\frac{2}{m_s}(\mathcal{E} - \mu B)} \tag{1.44}$$

It should be reminded once again that the electrostatic potential has been considered $\phi = 0$. It is therefore straightforward that, depending on the value of its energy $\mathcal{E}$, the particle can be trapped in specific regions where the term μB describes a well of potential. In other words, when the relation

$$\frac{\mathcal{E}}{\mu} = B\left[1 + \left(\frac{v_\parallel}{v_\perp}\right)^2\right] \leq B_{max} \tag{1.45}$$

is satisfied, with B_{max} the maximum value of the magnetic field in the particle trajectory, the particle cannot exit the potential well. In a given radial r and poloidal

angle θ position, where $\mathcal{E} = \mu B_{max}$, the parallel velocity becomes null, and so the particle has only perpendicular velocity. Therefore, the particle is forced to change the sign of the parallel velocity periodically, bouncing thus back and forth in such specific regions of the torus. When instead the energy of the particle is $\mathcal{E} > \mu B_{max}$, the parallel velocity does not change sign along the particle trajectory, continuing thereby its unperturbed motion. In the latter conditions the particle is named *passing*, whereas in the former the particle is a *trapped* particle. From Relation 1.45, and reminding the radial dependence of the magnetic field strength – which can be approximately expressed as $B_{max}(r) = B_0(1 + \epsilon(r))$ – the trapping condition can be given as:

$$\frac{v_\parallel}{v_\perp} \leq \sqrt{2\epsilon} \tag{1.46}$$

This latter condition, depending on the poloidal angle θ due to the magnetic field variation along the radial direction, represents the boundary condition between passing and trapped particles at the outer mid-plane, i.e. $\theta = 0$.

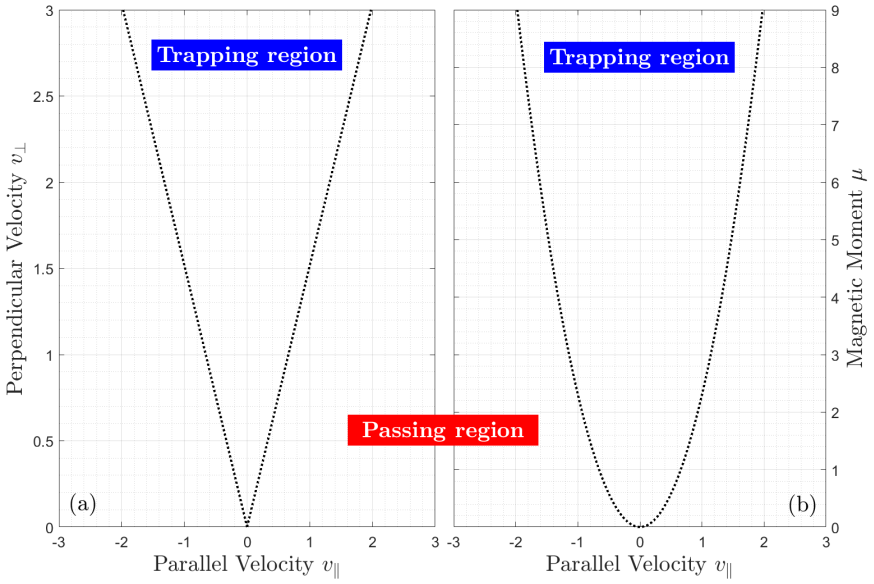

Figure 1.4: *Example of velocity phase space with the definition of the trapped/passing particle boundary region. Particle are trapped within the dashed boundary curves, termed trapping cone, and are passing outside. In panel (a), the velocity space is represented in* $(v_\parallel, v_\perp)$*, whereas in (b) in* $(v_\parallel, \mu)$*.*

It can also be shown that, in the ($v_\parallel$, $v_\perp$) space, the trapped and passing regions are delimited by a cone, as illustrated in panel (a) of Figure 1.4. The same condition in the equivalent ($v_\parallel$, μ) space is indeed described by a parabola, shown in panel (b). It should be also stressed that the trapping condition is not always a sharp transition from one particle behaviour to another one, but indeed some barely trapped or passing particles may exist at the boundary layer in the velocity space.

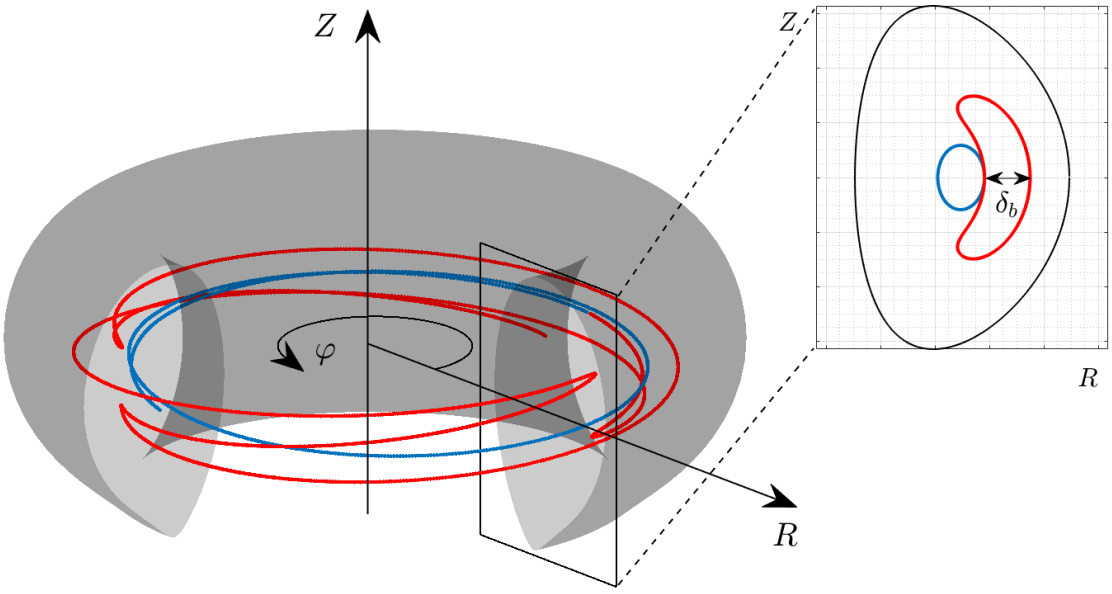

Figure 1.5: *The representation of the toroidal plasma system (taken from the MHD reconstruction of JET pulse #94701), including the charged particle orbits embedded in the magnetized plasma, is illustrated. The blue trajectory represent a passing particle, while the red one a trapped particle. The inset on the top-right of the figure represents the projection of the charged particle orbits on the poloidal cross section of the toroidal plasma, with δ_b indicating the width of the banana orbit.*

It is also instructive to look at the particle orbits along the magnetic field line for the two described conditions. Thus, in Figure 1.5, a 3-D plot of the whole toroidal plasma region of the JET pulse #94701 is reported, in which the passing particle trajectory is represented by the blue curve, whereas the trapped orbit is in red. Moreover, in the inset of Figure 1.5, the projection of the two described orbits – from these example particles – on the poloidal cross section is illustrated. It can be seen that the trapped particle experiences a banana-shaped orbit on the poloidal section, and therefore such particles can be also called banana particles. The width of the banana shape can be computed using the conservation of the toroidal kinetic momentum $P_\varphi = m_s R v_\varphi + e Z_s \psi(r)$ and approximating the toroidal velocity with the parallel velocity, i.e. $v_\varphi \sim v_\parallel$, in order to employ Relation 1.46. The final results is:

$$\delta_b = \frac{2q\rho_{\mathrm{L}}}{\sqrt{\epsilon}} \tag{1.47}$$

It can be seen that the banana width can be larger by almost an order of magnitude with respect to the Larmor radius. Therefore, from a simplistic calculation, in ITER the width of the banana orbits for a fusion born alpha particle in the plasma core is predicted to be of the order $\delta_b \sim 0.3$ m.

Eventually, another point is worthy to be mentioned: from the conservation of

the toroidal kinetic momentum, it could be shown that the orbits of the charged particles embedded in an unperturbed toroidal magnetic field depart from the magnetic flux surfaces. Basically, the passing particles follow the magnetic field lines only in a first approximation. This stems from the variation of the poloidal flux ψ along the particle trajectory and can be quantified as:

$$\delta_r = \frac{q\rho_{\mathrm{L}}}{\epsilon} \tag{1.48}$$

This consideration is also useful to explore a subtle point that is often misinterpreted. In fact, the trapping condition 1.46 has been derived with important approximations, among which only thermal particles have been considered. As it has already been hinted and will be fully introduced in the next section, in tokamak plasmas a significant population of energetic ions exists. Thus, a particular characteristic of those particles is to have parallel velocities much larger than those of bulk ions. Therefore, the shift from the magnetic flux surface for these much energetic ions is very significant. This has also an implications on the trapping condition of such particles. In fact, whereas the trapping cone in the velocity space for the bulk species can be considered approximately symmetric, this is not the case for the more energetic ions, whose large parallel velocities prevent the trapping condition to be fulfilled for co-passing particles ($v_\parallel < 0$). Therefore, a non-symmetric trapping region in the ($v_\parallel$, $v_\perp$) space (subsequently also in the ($v_\parallel$, μ) space) is obtained. An example of such particular features will be addressed also in section 3.3.4.

1.3 Introduction to instabilities in tokamaks

The feasibility of the nuclear fusion reaction as an alternative energy source is largely undermined by the arising instabilities which lead, in the nonlinear regime, to the so-called turbulent transport. Such turbulent transport dominates over the neoclassical (collisional) transport [27] by more than an order of magnitude, and limit thus the confinement performance of the present fusion devices. However, since a magnetized fusion plasma is an out-of-equilibrium system, instabilities are almost inevitable. A small perturbation of the electromagnetic field can lead to fluctuations of the particle distribution function, as illustrated by Relation 1.35. Indeed, in the presence of steep gradients of the particle distribution function both in the spatial $\mathbf{x}$ and velocity $\mathbf{v}$ phase space, the original perturbation can grow unstable. In this sense, the gradients $\partial_{\mathbf{x}} F_0$ and $\partial_{\mathbf{v}} F_0$ represent the reservoir of free energy for the growing instabilities. Although the instabilities in a magnetized plasma can be of the most diverse nature, in the remainder of this thesis the main focus will be put on the microinstabilities and on the high-frequency fast-ion-driven instabilities.

Microinstabilities are so called because of the spatial scales at which they develop, which is in the order of the ion Larmor radius ρ_i. Another intuition on the difference between microinstabilities and the fluid or large-scale instabilities

can be made upon the exciting mechanism. In fact, the macroscopic instabilities affects a largely extended region of the entire plasma volume. On the other hand, the microinstabilities interacts with only a reduced number of particles. Moreover, this wave-particle interaction can take place both in the spatial space, due to the steep radial gradient, and in the velocity phase space. Although their contribution to the total radially outward transport may seem modest, microinstabilities have been demonstrated to strongly limit the performance of the present devices [28, 29, 12], defining the plasma insulation and thereby the fusion yield.

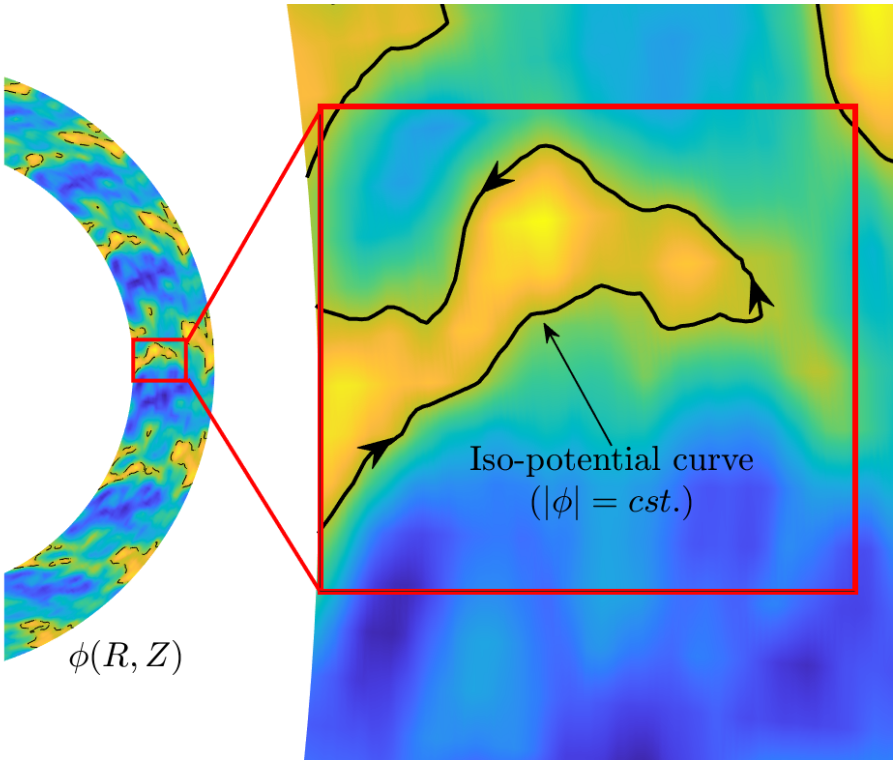

Figure 1.6: *Illustration of the radially elongated convective cells induced by microinstabilities in a portion of a circularly shaped poloidal cross section of a tokamak plasma. The view on the right is a zoom over a specific region of the poloidal section, with the solid line highlighting the curves at iso-potential ($\phi = cst.$).*

It is worthy to provide a heuristic explanation of the transport induced by the microinstabilities. As an illustrative picture, Figure 1.6 shows a portion of a poloidal cross-section, with the inset representing the zoom on a smaller region. The bold curves highlight the isocontour levels of the electrostatic potential perturbations. A particle traveling along the magnetic field lines can thus encounter such a convective cell, which is radially elongated, and can be trapped within. Hence, these convective cells effectively link the inner core to the outer regions of the system. Thus, the particle are forced to follow the isocontour curves and experience a transport outwards. In this manner, both particle and energy (carried by the particles) are radially transported towards the outer regions.

Being the plasma in thermodynamical equilibrium accurately described by the isotropic Maxwellian distribution function, which decays at higher energies of the particles, the so-called fast ions (or energetic ions) are expected to only slightly affect the plasma stability. Yet, in present and future fusion devices, fast ions, with an energy much larger than the bulk particles, are inevitable. First of all, alpha particles with 3.5 MeV of energy are the products of the total fusion reaction, essential to sustain the total process by transferring their energy to the thermal part of the plasma by Coulomb collisional interactions. Moreover, fast ions can also be externally generated – and generally they are – in fusion tokamak experiments, with the aim of heating the bulk particles. The main ion heating systems currently employed in tokamaks are the Neutral Beam Injection (NBI) and the Ion Cyclotron Resonance Heating (ICRH). The NBI mechanism is based on the injection of neutral particles which can penetrate thus the confining magnetic field (charged particles would be rejected and bounced back by the magnetic field). Subsequently, such neutral particles undergo a ionization process via the interaction with the charged plasma particles and enrich the suprathermal population. Eventually, they exchange energy by collisions with the bulk part of the plasma, transferring in such a way the original beam energy to the final target. The ICRH relies on the generation of waves within the plasma at the desired frequency which is absorbed by the particles via wave-particle interactions (described in section 1.2.4). In this specific case of the ICRH, the desired frequency is the ion cyclotron frequency ω_{ci}. The ions that absorb the wave energy become suprathermal particles, heating subsequently the thermal part of the plasma again through Coulomb collisional interactions. Both systems are therefore largely used in present devices to heat the bulk plasma. They generate a substantial population in the tail of the Maxwellian particle distribution. The distribution function can also present a bump in the tail, leading to a positive gradient in the velocity phase space. Such distribution functions, both monotonic and non-monotonic, may have a detrimental effect on the plasma stability, as it is also illustrated by Relation 1.35. Indeed, instabilities can grow due to the steep gradients both in spatial and velocity phase space, resulting in a significant transport of the fast ions outwards. Yet, fast ions, and in particular the fusion-born alpha particles, must be well confined in order to have the time for the slowing-down process which ensures the heating of the bulk plasma and the self-sustaining of the fusion reaction. The transport of the suprathermal particles may also result detrimental for the plasma facing components which are damaged by the fast ions more intensively than by the thermal particles. The wide range of fast-ion-driven modes will be limited to a general introduction of these instabilities and to a specific class of undamped modes in the magnetized plasmas, called Alfvénic modes. The description of such instabilities is reserved to the following sections.

Therefore, as already described, a first classification can be made based on the particles that excite the instability. In contrast to the fast-ion-driven modes, the general belief for the microinstabilities is to consider them to be driven by the bulk particles, at a much lower energy with respect to the fast ions. Therefore, in the following such a classification will be exploited to present the various plasma

instabilities that are the main topic of this thesis. So, in the next section, the main mechanism and the most common plasma instabilities excited by the thermal particles in tokamaks are presented. The fast-ion-driven modes indeed are treated in section 1.3.2.

1.3.1 Microinstabilities driven by the thermal particles

The microinstabilities driven by the thermal particles can be further classified based on the excitation mechanism. After describing the fundamental mechanism of the drift wave, a heuristic explanation of the drift-wave and interchange instabilities will be given in the following paragraphs. Both instabilities are generally present in tokamak plasmas, and while the latter occurs in the 2-D *flute* approximation (i.e. along the magnetic field line direction), the former instability requires a three dimensional description. Then, the principal microinstabilities responsible of the anomalous transport in tokamaks, and also important for the comprehension of the remainder of the thesis, are described and treated individually.

Drift wave instability

The drift wave is a perturbation originated by the fluctuations of the electrostatic potential and the particle density, which can concern both electrons and ions. In this context, the *adiabatic* electron response is a relevant approximation. It assumes that the electrons, which have a very low inertia, promptly accommodate any perturbation of the electrostatic potential, which can be expressed by a plane wave of the form $\delta\phi \mathrm{e}^{i(k_y y-\omega t)}$. Thus, in the limit $\omega \ll k_{\|} v_{th,e}$, the electron density perturbation δn_e is in phase with the electrostatic potential perturbation $\delta\phi$, and the fast motion of the electrons along the parallel direction allows the Boltzmann description of the electron response to the electrostatic potential perturbation:

$$\frac{\delta n_e}{n_e} \simeq \frac{e\delta\phi}{T_e} \tag{1.49}$$

where the assumption of isothermal conditions has also been employed. Thus, in the framework of the adiabatic electron response, the resulting oscillation of the electrostatic potential is a wave propagating along the y direction, as also illustrated in Figure 1.7(a). The drift wave frequency ω is of the order of the electron diamagnetic frequency $\omega_e^* = k_y T_e/(eBL_n)$, where $L_n^{-1} = -\partial_x log(n_e)$ is the normalized density gradient scale length.

Nevertheless, the electron density and the potential can be de-phased by various mechanisms, such as the plasma resistivity and wave-particle resonant interactions. For the phase shift to occur, a force acting on the electrons along their parallel motion is needed. When this occurs, it will be shown that net result is that the original perturbations of the density grow, leading to the so-called drift-wave instability. Figure 1.7(b) is useful to depict this excitation mechanism, in the presence of a static magnetic field directed along z. It is indeed clear that

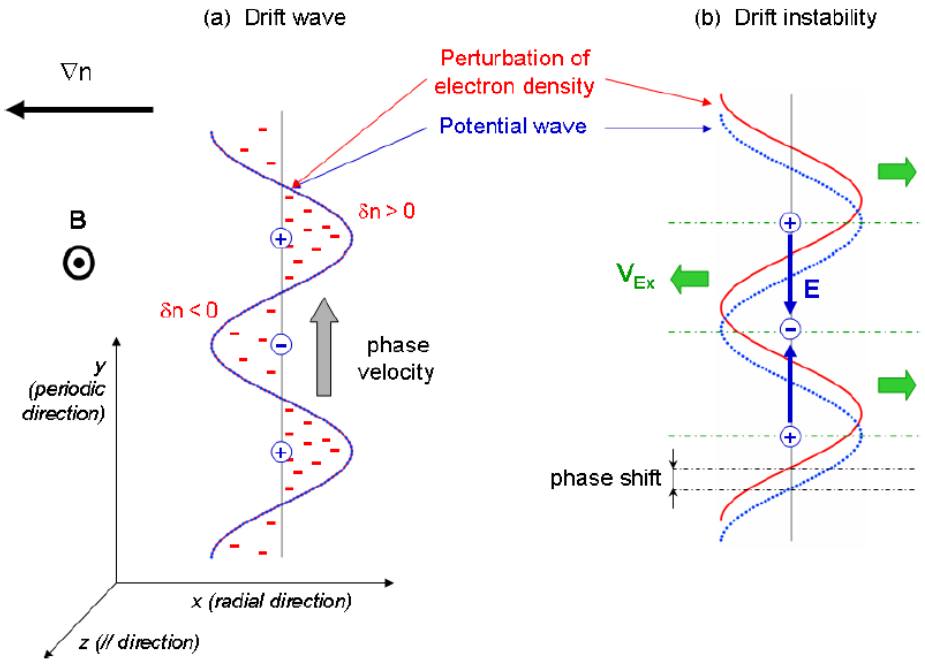

Figure 1.7: *Schematic representation of drift wave generation (a) and drift wave instability exciting mechanism (b). This figure has been adapted from Ref. [30] with permission of Yanick Sarazin.*

the $E \times B$ drift velocity has now a radial x component which tends to amplify the sinusoidal shape of the perturbed particle density, and increase thereby the fluctuation amplitude of the respective perturbed regions.

Eventually, it must be stressed that such destabilizing mechanism is effective not only in the case of particle density perturbation. The same reasoning can also be applied to an original perturbation of the electrostatic potential which is found to be not in-phase with that of the particle temperature. This latter condition is often present in current tokamak devices, and the resulting instabilities will be discussed in the next paragraphs.

Interchange instability

The name of the interchange instabilities is after the fundamental mechanism leading to the excitation, which is based on the interchanging of two convective cells elongated in the parallel direction. Figure 1.8 shows a schematic representation of the interchange mechanism in a poloidal cross section, in which the key role of the magnetic field inhomogeneity and radial gradients of the plasma parameters in a toroidal configuration is highlighted. It is also highlighted here that, unlike the drift-wave type, interchange-like instabilities required a toroidal geometry of the system to be explained. The elliptic structures represent a contour line of a region at constant electrostatic potential, thus fluctuating with a positive ($\delta\phi > 0$) or negative ($\delta\phi < 0$) perturbations from the background static field. The

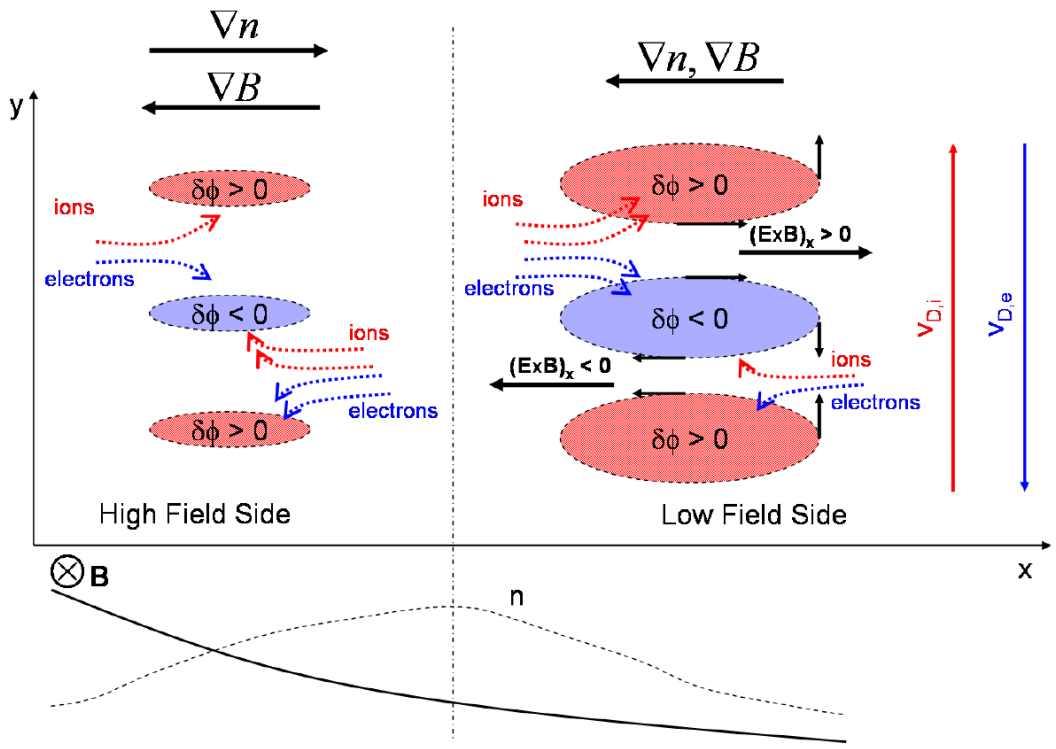

Figure 1.8: *Schematic representation of the interchange exciting mechanism in a toroidal system configuration. This figure has been adapted from Ref. [31] with permission of David Zarzoso.*

opposite polarization of these convective cells generates an electric field, which is directed from the positive cells to the negative ones, following the common convention. Being the plasma system embedded in a magnetic field (here considered to be static for simplicity), the $E \times B$ drift velocity perturbs the particle motion, for both ions and electrons, along the radial direction, and in the illustration is represented by the black arrows. In the toroidal configuration here considered, the curvature drift velocity contributes to the particle motion depending instead on the particle charge, bringing the ions upwards and the electrons downwards. The total particle motion is illustrated by the dashed arrows in Figure 1.8. It is, thus, clear that in the Low Field Side (LFS) of the poloidal cross section (right region of the schematic view), the density radial gradient for both ions and electrons lead to the growth of the convective cells, and to the subsequent appearance of the instability. In fact, the electrons filling the negative convective cell and coming from the magnetic axis are more numerous than the ions coming from outer regions, and thus the final balance results in a net increase of the charge accumulation. The same explanation applies also to the positive perturbation of the isopotential cell, obviously switching the electrons with the ions. At the same time, it is also clear that such a mechanism is damped in the High Field Side (HFS), where the density gradient and the magnetic field gradient are pointing in opposite directions ($\nabla n \cdot \nabla B < 0$). For this reason, the convective cells, represented by smaller

structures in Figure 1.8, are damped by the particle motion. This is frequently observed in experiments and in numerical studies of tokamak plasma stability. Moreover, this latter consideration will reveal extremely relevant when the configuration of the negative magnetic shear, obtained in particular experimental conditions and treated in section 3.7, leads to a beneficial effect on the thermal confinement. As it will be explained in that section, the negative magnetic shear configuration leads to a twisting of the convective cells (in that precise case of the flux-tubes) which thus spend more time in the HFS than in the LFS. Such a beneficial twisting, therefore, results in a decrease of the instability growth rate.

Brief excursus: Main microinstabilities in the core of tokamak plasmas

After having described the two principal processes for the instability excitation, a brief excursus on the most common instabilities driven by the thermal particles is given. Reminding the fundamental wave-particle mechanism discussed in section 1.2.4, the kinetic approach to such a topic can be easily framed by Relation 1.35. Indeed, while the denominator of this relation represents the wave-particle interaction, the numerator provides the drive of such a fundamental mechanism, and as can be seen this is determined by the gradients of the distribution function in both spatial and velocity spaces.

As it has emerged during the description of the drift-wave and interchange instabilities, the radial gradient of the physical parameters that can be derived by the particle distribution function is a key ingredient for the wave destabilization. Specifically, likely the most common microinstability considered in tokamak plasmas is the Ion Temperature Gradient (ITG) modes [32]. The ITG modes are driven by the finite radial gradient of the thermal ion temperature, and can be subdivided in two different branches: in the slab branch, the destabilizing mechanism for the ITG is fully represented by the drift-wave type of instability, whereas the toroidal branch requires the introduction of the magnetic field curvature, as it occurs in the interchange type of instability.

The ITG modes have a companion instability at the electron scales, always driven by the finite radial temperature gradient (of the electrons in this case), and hence called Electron Temperature Gradient (ETG) modes [33, 34, 35]. As a crucial difference, ETG modes are driven at spatial scales close to the electron gyroradius ρ_e, which is much smaller than the thermal ion gyroradius ρ_i, at which the ITG modes instead develop.

Another tokamak-relevant instability, driven by the motion of the trapped electrons, can be identified. This is the so-called Trapped Electron Mode (TEM) [36, 29], which is excited through a resonance in the velocity space with the toroidal precessional frequency of the trapped electron motion. Although the excitation mechanism of TEMs concerns the characteristic velocity of the trapped electrons, the main contribution to the destabilization comes from the steep radial gradient, i.e. from $\partial_x F_0$ in Relation 1.35. In fact, the main drivers for the TEMs are generally the radial gradients of electron temperature and density. The TEMs are often destabilized in present devices, and therefore constitute an im-

portant source of outward *anomalous* transport. Despite being driven by the electrons, TEMs develop at the thermal ion scales, and are mainly stabilized by the electron-ion collisionality [13, 37].

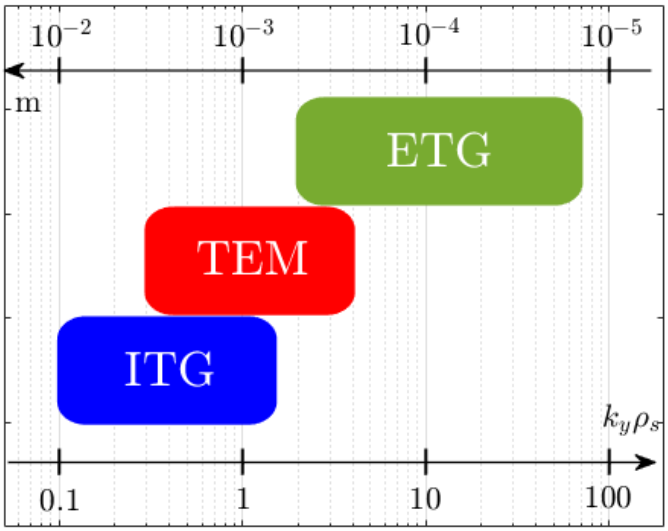

Figure 1.9: *Schematic view of the spatial scales at which the main treated microinstabilities in this thesis, namely ITG, TEM and ETG, develop.*

Eventually, a simple scheme is reported in Figure 1.9, summarizing the main differences in the spatial scales of the above described microinstabilities. As a final remark, it should be stressed once more that the context describing the excitation mechanisms here reported is purely electrostatic. This choice has been done for the sake of simplicity. Nevertheless, the introduction of fluctuations in the magnetic field does not alter consistently the described picture. Indeed, ITG, ETG and TEMs are mainly electrostatic instabilities [29], with a clear dependence on the magnetic pressure only for the ITG modes [38].

1.3.2 Instabilities driven by the fast ions

Both fusion born alpha particles and externally generated fast ions have been shown earlier to modify the tail of the ion distribution function. As it is illustrated by Relation 1.35, and as already described earlier, the contribution to the destabilization of the fast-ion-driven instabilities can come from both spatial gradients of the equilibrium distribution, namely the radial gradients, and from the gradients in the velocity phase space. Fusion-born alpha particles are expected to have a monotonic slowing-down distribution. In this case, therefore, the main drive of the eventual alpha-driven instabilities is the slope of the equilibrium distribution function in the spatial phase space. In the case of a non-monotonic distribution

function, the main drive of the instabilities is instead the so-generated bump in the velocity phase space. A schematic representation of such a bump is illustrated in Figure 1.10.

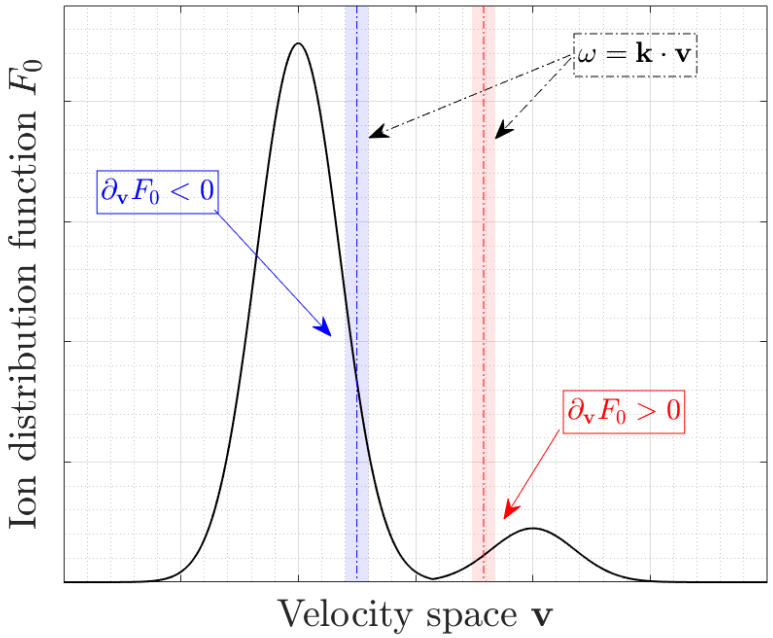

Figure 1.10: *Example of a non-monotonic ion distribution function in the velocity space. Indications on the sign of the gradient in the velocity space are reported, highlighting thus the excitation mechanism for instabilities in plasmas via wave-particle resonance mechanism.*

As it is explained in section 1.2.4, the wave-particle interaction is strongly determined by the terms $\partial_{\mathbf{x}} F_0$ and $\partial_{\mathbf{v}} F_0$, defining the direction of the energy transfer, from the particle to the wave in case $\partial_{\mathbf{x}} F_0 < 0$ and $\partial_{\mathbf{v}} F_0 > 0$ or from the wave to the particle in case $\partial_{\mathbf{x}} F_0 > 0$ and $\partial_{\mathbf{v}} F_0 < 0$. The former cases can be associated to excitation mechanisms, while the second to damping mechanisms. Therefore, the steep monotonically decrease radial gradients and the generation of a bump in the ion distribution function can both trigger fast-ion-driven instabilities. These instabilities in turn can be deleterious for the plasma stability. Fast ions transferring their energy to the wave are thus transported from the hot region of the plasma to the edge, where lower temperatures are reached.

It is thus shown that the fast ions can have a strong impact on the plasma confinement, destabilizing severe instabilities impairing the overall performance of the devices. In this section, the main focus will be put on the description of two particular instabilities in the whole wide zoology that has been built and continuously fed during the last decades. Comprehensive topical reviews can be found in Refs. [39, 40, 41, 42, 43].

Shear Alfvén Waves

The first analyzed instability excited through the interaction with fast ions are the so called shear Alfvén waves (SAW). These instabilities are occurring at larger spatial scales and higher frequency range with respect to the microinstabilities driven by the thermal particles, which have been introduced earlier (cf. section 1.3.1). They are extremely relevant in the framework of the energetic particles, since their propagating velocity in the tokamak plasmas is in the range $v_{\mathrm{A}} = B_0/\sqrt{4\pi\rho_d}$, with ρ_d the plasma mass density. Such a velocity, which is the Alfvén velocity, is in the range of the motion dynamics of the energetic particles in tokamak plasmas, and therefore wave-particle interactions are expected to occur. In the following, a basic introduction to the physical framework of the SAW excitation is given by firstly introducing the Alfvén waves.

Alfvén waves are waves propagating in the parallel direction with respect to the magnetic field lines due to perpendicular perturbation of the equilibrium magnetic field [44]. Alfvén waves always exist in a conducting fluid – as it is the plasma – plunged in a external magnetic field, whatever the geometry of the system is. If tokamak plasmas are considered, it is thus introduced the bending of the magnetic field lines and the magnetic shear $s = (r/q)(dq/dr)$, as already seen in section 1.2.1. Taking this into account, Alfvén wave velocity varies within the plasma region with a radial dependency. Because of this, the Alfvén waves in tokamaks are called Shear Alfvén waves. The SAW general dispersion relation, obtained in the incompressible ideal MHD limit (i.e. for $E_{\parallel} = 0$) and in a cylindrical configuration, takes the form of:

$$\omega^2_{SAW} = k^2_{\parallel}(r)v^2_{\mathrm{A}} = \left(\frac{m - nq(r)}{q(r)R_0}\right)^2 v^2_{\mathrm{A}} \tag{1.50}$$

Such a dispersion relation 1.50 is satisfied at all different radial positions (r) by a singular solution depending on the value of $k_{\parallel} = (m - nq)/qR_0$. All together, those solutions form the Alfvén *continuum* for the various $k_{\parallel}$ values. An example of the Alfvén continua is shown in Figure 1.11 for a constant toroidal number n and successive poloidal mode numbers m. Hence, if a wave propagating in the plasma satisfies the dispersion relation 1.50, it is a singular solution with the form (for a complete derivation the reader can refer to [45]):

$$v_p(r,t) \simeq \mathcal{A}(r,t)\frac{e^{i\omega_{SAW}(r)t}}{t} \tag{1.51}$$

where v_p is the component of the perturbation velocity in the radial direction and $\mathcal{A}$ is a function representing the response amplitude to the initial perturbation. It can be seen thus that such a solution has a decaying time evolution. This behaviour can be related to a damping mechanism, which is usually called *phase mixing* effect or continuum damping [46, 47]. Therefore, any Alfvén wave with a specific frequency of propagation crosses the continua in the radial movement at least once. SAWs are thus damped, and it is unlikely that instabilities can grow.

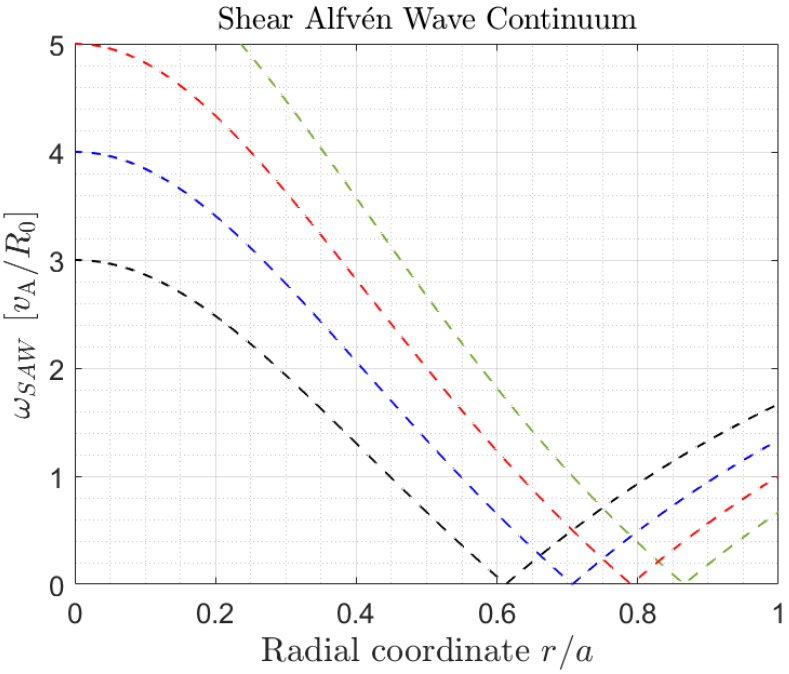

Figure 1.11: *Shear Alfvén wave continuum in cylindrical geometry obtained by plotting Relation 1.50 over the normalized radial direction r/a. For the sake of completeness, these continua referred to $n = 4$ and $m = [-10, -7]$.*

However, in a more realistic configuration of the plasma system, gaps are opened in the continuous spectrum, and in these gaps SAWs are not anymore damped. Hence, SAWs can interact with the particles and exchange energy, growing thereby unstable. The existence of frequency gaps is a ubiquitous phenomenon in Nature [48]. Several diverse gaps in the continua can be opened in function of the approximations on the magnetic geometry that have been relaxed. As already observed in section 1.2.1, the magnetic field topology of the present tokamaks strongly deviates from a circular, large-aspect ratio configuration. As a first order approximation, the toroidal configuration modifies the SAW dispersion relation 1.50. In the same way, other minor-order geometrical effects may arise and open different gaps in the Alfvén continua. Those are, e.g., the gaps induced by the elliptic (or non-circular) and by the non-up-down-symmetric (or triangular) shape of the poloidal cross section.

Focusing now on the effects on the Alfvén spectrum induced by the system toroidicity, the dispersion relation of the SAWs presents the coupling of singular solutions for neighboring poloidal mode numbers, m and $m + 1$. Thus, the dispersion relation for the two coupled branches reads as [49]:

$$\omega^2_{TAE} = \frac{k^2_{\parallel,m} v^2_A + k^2_{\parallel,m+1} v^2_A \pm \sqrt{(k^2_{\parallel,m} v^2_A - k^2_{\parallel,m+1} v^2_A)^2 + 4\epsilon^2 r^2 k^2_{\parallel,m} v^2_A k^2_{\parallel,m+1} v^2_A}}{2(1 - \epsilon^2 r^2)} \tag{1.52}$$

where the two branches of the coupling could be termed as ω^{+}_{TAE} and ω^{-}_{TAE}. It could be shown that at the crossing of the two continua for the consecutive poloidal modes, a gap appears. An example is reported in Figure 1.12, where only two continua are shown. Over-plotted are the continua as obtained from the dispersion relation 1.52, including therefore the toroidicity-induced effects. It can be appreciated that the two different continua are almost overlapping in the whole radial coordinate, except for the crossing point, occurring around $r/a = 0.75$, where the two branches ω^{+}_{TAE} and ω^{-}_{TAE}, illustrated in violet solid lines, open a gap. The inset over the specific location facilitates the gap identification. Global

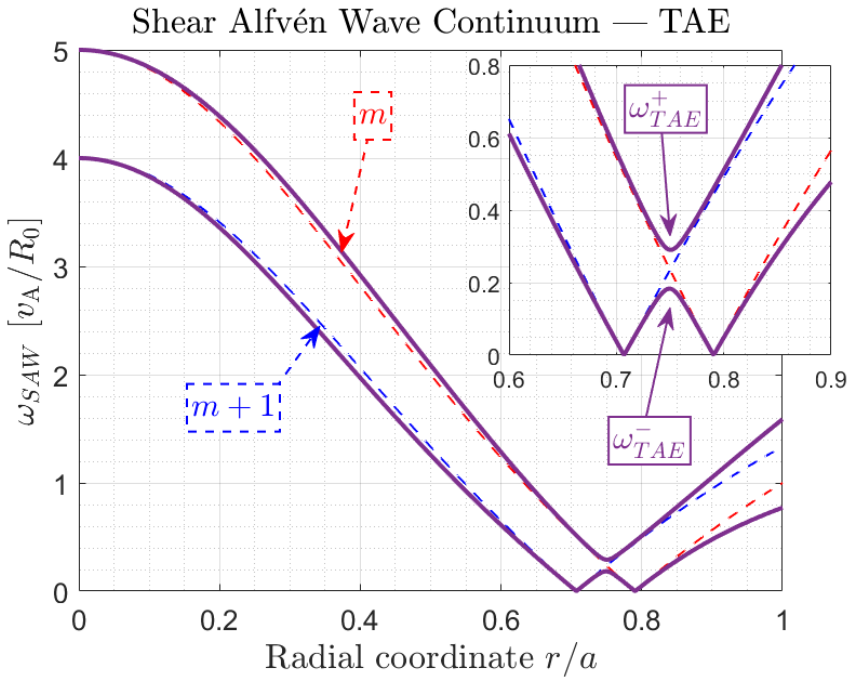

Figure 1.12: *The shear Alfvén wave continuum in toroidal geometry obtained by plotting Relation 1.52 over the normalized radial direction r/a is plotted in purple. Here, $n = 4$, $m = -9$ and $m + 1 = -8$. The red and blue dashed curves are the continua obtained in cylindrical geometry.*

Alfvén waves are thus not damped by phase mixing effects within this gap, and their unstable growth is possible. The non-damped eigenfunctions living in this gap induced by the toroidicity of the plasma system are called Toroidal Alfvén Eigenmodes (TAEs) [50, 51, 49].

A brief parenthesis could be opened about the width and the center position of the toroidicity-induced gap in the SAW spectrum. As it can be easily appreciated, the SAW dispersion relation depends on the value of the q-profile, which is generally a monotonically increasing function of the radial coordinate in tokamaks. Thus, the center of the frequency gap, located at $\omega = v_A/(4\pi qR)$, slowly bends down going outwards. The width of the gap depends on the magnetic

field strength, which in turn is decreasing when the radial coordinate increases. Hence, as the $\Delta B = B_0 - B(r)$ decreases – or otherwise, as the radius is increased – the width of the gap gets larger.

It is now addressed another limit of the SAW dispersion relation in a cylindrical geometry in the incompressible ideal MHD approximation, namely Relation 1.50. In the specific, it has been experimentally observed [52] and theoretically explained [53, 54] that fast ions can excite Alfvénic modes lying in a frequency range below the TAE gap. Indeed, a frequency gap in the Alfvén continuum is open when the incompressibility assumption is relaxed. In this gap induced by the finite β value, eigenmodes can live undamped, similarly to what occurs in the TAE gap, and can resonate with a characteristic frequency of the fast-ion motion, being thus excited. The instability arising is the so-called beta-induced Alfvén eigenmode (BAE) [52]. If the toroidicity-effects are neglected at this stage for the

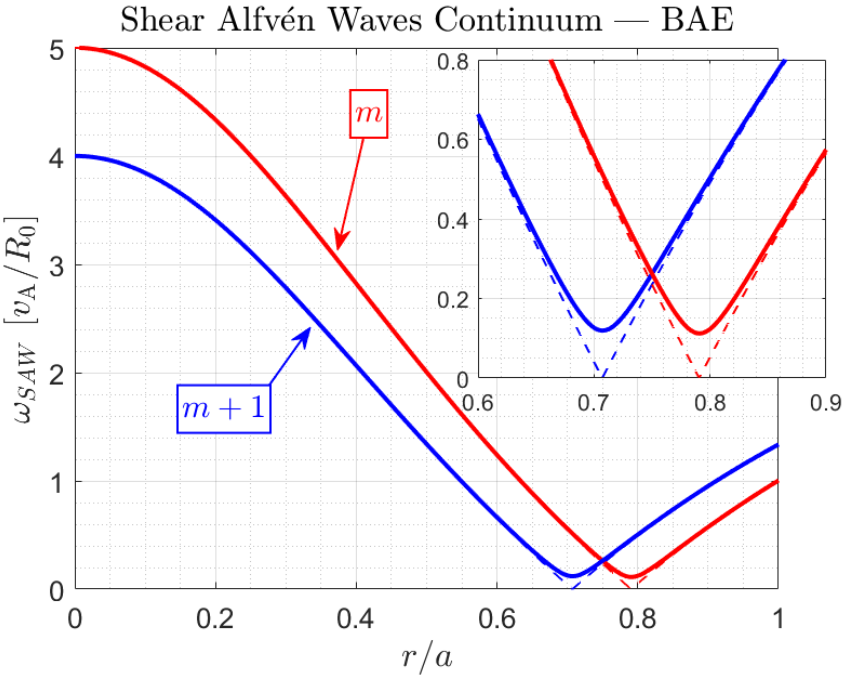

Figure 1.13: *The shear Alfvén wave continuum in cylindrical geometry retaining compressible effects, obtained by plotting Relation 1.53 over the normalized radial direction r/a are reported in solid curves. Here, $n = 4$, $m = -9$ and $m + 1 = -8$. The red and blue dashed curves are the continua obtained in the incompressible cylindrical system.*

sake of simplicity, the dispersion relation can be approximated as:

$$\omega_{BAE}^2 = k_{\parallel}^2(r) v_{\mathrm{A}}^2 + 2\left(\frac{v_{th,i}}{v_{\mathrm{A}}}\right)^2 \tag{1.53}$$

From Relation 1.53, it appears clear the coupling between the acoustic waves (i.e. waves in the acoustic range of velocities $v_{th,i}$) and the Alfvén waves, which

sum an additional term to the general dispersion relation shifting up the spectrum. Such a coupling is essentially due to the geodesic curvature necessarily determined by the toroidal configuration of the system. The center of the BAE gap can be written as:

$$\omega_{BAE,center} = \sqrt{\left(\frac{2}{\tau} + \frac{7}{2} + \frac{1}{\tau q^2}\right)} \tag{1.54}$$

with with $\tau = T_i/T_e$. It must be stressed that Equation 4.1 is physically correct only in the limit of $k_{\|} = 0$, where the mode frequency of the BAE accumulation point collapses into the one of the Geodesic Acoustic mode (GAM) [55]. An example of the BAE gap in the Alfvén continuum is given in Figure 1.13, in which the shifting-up of the spectrum is clearly visible, leading to a undamped range of frequencies below the TAE gap (cf. with Figure 1.12).

Fast-ion modes (or Energetic particle modes)

In the previous paragraphs, it has been observed as global modes, called Alfvén eigenmodes can live undamped within open gap in the Alfvén continuum, and these modes can interact with the fast ion motion leading to the excitation of instabilities driven by the suprathermal part of the plasma. It has also been noted that when a wave in the Alfvén range crosses the continuum is largely damped by the phase mixing effect. Nevertheless, when the fast ion contribution overcomes a threshold – generally when the fast ion pressure becomes comparable to the thermal pressure [56] – the phase mixing effects are not sufficient to damp the propagating wave, which can thereby grow unstable gaining energy from the fast particles. Via this mechanism, the fast-ion modes – usually called also as energetic particle modes (EPMs) – are destabilized.

The main differences between the fast-ion modes and the AEs resides in the fact that the latter exist even in the absence of the suprathermal part of the plasma, whereas the former are only excited in the presence of fast ions in the plasma. Fast-ion modes are fluctuations of the electromagnetic field forced by the interaction with the fast particle dynamics, and the frequency is therefore set by the characteristics of the fast particle motion. The characteristic frequencies of the fast-ion dynamics are a continuous spectrum of values, and so the fast-ion modes can be destabilized in the whole spectrum. On the other hand, the frequencies of the AEs are defined by gap in the continuum, which are in turn determined by the plasma background features. Therefore, the various AEs can explore only a limited range of frequencies, in which the resonant conditions between the undamped eigenmodes and the fast-ion motion characteristics.

1.4 Nonlinear regime of plasma dynamics

In this section, the main features concerning the nonlinear evolution of the instabilities in tokamak plasmas are explained. It is firstly addressed the coexistence

of multiple instabilities, which in the nonlinear regime can give rise to the turbulent dynamics of the plasma, and so to the turbulent transport. In a second dedicated paragraph the principal nonlinear mechanisms leading to the saturation and, thereby, self-regulation of the turbulence are explored.

1.4.1 Introduction to turbulence

First of all, it is mandatory to stress that turbulence is a pure nonlinear phenomenon. In the linear stability studies addressed in previous section 1.3, turbulence has never been involved in the discussion because the linear growth of a single isolated instability cannot give rise to turbulence. An essential ingredient for such a mechanism to take place is the multiple nonlinear interactions among the various actors that populate the plasma system, i.e. particles and waves. It must be also said that turbulence is an universal physical concept which affects several aspects of the boundless Nature system, from the large-scale solar flares to the air flow colliding over a flying plane. In this thesis, the attention is paid on the magnetized plasmas confined inside the tokamak devices. In Figure 1.14,

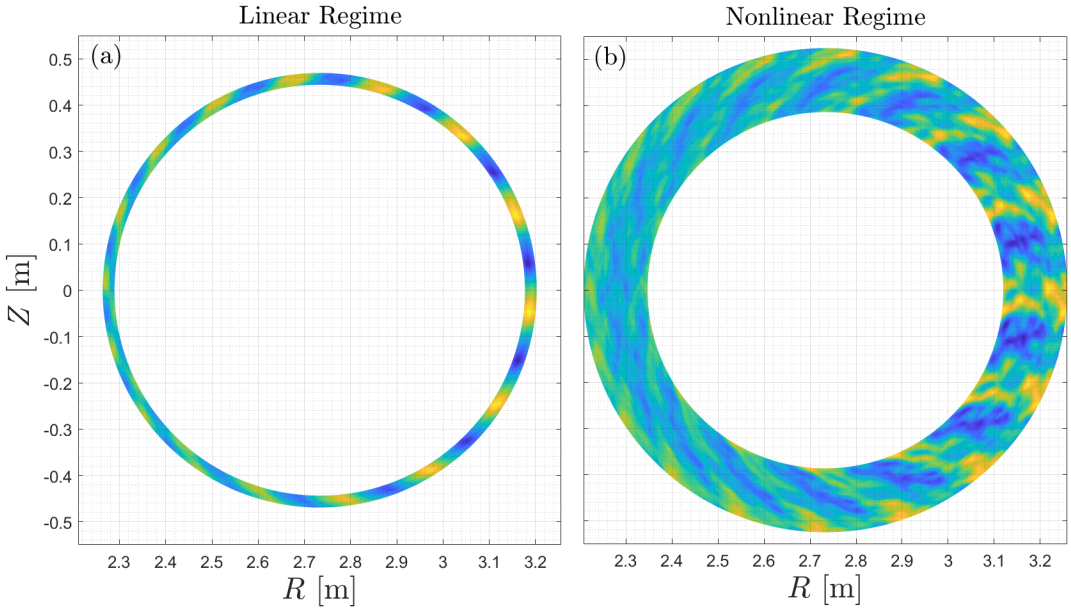

Figure 1.14: *The fluctuations of the electrostatic potential are plotted in the linear regime for one single mode in (a) and in the nonlinear regime for diverse modes in (b). The difference in the structures can be easily appreciated.*

the clear distinction between the linear phase of the system and the nonlinear regime is highlighted by looking at the computed electrostatic potential perturbations by the GENE code [57] plotted in the poloidal cross section of the tokamak. It can be appreciated the disparate sizes of the turbulent structures in the nonlinear regime, with respect to the well-arranged peaks and wells of the fluctuations in the linear phase. As it has already stated, in panel (a), the effects of

only one single unstable mode on the perturbed ϕ are represented. Instead, in panel (b), several different stable and unstable modes are accounting in the same system, giving them the possibility to interact and generate the turbulent flow of the disparate eddies. Multi-scale interactions clearly occurs, since the structures here appearing have different characteristic spatial scales and, although frozen in such a picture, also different characteristic temporal scales. As it will be shown in the following Chapter 2, the results reported in panel (a) of Figure 1.14 have been computed by removing from the set of equations the terms with nonlinearities. To better visualize these interactions, a representative formula about the nonlinear time evolution of the electrostatic potential fluctuations is reported in the following. It fully represents the fundamental physical mechanism of the three-wave nonlinear interaction:

$$\frac{\partial \phi_a}{\partial t} = \gamma_a \phi_a + \frac{1}{2} \sum_{b,c} M_{abc} \phi_b \phi_c \tag{1.55}$$

where M_{abc} is the coefficient tensor of the nonlinear coupling, and the condition $a + b + c = 0$ is fulfilled. The first term on the right hand side represents the linear mechanism of the instability growth, whereas the second one the nonlinear coupling between the various modes. The infinite series of the possible nonlinear couplings can lead to have multi-scale interactions, for instance when $b \sim c \gg a$.

An important remark about the turbulence in tokamak plasmas, and as well in all the other examples in Nature, is that the turbulent flow cannot be determined only by defining the boundary and initial conditions of the system. Nonetheless, their statistical properties can be a sufficiently accurate parameter of merit [58].

Considering a single instability rising, its growth is in principle indefinite in a linear system, since no other mechanisms are involved. Yet, this is not the case in the nonlinear regimes, where self-regulation mechanisms can saturate the growth of the instabilities and lead to quasi-stationary states of the plasma system. Such mechanisms will be addressed in the following section.

1.4.2 Nonlinear saturation mechanisms

In tokamak plasmas, the instabilities have a detrimental effect on the density and energy confinement, as already observed. This is because of the induced outward transport of the particles carrying their kinetic energy along the radial direction. Such resonant instabilities can be driven by the gradients in either radial or velocity space, and thus the redistribution of the particles in the phase space following the induced transport leads to the flattening of the radial and velocity gradients [59]. In this way, the driving mechanism for the instability growth is effectively mitigated. It should be stressed that for this saturation mechanism to be effective, the characteristic time of the profile flattening must be comparable to the linear growing time of the instability (or to the inverse of the growth rate). This is however not always the case in a tokamak plasma, since the characteristic time of the relaxation of the equilibrium profiles is generally associated with the energy

confinement time τ (of the order $\sim$1 s), which is not comparable with the inverse of the microinstability growth rate ($\sim 10^{-3}$ s). Yet, the local gradients around the resonant layers can evolve much faster than the characteristic time τ of the equilibrium profile.

A more exhaustive heuristic example about the nonlinear mechanism leading to turbulence saturation can be given by inspecting the wave-particle interactions in the AE excitation framework. Indeed, as already stated, the undamped AEs are excited at the resonant layers where particles with characteristic frequencies of the motion match the interacting conditions. The nonlinear process for the saturation of the energy transfer between wave and particle is the so-called particle trapping [60, 61]. Basically, the particle is trapped by the wave and tends to bounce back and forth in the potential well of the wave, transferring its energy to the growing AE until the integration over the bounce frequency of the energy transfer is null. This leads to the saturation of the linear excitation of the Alfvénic instability. Such a saturation process is also called de-tuning of the particle and wave. In other words, when the bounce frequency of the particle in the trapping well is similar to the linear growth rate of the instability, the process is saturated and there occurs the de-tuning of the non-interacting particle. Subsequently, the particle, which has lost energy, experiences a radially outward motion. The transport of the particle, which can occur in the spatial or velocity domain, leads thus to the flattening of the profile.

Instabilities can also saturate their indefinite growth by interacting with other waves, via the so-called mode-mode coupling. Indeed, the unstable modes can couple to stable modes, and transfer their turbulent energy to them. In this way, the driver of the turbulence is damped, and the transport saturated. An example of this mode-mode coupling is the generation of large-scale flows, called zonal flows, which can act as a great reservoir of free energy, as it will be explained above in more details.

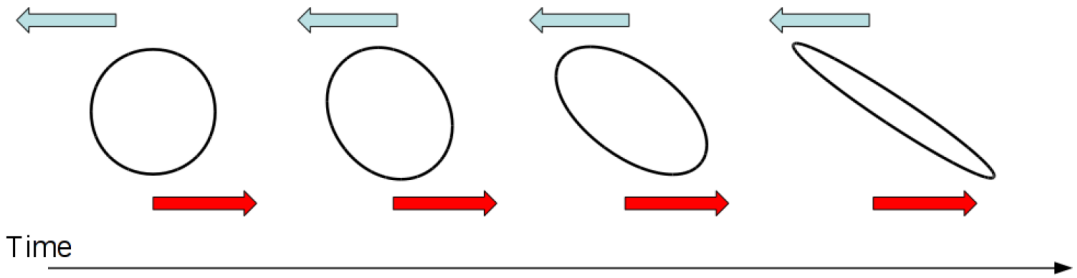

Figure 1.15: *Schematic representation of opposite poloidally oriented flow layers shearing convective eddies. This figure has been adapted from Ref. [31] with permission of David Zarzoso.*

Another particular mechanism for the self-regulation of the turbulence in the magnetized plasmas are the sheared flows along the poloidal direction, which can de-correlate the turbulent radial structures [62]. These sheared flows can be

generated by the poloidal component of the mean $E \times B$ drift velocity, which induces a shearing effect in the radial electric field. This stems from the following relation: $v^{\theta}_{E\times B} \simeq \partial_r \phi = -E_r$. This is illustrated with a schematic view in Figure 1.15, where the arrows directed in opposite ways represent the velocity of the contiguous poloidal layers. It is possible to see that the original turbulent structure is stretched along the velocity direction. Being fully distorted and limited to smaller radial scales, the contribution to the total radial transport is strongly reduced. This can also be illustrated by looking again at Figure 1.6. In fact, if the poloidal component of the propagating turbulent structure is expressed as $e^{im\theta}$, after some time it will reach a different position in the flux surface, i.e. a different poloidal angle θ. This time evolution of the angle in the turbulent motion can be described as:

$$\theta(t) = \theta_0 + \frac{1}{r}(r - r_0)\frac{\partial^2 \phi}{\partial r^2} t \tag{1.56}$$

where θ_0 is an arbitrary poloidal angle at the initial time t_0. Therefore, the turbulent structure after a Δt can be expressed as:

$$e^{im\theta_0 + i\frac{m}{r}(r-r_0)\frac{\partial^2 \phi}{\partial r^2}\Delta t} \tag{1.57}$$

whose radial wavenumber is:

$$k_r = k_{r,0} + k_\theta \frac{(r - r_0)}{r}\frac{\partial^2 \phi}{\partial r^2}\Delta t \tag{1.58}$$

where $k_{r,0}$ is the wavenumber at the initial time t_0. It is thus clear that for increasing Δt, the radial wavenumber at a specific flux surface is increased. To higher radial wavenumbers correspond smaller radial scales, meaning that the turbulent structure is continuously sheared to smaller pieces. At smaller scales, the dissipative processes are dominant and thus the turbulent structures are ceased.

Another key physical mechanism can be the cause of the sheared flows in the poloidal direction, and those are the *zonal flows* [63], treated in the following dedicated paragraph.

Zonal Flows

Zonal flows are axisymmetric perturbations of the electric field along the poloidal direction, and therefore only dependent on the radial coordinate. The zonal flows can only exist in nonlinear regime, since they are only triggered by nonlinear coupling with smaller scales modes, i.e. at higher toroidal and poloidal mode numbers, as already stated earlier. Moreover, another difference with respect to the mean $E \times B$ velocity is that zonal flows are sustained by the turbulent modes, and can therefore exist only in the presence of such a turbulent source. When the small-scale modes are damped, regardless of the mechanism, zonal flows are not anymore fed by the turbulent energy and therefore are quenched. This can be

demonstrated more accurately by inspecting the relation obtained by multiplying the Vlasov Equation 1.20 for the species s by the velocity $\mathbf{v}$ and integrating over the velocity space. Such a relation is generally called the first-order fluid equation or momentum equation, and it reads as:

$$m_s n_s \frac{\partial \mathbf{u}_s}{\partial t} + m_s n_s (\mathbf{u}_s \cdot \nabla)\mathbf{u}_s = eZ_s n_s (\mathbf{E} + \mathbf{u}_s \times \mathbf{B}) - m_s n_s \nabla \cdot \mathbf{\Pi} \tag{1.59}$$

where the Reynolds stress tensor $\mathbf{\Pi} = \langle \mathbf{u}_s \cdot \mathbf{u}_s \rangle$ have been introduced. Projecting Relation 1.59 over the poloidal cross section in a simplified cylindrical geometry and in the ideal MHD limit allows to obtain the equation for the time evolution of the poloidal velocity:

$$\frac{\partial u^\theta}{\partial t} = -\frac{1}{r^2}\frac{\partial}{\partial r}(r^2 \Pi^{r\theta}) \tag{1.60}$$

where the Reynolds stress tensor is limited to the r and θ components, $\Pi^{r\theta} = \langle u^r u^\theta \rangle$. It is therefore clear that the generation of the poloidal velocity, which can be again associated to the radial electric field, is controlled by the Reynolds stress tensor which is determined by the fluctuation of the velocity components. In other words, the sheared zonal flows, which are a quenching mechanism of the turbulent fluctuations, are generated by the turbulent fluctuations themselves, in a proper self-regulating process.

Thus, the first saturating effect of zonal flows is acting as a reservoir of turbulent energy. Indeed, it is of prime importance to underline that zonal flows, being axisymmetric perturbation of the electrostatic potential, do not contribute to the radial transport. This last consideration is based on the fact that the derivative of the zonal components of the electrostatic potential with respect to the poloidal direction is null (i.e. $\partial_\theta \phi_{00} = 0$), and thus the $E \times B$ radial transport expressed as $\partial_\theta \phi_{00} \cdot B_\varphi$ is null. Therefore, the nonlinear triggering of the zonal flows by the turbulent modes at smaller scales can be seen as a dissipative mechanism of the turbulent energy, or the zonal flows can be confused as a great reservoir for the turbulent energy.

Moreover, as already observed for the mean velocity sheared flows, is the decorrelation of the turbulent eddies. This, in turn, lead to shear apart the convective cells and to reduce the radially outward transport of particles and energy.

In Figure 1.16, the electrostatic potential is plotted on the poloidal cross section (actually restricted to a portion centered around $\rho_{tor} = 0.23$) of two different simulations performed by means of the GENE code. In panel (a) the plasma system is dominated by the ITG transport, as the small scale turbulent eddies, predominantly elongated in the radial direction, clearly show. Yet, poloidally oriented layers, representing the zonal flows, can also be observed. This picture is fully consistent with the paradigm of zonal flows as main saturation mechanism of the drift-wave ITG instability [64, 63]. On the contrary, panel (b) illustrates a totally different pattern of the electrostatic potential perturbations, where the turbulence

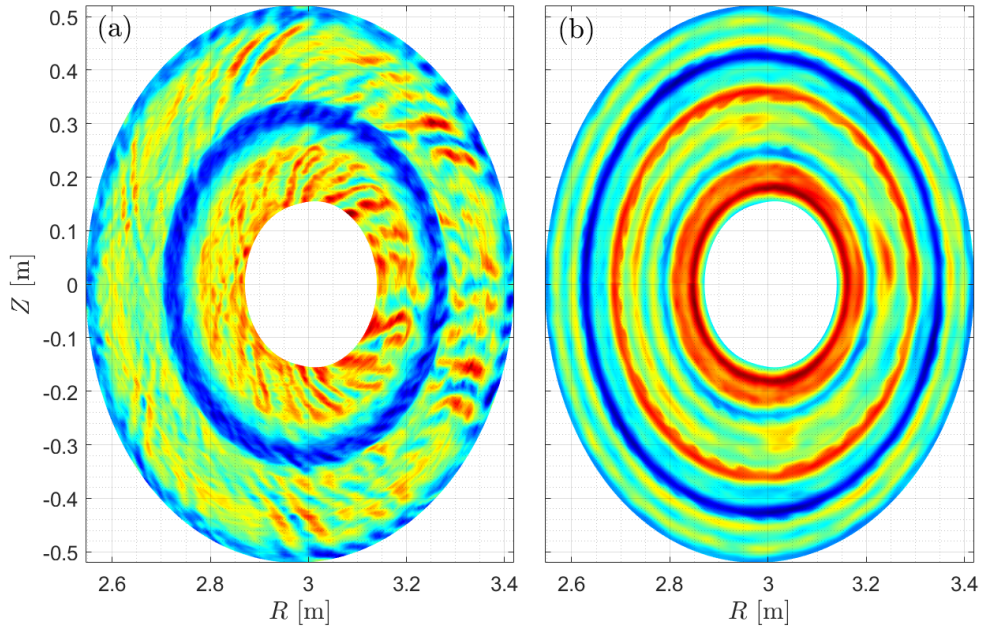

Figure 1.16: *The fluctuations of the electrostatic potential in two different systems are plotted: in (a) the plasma is dominated by radially elongated turbulent structures, induced by the ITG microinstabilities, whereas in (b) the zonal components of the potential are dominating, showing poloidally elongated layers. These poloidal cross sections are obtained from the* GENE *simulations of the inner core of JET pulse #94701, also reported and explained in great details in Chapter 3.*

at the thermal-ion scales is strongly reduced and the zonal components dominate. As it is clear, the radial transport is quenched, since no radially elongated turbulent structures appear.

1.5 Brief history on the impact of fast ions on microturbulence

As a final additional section, a brief background on earlier studies performed on the impact of fast ions on microturbulence in tokamak plasmas will be given. The main goal of this latter section is to plunge the reader into the right and exhaustive context in order to evaluate the results that will be mainly presented in Chapters 3 and 4.

Although the impact of fast ions, and more in particular of fusion-born alpha particles, on the plasma confinement is a long-standing issue [65], some first clear experimental observations of the possible interaction between microturbulent transport and externally generated fast ions were produced in both JET L-mode [66, 67] and H-mode [68] confinement plasmas. Firstly hypothesized to be related to the perpendicular shearing generated by the substantial amount of tan-

gential NBI power introduced in the plasmas or dilution effects [69], the decrease of the thermal ion stiffness was eventually strongly linked to the poloidal plasma current and the β_p [70]. This latter parameter is defined as the ratio between the thermodynamical pressure over the magnetic pressure generated by the poloidal magnetic field. Indeed, for the sake of clarity, the stiffness of the temperature profile is basically the relation between the local ion heat flux with the normalized ion temperature gradient, intimately related to the turbulent transport levels.

The observation of the strong effect of β_p on the confinement was followed by the intuition on the crucial role of the externally generated fast ions, whose high energy strongly contributes to the value of β_p. In this context, the gyrokinetic simulations started to be the fundamental tool to deeply investigate such a physical mechanism leading to the ion stiffness decrease. In fact, numerical analyses with the gyrokinetic code GENE [57] highlight the strong impact of the suprathermal species on the ion turbulent flux, which was reduced in the nonlinear regime down to experimental values only in simulations retaining the fast ions and the fluctuations of the magnetic potential [71]. Already in those studies, the beneficial effects of the fast ions on the linear growth rate, although of minor importance with respect to the nonlinear effects, were also observed. Such linear effects were firstly traced back to the dilution and to the increase of the Shafranov shift, both having well-known positive impact on the linear ITG excitation [12], but the growth rate reduction, and the subsequent heat flux reduction, overestimated the theoretical prediction of those two latter effects. The linear wave-wave interaction between the ITG mode frequency and the magnetic drift of the suprathermal particles was established to be the main cause of this growth rate reduction [72]. Such a linear electrostatic mechanism was achieved and further optimized in ICRH-heated plasmas for a narrow range of fast ion temperature, beneficially impacting at the local ratio $T_{fast}/T_e \sim 10$ and strongly decreasing its significance at higher fast ion temperature [73]. Although not effective thereby for fusion-born alpha particles in burning plasmas, this beneficial impact was experimentally validated firstly in L-mode plasmas with strong ICRH power at JET [74], and more recently found to be strongly active in building Internal Transport Barriers in ASDEX-U scenarios [75], leading thus to a turbulent transport reduction.

A crucial point throughout the gyrokinetic studies on the fast-ion impact on ITG transport was the destabilization of large-scale high-frequency modes excited by the suprathermal particles. Such modes are mainly electromagnetic instabilities, driven by the fast-ion pressure gradient, by the β parameter or by a combination of those two parameters, nonetheless they were never detected in the experiments. At this point, it should be stressed the fact that fast-ion characterization is not an easy task, and poorly accurate modeling can only be obtained. Therefore, any inference on the local gradients or fast-ion parameters reveals to be affected by large error bars. Furthermore, in most of the integrated modeling suites, the module dedicated to the computation of the fast ion distribution function does not take into account the anomalous transport of suprathermal particles induced by fast-ion-driven MHD modes, and therefore an overestimation of the

fast ion confinement could be also expected. For this reason, the fast ion pressure gradients employed in the subsequent gyrokinetic studies must be further assessed and validated by large scans, which could be, sometimes, not affordable. For this reason, the issue related to the destabilization of fast-ion-driven modes has been overcome in the modeling by lowering the pressure gradient [76, 77], i.e. the drive of the high-frequency instabilities. Beyond the experimental absence of the modes, such an artificial stabilization was also required for matching the power balances computed by the integrated modeling. In fact, in the parameter setup with unstable fast-ion modes, the resulting fluxes from the gyrokinetic simulations were largely beyond those computed via integrated modeling [76, 78]. Especially, the electron confinement was strongly degraded, with the magnetic transport extremely enhanced by the large-amplitude fluctuations of the electromagnetic fields induced by the destabilized fast-ion modes. Such a degradation of the electron confinement has also been consistently observed in spherical tokamak experiments with fully destabilized AEs [79].

Perfectly embedded in this context, a first investigation on a possible complex interaction between the externally generated fast ions and the turbulence dynamics was reported in Ref. [80], where flux-driven global electrostatic simulations with the GYSELA code [81] shows a modification of the dynamics of the oscillating component of the zonal flows, i.e. the geodesic acoustic modes (GAMs) [82], in an ITG-driven turbulence regime. Basically, the fast ion energy is channeled through a resonant wave-particle interaction [83] to the radially oscillating GAMs, which take the name of energetic-particle-induced GAMs (EGAMs) [84]. Yet, although a first phase of reduced turbulent transport is obtained with the introduction of the fast-ion source in the simulations [80], the developed EGAMs further lead to an increased level of turbulence amplitude, differently to the reduction observed in JET L-mode plasmas [71]. This increase of turbulent transport could be explained by means of nonlocal interaction between the ITG avalanches and the stationary EGAM oscillations [80, 85] and also by a local three-wave coupling (between one EGAM and two ITGs) [86]. Meanwhile, starting from these first observations, an increased thermal ion confinement was also obtained in other devices, such as ASDEX-U [87] and DIII-D [88, 89]. Thus, more efforts have been spent in understanding the possible complex interaction underlying the beneficial impact of externally generated suprathermal particles on the ITG turbulent transport, leading to some very interesting and surprising discoveries. Indeed, the aforementioned fast-ion-driven modes were established to be a key ingredient in order to build a complex mechanism leading to the turbulent transport reduction. Subdominant large-scale TAEs, only unstable in electromagnetic systems with a substantial presence of fast particles, play the determinant role of intermediate stage in the energy flow from the ITG unstable modes to the zonal component of the electrostatic potential [90]. Thus, the zonal flows, acting on the ITG turbulent eddies [62, 63], increase the ion confinement. This mechanism, however, has been established up to the fully destabilization of the fast-ion-driven modes, which demarcate an upper limit to the achievable pressure regimes. This work requires indeed a linear marginally stable – or subdominant destabilized – TAEs

for the turbulent transport reduction to be active [78], which are somehow subtle conditions to be pursued and designed experimentally. It should be also stressed that the gyrokinetic modeling reporting the ITG turbulence reduction was performed at parameters setup range far from the experimental ones, and therefore not accurately validated. Moreover, contrarily to the turbulent transport partial *reduction* obtained at experimentally relevant conditions, the turbulence *suppression* could be only achieved in unrealistic range of parameters, namely L-mode plasma parameters at values of $\beta_e = n_e T_e / B^2 / (2\mu_0)$ (with T_e in energy units) rather belonging to H-mode confinement.

Eventually, preliminary studies have also been devoted to extend the comprehension of the fusion-born alpha particle impact on ITG microturbulence, more relevant for burning plasmas and future fusion reactors. JET plasmas from the previous deuterium-tritium DTE1 campaign [7] have been analyzed to understand the long-standing issue about the *anomalous* ion heating in the presence of alpha particles. These analyses already highlighted a possible role of the alphas in reducing the ITG growth rate [91, 92], but no indications about the nonlinear regime are given. More recent numerical efforts [93] have been applied to study a predicted ITER advanced scenario [94] with the gyrokinetic code GENE. Beyond a linear stabilization of the ITG modes (mainly due to dilution), a stronger electromagnetic reduction of the thermal ion heat fluxes in the presence of both externally generated fast ions and fusion-born alpha particles is measured, suggesting thus that a complex mechanism could be active in increasing the ion confinement. It should be stressed that, as observed by linear stability analysis, in this ITER scenario the threshold for the excitation of large-scale fast-ion modes was approached, and also that in the nonlinear regime the beneficial reduction of ITG turbulent transport is mainly driven by the alphas with respect to the externally generated fast ions [93].

1.6 Thesis outline

After introducing the basics of the controlled thermonuclear fusion and the physical principles of the magnetically confined plasmas in tokamaks, the short context given in section 1.5 opens the doors to further studies of the impact of fast ions on the microturbulent transport. Namely, the two main points that this thesis will address are: (i) the necessity of analyzing experimental conditions with a substantial population of fusion-born alpha particles, in order to predict and further optimize the future burning plasma scenario in the forthcoming ITER campaigns, and (ii) the investigation of the impact of fast ions on microturbulence in regimes different from the well-established ITG-dominated one.

In Chapter 2, the principles of the flux-tube (or local) approximation are given, together with an important overview of the numerical tool that has been used to produce the modeling results presented in the next chapters. Chapter 3 is devoted to point (i). This will be done by exploiting the recently developed three-ion heating scheme scenario at JET where a significant population of deuterons in the MeV energy range is generated in the plasma core. The relevant and striking ex-

perimental findings related to such JET scenario are firstly introduced, preparing the testing ground for the subsequent modeling analyses and qualitative comparison with the experimental outcomes. The main purpose of these in-depth gyrokinetic analyses is to understand the fine physical process which may explain the noteworthy experimental observations systematically present in such a JET scenario. A complex mechanism has been found to play an important role in the improvement of the thermal ion confinement in the presence of fully destabilized fast-ion-driven TAEs, consistently with the experiments. A comprehensive study is carried out to explore all the possible hallmarks of such a complex mechanism, firstly to corroborate the gyrokinetic modeling, but also to capture the key players for the reproduction of such a mechanism in present and future tokamak scenarios.

Therefore, whereas the beneficial fast-ion effect on the ITG-dominated turbulence regime has been established up to highly energetic ions, mimicking the fusion-born alpha particle's energy, not so many efforts have been spent on exploring the potential impact on turbulent transport regimes dominated by different instabilities. Such an unexplored subject, addressing the aforementioned point (ii), is thoroughly investigated in Chapter 4. In such a chapter, the core of a JT-60U scenario strongly populated by NBI-generated fast ions and dominated by TEM-driven turbulent transport is analyzed in a first instance. After elucidating the absence of fast-ion impact on the TEM-induced fluxes by means of extensive gyrokinetic simulations in a validated framework, a numerical experiment is performed on a tailored TEM-dominated system in order to recover the results achieved for the ITG-dominated regime and reported in section 4.7. A crucial parallelism with the modeling outcomes of Chapter 3 is drawn, highlighting the possibility of experimentally pursuing such a direction for reducing also the TEM-dominated turbulent transport in the presence of unstable high-frequency fast-ion-driven modes.

Chapter 2

Flux-tube simulations of tokamak plasmas

Contents

The complex behaviour of a magnetized plasma confined in tokamak devices cannot be only addressed by analytical or heuristic approaches, as did in the previous Chapter 1. Indeed, solving the multi-scale (in space and time) and fully nonlinear equations governing the plasma dynamics, retaining the extremely wide range of physical phenomena taking place in such a system can only be done by means of state-of-the-art numerical tools. Therefore, this chapter aims at giving a brief description of the numerical tool used throughout this thesis to model the behaviour of magnetized plasmas in tokamaks.

2.1 Flux-tube approach

As it has already been anticipated in section 1.2.5, a strong anisotropy in the dynamics of the turbulent structures is present in the magnetized plasmas, mainly due to rapid motion along the field lines with respect to the perpendicular component. Essentially, the parallel correlation length is typically orders of magnitude larger than perpendicular one (or equivalently $k_\perp \gg k_\parallel$) [95]. Because of this, employing a field-aligned system of coordinates seems to be more than a reasonable choice. The adoption of field-aligned coordinates also allows to reduce substantially the cost of the numerical simulation, essentially by reducing the number of grid points in the direction parallel to the magnetic field lines. Yet, the numerical analysis of the whole plasma domain, i.e. the whole torus, is still a very challenging task, since it requires huge numerical resources not readily available at the present. For this reason, an additional constraint is posed on the spatial extension of the domain to be analyzed with the numerical tools. Basically, the simulated domain is reduced to be only a flux-tube from the entire plasma volume. Mapped into a rectangular box which follows the magnetic field line along the flux surface, such a domain is curved by the toroidal curvature and twisted by the magnetic shear. A common choice for the system of coordinates is to indicate the perpendicular length of the rectangular box with x and y, where x is the radial coordinate, thus perpendicular to the magnetic flux surface and to the field line, and y the so-called binormal coordinate, which is instead perpendicular to the field line but standing on the flux surface. The last spatial coordinate is indicated as z and it defines the parallel coordinate running along the magnetic field line. Such a nomenclature has been chosen to be consistent with that of the GENE code, that will be briefly described in the following section 2.2 and it will be the principal tool used to pursue the goals of the thesis.

The numerical box is centered at the considered magnetic flux surface, with a reduced extension in the perpendicular directions. The plasma parameters, such as the temperature, the density and the radial gradients, are evaluated at the selected radial position and considered to be constant in the whole numerical domain. This approximation holds when the radial extent of the numerical box is much smaller than the whole system size, generally associated to the minor radius a of the fusion device, but sufficiently enough times larger than the turbulent structure correlation length. This consideration essentially represents the scale separation between the microturbulent local effects, such as the radial

correlation length of the turbulent structures ($\sim 10\rho_i$), with respect to the global phenomena occurring in the whole device (which vary on a scale $\sim a$). Thus, a common parameter of merit in the gyrokinetic flux-tube approach is $\rho^* = \rho_{ref}/a$, for which, in the vanishing limit ($\rho^* \to 0$), the flux-tube approximation is justified. Moreover, being the boundaries of such a simulated domain different from the physical ones at the edge of the torus, the following convenient periodic boundary conditions in the perpendicular directions are employed for a generic plasma parameter $\mathcal{A}(x, y, z)$:

$$\begin{aligned} \mathcal{A}(x + L_x, y, z) &= \mathcal{A}(x, y, z) \\ \mathcal{A}(x, y + L_y, z) &= \mathcal{A}(x, y, z) \end{aligned} \tag{2.1}$$

with L_x and L_y respectively the size of the numerical box in the radial and binormal directions. for the domain to match at each toroidal turn in the real space, the numerical box must be shifted also in the binormal direction y by a factor $Cq(x)2\pi$ depending on the radial coordinate x. In fact, this dependence is necessary to still ensure the radial discretisation of the additional rational surfaces (beyond the original one at x_0) accounted for in the simulated box. Thus, along the parallel direction, the boundary conditions are pseudo-periodic [96], and can be expressed as:

$$\mathcal{A}(x, y + Cq(x)2\pi, z + 2\pi) = \mathcal{A}(x, y, z) \tag{2.2}$$

with C a constant geometric factor, and the parallel coordinate is bounded by $[-\pi, \pi]$, i.e. by a 2π periodicity.

Using periodic boundary conditions along the perpendicular directions allows to employ a spectral decomposition:

$$\mathcal{A}(x, y, z) = \sum_{k_x, k_y} \hat{\mathcal{A}}_{k_x, k_y}(z) e^{i(k_x x + k_y y)} \tag{2.3}$$

which simplifies the analytical treatment of the equations to be solved in the gyrokinetic framework [21]. Especially, it gives a simple treatment of the gyroaverage operator Relation 1.42, which can be approximated with the Bessel function. More specifically, it can be demonstrated that the Fourier mode of a gyroaveraged quantity $\hat{\mathcal{J}_0}(A)$ is the product of the Bessel function and the Fourier mode of the quantity $\hat{A}$:

$$\begin{aligned}\hat{\mathcal{J}}_0(A)(\mathbf{k}) &= \frac{1}{2\pi}\int_{\infty}^{+\infty}\int_0^{2\pi}\hat{\mathcal{A}}\mathrm{d}\varphi_c e^{-i\mathbf{k}\cdot\mathbf{x}}\mathrm{d}\mathbf{x} \\ &= \frac{1}{2\pi}\int_{\infty}^{+\infty}\int_0^{2\pi}\hat{\mathcal{A}}\mathrm{d}\varphi_c e^{-i\mathbf{k}_\perp x\cos(\varphi_c)}\mathrm{d}\mathbf{x} \\ &= \left(\frac{1}{2\pi}\int_0^{2\pi} e^{-i\mathbf{k}_\perp x\cos(\varphi_c)}\mathrm{d}\varphi_c\right)\hat{\mathcal{A}}(\mathbf{k}) \\ &= J_0(\mathbf{k}_\perp x)\hat{\mathcal{A}}(\mathbf{k})\end{aligned} \tag{2.4}$$

Because of the finite extent of the numerical domain, the wavevectors k_x and k_y must be discretized as:

$$\begin{aligned}k_x &= k_{x,center} + ak_{x,min} \\ k_y &= bk_{y,min}\end{aligned} \tag{2.5}$$

where $k_{x,min} = 2\pi/L_x$ and $k_{y,min} = 2\pi/L_y$, and with the integer coefficients a and b determining the extension.

Nevertheless, the magnetic field lines are distorted in their path along the parallel direction. The grade of the distortion is defined by the local magnetic shear parameter $\hat{s} = (x_0/q_0)(\mathrm{d}q/\mathrm{d}x)$ evaluated at $x = x_0$ (see section 1.2.1). Basically, the domain is assumed to be a rectangle only at the LFS (indicated for convenience with the parallel position $z = 0$), whereas it is strongly twisted along the parallel pathway becoming a sheared parallelogram. This picture in the real toroidal space translates into the issue of matching the distorted numerical box at the HFS, i.e. at $z = \pm\pi$. The choice of defining the parallel boundary conditions at the HFS is made consistently with the general ballooned property of the microturbulent structures in tokamak plasmas, and thus to reduce artificial effects on the physical dynamics. Therefore, the parallel boundary conditions are expressed in the Fourier space for one k_y mode as:

$$\sum_{k_x}\hat{\mathcal{A}}_{k_x,k_y}(z+2\pi)e^{2\pi i k_y C q_0}e^{i(k_x+2\pi k_y\hat{s}x)} = \sum_{k_x}\hat{\mathcal{A}}_{k_x,k_y}(z)e^{ik_x x} \tag{2.6}$$

with q_0 the safety factor evaluated at x_0. It can be thus seen that in the Fourier space, there is a shift in the k_x radial coordinate, represented in the second exponent in the LHS of Relation 2.7. This shift was also observed in the real space illustrated by Relation 2.2. Yet in that case, the shift was in the binormal direction y and it was useful for matching the sheared simulation boxes at the parallel boundaries. In other words, the latter relation ensures the coupling of consecutive k_x modes at the LFS of the considered flux-tube for the same k_y mode, and can be visualized as:

$$\hat{\mathcal{A}}_{k_x,k_y}(z=-\pi) = \hat{\mathcal{A}}_{k_x+2\pi k_y(\hat{s}+iCq_0),k_y}(z=+\pi) \tag{2.7}$$

These considerations are also in accordance with the basis of the ballooning representation [97], which will be used in the following Chapters 3 and 4 to illustrate the structure of the eigenmodes computed by the local flux-tube numerical code (see, e.g., section 4.3.3).

2.2 The GENE code

The results presented in the remainder of this thesis have been mainly obtained by means of the GENE code [98] in its flux-tube version [57]. The GENE code solves the gyrokinetic equation for the perturbed distribution function δf coupled to the Maxwell's Equations 1.12 on a grid built on a field-aligned system of coordinates, which is consistent with what has been presented in the previous paragraphs. In this section, a brief overview on the system of equations solved by the GENE code is given, with some insights on the particular features that will be exploited in the remainder of this thesis.

2.2.1 System of equations solved in GENE

For a complete derivation of the equations solved by GENE, the reader is reminded to, e.g., Refs. [21, 99, 100]. First, the equation for the particle distribution function in the gyrokinetic framework is illustrated, while in a second paragraph the coupled relations on the time evolution of the electromagnetic fields are described.

Gyrokinetic equation for the distribution function

To begin with, the gyrokinetic equation for the total particle distribution function $\bar{F}(\mathbf{X}, \mathrm{v}_\parallel, \mu, t)$, evaluated at the guiding center position and previously reported in Relation 1.43, could be further extended as:

$$\begin{aligned} &\frac{\partial \bar{F}}{\partial t} + \left[\mathrm{v}_\parallel \mathbf{b} + \frac{B_0}{B^*_{0\parallel}}(\mathbf{v}_{E\times B} + \mathbf{v}_{\nabla B} + \mathbf{v}_c)\right] \\ &\cdot \left\{\boldsymbol{\nabla}\bar{F} - \frac{1}{m\mathrm{v}_\parallel}\left[q\boldsymbol{\nabla}\bar{\phi} + q\bar{A}_\parallel \mathbf{b} + \mu\boldsymbol{\nabla}(B_0 + \bar{B}_\parallel)\right]\frac{\partial \bar{F}}{\partial \mathrm{v}_\parallel}\right\} = \left(\frac{\partial \bar{F}}{\partial t}\right)_c \end{aligned} \tag{2.8}$$

where $B^*_{0\parallel} = \mathbf{b}\cdot[\boldsymbol{\nabla}\times(\mathbf{A}_0 + m\mathrm{v}_\parallel \mathbf{b}/q)]$ is the Jacobian of coordinate transformation from particle to guiding center position. The drift, respectively the $E\times B$, grad-B and curvature, velocities have been explicitly introduced in the equation with the following definitions:

$$\mathbf{v}_{E\times B} = \frac{\mathbf{b}\times\boldsymbol{\nabla}\zeta}{B_0} \tag{2.9}$$

$$\mathbf{v}_{\nabla B} = \frac{\mu}{m\omega_c}(\mathbf{b}\times\boldsymbol{\nabla}B_0) \tag{2.10}$$

$$\mathbf{v}_c = \frac{\mathrm{v}_\parallel^2}{\omega_c}(\boldsymbol{\nabla}\times\mathbf{b})_\perp \tag{2.11}$$

In these latter relations, the modified potential $\zeta = \bar{\phi} - \mathrm{v}_\parallel\bar{A}_\parallel + \mu\bar{B}_\parallel/q$ has been employed. It must be noted at this point that the $E\times B$ drift velocity contains contribution from both ϕ and $\mathbf{A}$ potentials. This consideration will reveal useful in the following definition of electrostatic and electromagnetic contributions to the particle and heat fluxes (see section 2.2.2)

As it has already been stated, the δf-splitting approach allows to separate the background distribution F_0 from the quickly varying perturbed counterpart f, by assuming $f \ll F_0$. This stems from the hypotheses within the gyrokinetic approximation in the adiabatic framework for which the static background quantities are of the zeroth order, whereas the perturbed ones are of the order $\epsilon_p = \rho_\mathrm{L}/a$. Thus, Relation 2.8 can be divided into a static part:

$$\frac{\partial F_0}{\partial t} + \mathrm{v}_\parallel\mathbf{b}\cdot\left(\boldsymbol{\nabla}F_0 - \frac{\mu}{m\mathrm{v}_\parallel}\frac{\partial F_0}{\partial \mathrm{v}_\parallel}\boldsymbol{\nabla}B_0\right) = \left(\frac{\partial F_0}{\partial t}\right)_c \tag{2.12}$$

and into a fluctuating part by retaining only the first order terms in ϵ_p:

$$\begin{aligned}\frac{\partial g}{\partial t} + \frac{B_0}{B_{0\parallel}^*}(\mathbf{v}_{E\times B}+\mathbf{v}_{\nabla B}+\mathbf{v}_c)\cdot\left(\boldsymbol{\nabla}F_0 - \frac{\mu}{m\mathrm{v}_\parallel}\frac{\partial F_0}{\partial \mathrm{v}_\parallel}\boldsymbol{\nabla}B_0\right)\\ + \left[\mathrm{v}_\parallel\mathbf{b} + \frac{B_0}{B_{0\parallel}^*}(\mathbf{v}_{E\times B}+\mathbf{v}_{\nabla B}+\mathbf{v}_c)\right]\cdot\left(\boldsymbol{\nabla}g - \frac{q}{m\mathrm{v}_\parallel}\frac{\partial F_0}{\partial \mathrm{v}_\parallel}\boldsymbol{\nabla}\zeta + \frac{q}{m}\bar{A}_\parallel\boldsymbol{\nabla}\frac{\partial F_0}{\partial \mathrm{v}_\parallel}\right) = \left(\frac{\partial f}{\partial t}\right)_c\end{aligned} \tag{2.13}$$

where the modified perturbed distribution function

$$g = f - \frac{q}{m}\frac{\partial F_0}{\partial \mathrm{v}_\parallel}\bar{A}_\parallel \tag{2.14}$$

has been introduced. Actually, the present version of the GENE code solves the system of equations for the modified distribution function g, instead for f, for computational matters (principally to avoid the computation of the time derivative of $A_\parallel$). Firstly, it must be noted that the terms $(\mathbf{v}_{E\times B}+\mathbf{v}_{\nabla B}+\mathbf{v}_c)\cdot(\boldsymbol{\nabla}F_0 - \frac{\mu}{m\mathrm{v}_\parallel}\frac{\partial F_0}{\partial \mathrm{v}_\parallel}\boldsymbol{\nabla}B_0)$ are of first order in ϵ_p, although the perturbed distribution function (or g) does not appear. In fact, the gradients of the background quantities (F_0 and B_0) are $\sim a^{-1}$ and the drift velocities develop at the ion Larmor radius. Hence, combining the two considerations, the small parameter $\epsilon_p = \rho_\mathrm{L}/a$ is recovered for

these terms. Moreover, in Equation 2.13, the term $\propto \mathbf{v} \cdot \boldsymbol{\nabla}\phi\partial_{v_\parallel} f$, which is usually referred to as parallel nonlinearity is not retained because it has been shown to have only a minor order effect on the transport with respect to the $E \times B$ nonlinear term [101, 102, 103]. However, such a term could be non-negligible for the nonlinear dynamics of zonal modes with finite frequency [100].

The simulations performed with the GENE code throughout this thesis approximate the background particle distribution function for all the particle species with a Maxwellian distribution, with the form:

$$F_0 = \left(\frac{m}{2\pi T_0}\right)^{3/2} n_0 e^{-\frac{mv_\parallel^2/2+\mu B_0}{T_0}} \tag{2.15}$$

where n_0 and T_0 are respectively the particle density and the temperature calculated as described in Equations 1.23 and 1.30. Whereas for the thermal plasma species the Maxwellian is an accurate function to describe their distribution in the phase space, as already stated, this is not true for the suprathermal ions externally generated by the heating systems. However, it has been shown that the use of arbitrary distribution function for the fast ions does not change the qualitative picture described by the Maxwellian distribution [104, 74], despite the substantial increase in the computational cost of the numerical analysis [100].

Moreover, the collision operator appearing at the right hand side of the gyrokinetic equation (see, e.g., 2.8) has not been defined yet. Although not deeply analyzed throughout this thesis, collisions in the core of tokamak plasmas may have an effect on the structures of the microinstabilities, as well as concerning the dynamics of the sheared zonal flows, which have been demonstrated to be damped by the nonclassical collisional effects [105, 63]. In all the performed numerical analyses with the GENE code, reported in the following chapters, a linearized Landau Boltzmann collision operator has been employed, for which a detailed derivation can be consulted in Ref. [106]. Such a collision operator takes the form of a bilinear function between two species i and j accounted for in the system, which can be visualized as:

$$\left(\frac{\partial f_i}{\partial t}\right)_c = C(f_i, F_{0,j}) + C(F_{0,i}, f_j) \tag{2.16}$$

Basically, it is formed by the perturbed distribution function of the species a scattering off the background distribution function of the species b, and of a complementary term describing the opposite process, with the former term called test-particle operator and the latter field-particle operator. A control on the collision operator in GENE can be set by tuning the normalized collision frequency parameter, here reported as a function of the electron-ion collision rate ν_{ei} of Hinton and Hazeltine [27]:

$$\nu^* \equiv \left(\frac{a n_e}{4e^2 n_i}\right)\nu_{ei} \tag{2.17}$$

with n_e and n_i the normalized density of electrons and ions, respectively, and a the minor radius.

Electromagnetic field equations

In order to evaluate the dynamics of the plasma system self-consistently, the gyrokinetic Equation 2.13 has to be coupled to the relations for the time evolution of the electromagnetic fields. These latter relations, i.e. the Maxwell Equations have already been explicitly reported in section 1.2.2 (see Equations 1.12) with the charge and the current densities (Equations 1.15) evaluated at the particle position. These two latter plasma parameters can be expressed as fluid moments of the distribution function for each species s (see section 1.2.3):

$$\varrho_s(\mathbf{x}) = q_s \int F_s(\mathbf{x}, \mathbf{v}) \mathrm{d}^3\mathbf{v} \tag{2.18}$$

$$j_{\parallel,s}(\mathbf{x}) = q_s \int v_\parallel F_s(\mathbf{x}, \mathbf{v}) \mathrm{d}^3\mathbf{v} \tag{2.19}$$

$$\mathbf{j}_{\perp,s}(\mathbf{x}) = q_s \int \mathbf{v}_\perp F_s(\mathbf{x}, \mathbf{v}) \mathrm{d}^3\mathbf{v} \tag{2.20}$$

where the current density moment has been split in its parallel and perpendicular contributions.

However, the particle distribution function that is computed in Equation 2.8 (and the following Equations 2.12 and 2.13) is expressed in the gyroaveraged guiding center system of coordinates. Because of this, the computation of the charge and current densities requires the distribution function to be transformed back to the non-gyroaveraged coordinates $(\mathbf{X}, \mathbf{v}_\parallel, \mu, \varphi_c)$. This is done by means of the so-called pull-back operator T^*, which, as already said, represents the transformation $F(\mathbf{x}, \mathbf{v}) = T^*[\bar{F}(\mathbf{X}, \mathbf{v}_\parallel, \mu)]$. For a Maxwellian distribution function, the pull-back operator can be made explicit as:

$$T^*[F] = \bar{F}_0(\mathbf{X}) + f(\mathbf{X}) + \frac{\mu}{T_0}\bar{B}_\parallel(\mathbf{X})\bar{F}_0(\mathbf{X}) - \frac{q}{T_0}\left[\phi(\mathbf{X} + \boldsymbol{\rho}_\mathrm{L}) - \bar{\phi}(\mathbf{X})\right]\bar{F}_0(\mathbf{X}) + \mathcal{O}(\epsilon_p^2) \tag{2.21}$$

In the following, the equations concerning the evolution of both the electrostatic ϕ and magnetic A potentials will be given. For an accurate and detailed derivation the reader could refer to [21] where the case considering only Maxwellian as background distribution function is treated, or to [100] for the calculations with a more generalized distribution function.

Thus, the Poisson Equation 1.36, which links the spatio-temporal evolution of the electrostatic potential to the charge density, can be expressed as:

$$\begin{aligned}\nabla_\perp^2\phi(\mathbf{x}) &= -\sum_s \varrho_s \\ &= -\sum_s q_s \int \delta(\mathbf{X}+\boldsymbol{\rho}_\mathrm{L}-\mathbf{x}) T^*[\bar{F}_s]\mathrm{dv}_\parallel \mathrm{d}\mu \mathrm{d}\varphi_c\end{aligned} \tag{2.22}$$

where the laplacian operator in the left hand side has been approximated with only the perpendicular contributions ($\nabla^2 \approx \nabla_\perp^2$), because of the anisotropy of the turbulent electrostatic structures exploited also in the flux-tube framework. In the Fourier space for the perpendicular spatial directions (k_x, k_y) (while the parallel direction z is still solved in the real space), the Poisson's equation finally reads:

$$\begin{aligned}\nabla_\perp^2\phi(k_x,k_y) = -\sum_s q_s \Bigg[&\cancel{n_{0,s}} + \frac{2\pi B_0}{m_s}\int J_0(\rho_s k_\perp) f(k_x,k_y)\mathrm{dv}_\parallel \mathrm{d}\mu \\ &+ \frac{q_s}{T_{0,s}} n_{0,s}\Big(\Gamma_0(\rho_s^2 k_\perp^2) - 1\Big)\phi(k_x,k_y) \\ &+ \frac{n_{0,s}}{B_0}\Delta(\rho_s^2 k_\perp^2) B_\parallel(k_x,k_y)\Bigg]\end{aligned} \tag{2.23}$$

where J_0 is the Bessel function, $k_\perp = (k_x, k_y)$ and the operators:

$$\begin{aligned}\Gamma_0(\cdot) &= e^{-(\cdot)} I_0(\cdot) \\ \Delta(\cdot) &= \frac{I_0(\cdot) - I_1(\cdot)}{e^{(\cdot)}}\end{aligned}$$

with I_n the modified Bessel function of order n. Being the magnetized plasma at the equilibrium quasi-neutral, the first term on the right hand side of Equation 2.23 can be neglected. It is thus visible the contribution of the parallel fluctuations of the magnetic field $B_\parallel$ to the evolution of the electrostatic potential.

It is now reported the Ampère's equation, which will be split in the parallel and perpendicular contribution of the vector potential A. The following relations are expressed in the absence of static electric fields ($E = 0$) and the Coulomb gauge ($\boldsymbol{\nabla} \cdot A = 0$) has been employed.

$$\nabla_\perp^2 A_\parallel = -\sum_s j_{\parallel,s} = -\sum_s q_s \int v_\parallel \delta(\mathbf{X}+\boldsymbol{\rho}_\mathrm{L}-\mathbf{x}) T^*[\bar{F}_s]\mathrm{dv}_\parallel \mathrm{d}\mu \mathrm{d}\varphi_c \tag{2.24a}$$

$$(\boldsymbol{\nabla}\times\mathbf{B})_\perp = \sum_s \mathbf{j}_{\perp,s} = \sum_s q_s \int \mathbf{v}_\perp \delta(\mathbf{X}+\boldsymbol{\rho}_\mathrm{L}-\mathbf{x}) T^*[\bar{F}_s]\mathrm{dv}_\parallel \mathrm{d}\mu \mathrm{d}\varphi_c \tag{2.24b}$$

Again, the parallel derivatives have been neglected because of the strong anisotropy

of the electromagnetic field fluctuations. Examining firstly the parallel component of the Ampère's equation, it can be written in the Fourier space for the perpendicular spatial coordinates as:

$$\nabla_\perp^2 A_\parallel(k_x,k_y) = -\sum_s \frac{2\pi B_0 q_s}{m_s}\int v_\parallel J_0(\rho_s k_\perp) f_s(k_x,k_y)\mathrm{dv}_\parallel \mathrm{d}\mu \tag{2.25}$$

The perpendicular component indeed has a more complicated expression, due to the nature of the Maxwellian distribution function. In fact, it is even in $\mathrm{v}_\parallel$, and therefore in the calculations of the parallel density current, the integrals of the form $\int \mathrm{v}_\parallel F \mathrm{dv}_\parallel = 0$. Instead, this does not occur for the integrals of the form $\int \mu F \mathrm{dv}_\parallel = 0$. So, the the perpendicular component of the Ampère's equation in the Fourier space reads:

$$\begin{aligned}(\boldsymbol{\nabla}\times\mathbf{B})_\perp = \Bigg\{ \sum_s q_s \Bigg[&\frac{\pi}{k_\perp}\left(\frac{2B_0}{m_s}\right)^{3/2}\int \sqrt{\mu} J_1(\rho_s k_\perp) f_s(k_x,k_y)\mathrm{dv}_\parallel \mathrm{d}\mu \\ &+ \frac{q_s n_{0,s}}{m_s\omega_{c,s}}\Delta(\rho_s^2 k_\perp^2)\phi(k_x,k_y) \\ &+ \frac{v_{th,s} n_{0,s}}{B_0\omega_{c,s}}\Delta(\rho_s^2 k_\perp^2) B_\parallel(k_x,k_y)\Bigg]\Bigg\} i(k_y \mathbf{e}_x - k_x \mathbf{e}_y)\end{aligned} \tag{2.26}$$

where the versors $\mathbf{e}_x$ and $\mathbf{e}_y$ respectively along the radial and binormal direction have been introduced.

Eventually, it is worthy to highlight the effect of the Bessel functions which are present in the equations for the spatio-temporal evolution of the perturbed electromagnetic fields. These are introduced in the gyroaveraging operation [21]. Moreover, the low-order Bessel functions (as well as for the modified Bessel functions) go to zero when the argument is large, i.e. $J_n(x) \to 0$ for $x \to \infty$. In this sense, the presence of the product $\rho_s k_\perp$ as argument of the Bessel functions leads to vanishing contributions for small-scale phenomena ($k_\perp \gg 1$). This result can be related to what already presented in section 1.4.2 about the de-correlating effects induced by the sheared flow.

2.2.2 Diagnosed quantities

It is to be stressed that the distribution function of gyrocenters contains information in a 5D phase space. Such high-dimensional information is most of the times not directly exploitable. Therefore, further operations need to be done in order to reduce the dimensionality and have access to physical phenomena. Such operations are based on the fluid moments of the distribution function and exhibits the advantage that the results can be easily compared to experimental data. In the following, the expressions of the main quantities exploited in this thesis are provided. They can be linked to the fluid moments already described in the introductory chapter, but here a more specific treatment for the local approach modifies the general expressions given in section 1.2.3.

In the context of this thesis, indeed, two quantities that are extensively exploited are the particle and heat fluxes along the radial direction, since they are intimately related to the plasma confinement, and can be efficiently compared with the experimental power balances. In the GENE code, the radial particle and heat fluxes are representative of the outward/inward advection of particle and energy due to the $E \times B$ drift velocity, defined in Equation 2.9. The contributions of the other drift velocities to the fluxes in the core of tokamak plasmas, with weak asymmetries, constitute a small-order correction and are thereby neglected [99]. The definitions of these diagnosed quantities averaged over the flux surface are:

$$\Gamma^s = \left\langle \int \mathrm{v}^x_{E\times B}(\mathbf{x}) f_s(\mathbf{x},\mathbf{v}) \mathrm{d}\mathbf{v} \right\rangle_{FS} \tag{2.27}$$

$$Q^s = \left\langle \frac{m_s}{2} \int \mathrm{v}^2 \mathrm{v}^x_{E\times B}(\mathbf{x}) f_s(\mathbf{x},\mathbf{v}) \mathrm{d}\mathbf{v} \right\rangle_{FS} \tag{2.28}$$

where $\mathrm{v}^x_{E\times B}$ is the counter-variant radial component of the $E \times B$ drift velocity, i.e. $\mathrm{v}^x_{E\times B} = \mathbf{v}_{E\times B} \cdot \nabla x$, and $\langle \cdot \rangle_{FS}$ denotes the flux-surface average operation. Being the $E \times B$ drift induced by the perturbations of both the electrostatic ϕ and magnetic A potentials, the particle and heat fluxes can also be further subdivided into an electrostatic and an electromagnetic contributions. The former counterparts, Γ^s_{ES} and Q^s_{ES}, are calculated by retaining only the ϕ-dependent terms of Equations 2.27 and 2.28, whereas the latter, Γ^s_{EM} and Q^s_{EM}, by retaining the contributions of the $A_\parallel$- and $B_\parallel$-dependent terms.

It is also worthy to introduce the particle D and heat χ diffusivities, averaged within the considered flux surface, which are related to the particle and heat flux definitions via the Fick's first law, and will be used in the remainder of this thesis:

$$D^s = \frac{\Gamma^s}{n_{0,s}\omega_{n,s}\langle g^{xx}\rangle_{FS}} \tag{2.29}$$

$$\chi^s = \frac{Q^s}{n_{0,s}T_{0,s}\omega_{T,s}\langle g^{xx}\rangle_{FS}} \tag{2.30}$$

with $\omega_{\sigma,s} = -\frac{a}{\sigma_{0,s}}\frac{\mathrm{d}\sigma_s}{\mathrm{d}x}$ the normalized radial gradient of density or temperature and g^{xx} representing the $\nabla x \cdot \nabla x$ element of the metric tensor related to the coordinate transformation. Obviously, also the diffusivities can be split into electrostatic and electromagnetic counterparts when only the electrostatic or electromagnetic contribution to the total fluxes is used in Expressions 2.29 and 2.30.

Chapter 3

Impact of MeV ions on ITG-driven turbulence

Contents

In the previous dedicated sections of Chapter 1, it has been shown that ITG turbulence could be strongly reduced in the presence of a significant population of fast ions. Theoretical and numerical studies demonstrated that different beneficial mechanisms act to reduce the ITG-driven transport by modifying the linear properties of the system [72, 73] and by triggering complex interactions in the nonlinear regime [90]. However, the former effect is restricted to a linear wave-particle interactions between the magnetic drift of the fast particle population and the ITG frequency mode [72], which could be difficult to achieve experimentally, and furthermore do not explain the strong reduction of the ITG transport clearly obtained in dedicated numerical simulations [71, 77, 87, 90]. On the other hand, the latter nonlinear effect is limited by the access to unstable branch of the large scale fast-ion-driven modes beyond a critical threshold. These instabilities lead to particle and heat fluxes matchless to the experimental power balances [76], essentially by enhancing the amplitude of the electrostatic and electromagnetic field fluctuations. Thus, the turbulence reduction is obtained only when the threshold is not exceeded, i.e. when the fast-ion-driven modes are stable or, at best, marginally unstable [90]. Even these particular conditions of submarginal stability may be difficult to achieve, because of the narrow range of possible parameters, and thereby little appealing in the experiments. It must be however reported that recent studies performed at JET by means of the Alfvén Eigenmode Active Diagnostic coupled to the plasma-antenna succeed in experimentally measuring and tracking the frequencies of stable TAEs [107]. This opens up the new possibility of validating the results obtained in the gyrokinetic modeling framework of marginally stable AEs with experimental measurements. As an additional constraint to the accurate predictions of burning plasmas, the energy of the analyzed fast ions is much lower than the 3.5 MeV alpha particles born from the D-T nuclear reactions. Although recent modeling studies potentially revealed that alpha particles may beneficially impact on the ion-scale transport by reducing the ITG turbulence in an ITER predicted hybrid scenario [93], an experimental validation of the impact of the alphas is still missing. It must be noted that some insights have been provided in a study about the outcomes of the first D-T experimental campaign at JET [7] by means of a combined theoretical and numerical analysis [92]. However, such an analysis, aiming to find an explanation on the puzzling anomalous ion heating measured during that experimental campaign [65], is based on linear calculations. Partial conclusions were given linking the decrease of the ITG growth rate in specific radial regions to the presence of not-thermalized alpha particles born from the nuclear fusion reactions. Eventually, the favorable effect of the fast ions on the ITG-induced turbulent transport may be achievable only for a limited range of parameters and only through the tailoring of the externally generated population of fast ions, which are not expected to be the main heating source in a future fusion reactor.

Recent experiments conducted at the JET tokamak aimed at demonstrating the efficacy of the three-ion heating scheme [108, 109, 110] for the efficient generation of a substantial fast ion population [111, 112] and for the application to future generation of fusion reactors [113]. In this framework, the novel combination of

ICRH and NBI systems in the three-ion ($D - D_{NBI} - {}^3He$) scenario revealed that NBI deuterons (in the order of 100 keV) are further accelerated by the ICRH up to MeV range of energies [111, 113]. Although such MeV-ions strongly destabilized a rich variety of Alfvén eigenmodes and mainly deposited their energy to the electrons by collisional heating [18], several experimental indicators suggested an improvement of the thermal ion confinement. The results obtained in such experiments represent a suitable test-bed case to extend the comprehension of the fast-ion effect on the microturbulent transport also in the presence of fully destabilized large scale modes driven by the presence of MeV ions.

Therefore, this chapter is dedicated to illustrate the detailed and comprehensive analysis performed in a broader context about three-ion ($D - D_{NBI} - {}^3He$) scenario implications. The numerical simulations are carried out with the GENE code in its flux-tube version. A novel complex mechanism is demonstrated to take place in the presence of highly energetic ions and to lead to an optimum plasma state in which the ion-scale turbulence is totally suppressed. Diverse experimental validating features are provided in support of the numerical outcomes for the first time in this framework.

3.1 Experimental observations in JET three-ion heating scheme scenario

In this section, the main experimental observations for the JET three-ion ($D - D_{NBI} - {}^3He$) scenario are presented. In order to facilitate the reader, only the striking experimental measurements which has raised the interest about this scenario are provided, whereas the strong linking between the numerical and the experimental outcomes is used as a guideline throughout all the chapter. Therefore, some measurements directly derived from active diagnostics could be presented also together with the modeling results in the following sections.

We already warn the reader that a systematic comparison between two different experimental conditions will be shown throughout the whole chapter. The compared experimental conditions are yet very similar, but they differ in a key feature, i.e. the external heating mechanism. In fact, JET pulses #94701 and #94704 have been chosen for this comparison because they are performed at very similar conditions (and even in the same experimental session), with the three-ion heating scheme applied in pulse #94701. In pulse #94704, the same heating power is provided but it is injected only through NBI. Such a difference in the auxiliary heating systems is fundamental to highlight the effect of the highly energetic ions generated via the three-ion heating scheme on the global confinement and plasma stability. In the following figures, the red color is used to refer to pulse #94701 heated through the three-ion scheme, whereas the blue color to refer to pulse #94701 heated by only NBI. For an overview of the two pulses see Figure 3.3.

3.1.1 Three-ion heating scheme: Generation of MeV-range ion population

As a first step, it is important to determine the characteristics of the suprathermal population, which are the principal actors of these broad studies. As already stated, the three-ion heating scheme, which makes use of the ICRH as main heating auxiliary device [108, 109, 110], is applied in an efficient combination with the NBI system. The three-ion ($\mathrm{D} - \mathrm{D}_{\mathrm{NBI}} - {}^{3}\mathrm{He}$) scenario at JET is schematically pursued by stabilizing the plasma with only NBI in a first phase, hence injecting in the systems a significant concentration of fast ions at the energy range $\sim$100 keV. After the first NBI-only phase, the ICRH is set on. Various ICRH input power levels have been examined throughout the scenario, without exceeding the 6 MW [111]. Thanks to the ideal density ratio among the three ion species in the plasma, it is possible to suitably determine the location of the mode conversion layer [108]. If the radial location of this particular layer coincides with the position of the resonant absorber ion species s and the injected frequency ω with the characteristic cyclotron frequency $\omega_{c,s}$ of such a species or its Doppler-shifted harmonics [113]:

$$\omega = h\omega_{c,s} + k_{\parallel} v_{\parallel,s} \tag{3.1}$$

with $h = (1, 2, 3, ...)$ the harmonic number, an almost perfect absorption of the ICRH power by the resonant absorber is achieved. Thus, depending on the ICRH input power, the resonant absorber species, generally present in only weak concentrations ($n_{absorber}/n_e < 3\%$), can be accelerated up to MeV energies [108]. For more details on the three-ion heating scheme, the readers can refer to e.g. [110] and references within.

This scheme is applied also in the ($\mathrm{D} - \mathrm{D}_{\mathrm{NBI}} - {}^{3}\mathrm{He}$) scenario at JET, where the two majority ion species D and ${}^{3}\mathrm{He}$ are injected in the ratio $X[\mathrm{D}] : X[{}^{3}\mathrm{He}] \approx 75\% : 25\%$. This ratio combined with the characteristics of the third ion species, i.e. $\mathrm{D}_{\mathrm{NBI}}$, moves the mode conversion layer in the deep core of the tokamak [111, 113]. Thus, the deuterium is appositely injected by the NBI in the core plasma, where the ICRH power is very efficiently absorbed. Detailed analyses by means of reconstructed fast-ion distribution from the neutron camera diagnostic at JET [114] confirm that the spatial distribution of the highly energetic ions produced by the three-ion scheme is localized in the deep core of those JET plasmas [115, 111].

In Figure 3.1, the energy of the ions recalculated from the TOFOR diagnostic [116] measurements of the neutron time-of-flight is illustrated for JET pulses #94701 and #94704, respectively represented in red and in blue. The energy of D ions is computed by measuring the time of flight of the neutron born from the $\mathrm{D} + \mathrm{D} \rightarrow {}^{3}\mathrm{He} + n$ (with the neutron energy $E_n = 2.5$ MeV) fusion reactions. Basically, kinematic considerations can relate the time of flight t_{TOF} of the fusion-born neutrons to the minimum energy of the reactant D ions [117]. This relation can be approximated by $E_n \approx 2.9$ MeV $\times(60\ \mathrm{ns}/t_{\mathrm{TOF}})$ Such a relation is illustrated in panel (b), where a monotonic function indicates that shorter time of flights

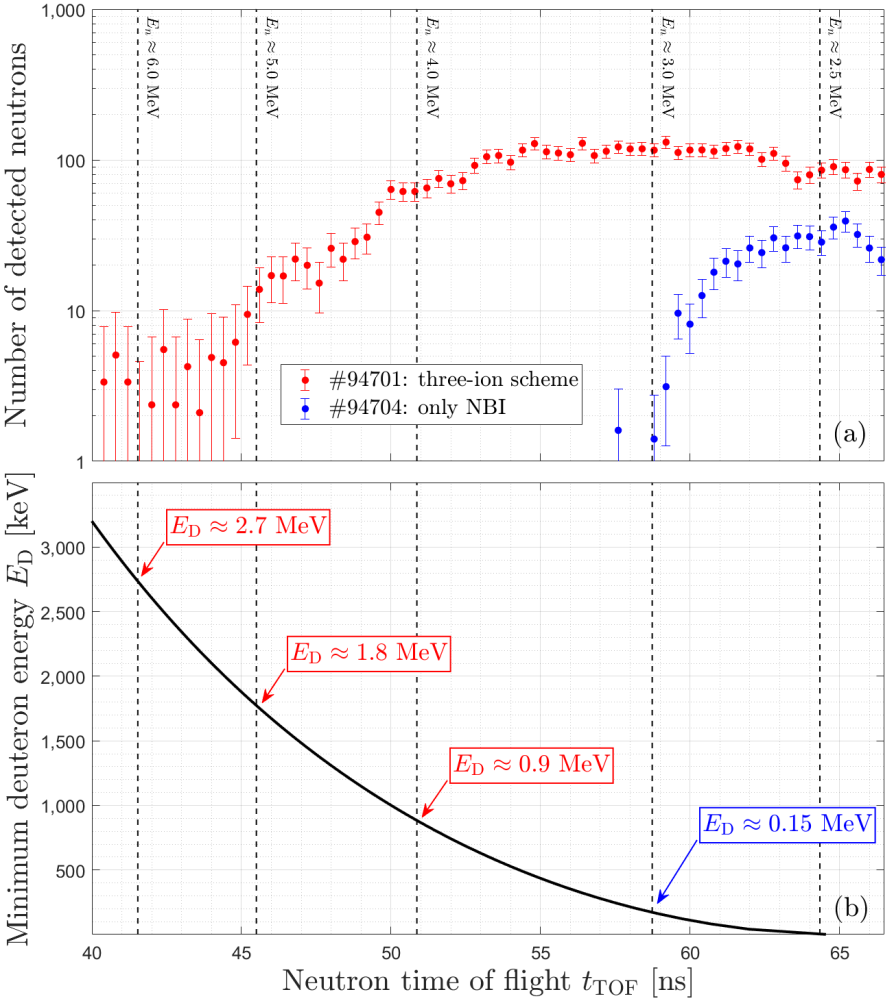

Figure 3.1: *In (a), number of counted neutrons by the TOFOR diagnostic in JET pulses #94701 and #94704 are respectively shown in red and blue. In (b), the kinematic relation between the neutron time-of-flight and the minimum energy of the deuteron giving rise to that fusion reaction is reported with a black solid curve. The vertical dashed lines help in identifying the corresponding energy of the deuterons at a given time-of-flight.*

correspond to more energetic reactant ions. As can be clearly seen from the red curve in panel (a) of Figure 3.1, when the three-ion heating scheme is applied the energy of the suprathermal ions reaches the MeV range. This ion energy is achieved via the efficient combination of the external heating systems NBI and ICRH applied within the three ion scheme. Whereas in pulse #94701 the fast ions are thereby measured up to 2.7 MeV, pulse #94704 heated by only NBI shows a maximal detected energy around 100 keV. This latter level of fast-ion energy is consistent with typical measurements in NBI heated plasmas at JET [117].

It has thus been shown that the three ion heating scheme applied in the $(D - D_{NBI} - {}^3He)$ scenario at JET can generate a significant population of fast

ions in the MeV-range of energy. In Figure 3.2, the Deuterium distribution function calculated from integrated modeling TRANSP is now shown in the velocity pitch angle $\lambda = v_{\parallel}/v$ and energy E_{D} space. The first conclusion that we can draw is about the anisotropy of the fast-ion distribution function. Although the energy range approaches the 3.5 MeV energy at which the alpha particles are born, the distribution of the so-generated fast ions is different from a Maxwellian. The isotropic distribution is indeed expected for the fusion-born alpha particles in burning plasmas. This consideration is relevant for the approximation employed in the following gyrokinetic analysis. Furthermore, the energy distribution function for the generated fast ion population reported in Figure 3.2 indicates that, although ICRH is expected to predominantly produce ions with large perpendicular velocities, co-passing ions (with $v_{\parallel} > 0$) are mainly generated in the three-ion ($\mathrm{D} - \mathrm{D}_{\mathrm{NBI}} - {}^{3}\mathrm{He}$) scenario. This singular feature is caused by the particular conditions developed in this scenario. Indeed, the ICRH energy is deposited to the absorber species in a strongly localized region of the deep core [111, 113], where the ions mainly experience a passing trajectory. This result is crucial for the full

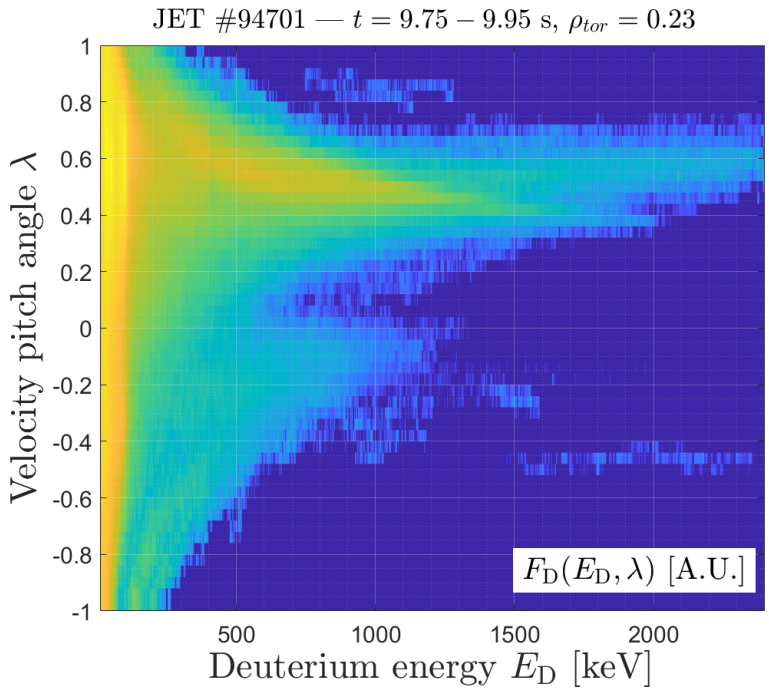

Figure 3.2: *The distribution function of the Deuterium species computed by TRANSP integrated modelling of JET pulse #94701 is shown in the energy/pitch-angle space for the time window* $[9.75 - 9.95]$ *s at* $\rho_{tor} = 0.23$.

comprehension of the striking phenomena occurring in several pulses of this scenario. As an example, the strong generation of co-passing ions in the core plasmas may explain the destabilization of the RSAEs. The RSAE gap in the Alfvén spectrum opens when the shape of the q-profile is non-monotonic, and RSAEs are generally localized at the minimum of the q-profile [118]. Nevertheless, the

systematic RSAE destabilization in the three-ion scheme scenario still needs to be further analyzed in dedicated studies. For this reason, the gyrokinetic modeling of pulse #94701 has been constrained to explore only the time slice before the excitation of the RSAEs, as it will be discussed in the following sections.

3.1.2 Impact of MeV-range ions on global plasma confinement

The main effects of the presence of the highly energetic ions generated via three-ion heating scheme on the global plasma characteristics are now illustrated. In Figure 3.3, the time evolution of the principal experimental indicators is shown for both JET pulse #94701 (in red) and pulse #94704 (in blue). Panels (a) and (b) illustrate, respectively, how the external heating power is subdivided between NBI and ICRH systems and the evolution of the line integrated electron density $\int n_e \mathrm{d}l$ measured by a combination of the high resolution Thomson scattering and electron cyclotron emission diagnostics for the two pulses. Whereas the totality of the external input power is introduced by NBI in pulse #94704, for #94701 after the first phase with only NBI the ICRH is introduced and the total input power is thereby equal ($P_{aux} = 14$ MW) for both pulses, as already pointed out. Although the two pulses are performed at very similar experimental conditions (namely at, e.g., very similar toroidal magnetic field B_t, plasma current I_p, plasma shape, input power from the auxiliary heating systems P_{aux}, electron density n_e, relative concentration of majority ion species $X[\mathrm{D}] : X[^3\mathrm{He}]$, etc.), striking differences are already visible from the waveforms. As it is expected, the electron temperature peaking T_{e0} is notably higher for the pulse heated via three-ion scheme. The increase of ∼50% with respect to the only-NBI pulse is essentially due to the presence of the MeV-range ions in the plasma core of pulse #94701. Being well above the critical energy (which has been calculated to be ~ 500 keV), the fast ions are predominately heating the electrons by Coulomb collisions [18]. This result can also be appreciated in Figures 3.4(a), in which the electron temperature profiles of the pulse #94701 and #94704 are compared for specific time windows, and in Figure 3.5, where the power deposition to the electrons computed by TRANSP is shown.

Another important effect of the MeV ions on the plasma stability is the stabilization of the sawtooth instability [119]. This is reported again in Figure 3.3(c), where the MeV-ions generated via three-ion heating scheme lead to monster sawtooth dynamics with respect to much shorter sawtooth period in pulse #94704 and in the first phase with only NBI of pulse #94701 [111]. Since the beneficial impact of long-period sawtooth dynamics on the global confinement is well-know [120], it is important to address this specific point in order to disentangle it from any other possible mechanism leading to better plasma insulation.

In panels (d) and (e) of Figure 3.3, two main indicators of the confinement performance, respectively the total plasma energy content W_p and the neutron rate γ_n, are reported. The plasma energy content of pulse #94701 is indeed increased when the ICRH is introduced and the three-ion heating scheme is thereby applied. An additional enhancement is observable when the ICRH input power

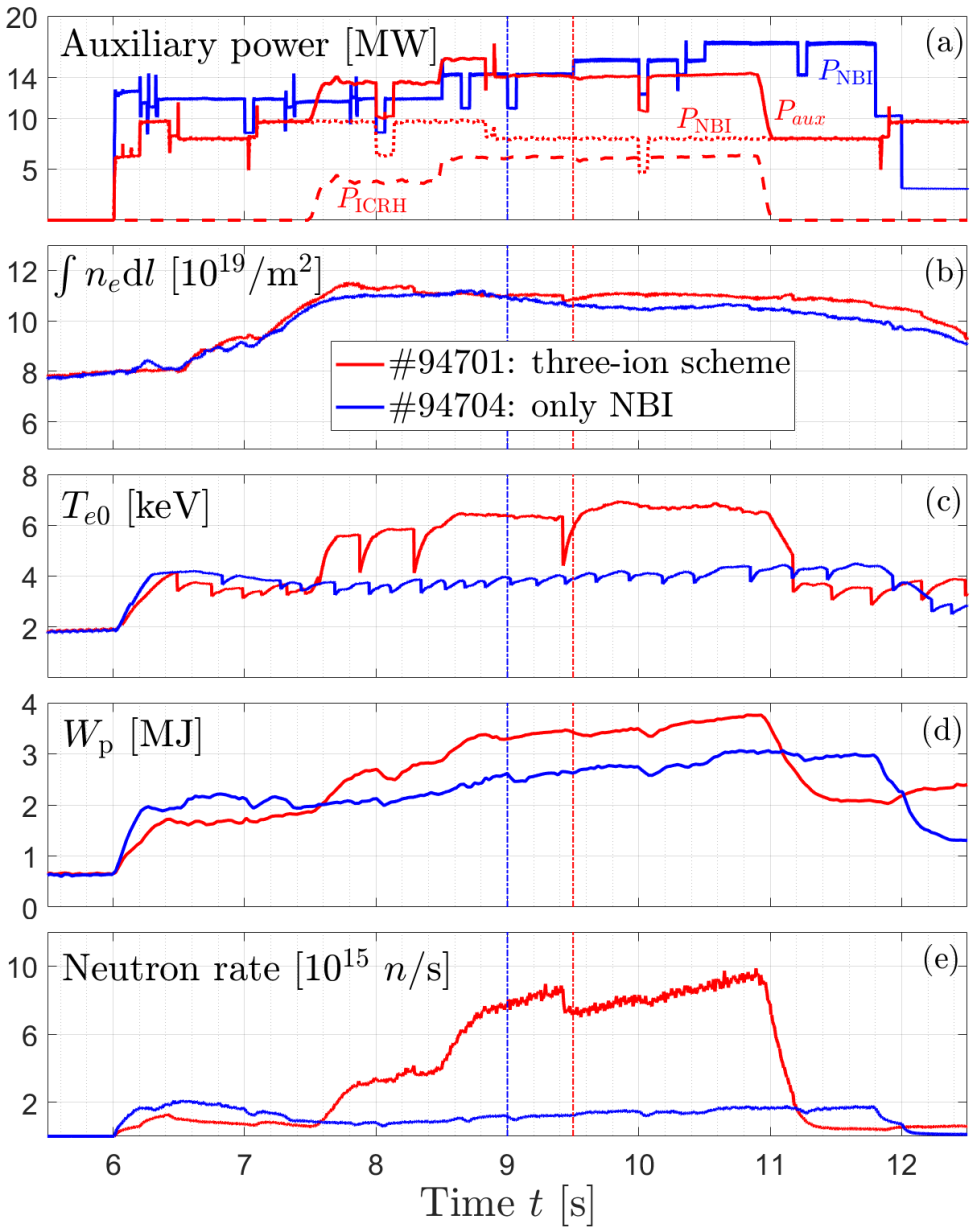

Figure 3.3: *The experimental waveforms of the main physical parameters for JET pulses #94701 and #94704 are plotted respectively in red and in blue for the significant time windows of both pulses. In (a), the auxiliary injected power through ICRH (P_{ICRH}) and NBI (P_{NBI}) is reported in MW. The sum of the two signals for JET pulse #94701 is represented in solid red line as P_{aux}. In the case of pulse #94704, $P_{\mathrm{ICRH}} = 0$. In (b) and (c), the line-averaged electron density at the magnetic axis $\int n_e \mathrm{d}l$ and the core electron temperature T_{e0} are respectively illustrated. In the last two panels, (d) and (e), the plasma stored energy W_{p} and the neutron rate γ_n show clearly the improved performance of pulse #94701 with respect to #94704. The vertical dashed lines represent the time slices which Figures 3.4 and 3.5 refer to.*

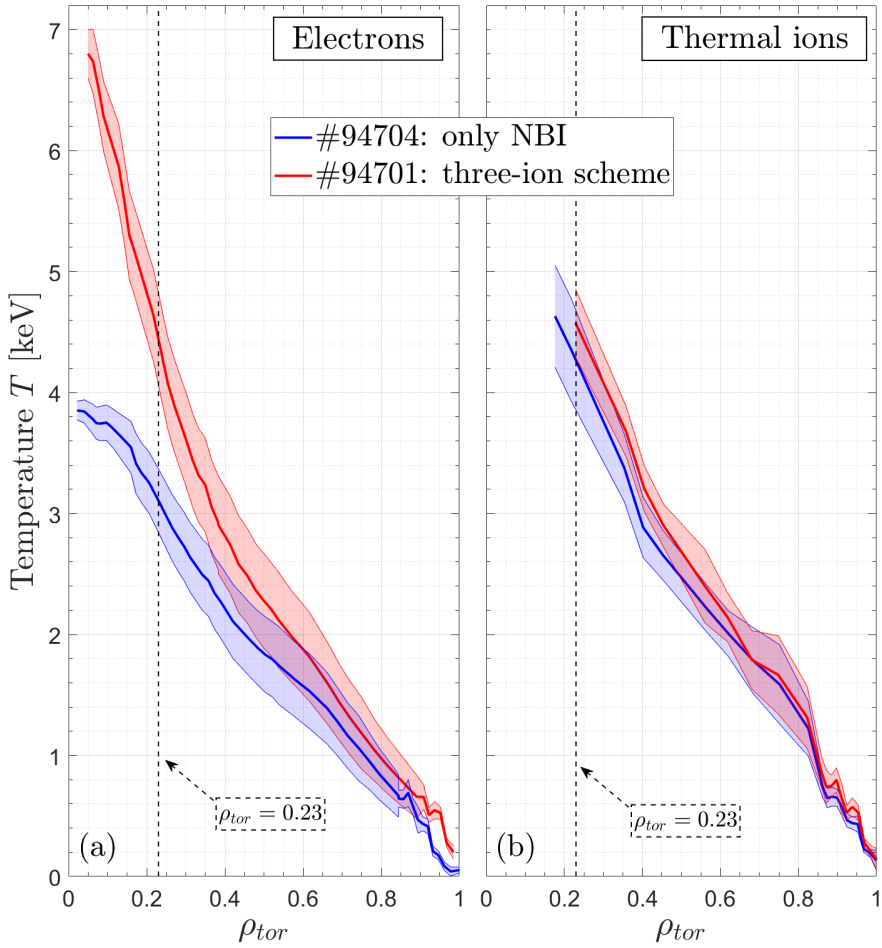

Figure 3.4: *The electron (panel (a)) and thermal ion (panel (b)) radial profiles of the experimentally measured temperatures are reported comparing the JET pulses #94701 and #94704 in red and blue respectively. The comparison is made at the time slices illustrated in Figure 3.3 with vertical dashed curves. The black dashed vertical lines represent the radial location $\rho_{tor} = 0.23$ at which the following gyrokinetic analyses have been performed.*

is further increased from $P_{\mathrm{ICRH}} = 4$ MW to $P_{\mathrm{ICRH}} = 6$ MW. However, such a W_{p} increase is not a synonym of improved confinement though. This is because the level of plasma energy content is strongly determined by the presence of the highly energetic ions. Nevertheless, it is remarkable that although a concentration of MeV ions in few percentage of the electron density can lead to such an increase with respect to the only-NBI pulse #94704. Even more remarkable is the comparison of the neutron rates in the two different pulses. Indeed, the neutron rate for the pulse heated by the three-ion scheme is almost an order of magnitude higher than the level achieved in the only-NBI pulse at the same heating power, $\gamma_n^{94701} \approx 8.0 \times 10^{15}\ n/\mathrm{s}$ vs. $\gamma_n^{94704} \approx 1.2 \times 10^{15}\ n/\mathrm{s}$. It must be stressed that the measured neutron rate is considering only the neutrons born from the $\mathrm{D} + \mathrm{D}$ fusion reaction. This consideration is crucial in order to properly evaluate

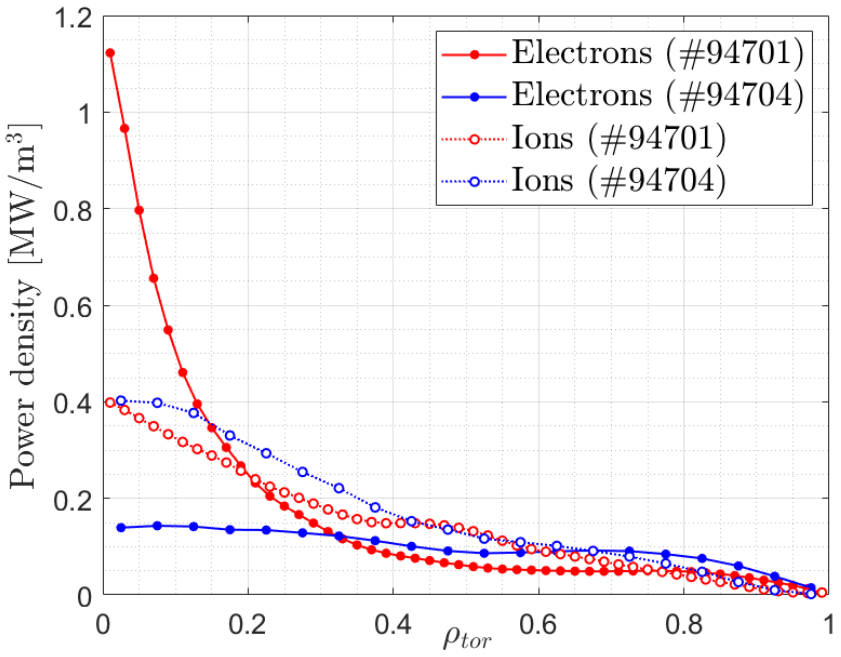

Figure 3.5: *The radial profile of the total power deposition on electron and ions for JET pulses #94701 and #94704 computed by TRANSP integrated modeling is illustrated. The comparison is made at the time slices illustrated in Figure 3.3 with vertical dashed curves. For the total input power deposition calculation, both the externally heating power (NBI + ICRH) and the electron/ion energy exchanges are considered.*

the increase of the neutron rate. In fact, the ($D - D_{NBI} - {}^3He$) scenario have been devised also with the purpose of validating neutron diagnostics at JET for the following experimental D-T campaign [112]. The concentration of ${}^3He$ is used not only for radially moving location of the mode conversion layer, but also to provide the reactant target for the nuclear fusion reaction $D + {}^3He \rightarrow {}^4He + p$ [111]. Thus, providing a substantial population of D ions in the MeV range strongly enhances the yield of this latter fusion reaction. Nevertheless, such a reaction does not contribute to the neutron rate plotted in Figure 3.3(e). On the other hand, even the neutron rate cannot be considered a definitive measure of the confinement performance. This is because the cross-section of the $D + D$ fusion reaction is strongly dependent on temperature of the reactants [8]. Basically the neutron yield for a population of fast D ions at ≈ 2 MeV is expected to be higher than for an equally-populated amount of fast D ions at ≈ 100 keV. In pulse #94701, the significant amount of MeV D ions generated via three-ion heating scheme could lead to the strong increase with respect to pulse #94704 reported in Figure 3.3(e). However, an interesting link can be set between the increase of the neutron rate and the destabilization of the RSAEs. This will be further analyzed in section 3.7.

Eventually, although it has been shown that the increase in plasma energy content and neutron rate with the onset of the three-ion heating scheme and the subsequent generation of MeV ions is not fully indicative of the improvement of

the global performance, it is quite remarkable if considered in the broad context. Indeed, also the ion temperature profile exhibits a particular behavior, which may indicate an improvement of the ion thermal confinement. In Figure 3.4(b), the experimentally measured ion temperature profiles for the two analyzed pulses are plotted. The striking observation is that the ion temperature of pulse #94701 is above the one of pulse #94704 at least in the region $\rho_{tor} < 0.4$ and up to the most inner available measurement. This was not expected, since the heating targets in the only-NBI pulse are the thermal ions, as it is also confirmed by the power density to the ions computed by TRANSP (see Figure 3.5). Indeed, the radial profile of the power deposited to the ions of pulse #94704 is higher in the region $\rho_{tor} < 0.4$ compared to the pulse #94701 (dotted lines with open symbols). On the other hand, in pulse #94701, as already said, the collisional fast-ion to electron heating is the dominant heating mechanism. This is again shown in Figure 3.5. It must be stressed that the comparison of the temperature profiles and power deposition shown in Figure 3.4 and 3.5 respectively between JET pulses #94701 and #94704 has been conducted in time windows with the same input heating power ($P_{aux} = 14$ MW) and very similar electron density ($n_e \approx 1.1 \times 10^{19}$ m^{-3}). Those time slices are represented by the vertical dashed lines in Figure 3.3, namely $t = 9.5$ s for pulse #94701 and $t = 9.0$ s for #94704. Therefore, such an observation about the ion temperature profile of pulse #94701 clearly indicates that the ion thermal confinement is somehow improved in conditions of strong electron heating. This latter consideration has essentially been the triggering reason for the in-depth transport analyses that have been carried out and will be presented in the remainder of this chapter.

3.1.3 Three-ion scheme as effective actuator of Alfvén activity

The experimental implications that follow the discussion made in the previous section are even more surprising if a further effect of the MeV ions is considered. Indeed, throughout the whole three-ion ($\mathrm{D} - \mathrm{D}_{\mathrm{NBI}} - {}^3\mathrm{He}$) scenario at JET, a rich variety of Alfvén activity has been systematically excited [111, 113]. A wide zoology of Alfvén modes are found unstable only in the ICRH phase, hence when the three-ion heating scheme is applied and the significant population of highly fast ions is generated. As an example, Figure 3.6 illustrates the spectrogram of the time derivative of the magnetic fluctuations measured by the Mirnov coil diagnostic for JET pulse #94701 (a Fourier transform of the Mirnov coil signal is applied in order to display the relevant frequency domain). TAEs are clearly destabilized in the frequency range $f \approx 185$-240 kHz with a constant frequency dynamics in the time period in which the three-ion heating scheme is efficiently applied (cf. Figure 3.3). The chirping-up mode born at $f \sim 100$ kHz are identified as RSAEs. As it has already been reported, RSAEs are a clear indication of the reverse of the q-profile slope. Beyond TAEs and RSAEs, also EAEs and $n = 0$ GAEs are found unstable [111], but here not reported as the Mirnov spectrogram is cut to only display the interesting region for the following gyrokinetic analyses.

In Figure 3.6, the TAE toroidal numbers are reported close to the signals. It is

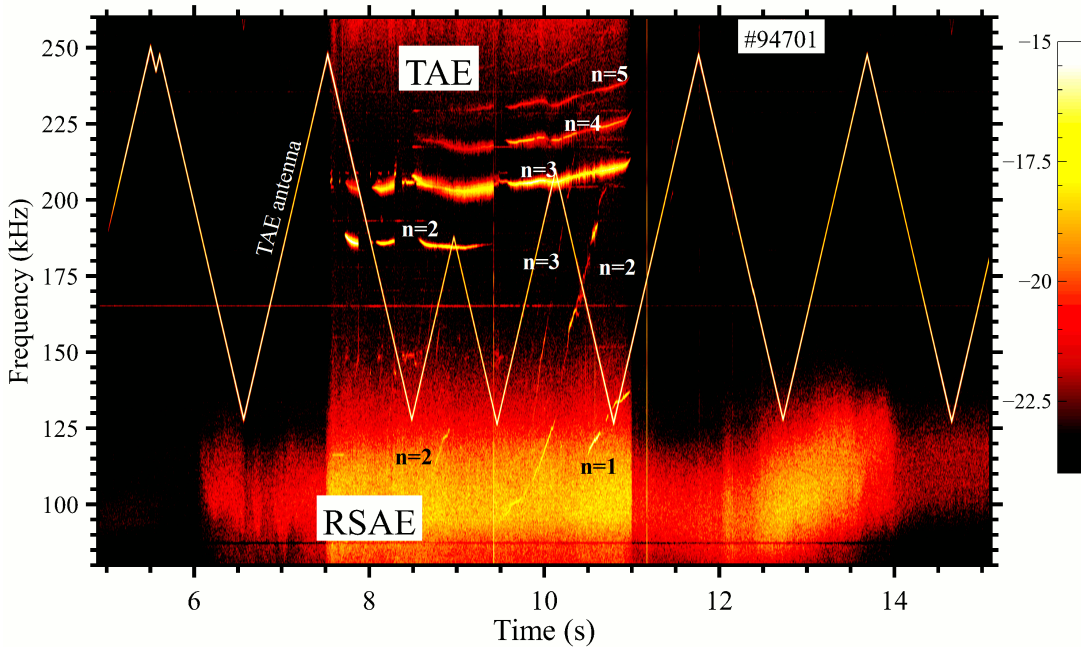

Figure 3.6: *Mirnov coil spectrogram measurements show strong Alfvén activity in the range* $100 - 250$ *kHz during the application of the three-ion heating scheme in pulse #94701.*

thus shown that TAEs are found unstable from $n = 2$ to $n = 5$. However, after the sawtooth crash occurring at $t \sim 9.4$ s, in the subsequent recovery phase the $n = 2$ TAE is not anymore detected. Indeed, a very weak signals is measured at $f \approx 240$ kHz in the time window $t = 9.4 - 10.5$ s which would suggest an unstable $n = 6$ TAE.

It is crucial for the following gyrokinetic analyses to determine the radial range at which the TAEs are found unstable. This has been evaluated by analyzing the experimental data collected by the X-mode correlation reflectometer [121, 122]. Since such measurements are not available for the JET pulse #94701, the analysis have been performed on pulse #95669, performed at very similar experimental conditions with respect to pulse #94701 [123]. The reflectometer is positioned at the horizontal line-of-sight, and it scans the radial positions going from the edge to the core plasma. To cover the whole minor radius the reflectometer takes ∼0.6 s. Basically, it measures the time derivative of the electrostatic potential perturbations, possibly indicating thus the presence of unstable TAEs in a specific radial range. The results of this analysis are illustrated in Figure 3.7. The top panel shows the spectrogram computed from the measured signals, while the bottom panel refers to the radial range explored by the reflectometer in its cyclic period. The highlighted gray shaded area facilitates the identification of the TAE radial range, i.e. 3.22 m $< R <$ 3.36 m. Although this analysis is performed for pulse #95669, the electrostatic spectrogram shown in Figure 3.7 is very similar to the magnetic spectrogram reported in Figure 3.6. For this reason, it is possible to

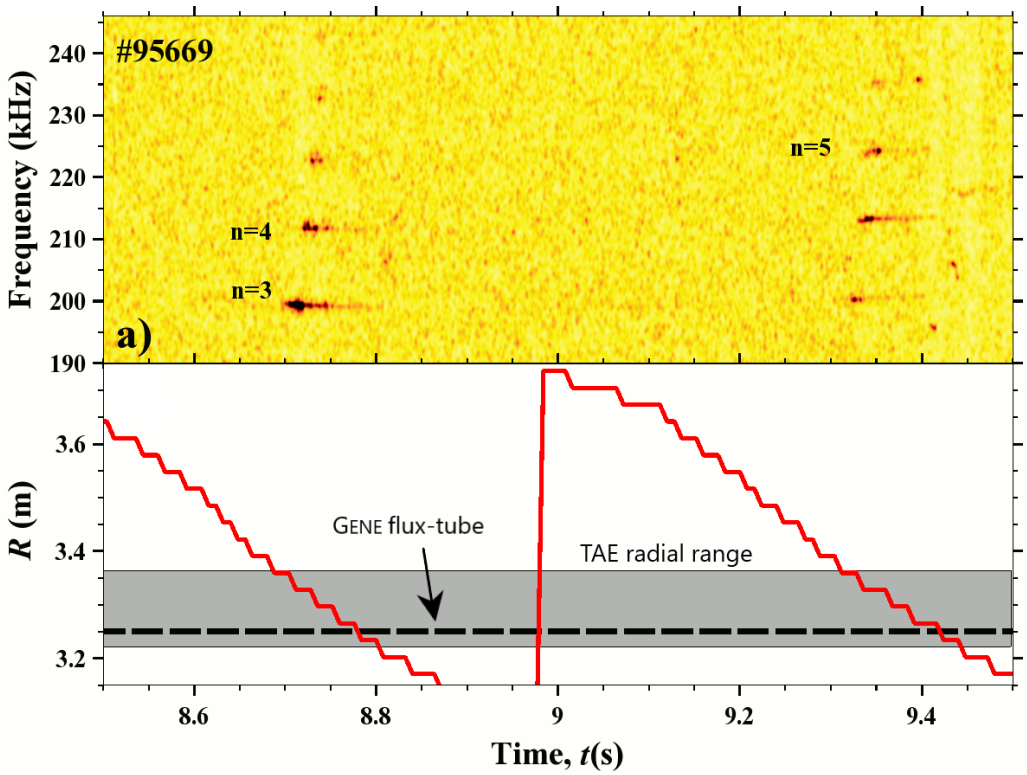

Figure 3.7: *The radial location of the TAEs is illustrated. In panel (a) the spectrogram of the radially moving reflectometer is shown in the frequency range where TAEs are measured. Panel (b) shows indeed the radial movement of the reflectometer, from the plasma edge to the core at the mid-plane line-of-sight. The gray shaded area illustrates the so-identified TAE radial location, with the black horizontal dashed curve representing the radial position of the mid-plane of the flux surface* $\rho_{tor} = 0.23$ *analyzed in the gyrokinetic analyses with the* GENE *code.*

assume that the radial localization of the TAEs for pulse #95669 can be applied also to pulse #94701.

To conclude the discussion about the experimental results of the three-ion $D - D_{NBI} - {}^3He$ scenario at JET, a relevant point for the following in-depth gyrokinetic analyses must be reported. This concerns the systematic destabilization of a still unidentified mode in the low-frequency range, around 20 kHz. An example of this mode is reported in Figure 3.8, in which the Mirnov coil spectrogram for JET pulse #94701 is shown for a restricted frequency window. Because such unstable modes were observed also in the only-NBI pulse #94704, at a first investigation no great importance has been given to. Nevertheless, further analyses by means of the X-mode reflectometer performed by Mykola Dreval on pulse #95669 highlighted that the radial location of this mode coincides with the detected TAE radial range. Some more insights will be given in the following Section 3.4.5, since a mode with similar characteristics has also been detected in the gyrokinetic analyses.

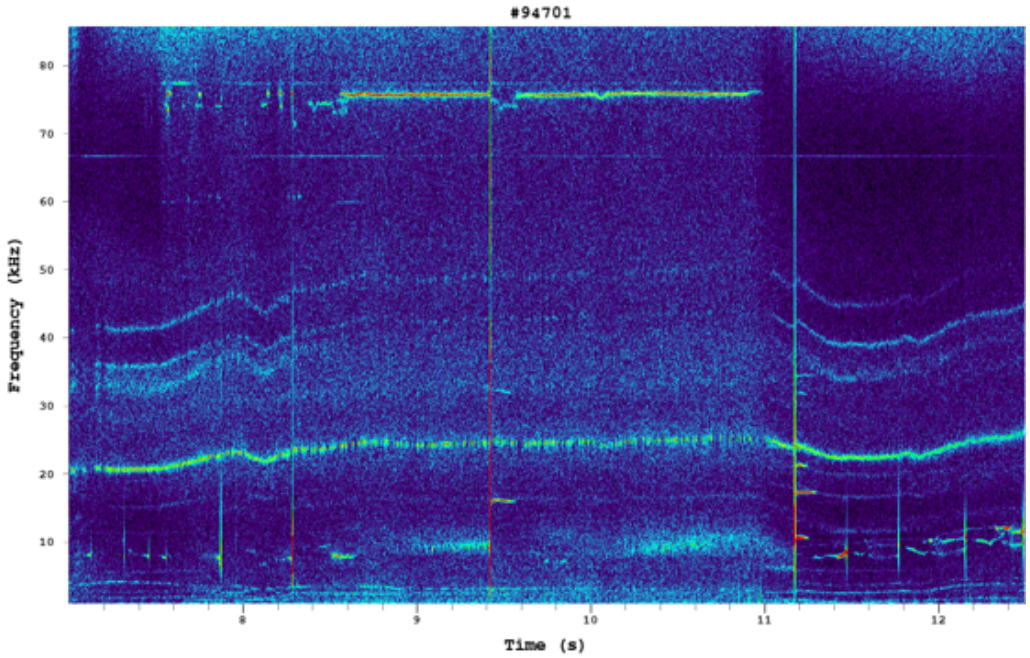

Figure 3.8: *The Mirnov coil spectrogram of JET pulse #94701 is now shown for the low frequency range $f < 85$ kHz, differently from the higher frequency range reported in Figure 3.6.*

3.2 Numerical setup

The results reported in the following sections have been achieved by performing numerical simulations of the JET pulse #94701 with the gyrokinetic GENE code. Employed in its local version, the GENE code is thereby considering only a flux-tube of the entire plasma extension. The considered flux-tube is located around the magnetic surface at $\rho_{tor} = 0.23$ at the time slice $t = 9.5$ s. Such a radial localization has been chosen for multiple reasons. First, a still considerable amount of fast ions generated via the three-ion heating scheme is computed by the TRANSP integrated modeling at this radial location, as it is shown in Figure 3.9. This figure is consistent with Figure 3.2, but an additional average over the pitch angle λ has been performed and various radial positions are displayed. In Figure 3.9, a significant tail of F_{D} at MeV range of energy could be seen up to $\rho_{tor} \approx 0.3$. In a second place, the experimental measurements of the ion temperature are still available. This is confirmed by Figure 3.4(b), where the radial location $\rho_{tor} = 0.23$ has been highlighted with a black vertical dashed line. It must be noted precautionally here that the extrapolation of the ion temperature profile in TRANSP is based on empirical assumptions, and therefore it could lead to big uncertainties on the quantitative assessment of the turbulent transport. To cope with this issue, a scan over the thermal ion temperature gradient R/L_{T_i} has been carried out, as it will be reported in a dedicated section in the following. Another important reason for choosing $\rho_{tor} = 0.23$ is the radial localization of the TAEs. As it has

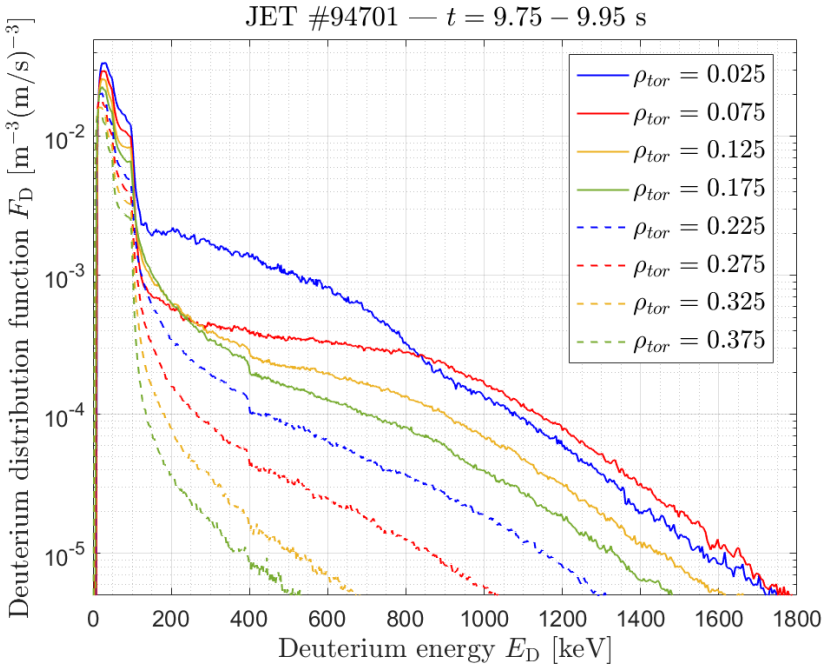

Figure 3.9: *Deuterium distribution function as computed by TRANSP at different radial locations of JET pulse #94701, and shown as a function of the Deuterium energy* E_{D}.

been shown in Figure 3.7, the radial range at which the TAEs are measured is $3.22\ \mathrm{m} < R < 3.36\ \mathrm{m}$, which roughly corresponds to $0.21 < \rho_{tor} < 0.37$. In the bottom panel of the same Figure 3.7, the black horizontal dashed line represents the radial localization of the GENE flux-tube domain at the mid-plane of the low field side (corresponding to $R = 3.25$ m). Furthermore, the limitation of the local approximation in approaching the magnetic axis ($\rho_{tor} \approx 0$) must be taken into account. Firstly, extending the simulation box up to the magnetic axis, where the neoclassical transport is supposed to dominate and the turbulent transport to be almost quenched, would lead to arguable evaluations of the system stability; in second place, since the numerical box has a radial extension that depends on the analyzed cases, getting closer to $\rho_{tor} \approx 0$ could lead to stretch the box up to, and beyond, the magnetic axis and therefore to a strongly unphysical interpretation of the system.

The use of the local approach is pushed to its limit for this specific case in which highly energetic ions are considered. Although the ratio of the Larmor radius to the minor radius $\rho_s/a = \rho_s^*$ of JET pulse #94701 for the thermal ions is $\rho_i^* \approx 1/240$ and fully justifies the local approximation, the same parameter for the fast deuterium generated via three-ion heating scheme is $\rho_{FD}^* = 1/90$. Such parameter is indeed non-negligible, as the local approximation would require. Nevertheless, the inclusion of kinetic species with large ρ_s^* ratio has already been reported in the literature, leading to reliable transport levels, also properly matching the experimental power balances. Examples of efficient local simulations with large ρ_s^* species can be appreciated e.g. in Refs. [124, 71, 93, 90, 125].

As it has already been reported, the interpretive integrated modeling framework has been carried out by means of the TRANSP modeling suite [126] for both JET pulses #94701 and #94704. The local absolute and gradient values employed in the configuration of the GENE local simulations for pulse #94701 have been extrapolated from TRANSP simulations, which are based on experimental measurement constraints and well-tested profile fitting techniques.

The realistic magnetic equilibria, on which the numerical equilibrium are based, are computed by means of EFIT, in which constraints of the magnetic measurements and pressure profiles (including also the suprathermal pressure) of JET pulse #94701 have been applied. As already pointed out, the GENE simulations have been carried out by employing a numerical Miller geometry [16]. This has allowed to locally modify the shape of the q-profile. In fact, the magnetic equilibrium reconstructed via EFIT led to a q-profile affected by a non-typical behavior in the deep core region, with strong uncertainties on the local values of both magnetic shear and q. For this reason, after a careful check with MHD experts at JET, the local (at $\rho_{tor} = 0.23$) q and the magnetic shear $\hat{s}$ input parameters have been set to the more accurate values of $q = 1.1$ and $\hat{s} = 0.63$, as reported in Table 3.1. For the numerical analyses not including the fast ions an alternative magnetic equilibrium based only on the thermal pressure profiles has been employed. Yet, the same values of q and $\hat{s}$ are retained.

Table 3.1: *Employed plasma parameters in* GENE *simulations modelling JET pulse #94701 at $\rho_{tor} = 0.23$ and $t = 9.5$ s. Here, ϵ represents the inverse aspect ratio, n the species density normalized to the electron density, $R/L_{n,T}$ the normalized logarithmic density and temperature gradient, β_e the electron-beta, and $\nu^* \equiv (an_e/4|e|^2 n_i)\nu_{ei}$ the normalized collision frequency, where a is the minor radius, e the electron charge and nu_{ei} the Hinton-Hazeltine electron-ion collision rate [27]. Eventually, the normalization factors in standard units are also reported, i.e. the on-axis magnetic field strength B_0, the local ($\rho = 0.23$) electron temperature T_e and density n_e, and the major radius R_0. The reported input parameters are common to all the numerical* GENE *simulation cases. The various cases, however, differ essentially in the fast ion pressure gradient $R/L_{p_{FD}}$.*

ϵ	q	$\hat{s}$	T_i/T_e	R/L_{n_e}	$R/L_{T_{e,i}}$
0.31	1.1	0.63	1.0	4.50	10.30
n_{D}/n_e	$n_{^3\mathrm{He}}/n_e$	$R/L_{n_{\mathrm{D}}}$	$R/L_{n_{^3\mathrm{He}}}$	n_{FD}/n_e	T_{FD}/T_e
0.43	0.27	3.70	4.97	0.03	33.8
β_e [%]	ν^*	B_0 [T]	T_e [keV]	n_e [m^{-3}]	R_0 [m]
0.68	$9.4 \cdot 10^{-5}$	3.68	4.41	$5.18 \cdot 10^{19}$	3.00

In the nonlinear simulations, the discretization of the numerical box is $(n_x, n_y, n_z, n_{v_\parallel}, n_\mu) = (256, 48, 32, 48, 64)$ with a perpendicular box width of $[L_x, L_y] = [264, 251]$ in units of ρ_s. The same numerical discretization and box size has been employed also in the simulations without including the fast ions,

with the only difference on the resolution of the magnetic moment space. This is due to the excitation of a fast-ion-driven instability well localized at large perpendicular velocities when the highly energetic fast ions are retained in the simulations, as it will be presented in the following. Such an instability is not excited in the system without fast ions, and therefore the discretization in the perpendicular velocity direction has been relaxed to $n_\mu = 16$. The value of $n_\mu = 64$ in the simulations including the suprathermal species has been chosen after demanding convergence tests performed in the nonlinear regime. It must be noted that the GENE discretization in μ-direction is not equidistant but it follows the Gauss-Laguerre distribution, and it has thereby a less dense number of nodes with increasing μ. Yet, the wave-particle resonance at hand occurs at large perpendicular velocities, hence n_μ must be strongly increased in order to acceptably capture and resolve the structure in the velocity space. Such an increase in the numerical discretization leads to highly demanding simulations, with a numerical cost up to 9 MCPUhs for a single point of the nonlinear scan.

For all the simulations except where explicitly said, four different species have been kinetically treated in the system. Those are: electrons, thermal deuterium (majority ion species), thermal helium-3 (minority ion species) and fast deuterium (ion absorber of the ICRH power in the three-ion heating scheme). The suprathermal distribution function, although accurately computed by TRANSP as can be seen in Figure 3.2, has been approximated with an equivalent Maxwellian in the numerical simulations with GENE. Because of the importance of using realistic distribution of the fast ions in studying the interaction with the turbulent transport, the fast-ion radial gradient has been widely scanned in order to compensate for such an approximation. The small traces of impurity concentration, mainly composed by beryllium, have been neglected in order to save computational time. This approximation is not expected to have dramatic effect on the transport, as the relative density of beryllium at $\rho_{tor} = 0.23$ is measured to be very low. The toroidal rotation and the flow shears have not been considered in the simulations, because of the low-torque conditions at which pulse #94701 has been performed.

3.3 Linear stability studies

In this section, the results of the linear stability analysis by means of the gyrokinetic GENE code in its flux-tube version are reported. Firstly, the system without suprathermal species is analyzed to highlight the dominant instabilities driven by the thermal species. It will follow a deeper study on the impact of the fast ions on the linear stability of JET pulse #94701.

3.3.1 Linear stability of the system without fast ions

Figure 3.10 illustrates the growth rate and mode frequency spectra in function of the binormal wavenumber normalized to the reference Larmor radius $k_y\rho_s$ in

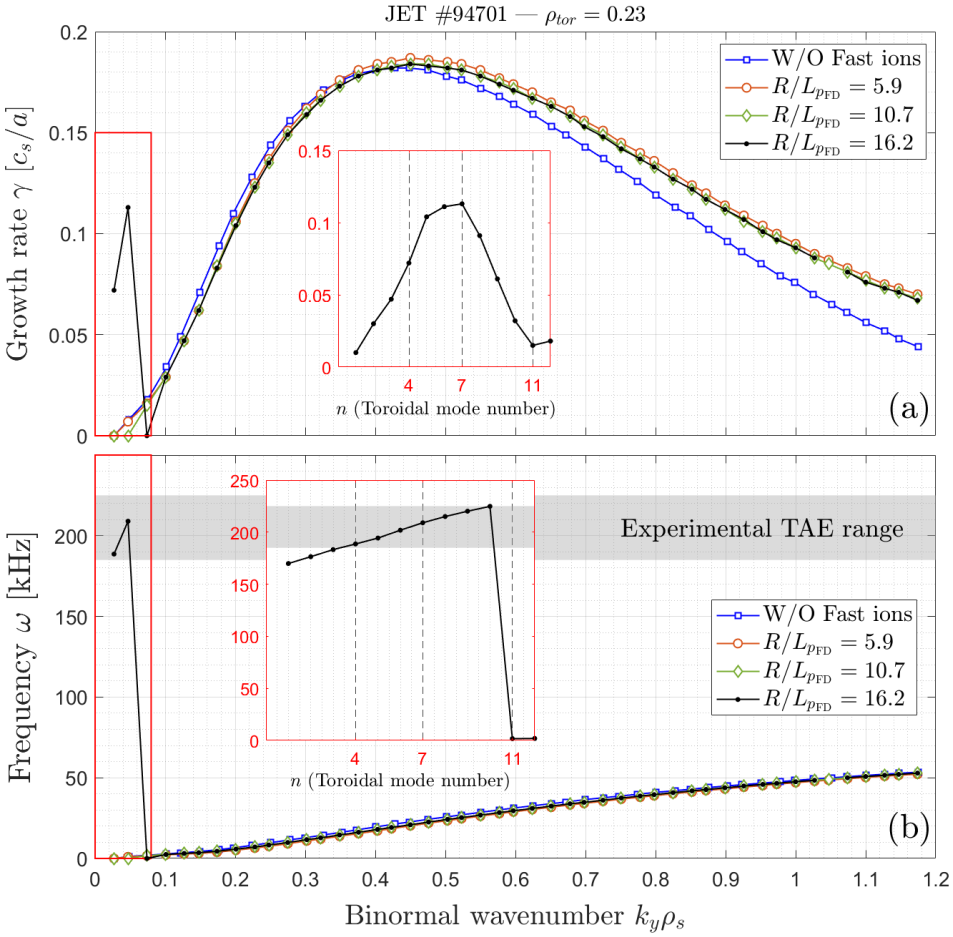

Figure 3.10: *Linear growth rates (a) and frequencies (b) computed by the* GENE *code for the JET pulse #94701 at* $\rho_{tor} = 0.23$ *are plotted against the binormal wavenumbers* (k_y) *normalized to the ion sound Larmor radius* (ρ_s). *The insets for the key region* $0.025 < k_y\rho_s < 0.08$ *are shown to indicate the corresponding toroidal mode numbers* n *of the fast-ion-driven unstable modes in larger-resolution linear scans for* $R/L_{p_{FD}} = 16.2$. *The highlighted toroidal numbers in red in the insets represent the retained binormal wavenumbers for the low-*k_y *region in the performed nonlinear* GENE *simulations. The gray shaded area in the frequency spectra displays the range at which the TAEs are experimentally detected by the Mirnov coils.*

panel (a) and (b), respectively. The blue curves represent the outcomes of the simulation without fast ions. The growth rate spectrum peaks at $k_y\rho_s \approx 0.45$ with the mode frequency rotating in the ion diamagnetic rotation. As expected from the large value of the thermal ion temperature gradients and as commonly obtained in core plasmas at JET, this instability has been identified as ITG modes. Also the ballooning structure with a dominant peak at the central $k_x\rho_s$ mode and very weak sidebands is the typical structure for an ITG mode (here not reported for the sake of simplicity).

The spectra reported in Figure 3.10 are limited to the ion-scale region ($k_y\rho_s < 1.2$) where the ITG modes are dominant. At smaller scales, due to the large value of R/L_{T_e} also the ETG modes are found unstable. The ETG instability peaks at $k_y\rho_s \approx 15$ and extends up to $k_y\rho_s \approx 30$, as it is illustrated by the blue curve in Figure 3.11. Although the ETG growth rate peak is larger than that of the ITG modes, the nonlinear simulations have been limited to the ion-scale region ($k_y\rho_s < 1.2$). The main reason for adopting such a solution is to focus on the thermal ion transport, since the main improvement observed in the experimental measurements concerns the thermal ion channel. Moreover, recent gyrokinetic studies of JET L-mode pulse with the GENE code reported that the ion-scale transport is almost unaffected when multi-scale analyses, including the unstable ETG scale, are performed [127, 128, 129]. Therefore, a minor impact is expected for the ITG-dominated transport from multi-scale interactions with electron-driven modes. To additionally enforce the choice of avoiding the electron scales, the rule of thumb proposed in Ref. [130] is applied. Such criterion is based on the evaluation of the ratio $\tau_{crit} = (\gamma_{ETG}/k_{y,ETG})_{max}/(\gamma_{ITG}/k_{y,ITG})_{max}$, where γ_{ETG} (γ_{ITG}) represents the growth rate of the ETG (ITG) mode peaking at the wavenumber $k_{y,ETG}$ in the electron scale ($k_{y,ITG}$ in the ion scale). If $\tau_{crit} > 1$, ETGs are expected to strongly affect the total electron transport. In Figure 3.11, the red dotted curve illustrates the criterion described above. Being the peak of the ETG region lower than that of the ITG region ($\tau_{crit} = 0.42$), the original choice of not retaining the ETG modes in the nonlinear numerical analyses is thus justified.

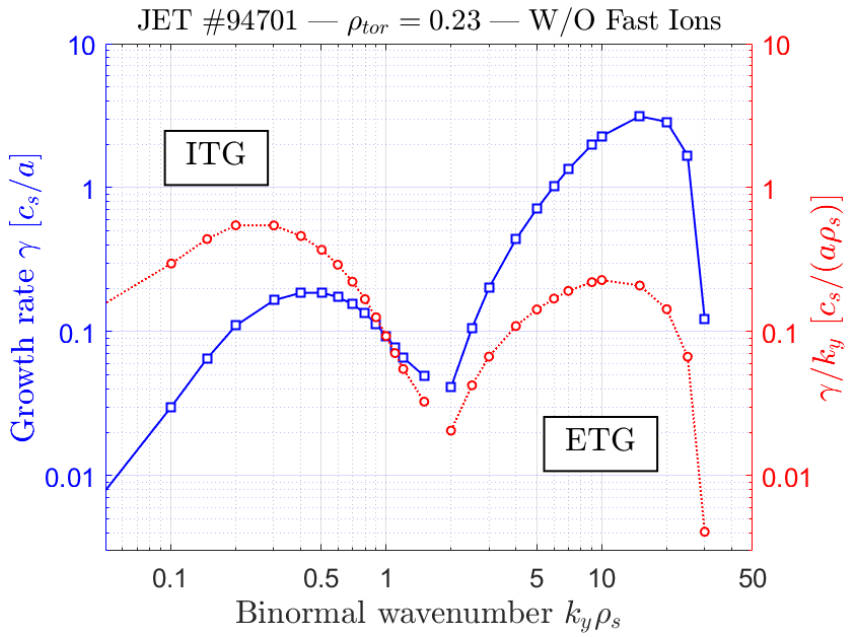

Figure 3.11: *The linear growth rate spectrum computed by the* GENE *code is shown as a function of the binormal wavenumbers k_y is shown in blue, highlighting the destabilization of ETG modes in the small scales. In red, the criterion represented by the parameter τ_{crit} is also reported.*

3.3.2 Impact of fast ions on the linear stability of JET pulse #94701

In Figure 3.10, a wide scan over the normalized fast ion pressure gradient $R/L_{p_{\mathrm{FD}}}$ is reported. The first observation is the almost null impact on the growth rate of the ITG modes when the $R/L_{p_{\mathrm{FD}}}$ is varied over a wide range. The only mild difference that could be measured between the cases with fast ions and the simulation without fast ions (blue curve) could be related to dilution effects and modification of the magnetic geometry. Despite the wide range of fast-ion pressure gradient that has been considered, such a difference remains almost negligible, especially for the most unstable ITG modes. The ballooning structure of the ITG mode in the various case presents only slight modifications, further corroborating the absence of fast-ion effect on the ITG modes. Additional analyses have been performed to exclude that a particular wave-particle resonance between the magnetic drift of the fast particle and the ITG mode frequency occur [72]. The described resonance has been envisaged to be the underlying mechanism for ITG growth rate stabilization found in previously reported gyrokinetic studies on the impact of fast ions on the ITG instability [76, 77]. Such a mechanism is found to be predominant for a specific range of fast-ion to electron temperature ratio ($T_{fast}/T_e \sim 12$), and to be almost non-active when $T_{fast}/T_e > 30$ [72], like in the present case (see Table 3.1 for the input parameters and specifically for the employed value of $T_{FD}/T_e = 33.8$). Thus, this could be the reason for the negligible impact of fast ions on the ITG growth rate of JET pulse #94701. A first conclusion that could be drawn from these considerations is the absence of linear interaction between the ion-scale instability and the suprathermal particles. This will help in identifying properly the possible eventual mechanisms leading to turbulence reduction.

Another striking observation is the destabilization of a high-frequency and large-scale instability when $R/L_{p_{\mathrm{FD}}}$ overcomes a critical threshold. Beyond such a threshold, determined to be $R/L_{p_{\mathrm{FD}}} = 10.7$ and represented by the green spectrum in Figure 3.10, the large-scale instability is excited. The present destabilization of low-k_y modes is reminiscent of some previously reported analyses in which fast-ion drivers (especially $R/L_{p_{\mathrm{FD}}}$ and β_e) were observed to excite the fast-ion-driven instabilities [76, 77, 90]. As it has already been reported in the previous section 1.5, in these latter studies the low-k_y instability represent a critical limit for achieving the beneficial fast-ion stabilization of the ITG turbulent transport and for matching thereby the experimental power balances. In fact, when the driver of the fast-ion modes is beyond the critical limit, the heat fluxes of the thermal species are strongly enhanced resulting in an explosion of the fluctuation amplitude of the same fluxes [76, 78]. This is especially true for the electron electromagnetic transport, which is well-known to be strongly related to the fluctuation amplitude of the magnetic potential due to the very large thermal velocity of the electrons [21]. For this reason the previous analyses were limited by the fast-ion destabilization. In the present study, indeed, the experimental measurements clearly indicate the systematic destabilization of specific Alfvén eigenmodes by the fast ions accelerated via the three-ion heating scheme. Additional analyses have also been performed to establish the effective destabilization of the Alfvén

eigenmodes in the specific JET pulse #94701. These analyses show that TAEs are expected to be unstable, which further corroborate the correct presence of the fast-ion unstable modes in the GENE gyrokinetic simulations. A more detailed explanation on the mode identification is reported in the following section 3.3.3.

Concerning the electron-scale modes, no substantial effect of the fast ions is observed on the growth rate and frequency of the unstable ETG modes (see Figure 3.12). The very mild discrepancies between the two case are likely related to the difference in the magnetic equilibria.

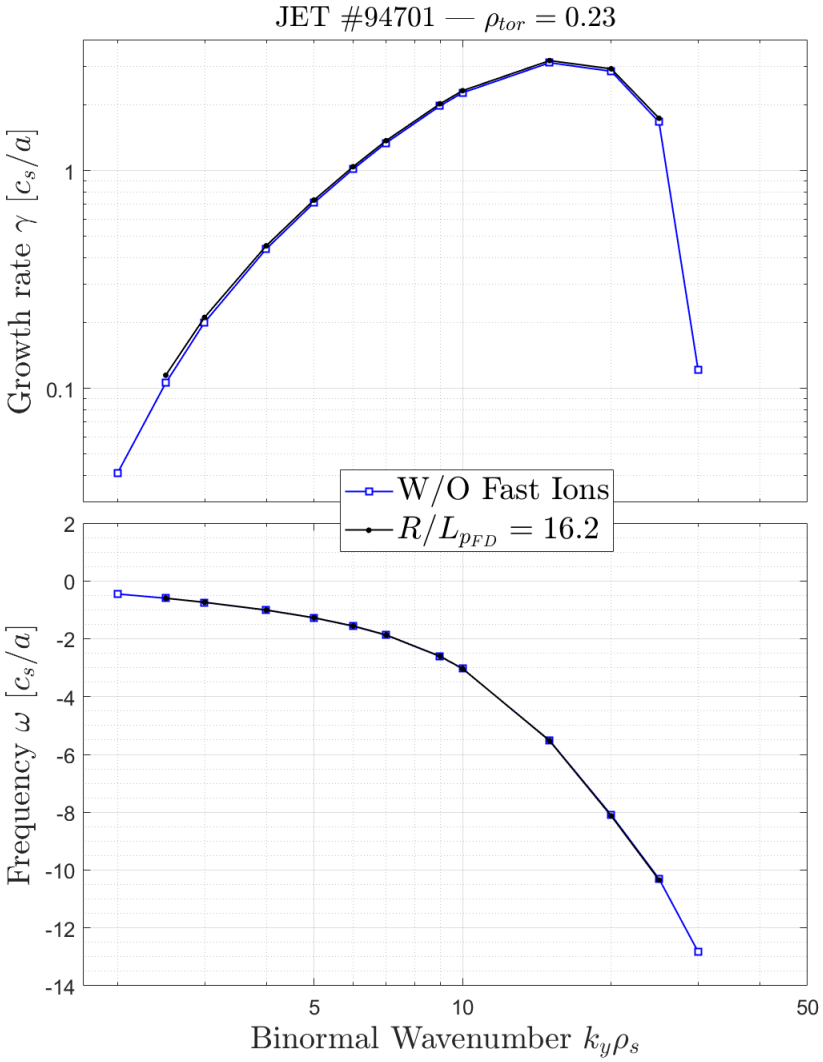

Figure 3.12: *The ETG linear growth rates of JET pulse #94701 at* $\rho_{tor} = 0.23$ *computed by the* GENE *code are compared between the case without fast ions and the case with* $R/L_{p_{FD}} = 16.2$.

3.3.3 Identification of the fast-ion-driven instability

In this paragraph, the focus is put on the low-k_y unstable modes, destabilized when the fast-ion pressure gradient is increased over a critical value, which has already been reported to be $R/L_{p_{\mathrm{FD}}} = 10.7$. In Figure 3.10, the $R/L_{p_{\mathrm{FD}}} = 16.2$ case (black curves) shows the destabilization of the $k_y\rho_s = 0.025$ and $k_y\rho_s = 0.05$ modes with a mode frequency within the TAE experimental range of frequencies, which is highlighted with a gray shaded area in the panel (b). It is to be noted that in Figure 3.10(b), the frequency are reported in kHz to facilitate the comparison with the experimental measurements. For the sake of completeness, the normalizing factor in these GENE modeling of JET pulse #94701 at $\rho_{tor} = 0.23$ is 1 kHz $= 0.009\ c_s/a$.

For the case with $R/L_{p_{\mathrm{FD}}} = 10.7$, no unstable modes in the same wavelength range are found, but for a very slight increase of the fast-ion pressure gradient (within 1% of relative modification) the high-frequency modes are destabilized. For this reason, the case with $R/L_{p_{\mathrm{FD}}} = 10.7$ is termed as *marginally stable* case. The latter case fully resembles the main focus of the previously reported studies at JET [76, 77, 90], where it was not justified to overcome the critical limit of the fast-ion mode destabilization since in the corresponding experiments no signs of mode excitation from several active diagnostics were observed.

Indeed, the case with $R/L_{p_{\mathrm{FD}}} = 5.9$ could be also termed in the remainder of the chapter as *stable* case, since the fast-ion pressure gradient value is far from the critical threshold for the destabilization of the low-k_y modes.

Focusing now on the configuration with $R/L_{p_{\mathrm{FD}}} = 16.2$, the spectra reported in Figure 3.10 show only the destabilized modes at $k_y\rho_s = 0.025$ and $k_y\rho_s = 0.05$, which correspond to the toroidal mode numbers $n = 4$ and $n = 7$ respectively. The reason for this choice is twofold, namely the modes represented in the spectra are the ones that have been retained in the following nonlinear simulations, and for not overfilling the curves. In order to be more explicit, an inset have been introduced in Figure 3.10 for both growth rate and frequency spectra with all the toroidal numbers from $n = 1$ to $n = 12$ only for the configuration with $R/L_{p_{\mathrm{FD}}} = 16.2$. The corresponding regions of the original spectra are highlighted with a red rectangle. As can be seen, the non-global dominant peak of the low-k_y instability is localized at $n = 7$ ($k_y\rho_s = 0.05$). The growth rate spectrum also suggests that for $n < 4$ and for $n > 9$, the unstable modes would mildly contribute to the total transport, since their rate values are small. This is not fully consistent with the experimental measurements, shown as magnetic spectrogram in Figure 3.6, in which the TAE most destabilized harmonic is the $n = 3$ especially at $t = 9.5$ s, and the $n = 7$ is not even detected. It is however remarkable the agreement with the frequency range measured by the Mirnov coil diagnostic, as can be appreciated in the inset of panel (b) of Figure 3.10.

Following this striking finding, the Alfvén spectrum has been computed taken into account the considerations made by Fu ad Van Dam and reported in Ref. [49] (cf. Equation (8) of such a reference) about the impact of the toroidicity on the continuum gaps. The results for $n = 4$ and $n = 7$, namely the two binormal wavelength retained in the nonlinear setup, are shown in Figure 3.13. As already

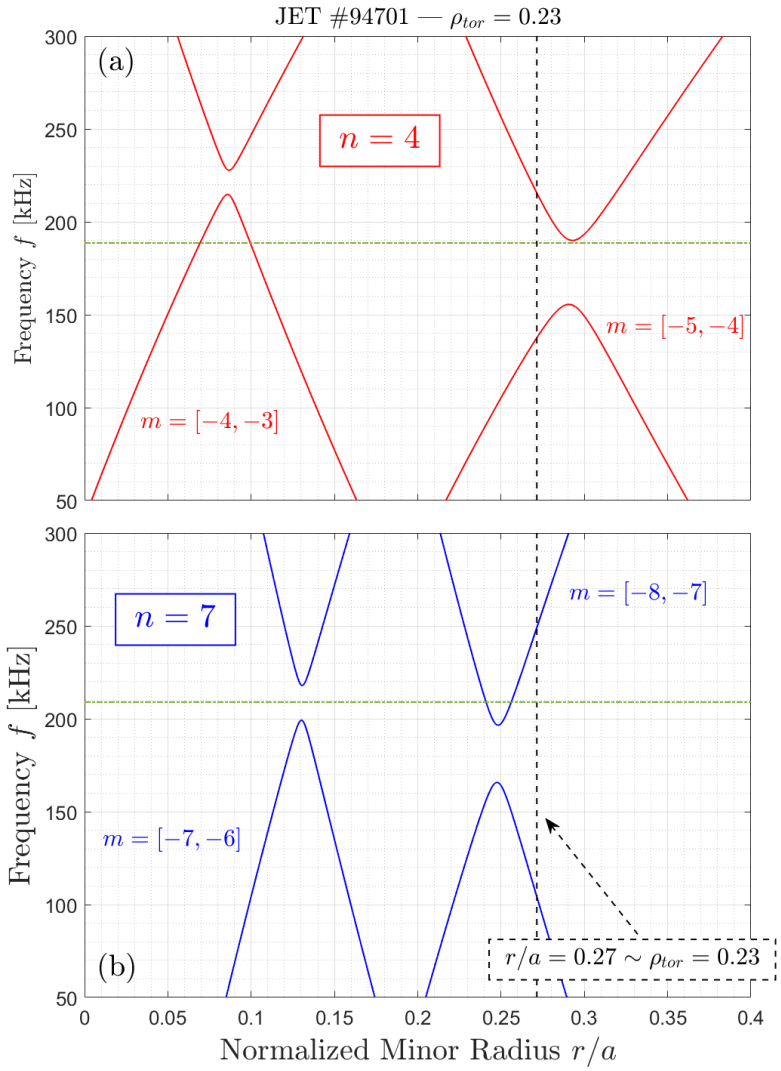

Figure 3.13: *The Alfvén continua of JET pulse #94701 for $n = 4$ (a) and $n = 7$ (b) and a couple of poloidal mode numbers are plotted. The continua have been computed using the Relation 1.52, which is the dispersion relation for a toroidal system [49], with the additional simplification of the linearized q-profile around the location $\rho_{tor} = 0.23$. Green horizontal dotted-dashed lines represent the linear mode frequency of the fast-ion-driven TAEs computed by* GENE. *The black vertical dashed lines are indeed illustrating the radial location at which the numerical analyses are performed, namely $r/a = 0.27 \sim \rho_{tor} = 0.23$.*

explained in Chapter 2 (section 1.3.2), neighboring poloidal modes are coupled in a toroidal geometry, and therefore a gap is open in the Alfvén continuum. Eigenmodes lying within the open gaps are not damped by the continuum through phase mixing [46]. Nevertheless, it must be noted that the continua represented in Figure 3.13 have been obtained under several approximations. First of all, the employed plasma parameters are fixed to those of the magnetic surface at

$\rho_{tor} = 0.23$. Hence, they do not vary along the radial coordinate, except for the q-profile which, consistently with the treatment in the flux-tube approximation [131, 132] (see also section 2.1), is linearized in the following manner:

$$q(x) = q_0\left(1 + \frac{\hat{s}_0(x - x_0)}{x_0}\right) \tag{3.2}$$

with x the radial coordinate, $q_0 = q(\rho_{tor} = 0.23)$, $\hat{s}_0 = \hat{s}(\rho_{tor} = 0.23)$, and x_0 the radial coordinate evaluated at $\rho_{tor} = 0.23$. It must be noted that in Figure 3.13, the radial coordinate is chosen to be $r/a \in [0, 1]$ consistently with the numerical Miller geometry also employed in the GENE simulations. As also reported in the plots, the radial coordinate $\rho_{tor} = 0.23 \sim r/a = 0.27$. As an additional approximation in computing the continua, the magnetic surfaces are considered to be concentric, differently to the elongated surfaces employed in the GENE simulations. Yet, since the focus of this analysis is on the core plasma, the elongation of the magnetic surfaces is much less significant than in the edge regions of the plasma. In Figure 3.13, the mode frequency computed by GENE and the location of the center of the considered flux-tube are represented in horizontal green dotted and vertical black lines respectively for $n = 4$ and $n = 7$ spectra. The intersection of these two latter curves indicate the accumulation point as computed by the gyrokinetic code. Therefore, although the simplistic treatment of the toroidicity-induced effects on the Alfvén continua, the agreement between the mode frequencies computed by the GENE code and the toroidicity-induced gaps in the continuum is notable. The poloidal mode numbers m of the consecutive eigenmodes creating the TAE gaps are $m_1 = -5$ and $m_2 = -4$ and $m_1 = -8$ and $m_2 = -7$ for $n = 4$ and $n = 7$ respectively, as can be seen in Figure 3.13. For a full consistent picture of the TAE identification, the electrostatic potential for the binormal wavevectors $k_y\rho_s = 0.025$ ($n = 4$ in panel (a)) and $k_y\rho_s = 0.05$ ($n = 7$ in panel (b)) is plotted projecting the flux-tube on the poloidal section of the tokamak for the simulation with $R/L_{p_{\mathrm{FD}}} = 16.2$ in Figure 3.14. Thus, the dominant poloidal structures of the linear eigenmode computed by the GENE code are visible. Indeed, counting the maxima of ϕ, it is possible to verify that the poloidal mode numbers evidenced by the Alfvén continua study in Figure 3.13 are consistent with the GENE computations.

Furthermore, the linear results regarding the frequency of the low-k_y modes which are illustrated in Figure 3.10 are also confirmed in the nonlinear regime. This is shown in panel (d) of Figure 3.19, where the frequency spectrum of the electrostatic potential fluctuations is shown for the case with $R/L_{p_{\mathrm{FD}}} = 16.2$. The two dominant peaks are within the TAE experimental range of frequencies, represented by the gray shaded area. It could be also noted that in the nonlinear regime, in which it is reminded that only $k_y\rho_s = 0.025$ ($n = 4$) and $k_y\rho_s = 0.05$ ($n = 7$) wavenumbers are retained, the dominant peak is corresponding to the fast-ion mode with lower frequency, and hence related to the lower k_y mode, unlike the linear stability analyses (cf. above and the inset of Figure 3.10). This is indeed more consistent with the experimental measurements in which the TAE most dominant harmonic is the $n = 3$.

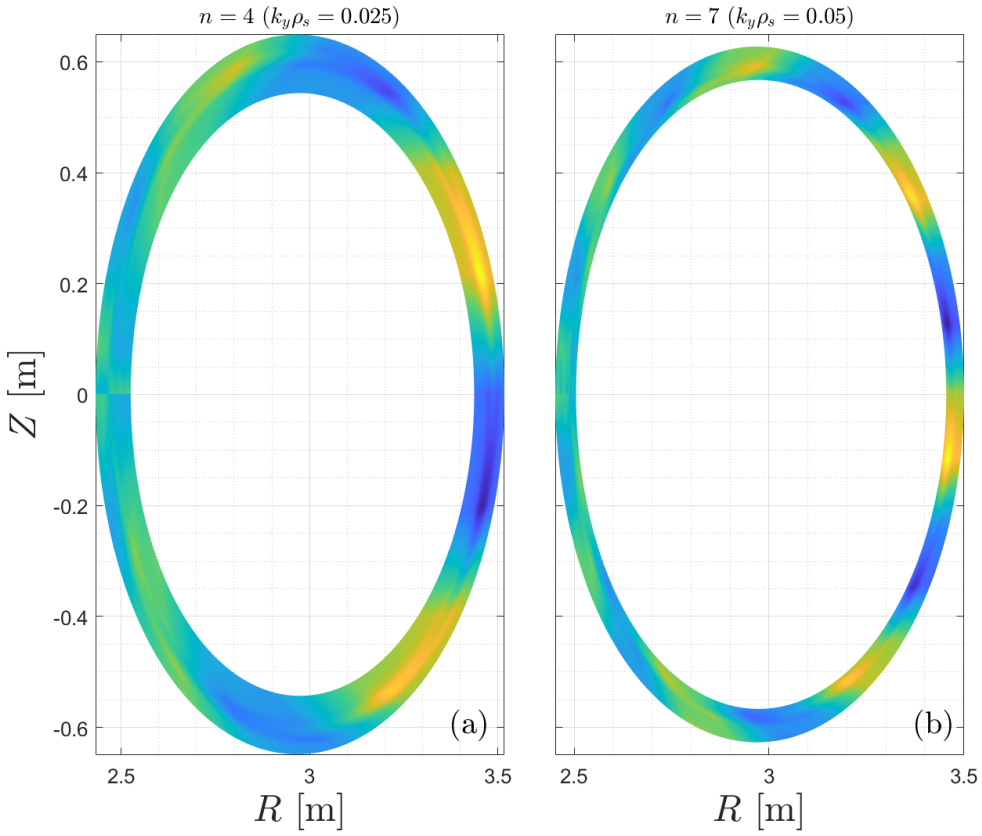

Figure 3.14: *The poloidal cross sections of the electrostatic potential, reconstructed from the flux-aligned system of coordinates, is shown for $n = 4$ ($k_y\rho_s = 0.025$) and $n = 7$ ($k_y\rho_s = 0.05$) respectively in panels (a) and (b). In this illustration, it is thereby possible to capture the poloidal mode numbers m of the dominant eigenmodes.*

Eventually, another piece of evidence for the identification of the low-k_y unstable modes is provided by the analysis of the X-mode correlation reflectometer data. In fact, the radial localization of the unstable TAEs is within the range 3.22 m $< R < 3.36$ m (cf. Figure 3.7). As it is explained in section 3.1.3, those measurements are not available for JET pulse #94701, and so this comparison is carried out for the very similar pulse #95669. The outer mid-plane radial position of the flux-tube simulated with the GENE code is within the radial range at which the TAEs are found unstable.

For the reasons listed above, the high-frequency large-scale modes destabilized when the fast-ion pressure gradient is beyond the critical threshold have been identified as fast-ion-driven TAEs. Therefore, in the remainder of this chapter, these modes will be termed as fast-ion-driven TAEs or, in a more compact way, TAEs.

The accurate description of large-scale modes would require a global approach, as the radial extension of these modes may break the assumption of the local flux-tube simulations (essentially $1/\rho^* \to \infty$). Nevertheless, previously pub-

lished studies [124] demonstrate the efficiency of the flux-tube code GYRO [20] in simulating fast-ion-driven modes. Those studies reveal that even without taking into account the retro-action of the turbulent transport on the radial flattening of the fast-ion profile, the large-scale modes can be accurately described and a steady-state of so-induced fluxes can be sustained. Examples of local approximation of fast-ion-driven instabilities can be found in the literature, see e.g. [124, 133, 90, 125] (for the latter reference, see also the next Chapter 4).

Another approximation that have been employed in the gyrokinetic GENE simulations is the use of an equivalent Maxwellian distribution for the suprathermal species, as it has already been reported in section 3.2. It is reminded that, indeed, the TRANSP-computed distribution of the fast ions departs from the isotropic Maxwellian function (see Figure 3.2). A more accurate description of the TAE drive would require the adoption of the realistic distribution of the fast ions, nonetheless previous works with the GENE code exhibits a remarkable qualitative agreement of the impact of different distributions of suprathermal species on the heat fluxes [104, 74]. Moreover, in the present study, in order to compensate for the deviation of the derivative in velocity space a wide range of the radial fast-ion pressure gradient has been scanned (see Figure 3.10 and Figure 3.16), as it has already been stated.

3.3.4 Study of the TAE excitation mechanism

After identifying the fast-ion-driven mode as a TAE instability, it is relevant to spend some words on the analysis of the TAE excitation mechanism. To do so, the free-energy exchange for the case with $R/L_{p_{\mathrm{FD}}} = 16.2$ is shown in the velocity space ($v_{\parallel}$,μ) for the two TAE wavenumbers retained in the nonlinear simulations, i.e. $k_y\rho_s = 0.025$ ($n = 4$) and $k_y\rho_s = 0.05$ ($n = 7$), in Figure 3.15.

This specific analysis is based on the study of the time evolution of the free energy E_{fe} in the phase-space, defined as the sum of the kinetic E_k and potential energy E_w contributions [134]. The potential energy can be identified as the energy contained in the field perturbations, associated thereby with the wave instability energy. When the system reaches a steady-state regime, the established free energy balance allows to identify the preferential direction of the transfer of the energy, evaluating the rate of energy flowing from the wave to the particles ($\partial E_k/\partial t$) and, in the opposite direction, from the particles to the wave ($\partial E_w/\partial t$). The former contribution can be linked to a damping mechanism, while the latter is the essential ingredient for an arising instability in the system. For this reason, the linear growth rate of a specific wavenumber can be studied as the sum of each species contribution to the total rate of the potential energy transferred from the particles to the wave, i.e.:

$$\gamma = \sum_s \gamma_s = \frac{1}{E_w} \sum_s \frac{\partial E_{w,s}}{\partial t} \tag{3.3}$$

where the subscript s refers to each considered species. Therefore, studying the

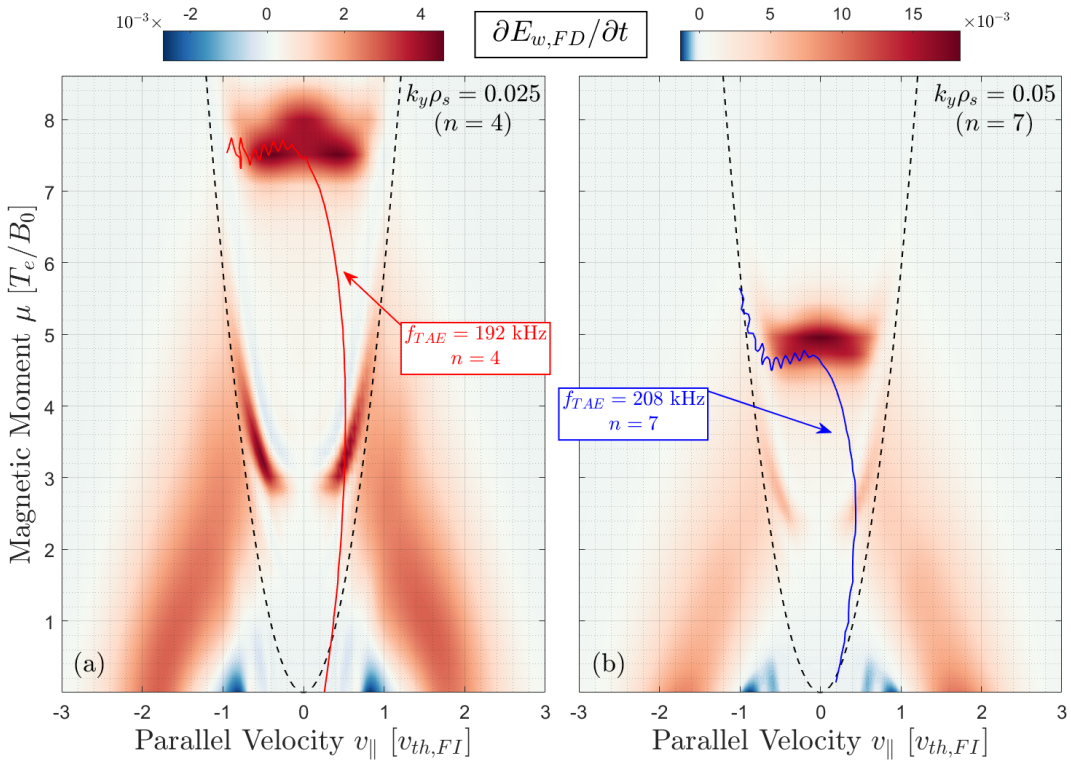

Figure 3.15: *The derivative in time of the potential energy of the fast ions $\partial E_{w,FD}/\partial t$ for $k_y\rho_s = 0.025$ and $k_y\rho_s = 0.05$ are plotted in the velocity space in panels (a) and (b), respectively. Positive and negative values of $\partial E_{w,FD}/\partial t$ indicate a destabilizing and stabilizing effects on the modes, respectively. The overplotted curves represent the resonant condition between the mode frequency and the toroidal precessional motion of the fast ions computed by means of the GCT code.*

single contribution for each species in the whole phase space, it is possible to distinguish the role of the single species. Positive and negative values of the potential energy transfer rate $\partial E_{w,s}/\partial t$ indicate that the mode is taking or giving energy to the plasma species, respectively.

The free energy rate $\partial E_{w,FD}/\partial t$ is averaged over the parallel direction (z in GENE convention), and positive (negative) values mean that the energy is flowing from the particles to the wave (from the wave to the particles). It must be also observed that the velocity space resolution in this case has been set to $(n_{v_\parallel}, n_\mu) = (120, 64)$ in order to better resolve the structures. Nonetheless in the following nonlinear simulations the resolution in the parallel velocity direction has been relaxed to $n_{v_\parallel} = 48$ for computational reasons.

For the wavevector $k_y\rho_s = 0.025$, corresponding to the toroidal mode number $n = 4$, the main resonant structure is localized around $\mu = 7.5$ at low parallel velocities. A strong contribution comes also from two symmetric resonant patterns at lower μ close to the trapping cone. A non-negligible contribution is eventually given by the passing particles, although minor with respect to that of the trapped

particles. Instead, for the wavevector $k_y\rho_s = 0.05$, corresponding to the toroidal mode number $n = 7$, the main structure appears at lower perpendicular velocities ($\mu \approx 4.9$) with the peak at null parallel velocity. The other patterns, outside and inside the trapping region, are less relevant for the total computation of the free energy exchange.

Furthermore, Such trapped particle resonant structures are also observed in the fast-ion perturbed distribution function in the nonlinear regime. This can be appreciated in panel (a) of Figure 3.39, reported in the last section of this chapter.

An additional analysis has been performed to further enforce the validity of the TAE excitation mechanism observed in GENE. For this purpose, the recently developed GCT guiding-center-tracing code [135] has been employed. GCT integrates the equations of motion at the particle guiding center in the gyrokinetic formalism, simulating thus the particle trajectories in the core of JET pulse #94701 for static electromagnetic fields. The realistic magnetic equilibrium is indeed used, but a linearized safety factor profile is employed to be consistent with the flux-tube approximation of the GENE code (cf. Relation 3.2). A statistically significant number of Deuterium tracers, with a Maxwellian distribution, is initialized at $\rho_{tor} = 0.23$ coherently with the GENE input parameters provided in Table 3.1, and the fundamental frequencies of their dynamics are studied. In Figures 3.15(a) and (b), the red and the blue lines represent the resonant condition $f_{TAE} - n\Omega_{prec} = 0$, where Ω_{prec} is the toroidal precession frequency of the trapped fast ions, for $[n, f_{TAE}] = [4, 192\,\text{kHz}]$ and $[n, f_{TAE}] = [7, 208\,\text{kHz}]$ respectively. The two selected frequencies f_{TAE} are the ones reported in the linear spectrum, displayed in Figure 3.10. It can be observed hence that a good agreement is obtained between the GENE outcomes and the resonant condition computed by the GCT code. Eventually, the fast-ion-driven TAEs are excited through a wave-particle resonant mechanism with the toroidal precession motion of the trapped fast ions in the plasma core of JET pulse #94701.

3.4 Ion-scale turbulence suppression via complex mechanism

In this section, the results of the nonlinear simulations and the subsequent detailed post-processing analyses are reported. Firstly, the principal effects of the highly energetic ions on the heat and particle fluxes of the thermal species are described. Then, a more detailed explanation of the complex mechanism triggered by the presence of the fast ions is given.

3.4.1 Assessment of the nonlinear impact of fast ions on the thermal confinement in JET #94701

In Figure 3.16, the nonlinear electrostatic heat diffusivity χ_{ES} for both thermal ion species, Deuterium in blue and ^{3}Helium in red is shown as a function of the

normalized fast ion pressure gradient $R/L_{p_{\mathrm{FD}}}$. The reported χ_{ES} values are determined by time-averaging over a sufficiently large time window of the nonlinear time evolution of the fluxes. The width of the time windows depends on each of the analyzed simulations, which are run for a sufficient normalized time to ensure the convergence of the time-averaged values. The points of the nonlinear scan span a range from $R/L_{p_{\mathrm{FD}}} = 5.9$ to $R/L_{p_{\mathrm{FD}}} = 16.2$, similarly to what already shown for the linear stability analysis (cf. Figure 3.10). The noteworthy

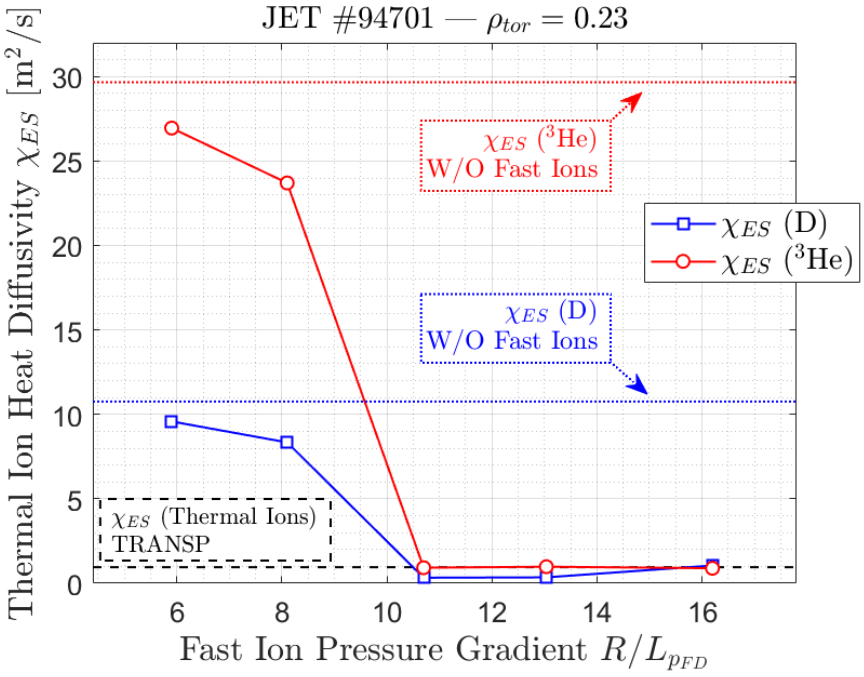

Figure 3.16: *The electrostatic heat diffusivity of the thermal ions is plotted as a function of the fast ion pressure gradient from* GENE *simulations of JET pulse #94701 at* $\rho_{tor} = 0.23$. *The dotted horizontal lines are referring to the heat diffusivities for the simulations without fast ions, to be compared with the values obtained in the scan retaining the fast ions. The black horizontal dashed lines represents indeed the heat diffusivity of thermal ions from power balances computed by TRANSP integrated modeling.*

observation is the strong decrease of χ_{ES}, with respect to the simulation without including fast ions, when a critical threshold in the fast ion pressure gradient is overcome. Note that the outcomes of the simulation without fast ions are represented by the horizontal dotted lines. The critical threshold for the onset of the thermal transport stabilization is found to be $R/L_{p_{\mathrm{FD}}} \approx 10.7$. In Figure 3.17, the relative stabilization of the electrostatic heat flux for only the ^{3}He is shown as a function of $R/L_{p_{\mathrm{FD}}}$. The stabilization is defined as the ratio, here expressed in percentage, of the electrostatic heat diffusivity as a function of $R/L_{p_{\mathrm{FD}}}$ over the same parameter evaluated for the case without including fast ions. Beyond the threshold the relative stabilization of the thermal fluxes are around 97%, as can be seen in the inset of Figure 3.17. So, these values justify the following use of the terminology *suppression* of the turbulent heat fluxes. It is relevant to stress the latter

consideration in order to highlight the strong difference with the previous studies on the beneficial impact of fast ions on the thermal transport [71, 77, 136, 72, 90].

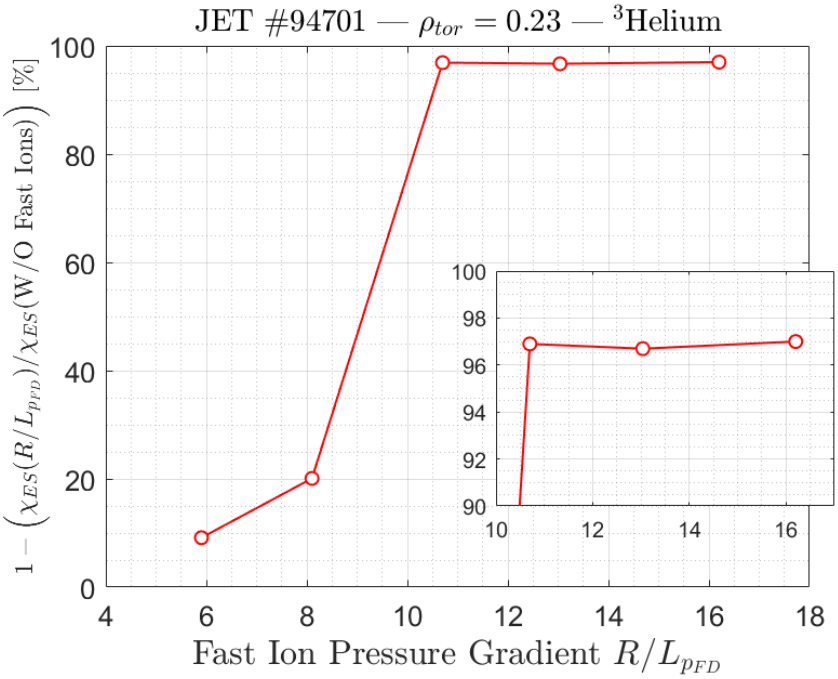

Figure 3.17: *The relative reduction (in percentage) of the ^{3}He electrostatic heat diffusivities with respect to the case without fast ions is plotted as a function of the fast ion pressure gradient from* GENE *simulations for JET pulse #94701 at $\rho_{tor} = 0.23$. The inset on the right is a zoom for the configurations with destabilized TAEs, in which the suppression is obtained.*

Reminding the linear characteristics of the system, the case with $R/L_{p_{\mathrm{FD}}} = 10.7$ coincides with the marginal stability of the fast-ion-driven TAEs. In fact, for $R/L_{p_{\mathrm{FD}}} > 10.7$ the TAEs are linearly unstable. In order to determine the dominant instability in the nonlinear regime, and thereby assess the role of the fast-ion modes on the confinement, the analysis of the fluctuations of the electrostatic potential ϕ is performed. The Fourier transform of the electrostatic potential signal in time for all the (k_x, k_y, z) modes considered in the nonlinear regime and then averaged over the radial and parallel direction leads to the frequency spectra illustrated in Figure 3.18. As an additional remark, the zonal component of ϕ are not included in this analysis. Only the four cases also explored in the linear stability analysis are reported, i.e. the simulation without fast ions (a), $R/L_{p_{\mathrm{FD}}} = 5.9$ (b), $R/L_{p_{\mathrm{FD}}} = 10.7$ (c) and $R/L_{p_{\mathrm{FD}}} = 16.2$ (d). Note that the ordinates are plotted in logarithmic scale to highlight the low-k_y range, and that the frequency range has been limited to $f \in [-400, 400]$ kHz. The simulation without fast ions shows a dominant structure peaking at low positive frequencies (∼10 kHz) in the ITG-scale, namely at $k_y\rho_s = 0.2$. A very similar structure is also present in the $R/L_{p_{\mathrm{FD}}} = 5.9$ spectrum, with a broadened peak reaching up to $k_y\rho_s = 0.1$. Those

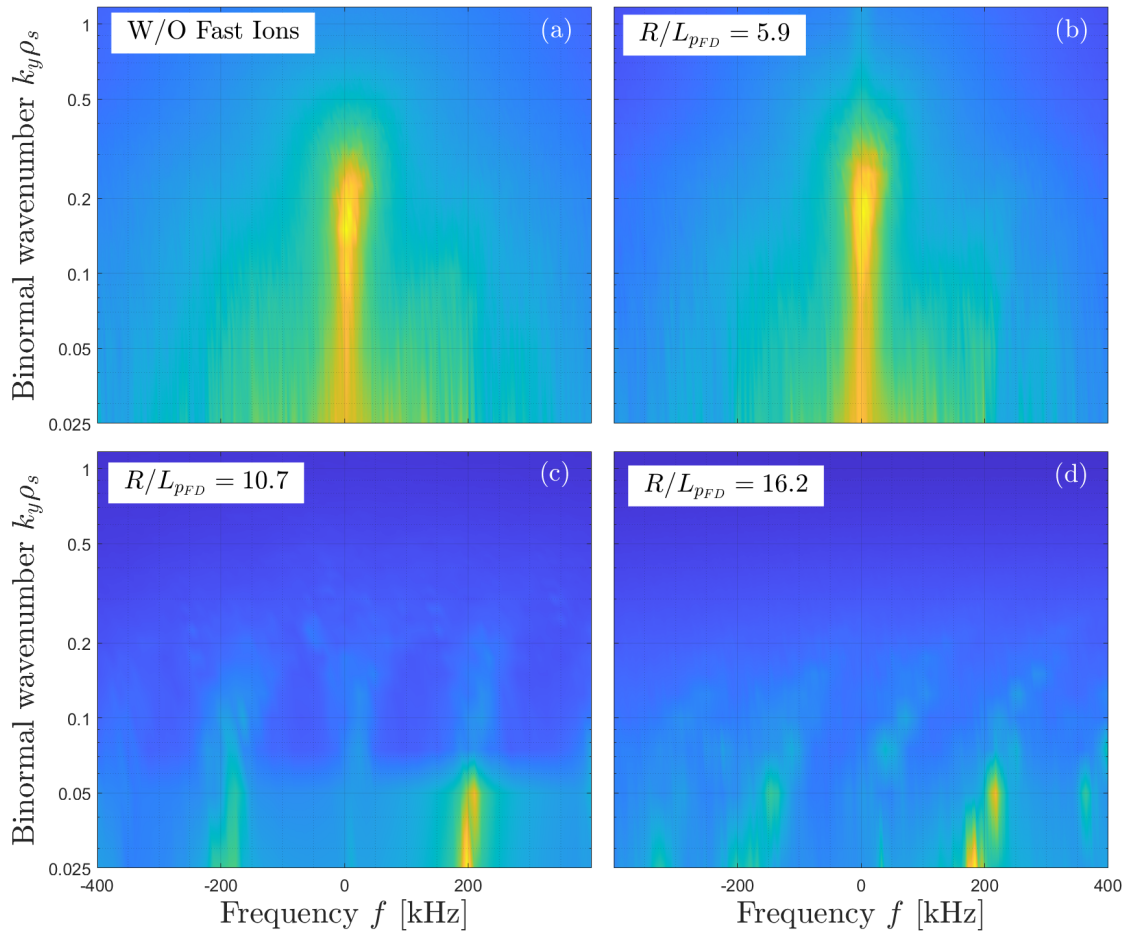

Figure 3.18: *The frequency spectra computed from the nonlinear* GENE *simulations are shown as a function of the binormal wavenumber for various configurations, highlighted with text boxes within the contour plots.*

two latter cases are indicative of an ITG-dominated turbulence pattern. The two remaining cases, i.e. the cases with $R/L_{p_{\mathrm{FD}}} = 10.7$ and 16.2, presents instead a totally different structures of the electrostatic potential spectrum. The dominant peaking is related to the frequency range $f \approx 200$ kHz, close to the TAE experimental range, and to the low-k_y region, where the fast-ion-driven TAEs are the dominant instability. Specifically, for the case with $R/L_{p_{\mathrm{FD}}} = 16.2$, the two peaks at $k_y\rho_s = 0.025$ and $k_y\rho_s = 0.05$ are clearly more distinguishable than those of the case with $R/L_{p_{\mathrm{FD}}} = 10.7$, in which the two structures almost overlap in one unique. The contrast between the first and the second row of Figure 3.18 is a clear sign of the transition to a different turbulence regime, from the ITG modes to the TAEs.

For the sake of simplicity, in Figure 3.19 an additional average over the binormal direction is performed, and the frequency range of the spectra is shrunk to only the positive frequency side (up to 300 kHz) to clearly highlight the dominant structures. The same cases of Figure 3.18 are reported. In panels (c) and

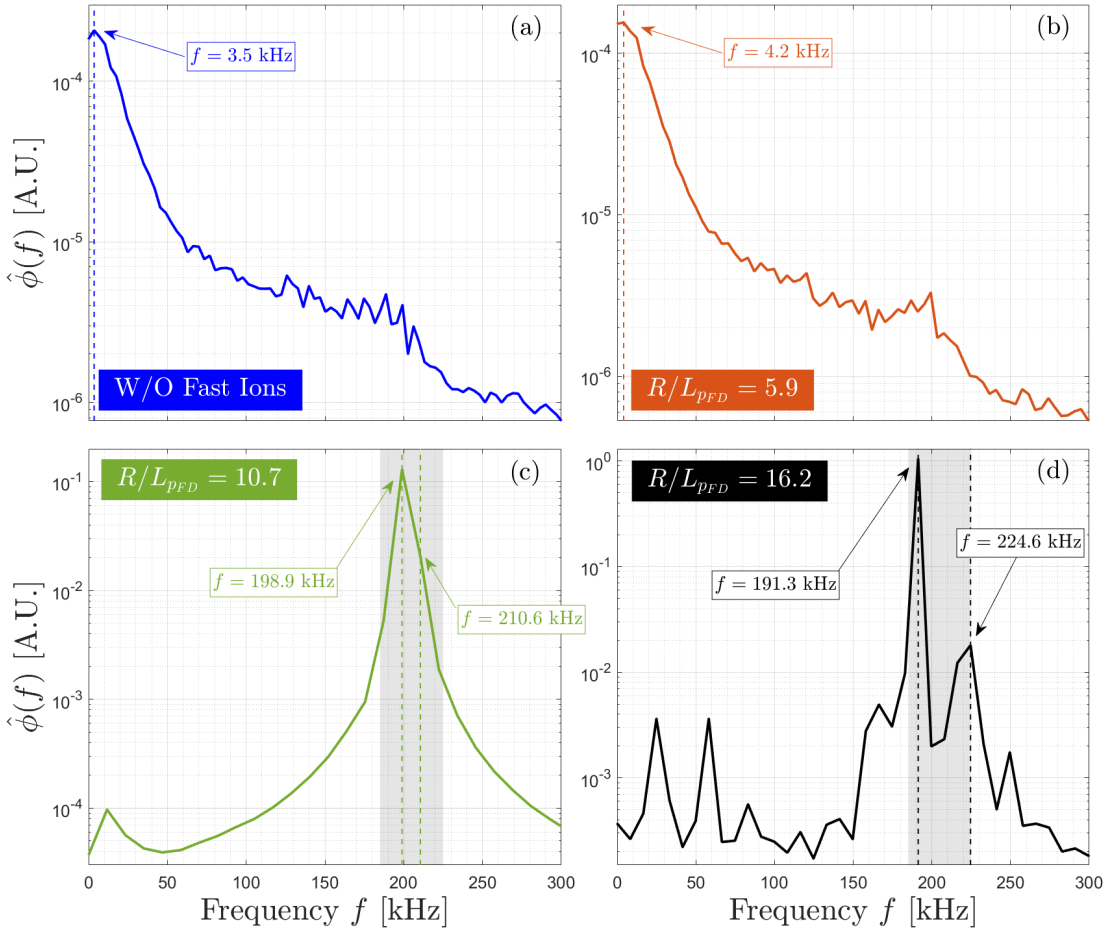

Figure 3.19: *The frequency spectra computed from the nonlinear* GENE *simulations are shown for various configurations, highlighted with text boxes within the contour plots, similarly to what reported in Figure 3.18 but additionally averaged over the binormal wavenumbers. In each panels, relevant frequency peaks are indicated, with additional gray shaded areas in panels (c) and (d) showing the experimental TAE range of frequencies.*

(d), the gray shaded area represents the TAE experimental range of frequencies. The frequencies of the dominant peaks in the Fourier spectra are also indicated, showing definitely the transition of the turbulence regime. It must be noted that this Fourier analysis of the electrostatic potential fluctuations has been carried out for diverse time windows of the simulations here considered, leading to a almost negligible variation of the dominant peak frequencies. Panels (c) and (d) of Figure 3.19 further shows that the globally dominant peak of the electrostatic potential in conditions of unstable TAEs correspond to the lower frequency structure. Assuming that the linear eigenmode stability is conserved, this means that most unstable TAEs in the nonlinear phase is the one corresponding to the largest-scale wavevectors, i.e. in this study $k_y\rho_s = 0.025$ ($n = 4$), differently to what observed in the linear growth rate spectrum (see Figure 3.10(a)). Such a consideration is

consistent with the magnetic spectrogram shown in Figure 3.6, where the TAE with the lowest toroidal number ($n = 3$) has the strongest intensity.

Therefore, it is distinctly pointed out the nonlinear destabilization of the high-frequency fast-ion-driven TAEs when $R/L_{p_{\mathrm{FD}}} \geq 10.7$, unlike in the linear regime where at $R/L_{p_{\mathrm{FD}}} = 10.7$ only a TAE marginal stability is observed. This is reminiscent of the mechanism already reported in Ref. [90], where the ion-scale ITG free energy is redistributed to the larger TAE scales by a three-wave interaction and thereby the TAE instability grows nonlinearly and becomes the dominant driver of the turbulence regime.

3.4.2 Strong TAE-induced fast-ion transport

In this section, the assessment of the fast-ion transport induced by the strong Alfvén activity in the JET pulse #94701 is provided. Indeed, it is essential for the correct evaluation of the effect of the highly energetic ions on the plasma confinement to address both the energy and particle transport of the fast deuterium species. It is well-known, as it has been explained in the previous section 1.3.2, the detrimental consequences of the destabilization of the Alfvénic instabilities [42, 43]. An excessive fast-ion transport induced by the AE-driven turbulent fluctuations of the electrostatic and electromagnetic fields could indeed lead to unsustainable levels of fast-ion fluxes which could impair the overall fusion performance.

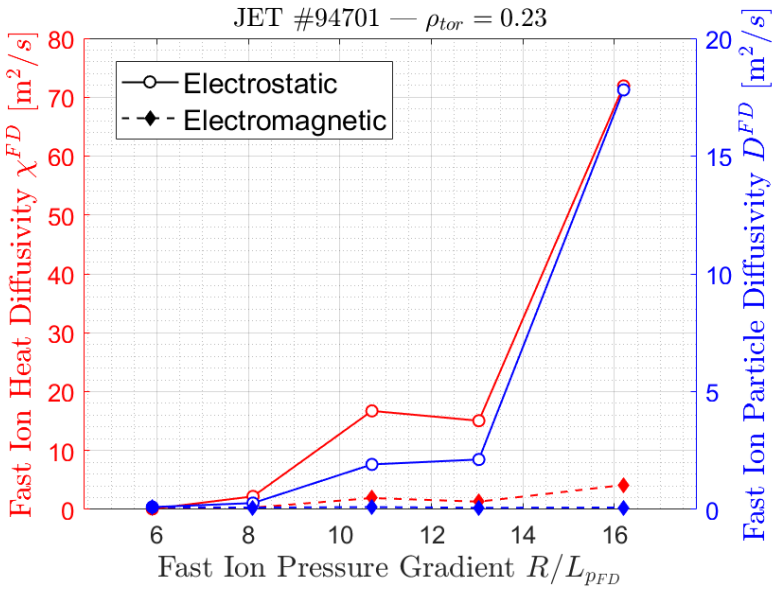

Figure 3.20: *Fast ion heat (in red) and particle (in blue) diffusivities are shown for the various configurations of the fast ion pressure gradient in the nonlinear simulations fro JET pulse #94701 at $\rho_{tor} = 0.23$. The empty symbols linked with solid lines and the filled symbols linked with dashed lines respectively represent the electrostatic and the electromagnetic contribution to the the total diffusivities.*

Therefore in Figure 3.20, both the electrostatic and electromagnetic heat χ^{FD} and particle D^{FD} fast-ion diffusivities computed by GENE are plotted in function of the normalized fast ion pressure gradient $R/L_{p_{FD}}$, similarly to what reported for the thermal ion transport in the previous sections. A strong increase of the heat fluxes (represented by the red curves) is measured with the increasing of the fast-ion drive. Very high levels of heat transport, dominated by the electrostatic contribution, are reached for the case with $R/L_{p_{FD}} = 16.2$ in which the fast-ion-driven TAEs are fully destabilized. The same is also measured for the particle diffusivities (the blue curves). Moreover, contrarily to the slow but continuous increase of the electromagnetic heat transport, D^{FD}_{EM} remains almost constant throughout the entire scan. Indeed, although weakly visible in Figure 3.20, the electromagnetic particle diffusivity establishes around $0.1\ \mathrm{m}^2/s$.

It is thus shown that the first effect of the fast-ion-driven TAEs is to enhance dramatically the fast-ion transport, consistently with the broad literature at this concern (see e.g. [43] and References therein).

3.4.3 ITG turbulence suppressed by enhanced zonal activity

After having evidenced the striking impact of the highly energetic fast ions on the thermal ion heat fluxes, it is crucial to understand the fine mechanism leading to ion-scale turbulence suppression. In this section, the heart of the discussion is focused on demonstrating the strong correlation between the enhancement of the zonal components of the electrostatic potential and the destabilized fast-ion-driven TAEs.

Plotting the electrostatic potential in the (x,y) space – respectively the radial and binormal directions of the simulated domain – a strong difference in the dominant structure clearly appears. In Figure 3.21, the comparison is made between the simulations without including fast ions (panel (a)), the case with $R/L_{p_{\mathrm{FD}}} = 5.9$ (panel (b)), with $R/L_{p_{\mathrm{FD}}} = 10.7$ (panel (c)) and with $R/L_{p_{\mathrm{FD}}} = 16.2$ (panel (d)). It is to be noted that in Figure 3.21, ϕ is focusing only on the low field side (at $z = 0$ in GENE convention). As it occurs for the frequency spectra of the electrostatic potential fluctuations reported in Figure 3.18, also in the real space (x,y) the dominant structures of ϕ clearly define the transition between two different turbulence patterns. In the first row, namely in the two cases in which the fast-ion-driven TAEs are stable, the turbulence regime is strongly affected by radially elongated eddies that propagate almost undamped. These pictures are consistent with an effective turbulent transport driven by the ITG instability at the thermal ion scale. Totally different structures appear in the second row of Figure 3.21. Such prevalent regular structures of the electrostatic potential elongated along the binormal direction are representative of the dominant zonal components of ϕ. Combining this information with the considerations made for Figure 3.19 about the TAE as the principal driver of the turbulent transport in the cases with $R/L_{p_{\mathrm{FD}}} = 10.7$ and $R/L_{p_{\mathrm{FD}}} = 16.2$, it can be concluded that a strong zonal flow activity is measured whenever the fast-ion pressure gradient is large enough to nonlinearly excite the TAEs. The same situation occurs also for the case with

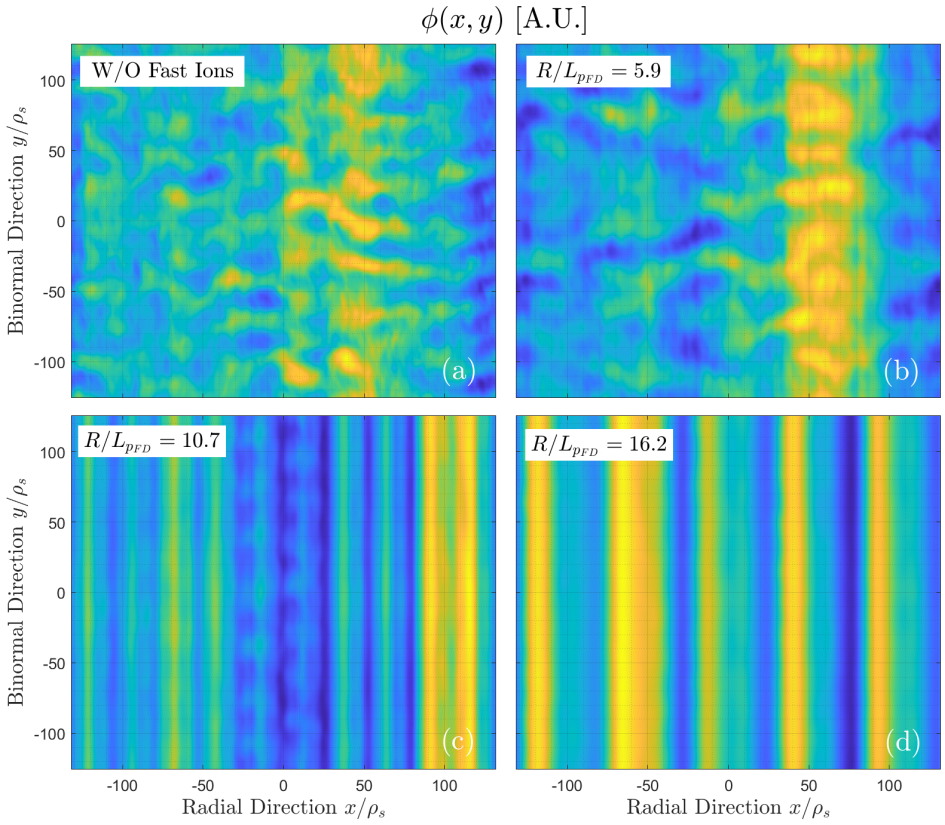

Figure 3.21: *The electrostatic potential computed from the nonlinear* GENE *simulations are shown in the radial x and binormal y space, for the parallel direction $z = 0$ (low field side), for various configurations highlighted with text boxes within the contour plots.*

$R/L_{p_{\mathrm{FD}}} = 13.1$, not shown here for the sake of simplicity.

The difference between the zonal pattern of the cases with $R/L_{p_{\mathrm{FD}}} = 10.7$ and $R/L_{p_{\mathrm{FD}}} = 16.2$ is essentially on the width of these structures along the binormal direction. In fact, in panel (c) of Figure 3.21 the vertical structures are less defined and narrower than those in panel (d). An explanation for such a difference is provided in Figure 3.22, where the zonal flow shearing rate, defined as $\gamma_{E\times B,\mathrm{zonal}} = |k_x^2\hat{\phi}(k_x,0)|$, is plotted in function of the radial wavenumbers $k_x\rho_s$ after being averaged on a sufficiently large time window. The zonal flow shearing rate is often used in the framework of gyrokinetic simulations to describe the strength of the zonal flow activity. Thus, it can be observed that for the cases with nonlinearly unstable TAEs $\gamma_{E\times B,\mathrm{zonal}}$ is enhanced with respect to the simulation without fast ions. Nevertheless, the increase of the zonal shearing rate for the case with $R/L_{p_{\mathrm{FD}}} = 16.2$ is much more concentrated in the low-k_x region with respect to the case with $R/L_{p_{\mathrm{FD}}} = 10.7$. This reflects into the width of the zonal structures, being proportional to $1/k_x$.

The increase of the zonal flow activity is the main mechanism of the ion-scale turbulence suppression observed in Figure 3.16. As already described in section

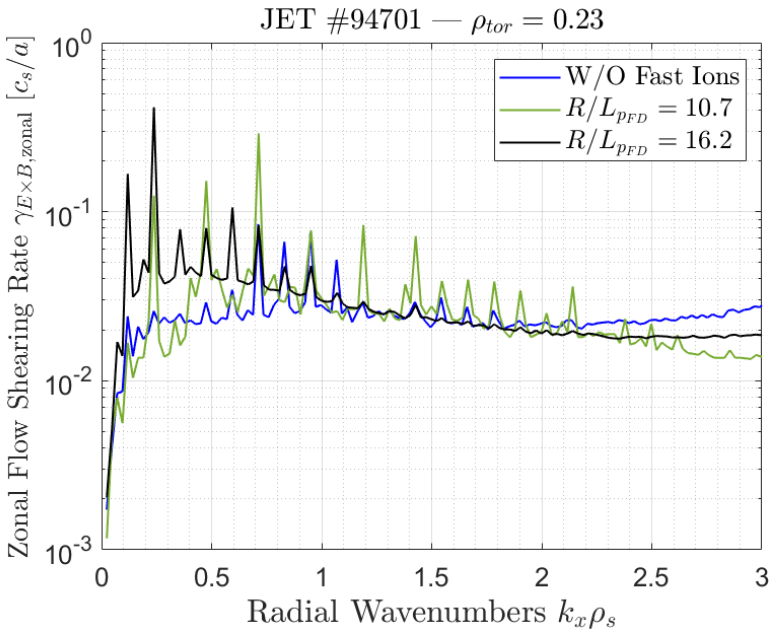

Figure 3.22: *The zonal flow shearing rate $\gamma_{E\times B,\text{zonal}}$ is plotted as a function of the radial wavenumber $k_x\rho_s$ for various configurations.*

1.4.2, the zonal flows are the principal saturation mechanism of the ITG turbulence, which is thus reduced by radial de-correlation of the generated turbulent eddies, like the ones shown in Figures 3.21(a) and (b). The beneficial impact of the sheared zonal flows on the ITG turbulence [63] is thus envisaged to be the main mechanism of the suppression of the thermal fluxes observed in this numerical modeling and in the plasma core of the JET three-ion scheme scenario.

It must be noted that the results reported in this paragraph – basically the occurring of dominant zonal structures for ϕ – have already been observed in the case of substantial reduction of the ITG turbulent transport in the presence of fast ions [137, 100]. Although the setup configuration in those previous work, as well as the experimental basis of the gyrokinetic analyses, was different from the present study, the increase of the electrostatic potential zonal components can be firmly related to the introduction of the suprathermal species in the system. This further suggests that a complex synergy between the TAE and the zonal spatio-temporal scales is underlying, as already reported in [90]. Additional proofs on the strong coupling between the fast-ion-driven TAEs and zonal flows are provided in the next section.

3.4.4 Nonlinear coupling between TAE and zonal flow spatio-temporal scales

The increase of the zonal flow activity following the destabilization of the fast-ion-driven TAEs in the numerical simulations performed with GENE is envisaged

to be the underlying mechanism leading to the thermal-ion turbulent transport suppression. As already observed, there should be a strong correlation between the fast-ion modes and the zonal components of the electrostatic potential to produce such an increase of the zonal flow shearing rate. In the following, a bispectral analysis of the binormal (k_y) and radial (k_x) spectral modes will be used to clearly demonstrate the nonlinear three-wave coupling between the the TAE and the zonal scales in the performed GENE simulations.

Firstly, the specific bispectral analysis that have been carried out in this work is introduced. Such an analysis is based on the wavelet transform of the diverse signal fluctuations that are considered. In this case, the signals at hand will be the perturbed electrostatic potential for each (k_x,k_y) mode, which is an output of the gyrokinetic modeling. The wavelet transform is defined as:

$$W_{\phi_{k_x,k_y}}(\omega,t) = \int_{\mathbb{R}} \phi_{k_x,k_y}(\tau)\psi_\omega(t-\tau)\mathrm{d}\tau \tag{3.4}$$

where ψ_ω is the Morlet wavelet function whose definition is the following:

$$\psi_\omega(t) = \sqrt{\frac{\omega}{2\pi}} e^{i\omega t} e^{-\frac{1}{2}(\frac{\omega t}{2\pi})^2} \tag{3.5}$$

with $\omega \in \mathbb{R}$ the frequency of the wavelet scale. It is observed that the relation described in 3.4 is essentially a convolutional product. Because of the convolution theorem [138], the Fourier transform of a convolutional product is equal to the product of the Fourier transform of each function. This consideration allows to write:

$$\mathscr{F}[W_{\phi_{k_x,k_y}}] = \mathscr{F}[\phi_{k_x,k_y}]\mathscr{F}[\psi_\omega] \tag{3.6}$$

with the notation $\mathscr{F}[\cdot]$ referring to the Fourier transform operation. Therefore the wavelet transform can be computed as the inverse Fourier transform of the right-hand side of Relation 3.6, such as:

$$W_{\phi_{k_x,k_y}} = \mathscr{F}^{-1}[\mathscr{F}[\phi_{k_x,k_y}]\mathscr{F}[\psi_\omega]] \tag{3.7}$$

with $\mathscr{F}^{-1}[\cdot]$ indeed referring to the inverse Fourier transform. Once the wavelet transform has been computed for each considered mode, the wavelet cross spectrum (or bispectrum) is defined as:

$$b^W(\omega',\omega'') = \left| \int (W_{\phi_{k_x,k_y}}(\omega,t))^\dagger W_{\phi_{k'_x,k'_y}}(\omega',t) W_{\phi_{k''_x,k''_y}}(\omega'',t)\mathrm{d}t \right| \tag{3.8}$$

where † indicates the complex conjugate. Such a relation is a powerful tool to individuate the possible nonlinear coupling between different scales in space and in time within the performed analyses with the gyrokinetic code. Indeed, the large complexity due to a nearly endless interaction occurring in the nonlinear

phase of the system evolution makes this approach a key tool to unravel dominant underlying mechanisms. As already explained in section 1.2.4, one of the most common nonlinear interaction is the three-wave coupling. Such a coupling requires that the triad fulfills the conditions $k_x = k'_x + k''_x$ and $k_y = k'_y + k''_y$. In addition, the cross spectrum is computed such as only the components having $\omega = \omega' + \omega''$ are taken into account.

In the present work, in order to alleviate the demanding time-consumption of the bispectral analysis, only specific triads have been wavelet-transformed and included thereby in the bispectrum computation. The selected triads are the most destabilized TAE mode $(k'_x, k'_y) = (0, 0.05)$, the zonal components of the field $(k''_x, k''_y) = (a, 0)$ and the modes completing the triplets $(k_x, k_y) = (a, 0.05)$, with $a \in [-k_{x,max}, k_{x,max}]$, for the case with fully destabilized TAEs ($R/L_{p_{FD}} = 16.2$). It must be stressed that this analysis is performed in the time window during the TAE linear growth phase, at which time the $k_y\rho_s = 0.05$ wavevector has the maximum growth rate (cf. Figure 3.10) and thus the largest impact on the system stability. Moreover, during the TAE growing time, the most significant increase of the zonal flow activity is measured. Although the restriction on the selected triads may seem to oversimplify the analysis, indeed this allow to clearly highlight the expected nonlinear interaction between the TAE and zonal spatio-temporal scales.

For the sake of clearness, in the following it is reported the precise definition of the wavelet cross power spectrum that is then illustrated in Figure 3.23:

$$b^W(\omega', \omega'') = \left| \left\langle \int \mathrm{d}t \sum_a (W_{\phi_{(a,0.05)}}(\omega, t))^\dagger W_{\phi_{(0,0.05)}}(\omega', t) W_{\phi_{(a,0)}}(\omega'', t) \right\rangle_z \right| \tag{3.9}$$

It can be seen that first of all more than one triplet is retained in the calculation of the bispectrum b^W. In fact, as already stated above, whereas the binormal wavenumbers are originally fixed, the radial modes span the entire range included in the gyrokinetic simulation. The only constraint for the radial modes is again on the coupling condition such as $k_x = k'_x + k''_x$. In this precise application, the most powerful TAE-induced fluctuation of the electrostatic potential is localized at $(k_x, k_y) = (0, 0.05)$, therefore the considered k_x modes must be the same ($a = 0 + a$). Another relevant consideration on Relation 3.9 concerns the average over the parallel direction represented by the brackets $\langle\cdot\rangle_z$. In fact, in order to properly account for the interaction between the more ballooned TAEs and the toroidal and poloidal symmetry of the zonal structures, the dependence on the parallel direction must be retained. For this reason, the wavelet transform has been applied to all the parallel points of the considered (k_x,k_y) wavevectors and then the result has been averaged over z. It is however noted that considering only the parallel position at the outer mid-plane ($z = 0$ in GENE convention), the results is qualitatively identical, but it differs in the absolute value of the modulus of the bispectrum. This is likely related to the parallel structure of the TAEs, which are mostly ballooned.

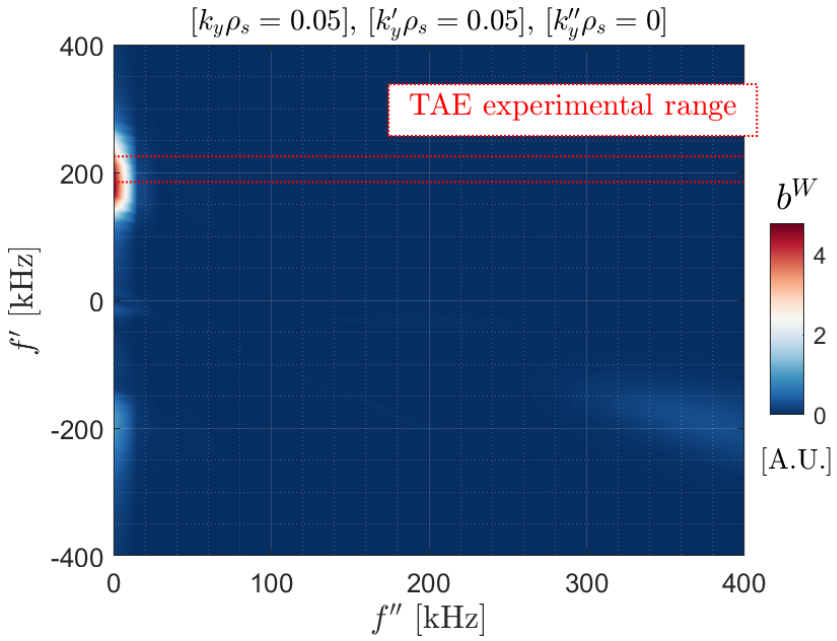

Figure 3.23: *Wavelet bispectrum for the electrostatic potential fluctuations highlighting the spatio-temporal coupling between the TAEs and zonal flows is shown for the selected triads, i.e. the most destabilized TAE mode ($k'_y = 0.05$), the zonal components ($k''_y = 0$) and the modes completing the triplets ($k_y = 0.05$), for the case with $R/L_{p_{FD}} = 16.2$. The TAE experimental range of frequencies is highlighted with red horizontal dotted lines.*

In Figure 3.23, the modulus of the wavelet cross spectrum of the electrostatic potential fluctuations for the selected triads is shown. It must be stressed that the cross spectra will be plotted in function of the frequency f in kHz instead of the angular frequency ω in GENE units ($f = \omega/(2\pi)$). The contour plot clearly shows that the dominant structure is localized at the intersection between the TAE ($f' \approx 185$-225 kHz) and the zonal ($f'' = 0$ kHz) frequency scales. It is worth also reporting the Fourier spectrum of $\langle\hat{\phi}(k_y = 0)\rangle_{k_x}$ to elucidate that the frequency spectrum peak for the zonal components of the electrostatic potential is equal to zero, as expected for an axisymmetric perturbation such as the zonal flows. This is done in Figure 3.24, in which it is clearly observed that the zonal components do not oscillate (or oscillate at zero frequency). In the inset, a zoom over the interesting region of the spectrum around $f = 0$ is reported to facilitate the view. Therefore, the dominance of that structure definitely indicates that a nonlinear coupling between the TAE and the zonal spatio-temporal scales exists.

These results can be compared to previous analytical studies, which focused on the nonlinear excitation of electrostatic potential zonal structures by TAEs [139] The proposed mechanism deals with a forced driven process in the linear growing phase of the fast-ion-driven TAEs, similarly to what observed in the present study. Moreover, earlier numerical simulations with the hybrid MHD-PIC code MEGA [140] showed a nonlinear triggering, when TAEs are purposely destabilized by the suprathermal species, of $n = 0$ zonal modes which decrease

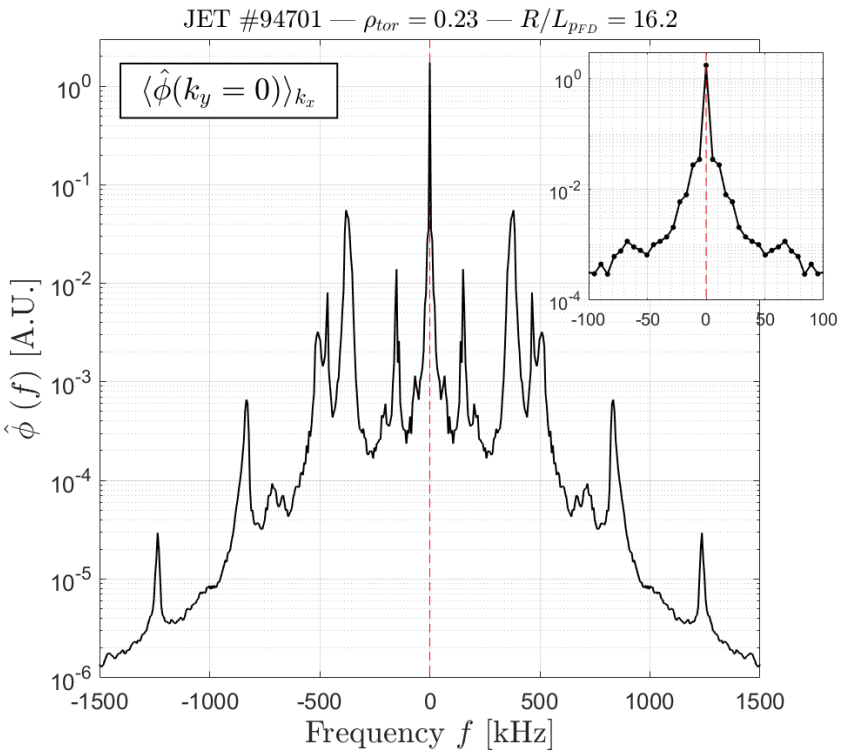

Figure 3.24: *The Fourier frequency spectrum $\hat{\phi}$ of the zonal components ($k_y\rho_s = 0$) averaged over the radial wavenumbers is shown for the configuration with $R/L_{p_{FD}} = 16.2$. The inset on the right is a zoom over the low frequency region of the frequency spectrum.*

the TAE saturation level [141] and thereby the radial induced transport.

3.4.5 Low-frequency modes excited by fully destabilized TAEs

In this section, an additional analysis is performed on the dynamics of a low-frequency mode destabilized in the gyrokinetic simulations with large fast ion pressure gradient. Indeed in Figure 3.19(d), two spikes in the low-frequency range are observed for the configuration with $R/L_{p_{\mathrm{FD}}} = 16.2$. Inspecting Figure 3.18(d), where the power spectrum is reported also as a function of the binormal wavenumbers, it can be observed that those subdominant modes are destabilized at $k_y\rho_s = 0.025$ and 0.05. As already reported at the end of Section 3.1.3, low-frequency instabilities in the frequency range of $f \approx 20 - 50$ kHz are detected in the frequency range of $f \approx 20 - 50$ kHz in the magnetic fluctuation spectrogram of pulse #94701 (cf. Figure 3.8). Moreover, these unstable modes were detected close to the TAE radial range by means of the X-mode reflectometer. Thus, a relevant link to the experimental outcomes is provided, indicating that the low-frequency modes observed in the gyrokinetic simulations could be related to the experimentally detected low-frequency instabilities. Nevertheless, the identifica-

tion of these unstable modes is still elusive. For this reason, in the following we will refer to these modes as low-frequency modes, often replaced by its acronym LFMs.

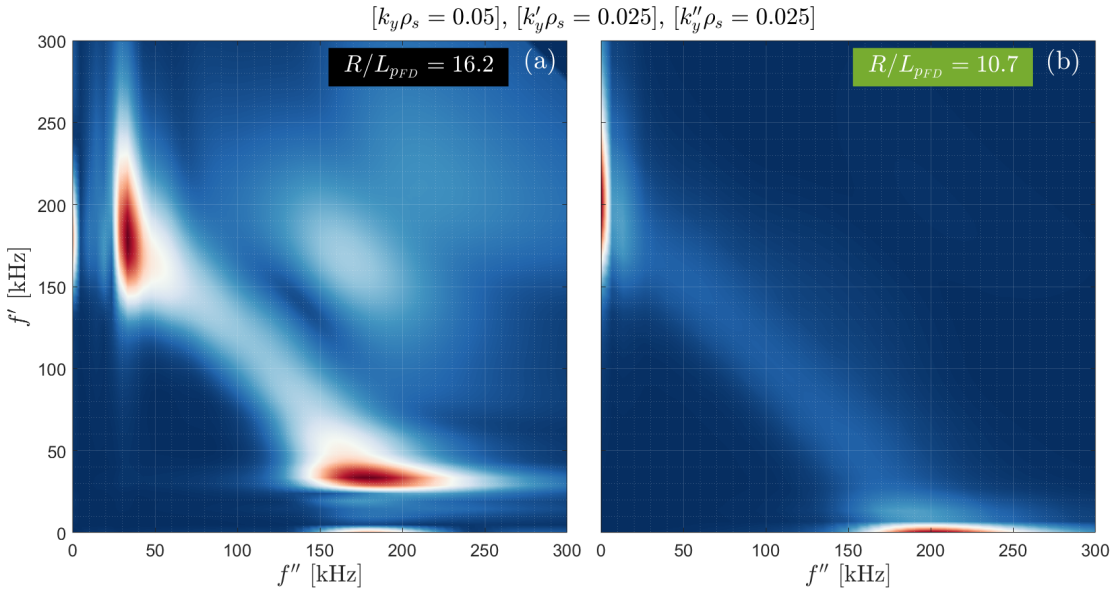

Figure 3.25: *Wavelet bispectrum for the electrostatic potential fluctuations highlighting the spatio-temporal coupling between the TAEs and the low frequency modes is shown for the selected triads, i.e. the most destabilized TAE mode ($k'_y = 0.05$), and the low-frequency mode range ($k''_y = 0.025$), for the case with $R/L_{p_{FD}} = 16.2$ (panel (a)) and with $R/L_{p_{FD}} = 10.7$ (panel (b)).*

Furthermore, the ranges of frequencies and binormal wavenumbers shown in Figure 3.18(d) suggest thereby that the conditions for the wave-wave coupling, i.e. $k_y = k'_y + k''_y$ and $f = f' + f''$, could be fulfilled. Hence, the excitation of the LFMs may be related to the strong destabilization of fast-ion-driven TAEs. For this reason, a bispectral analysis has been performed in order to corroborate these preliminary observations. The selected triplets are the TAE mode $(k_x, k_y) = (0, 0.05)$ and the wavenumbers at which the LFMs are localized $(k'_x, k'_y) = (a, 0.025)$ and $(k''_x, k''_y) = (-a, 0.025)$, with $a \in [-k_{x,max}, k_{x,max}]$. The modulus of the bispectrum, computed as already reported in Section 3.4.4, is illustrated in Figure 3.25(a) for the case with $R/L_{p_{\mathrm{FD}}} = 16.2$. The dominant structures is observed in the range of frequencies $[f', f''] \approx [180, 35]$ kHz and $[f', f''] \approx [35, 180]$ kHz. These structures clearly indicate an effective nonlinear coupling between the TAEs and the LFMs. It must be stressed that the bispectral analysis here displayed was performed in the TAE-saturated phase, since the same study carried out in the growing phase of the TAEs does not show a strong correlation between the TAE and the unstable LFMs. Therefore, this last consideration suggests that the LFMs are driven unstable through a nonlinear coupling with the TAEs by a net transfer of energy from the spatio-temporal TAE scales to the LFM ones.

The same bispectral analysis has also been performed on the gyrokinetic out-

comes for the configuration with $R/L_{p_{\mathrm{FD}}} = 10.7$. For this particular configuration, Figures 3.18(c) and 3.19(c) do not show the clear destabilization of the LFMs. In this case, indeed, the TAEs are only linearly marginal stable and nonlinearly destabilized, and their intensity is lower with respect to the fully destabilized case with $R/L_{p_{\mathrm{FD}}} = 16.2$. Consistently, the nonlinear interaction between the LFM and the TAE spatio-temporal scales is not clearly detected. This is illustrated in Figure 3.25(b). Yet, two less bright areas can be detected in the correspondence of the two characteristic frequencies of the TAEs and of the LFMs. This may additionally suggest that the nonlinear coupling is occurring, but the TAE drive – and hence the TAE intensity – is not large enough to excite the LFMs.

To conclude this section, it must be observed that a very similar nonlinear interaction has already been reported in the literature. Indeed, in Ref. [142], the three-wave interaction between energetic particle modes, identified as fishbones, and unstable TAEs was investigated by means of bicoherence analyses on electrostatic potential signals from the reflectometer in National Spherical Torus eXperiment (NSTX) pulses. This bicoherence analysis in Ref. [142] was carried out similarly to the present bispectral analysis. The conclusions of such an earlier study clearly highlight the nonlinear three-wave interaction between the energetic particle mode and the TAEs. Surprisingly, Figure 3 of Ref. [142] shows strong similarities with Figure 3.25(a). The disposition of the structure in the bispectrum is in good agreement between the two studies. This possibly indicate that strong TAE fluctuations easily couple to low-frequency modes and could be a systematic feature in this framework.

3.4.6 Study of the MeV-ion effect on the cross-phase

It has also been observed a crucial role of the cross phase between thermal-ion-flux-related physical parameters in the presence of destabilized TAEs and enhanced zonal flow activity. Because the cross phase together with the amplitude of the field fluctuations establishes the transports of both particle and energy, beyond identifying the turbulence regime, it is relevant to consider it in this wide framework. Such a detailed analysis is the focus of this section.

The simulations with $R/L_{p_{\mathrm{FD}}} = 10.7$ is selected as the test-bed case for the following analysis and preliminary conclusions. This is because the marginally stable case, similarly to what reported in Ref. [90], presents two distinct phases: a first phase where the subdominant fast-ion-driven TAEs are growing and the ITG modes dominate the turbulent transport; and a second phase in which the TAEs are nonlinearly destabilized and the thermal-ion fluxes are suppressed. In this manner, the transition between the two regimes is clearly identified and can be correlated with the modification of the structures in the cross phase space.

In panel (a) of Figure 3.26, the time evolution of the ^{3}Helium electrostatic heat flux for the simulation with $R/L_{p_{\mathrm{FD}}} = 10.7$ is illustrated together with the zonal flow shearing rate $\gamma_{E\times B,\mathrm{zonal}}$. Note that the value of $\gamma_{E\times B,\mathrm{zonal}}$ has been multiplied by 7.5 for the sake of visibility in the plot. Note also that in the remainder of the section, the normalization for the simulated time, i.e. a/c_s, will be often omitted

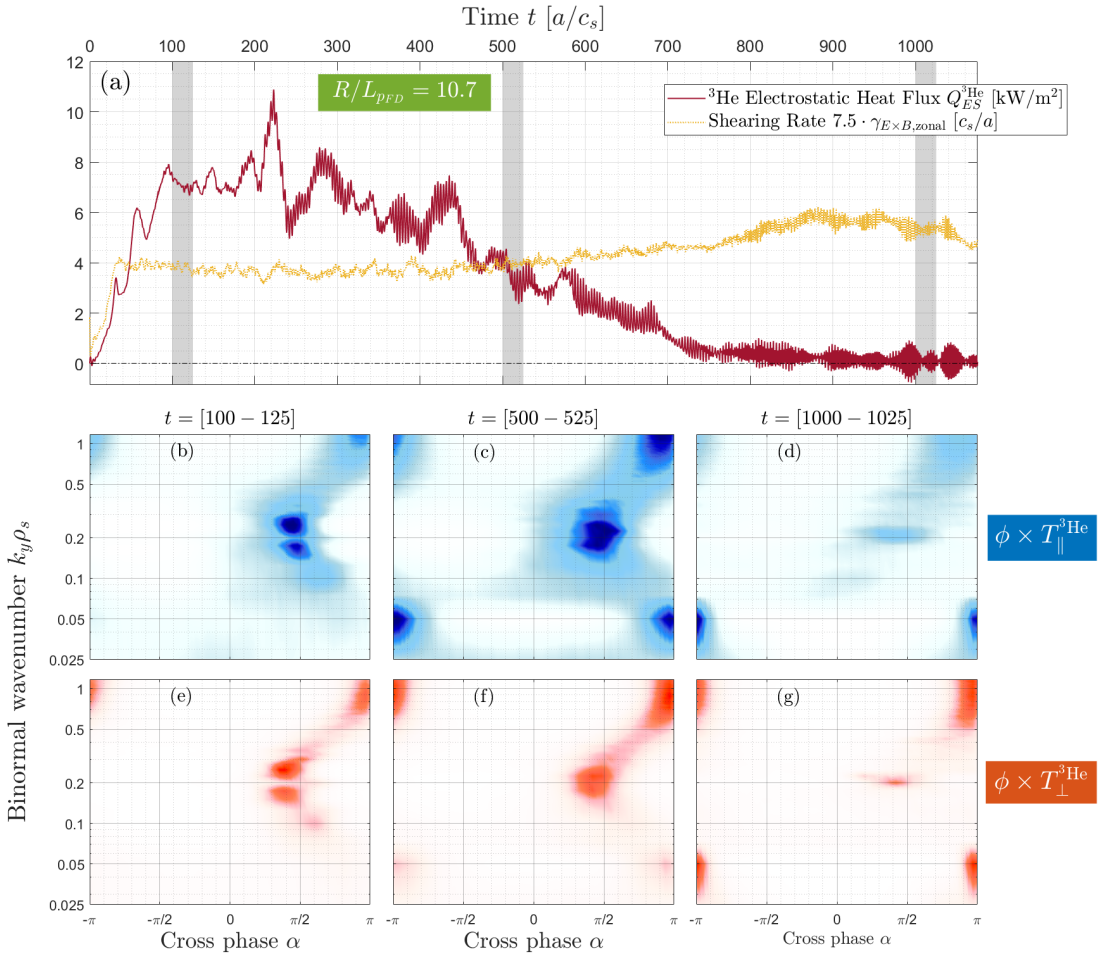

Figure 3.26: *In panel (a), the time evolution of the electrostatic heat flux of the ^{3}He species and the shearing rate (multiplied by a factor of 7.5 only for display purposes) are plotted. The vertical gray shaded areas represent three different time windows corresponding to the three phases shown in panels (b-g). In the first row, the panels (b-d) illustrate the cross-phase $\alpha(\phi \times T_{\parallel}^{^3\mathrm{He}})$ histograms, whereas in the second row the cross-phase is shown for $\alpha(\phi \times T_{\perp}^{^3\mathrm{He}})$.*

for simplicity. It is worthy to stress the fact that a very similar time evolution is observed also for the heat fluxes of the other thermal species. As already stated, this simulation presents two distinct phases. In the following, for the sake of simplicity, the normalizing units a/c_s for the time slices are omitted. The first phase can be approximately restricted to the time window $t = [0 - 500]$, in which the fluxes are oscillating around the ITG-induced level of transport and the zonal shearing rate has reached a quasi-stationary level. About $t = 500$, the shearing rate starts slowly to increase, reaching a higher quasi-stationary level around $t = 900$. The difference between the two levels of $\gamma_{E\times B,\mathrm{zonal}}$ is more than 40% ($\gamma_{E\times B,\mathrm{zonal}} = 0.46\ c_s/a$ vs. $0.75\ c_s/a$), which denotes a great increase of the zonal flow activity. Simultaneously with the increase of the shearing rate, the fluxes

measure a significant decrease, which settle to a long-term phase around $t = 900$. The time-average value of the fluxes drops to a very low level, mildly above the total suppression. This picture is in line with the results illustrated in Figure 3.17, showing a ∼97% of transport reduction. Hence, as already reported in section 3.4.3 a strong correlation between the enhancement of the zonal flow activity − actively driven by the fast-ion-driven TAEs − and the suppression of the ion-scale transport exists, consistently with the common paradigm of the zonal flow impact on the ITG turbulence [63].

It is worth observing also the high-frequency fluctuations of the fluxes starting in correspondence of the TAE destabilization. This can also be noticed in previous studies about energetic-particle modes in local gyrokinetic codes, see e.g. Refs. [124, 76, 90, 78]. Additional analyses have been performed to better characterize the oscillation frequency of the flux-surface averaged fluxes, which is measured to be $f \approx 50$ kHz, less than the TAE frequency range and marginally depending on the fast-ion pressure gradient. Nevertheless, a detailed identification of the physical mechanism driving those oscillations at that specific frequency is still elusive.

Respectively in panels (b-d) and (e-g) of Figure 3.26, the cross phase α between the electrostatic potential ϕ and the ^{3}Helium parallel temperature $T_\parallel$ and between ϕ and the ^{3}Helium perpendicular temperature $T_\perp$ fluctuations are shown for three different time windows. The cross phase is defined as:

$$\alpha(A \times B) = \tan^{-1}\big(Im(A/B)/Re(A/B)\big) \tag{3.10}$$

where A and B are the interested fluctuating physical parameters. It must be stressed that the values of the cross phase power spectrum are weighted by the amplitude of the product of the respective signals at different $k_y\rho_s$. Moreover, the cross phase is evaluated at all the radial wavenumbers $k_x\rho_s$ and parallel points z and then the distribution formed. Finally, the phase angle is collected in 62 bins spanning the range $[-\pi, \pi]$ and represented as histograms. The three time windows are represented by gray shaded areas in panel (a), and the cross phases are time-averaged within. Those time windows are $t = [100 - 125]$, $t = [500 - 525]$ and $t = [1000 - 1025]$, representing three different moments of the evolution of the fluxes. In the first time window, $t = [100 - 125]$, the system is dominated by the ITG instability. This is also confirmed by the cross phases α which shows a dominant structure in the wavenumber range $k_y\rho_s \sim 0.15 - 0.3$, linked to the ion-scale turbulence, at a phase angle of $\alpha = \pi/2$ [143]. In this conditions of out-of-phase quantities, the ITG transport can fully develop, with the high heat flux levels corroborating it. A structure at smaller scales (higher k_y) is also observed, but the physical parameters are almost perfectly in-phase ($\alpha = \pi$) and therefore low heat transport is expected to be driven at those scales. The second time window, i.e. $t = [500 - 525]$, corresponds to the onset of the second phase of the simulation, as explained above. In this precise moment, the fluxes already started to decrease and the zonal flow shearing rate to increase. In the cross phase power spectrum, three dominant structures are visible especially for the $\phi \times T_\parallel^{^3\mathrm{He}}$ param-

eters. The ITG pattern is still visible at $k_y\rho_s \sim 0.15 - 0.3$, as the transport is still not suppressed. The high wavenumber structures is reinforced, likely suggesting an enhanced direct cascade of free energy from ITG to lower scales. Interestingly, a in-phase structure appears at large-scale, peaking at $k_y\rho_s = 0.05$ where the TAE-induced fluctuations are predominant for the configuration with $R/L_{p_{\rm FD}} = 10.7$. Such a structure remains also in the last analyzed time window, $t = [1000 - 1025]$, corresponding to the second quasi-stationary state of the simulation. As previously observed in local gyrokinetic simulations [136] of large-scale instabilities, possibly driven by fast particles, their cross phases are different from gyrofluid studies in the ideal ballooning region [144]. Thus, the cross angle clearly points at a mode transition towards the larger scale instability. The electrostatic heat fluxes are totally suppressed in this time period, and consistently the ITG structure has almost disappeared.

The case of fully destabilized TAEs, i.e. the configuration with $R/L_{p_{\rm FD}} = 16.2$, is less favorable to clearly show the role of the cross phase transition in the turbulence suppression. In fact, having a non-null TAE growth rate, the complex mechanism of zonal flow activity enhancement and heat flux reduction is already ongoing from the very beginning of the simulations. Indeed, the so-called 'ITG phase' is hardly detectable. Therefore, the dominant structure in the low-k_y region is present from the TAE growing phase. For the sake of clarity, Figure 3.27 illustrates the cross phases $\phi \times T_{\parallel}^{^3\rm He}$ and $\phi \times T_{\perp}^{^3\rm He}$ for the simulations with $R/L_{p_{\rm FD}} = 16.2$ in the TAE growing (panels (a-b)) and saturated phases (panels (c-d)). The structure in the TAE spatial scales is firstly localized in the vicinity of $k_y\rho_s = 0.05$, consistently with the fact that the TAE largest growth rate is at $k_y\rho_s = 0.05$ for the configuration with $R/L_{p_{\rm FD}} = 16.2$, and therefore the principal contribution in the TAE growing phase comes from that wavevector. In the saturated phase, instead, is strongly localized at the lowest binormal wavenumber, $k_y\rho_s = 0.025$. However, in both phases, the angle between the electrostatic potential ϕ and both parallel and perpendicular temperature fluctuations is measured to be very close to π, leading to the suppression of the turbulent transport.

The interesting picture here described may outline a key role of the cross phase in the ion-scale turbulence suppression in the presence of highly energetic ions. Indeed, it has been demonstrated a clear correlation between the ion-scale turbulence suppression and the modification of the structures in the cross phase power spectrum. This mechanism is active when the fast-ion pressure gradient is large enough to drive TAEs unstable and to trigger, as explained before, a strong zonal flow activity. A substantial amount of previous studies in the literature already pointed out a strict relation between the modification of the cross phase in the presence of strong sheared flows. It has been also shown that the sheared flows affects much more the cross phase angle than the amplitude of the fluctuations [145]. It must be reminded once again that the combination of cross phase and fluctuation amplitude produces the heat flux level. In the present work, the strong zonal flow activity is a direct consequence of the destabilization of the fast-ion-driven TAEs, as shown in section 3.4.4. Beyond the well-known role as the principal saturation mechanism for ITG-driven turbulence [63], the zonal flows

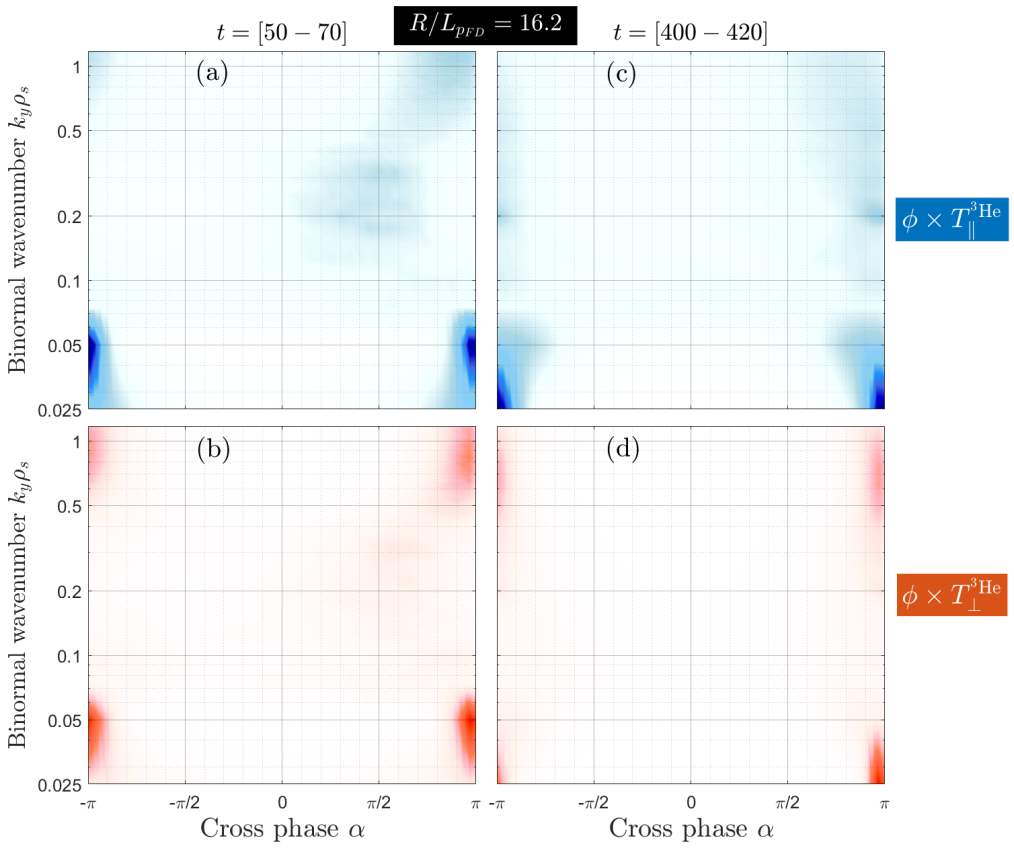

Figure 3.27: *The cross phase of $\alpha(\phi \times T_{\parallel}^{^3\mathrm{He}})$ is shown in panels (a) and (b) and of $\alpha(\phi \times T_{\perp}^{^3\mathrm{He}})$ in panels (c) and (d) for the configuration with $R/L_{p_{\mathrm{FD}}} = 16.2$. In (a) and (c) the TAE growing phase is represented, while in (b) and (d) the TAE saturated phase.*

may induce here another noteworthy effect on the turbulent transport by substantially modifying the cross phase angle among the heat-flux-relevant physical parameter fluctuations. Observations of such a phenomenon have been also obtained experimentally [146].

3.5 Residual electron transport in the presence of zonal fields

In this section, the effects of the highly energetic fast ions on the electron transport are analyzed. It will be essentially shown that, contrarily to previous experimental observations [79] and numerical analyses [76], the electron confinement does not degrade in the presence of large-amplitude fluctuations of the perturbed fields in conditions of unstable Alfvén eigenmodes.

As it has been already pointed out, the electrostatic component of the energy transport is totally suppressed when the destabilized TAEs nonlinearly couple to the $k_y = 0$ components of ϕ inducing a strong zonal shearing activity. In these

conditions, the electromagnetic transport of both thermal ion species is almost negligible, regardless the fast-ion pressure gradient. This is likely due to the low value of β_e corresponding to the L-mode plasma of JET pulse #94701. Instead the electromagnetic heat flux of the electrons is the dominant energy transport channel when the critical $R/L_{p_{FD}}$ threshold is overcome and the TAEs are destabilized. This can be seen in Figure 3.28, where the electron electrostatic (in blue) and electromagnetic (in red) heat diffusivities χ^{el} are shown in function of the fast-ion pressure gradient. It is to be noted that the leftmost points in the scan, the ones at $R/L_{p_{FD}} = 0$ are indeed computed without including the suprathermal particles in the simulations, and so they do not refer to the case with fast-ion flat profiles. The electrostatic counterpart of the electron transport follows the trend

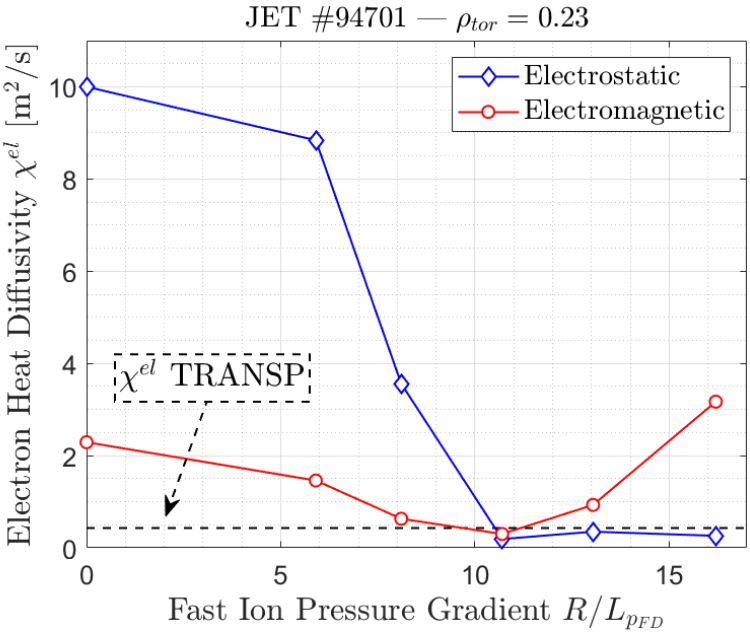

Figure 3.28: *The electron heat diffusivities, both electrostatic and electromagnetic contributions, are reported as a function of the fast ion pressure gradient. The case with $R/L_{p_{FD}} = 0$ is actually representing the case without fast ions. The black horizontal dashed line represents the electron heat diffusivity computed by TRANSP integrated modeling.*

already described for both thermal ion species (see Figure 3.16). It is indeed fully suppressed with destabilized TAEs, namely for $R/L_{p_{FD}} \geq 10.7$. This result could be expected since the simulations retain only the ion-scale region in the binormal direction, excluding therefore possible ETG-driven electron transport. The contribution from the unstable ETG modes to the ion transport are not expected to be significant [147, 127, 128], as reported earlier (see section 3.3.2), but it may play a non-negligible role for the electron transport at smaller scales. As stated in previous sections, subdominant TEMs may still be active in driving extra electron electrostatic transport. In the nonlinear regime, TEMs are expected to be unstable, and this can also be confirmed by inspecting Figures 3.18(a). Indeed,

the peak of the frequency power spectrum is not only localized in the positive side of the frequencies, but presents also a non-negligible component in the low-frequency negative region, where TEMs may be destabilized. This contribution is, however, not expected to be highly relevant to the overall electron heat flux in the performed simulations because of the subdominant nature of TEMs in pulse #94701.

Regarding the electromagnetic heat fluxes, the global trend depicted in Figure 3.28 is different. When TAEs are not nonlinearly destabilized, the electromagnetic fluxes decrease with increasing $R/L_{p_{FD}}$, similarly to the electrostatic counterpart. Being TEMs an electrostatic instability [29], the electromagnetic heat fluxes for $R/L_{p_{FD}} < 10.7$ are likely driven by ITG modes. Nevertheless, beyond the critical threshold the electron electromagnetic transport starts to increase, becoming more than one order of magnitude larger than the electrostatic counterpart for the configuration with $R/L_{p_{FD}} = 16.2$ ($\chi^{el}_{EM} = 3.17$ m^2/s vs. $\chi^{el}_{ES} = 0.26$ m^2/s). This is also corroborated by the heat flux spectra shown in Figure 3.29. It is to be noted that the spectra have been purposely trimmed to show only the interesting low-k_y region, since for the wavevectors $k_y\rho_s > 0.4$ the contribution to the overall fluxes is almost null. The spectra reveal the dominant role of the electron electromagnetic flux over the other channels. This is likely due to the prompt response of the electrons to the large-amplitude perturbations of the vector potential. Indeed, as highlighted by Relation 2.28, the heat flux is proportional to the thermal velocity, which in case of the electrons is much larger than that of thermal ions. The large-amplitude fluctuations are driven by the fully destabilized TAEs [79], which is also confirmed by the shape of the heat flux spectra, peaking in the TAE-dominated low-ky region. The stronger is the TAE driver, which in this case is the fast ion pressure gradient, the larger is the amplitude of the fluctuations of $A_\parallel$ and subsequently the electron electromagnetic flux. In Figure 3.30, the moduli square of the magnetic potential for the various points of the $R/L_{p_{FD}}$ scan are shown averaged over the parallel direction z and additionally over k_y (panel (a)) and over k_x (panel (b)). The direct comparison clearly illustrates that the vector potential is strongly increased in the low-k_y range, where TAEs dominate, with increasing fast-ion pressure gradient.

3.5.1 Strong zonal field activity in the presence of fully destabilized TAEs

Although the strong increase of the intensity of the $A_\parallel$ fluctuations, the electron heat fluxes do not exhibit a dramatic explosion of the average transport levels, as already reported in previous numerical studies (see e.g. Figure 11 of Ref. [76]). This striking observation could have multiple explanations. In the following, a first tentative to understand the underlying mechanism leading to the mitigation of the electron electromagnetic transport will be pursued. It is first reported a relevant result in Figure 3.31, where the magnetic potential $A_\parallel$ is shown in the (x,y) space after being averaged on the parallel direction for four different configuration of the fast ion characteristics. In panel (a) the case without including fast

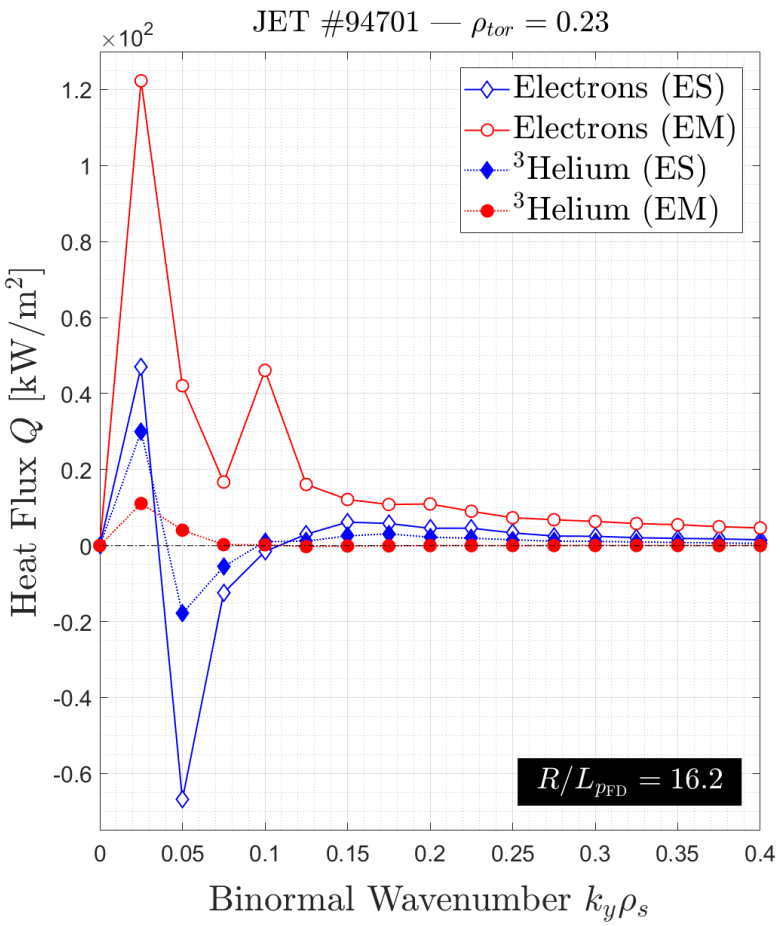

Figure 3.29: *The heat flux spectra against the binormal wavenumbers are shown for electron and Helium-3 species. Both electrostatic and electromagnetic contributions are displayed.*

ions, in (b) the case with $R/L_{p_{FD}} = 5.9$, in (c) with $R/L_{p_{FD}} = 10.7$ and in (d) with $R/L_{p_{FD}} = 16.2$ are displayed. Similarly to what occurs for the electrostatic potential (see Figure 3.21), the vector potential shows a transition of the dominant pattern with the increasing of the TAE driver, i.e. $R/L_{p_{FD}}$. Basically, the occurrence of a dominant zonal structure, with the formation of a preferential arrangement of the vector potential along the binormal direction, is effective for the simulations with nonlinearly unstable TAEs. In the configuration with $R/L_{p_{FD}} = 10.7$ however small scale turbulent eddies are still identifiable, indicating that certain non-null k_y modes still play a relevant role in the electromagnetic transport. It is also reported the parameter of merit $\bar{s}_{fluc} = qR_0\partial_x B_y(k_x, 0)$, generally termed as magnetic shear fluctuation rate. Such a parameter $\bar{s}_{fluc}$ is increased by 75% when the TAEs are driven unstable – moving from $\langle \bar{s}_{fluc} \rangle_{x,t} = 3.2 \cdot 10^{-2}\ c_s/a$ in the case W/O fast ions to $\langle \bar{s}_{fluc} \rangle_{x,t} = 5.6 \cdot 10^{-2}\ c_s/a$ for $R/L_{p_{FD}} = 16.2$. This can also be observed in Figure 3.32, where the magnetic shear fluctuation rates for three

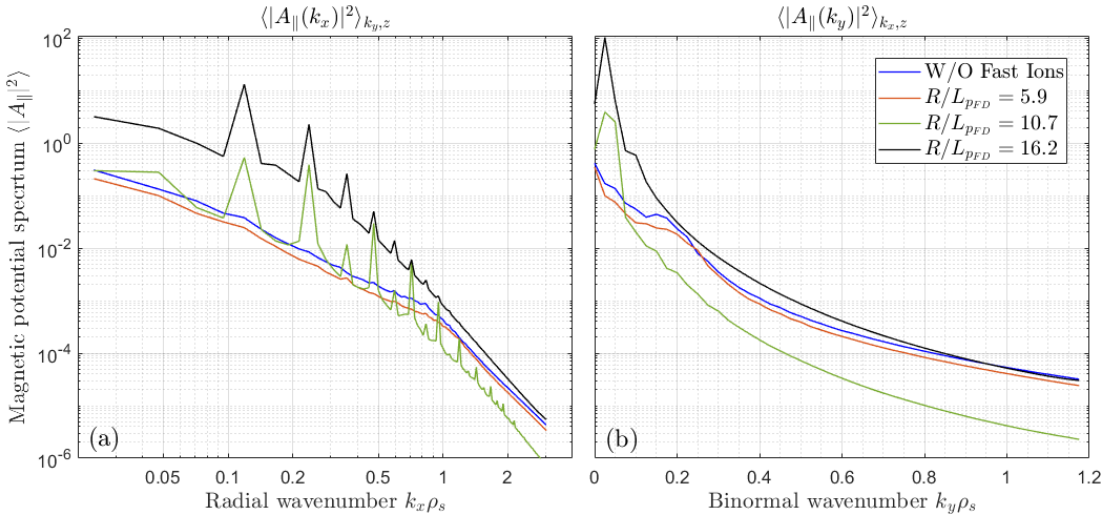

Figure 3.30: *The spectra of the vector potential averaged over the binormal k_y direction and over the radial k_x direction are shown respectively in panels (a) and (b) for various configurations of the fast ion pressure gradient.*

different cases are displayed in function of the radial wavenumber $k_x\rho_s$ after being time-averaged. Similarly to the zonal flow shearing rate (see Figure 3.22), the case with $R/L_{p_{FD}} = 10.7$ presents an increased contribution with respect to the case without fast ions in specific radial wavenumbers, likely related to the non-adiabatic dynamics of the electrons [132]. Instead, the case with fully destabilized TAEs shows a general boost of the zonal currents especially in the low-k_x range. Indeed, as observed also for the zonal flow shearing rate, the width of the vector potential vertical structures in panel (d) of Figure 3.31 is bigger than that in panel (c).

This behaviour may suggest again that a nonlinear synergy between the TAE and the zonal spatio-temporal scales also for the magnetic potential exists. Previous analytic studies predict a forced excitation of the zonal structures, preferentially dominated by the zonal magnetic fields, in the presence of unstable TAEs with the proper treatment of the trapped-ion response [148]. It is observed, as shown in Figure 3.15, that the dynamics of the trapped fast ions play a key role in the destabilization of the TAEs. The bounce motion of the highly energetic is hence envisaged to be a crucial ingredient also for the increase of the zonal structures in the performed GENE simulations.

In order to improve the quality of the present study on exploring the nonlinear dynamics of the vector potential perturbations and highlighting possible nonlinear couplings, an extensive bispectral analysis has been performed. The resulting picture after such an analysis increase the complexity of the conclusions, as it will be delineated in the following. As already stated and illustrated in Figures 3.31 and 3.32, concomitantly to the TAE destabilization, a strong zonal field activity is measured in the gyrokinetic analyses. The previous results in section 3.4.4 demonstrated the nonlinear interaction between the zonal and the

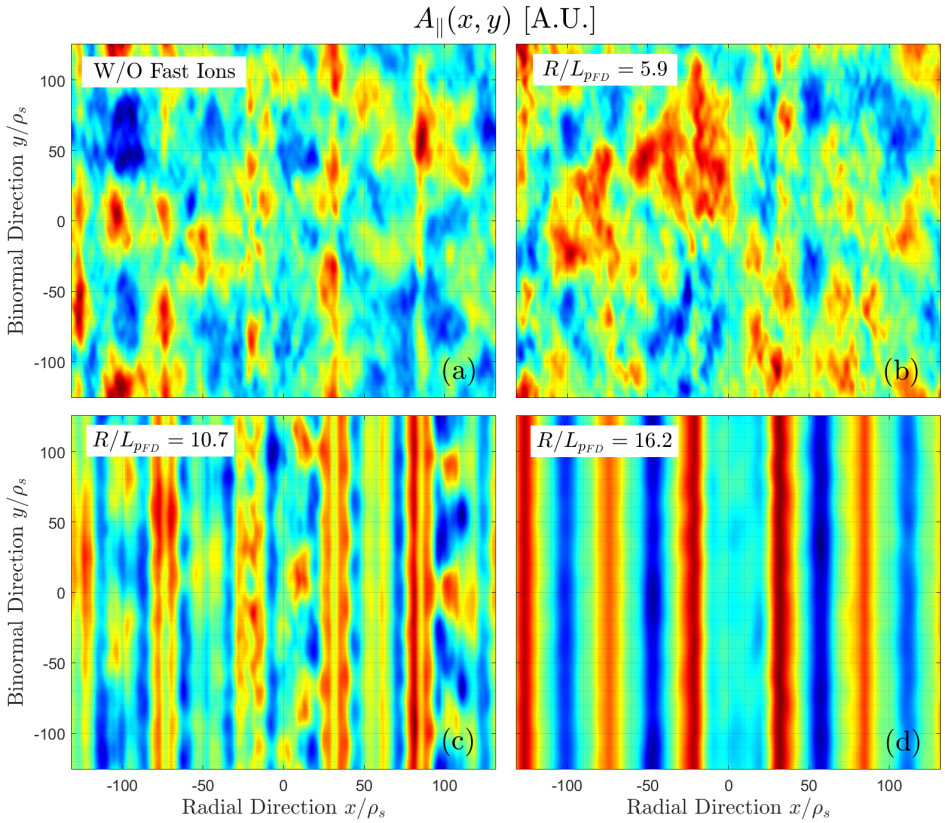

Figure 3.31: *The parallel magnetic potential computed from the nonlinear* GENE *simulations is shown in the radial x and binormal y space, after being averaged over the parallel direction z, for various configurations highlighted with text boxes within the contour plots.*

TAE components of the electrostatic potential. This may then suggest that the nonlinearly triggering of the zonal field may be again related to the destabilization of the fast-ion-driven TAEs. Thus, the multi-mode analysis is performed also for the dynamics of the $A_\parallel$ nonlinear fluctuations. It must be stressed that those analyses are still preliminary, and a more detailed study is required before drawing any firm conclusion. In Figure 3.33(a), the modulus of the bispectrum $b^W_{A_\parallel}$ of the triads $(k'_x, k'_y) = (0, 0.025)$, $(k''_x, k''_y) = (a, 0)$ and $(k_x, k_y) = (a, 0.025)$ (with $a \in [-k_{x,max}, k_{x,max}]$) is shown for the initial phase of the simulation with $R/L_{p_{FD}} = 16.2$. It is worthy to say that the bispectral analysis for the vector potential is carried out in the same fashion as it was done for the electrostatic potential (see Relation 3.9), replacing ϕ with $A_\parallel$. In this initial phase, the TAEs are destabilized and slowly saturate. The bispectral analysis shows that the main interaction between the low-k_y and the zonal components of the vector potential occurs at the intersection between the zonal field frequency ($f'' = 0$) and $f' \approx 20-30$ kHz. This latter range of frequencies is related to the destabilization of the LFMs previously detected in the fluctuations of the electrostatic potential and demonstrated to be

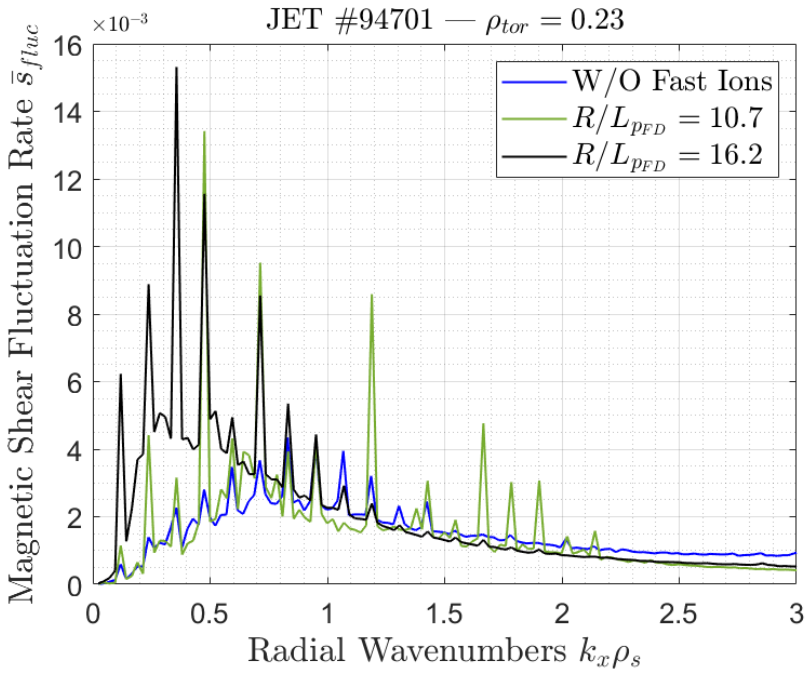

Figure 3.32: *The magnetic shear fluctuation rate $\bar{s}_{fluc}$ is plotted as a function of the radial wavenumber $k_x\rho_s$ for various configurations.*

driven by the TAEs (cf. section 3.4.5). Therefore, it is shown that the unidentified LFMs are also playing a determinant role for what concerns the vector potential dynamics. It should be also stressed that the LFM fluctuations in the vector potential are already detected in the first stage of the simulation, in which TAEs are not still completely saturated. On the contrary, the LFM fluctuations of ϕ are hardly visible in the linear growing phase of the TAEs.

Figure 3.33(a) illustrates that a minor interaction could be detected at the TAE high-frequency range. This suggests that a non-negligible contribution to the onset of the zonal field structures is provided by the TAEs, consistently with previous theoretical analyses [139].

In panel (b) of Figure 3.33, indeed, the modulus of the bispectrum is shown for the triad $(k_x', k_y') = (0, 0.05)$, $(k_x'', k_y'') = (a, 0)$ and $(k_x, k_y) = (a, 0.05)$ (with $a \in [-k_{x,max}, k_{x,max}]$). Here, the main interaction occurs at higher frequency ($f' \approx 400$ kHz). Nevertheless, it must be also observed that the amplitude of the modulus for the triads in panel (b) is much lower than the ones in panel (a). This indicates that the most intense coupling occuring with the zonal component of the vector potential is measured for the LFM localized at $k_y\rho_s = 0.025$.

3.5.2 Destabilization of high-frequency electron-driven modes

In the bispectral analyses performed on the vector potential, it has been shown that a high-frequency mode rotating in the electron diamagnetic direction is excited in the nonlinear regime. This section is devoted to illustrate with more

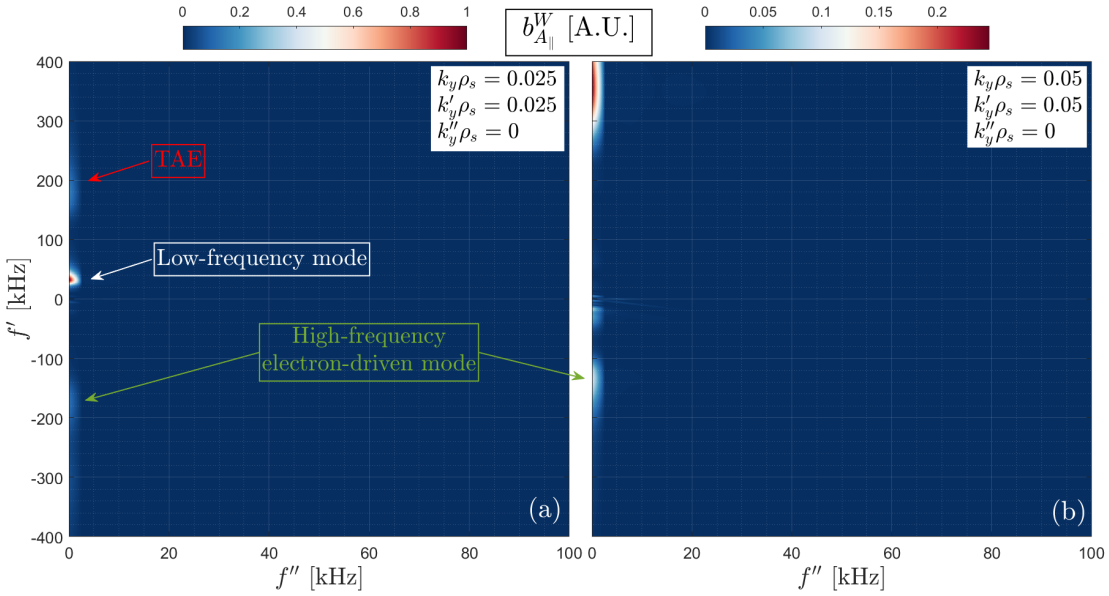

Figure 3.33: *The modulus of the wavelet bispectrum for the magnetic potential fluctuations highlighting the spatio-temporal coupling with the zonal flows is shown. The selected triads are $k_y\rho_s = 0.025$, $k'_y\rho_s = 0.025$ and $k''_y\rho_s = 0$ in panel (a) and $k_y\rho_s = 0.05$, $k'_y\rho_s = 0.05$ and $k''_y\rho_s = 0$ in panel (b), for the case with $R/L_{p_{FD}} = 16.2$. The TAE, low-frequency mode and high-frequency electron mode frequency ranges are highlighted with labels.*

details the excitation of these high-frequency electron modes. In Figure 3.34, the Fourier spectrum of the vector potential fluctuations averaged over the k_x, k_y (without considering the zonal fluctuations) and z directions in the first phase of the simulation with $R/L_{p_{FD}} = 16.2$ is shown. It can be observed that, beyond the high peaks of the TAEs and LFMs, another non-dominant structure is measured in the range $f \approx [-180, -120]$ kHz. These unstable modes will be called high-frequency electron-driven modes (HFEMs). An additional analyses on the fluctuations at the low-k_y region, specifically at $k_y\rho_s = 0.025$ and $k_y\rho_s = 0.05$, localize the HFEM in this region. Thus, HFEM is likely related to the TAE destabilization. It is worthy to note that even the electrostatic potential ϕ is perturbed in these range of frequencies (see Figure 3.18(d)). It must be also stressed that such modes are not detected in the marginally stable TAE case, i.e. the configuration with $R/L_{p_{FD}} = 10.7$. Hence, similarly to the LFMs, the HFEM destabilization is likely related to the TAE intensity. Therefore, it can be also concluded that the residual electromagnetic electron transport, enhanced by the increasing value of the TAE driver (namely $R/L_{p_{FD}}$) and shown in Figure 3.28, is related to the destabilization of the HFEMs.

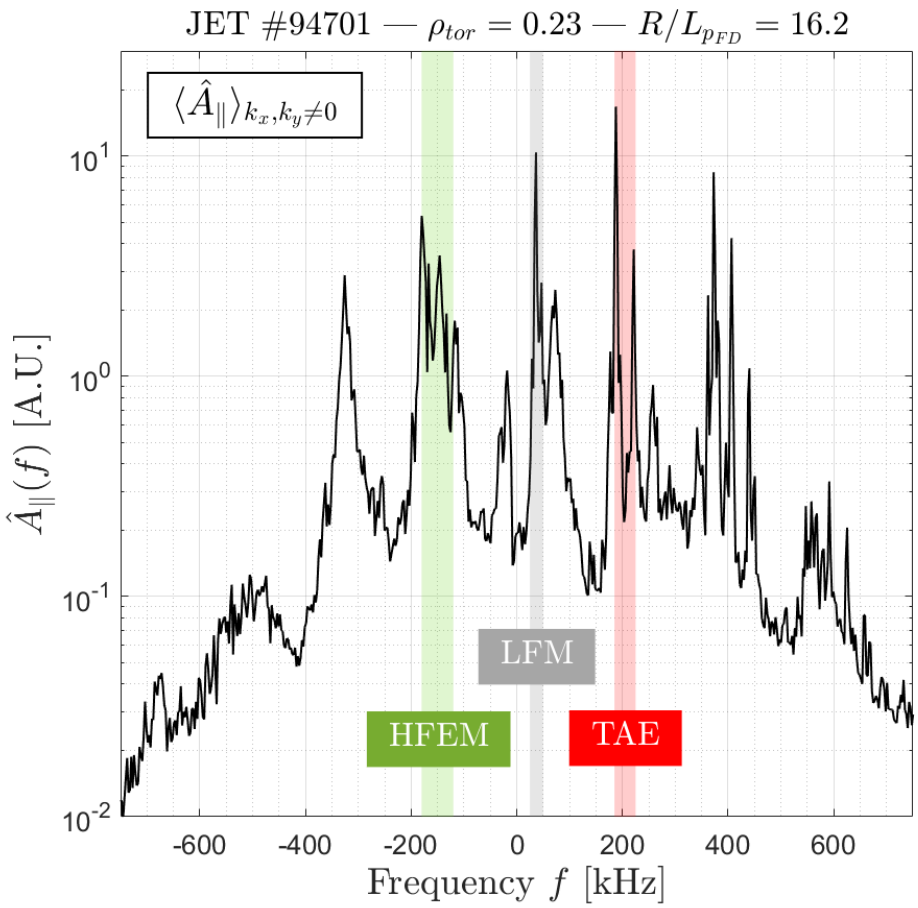

Figure 3.34: *The Fourier frequency spectrum $\hat{A}_{\parallel}$ averaged over the radial wavenumbers and over the finite binormal wavenumbers ($k_y \neq 0$) is shown for the configuration with $R/L_{p_{FD}} = 16.2$. The shaded areas correspond to the ranges of frequencies of the high-frequency electron-driven mode (green), low-frequency mode (gray) and TAE (red).*

3.6 Partial conclusions

In this brief section, a summary of the main findings reported above is provided. JET pulse #94701 is embedded within the three-ion heating scenario recently developed at JET [111, 113], in which a substantial population of MeV-range ions are generated. Striking experimental observations indicate that an improvement of the ion confinement is obtained in the presence of strong electron heating and strong Alfvén activity, both induced by the MeV ions. Thus, gyrokinetic simulations by means of the GENE code in its local version have been performed in order to investigate on the possible causes leading to such a beneficial improvement of the ion confinement. The simulations have been performed in the plasma core, at $\rho_{tor} = 0.23$, and before the onset of the RSAEs, at $t = 9.5$ s. The linear stability analyses showed that ITG is the dominant instability at the ion-scale, whereas fast-ion-driven TAEs are destabilized when a threshold in the fast ion pressure

gradient is overcome. No linear effect of the highly energetic ions on the ITG linear growth rate has been noticed, consistently with what reported in previous analyses [72]. Additional studies on the excitation mechanism of the fast-ion-driven TAEs show that those are mainly destabilized through a wave-particle resonant mechanism with the trapped fast ion precessional motion. After the assessment on the linear stability, demanding nonlinear simulations have been carried out. It has been thus unveiled a complex mechanism leading to the suppression of the ion-scale electrostatic turbulent transport, in good agreement with the power balances computed by TRANSP. The suppression is however obtained only when the fast ion pressure gradient $R/L_{p_{FD}}$ is large enough to nonlinearly excite the TAEs. The complex mechanism is based on a nonlinear interaction between the TAE and zonal flow spatio-temporal scales. Indeed, unstable TAEs efficiently couple to the zonal component of the electrostatic potential and trigger a strong zonal flow activity [139, 141, 90]. This has been confirmed by means of bispectral analyses. Whereas the effects of the zonal flows on the ITG transport are well-known [63], additional studies highlight a possible impact of the cross phase shift in the presence of nonlinear unstable fast-ion-driven TAEs on the reduction of the turbulent transport. It has also been reported, however, that high levels of fast ion turbulent transport, both electrostatic and magnetic, are measured in correspondence of the configurations with fully destabilized TAEs. Moreover, the TAEs are also shown in the numerical analyses to efficiently couple to low-frequency modes and possibly excite them when the TAE intensity is large. Low-frequency modes have also been measured in the experiments, localized in the TAE radial range, with strong similarity to those detected in the gyrokinetic simulations.

3.7 Further analyses: Negative magnetic shear effect on fast ion confinement

After illustrating in great details the impact of the highly energetic ions generated via three-ion heating scheme in the ITG-dominated JET pulse #94701 for the time window with positive magnetic shear, the possible effects of the reversed q-profile are discussed in this section. It must be reminded indeed that a systematic destabilization of RSAEs, which are significant MHD markers indicating the non-monotonic shape of the q-profile, in the three-ion scenario plasmas is observed. In JET pulse #94701, after the sawtooth crash occurring at $t = 9.43$ s and the plasma recover, different harmonics of RSAEs are visible (see the magnetic spectrogram of Figure 3.6). It is also reminded that the analyses detailed in the previous sections of this chapter have been carried out with a positive magnetic shear. Indeed, they were localized in the time slice just before the onset of the RSAE instability, for avoiding any possible effect of the non-monotonic q-profile on the impact of MeV-ions on the system stability.

As a first assessment, linear simulations with the GENE code have been performed to evaluate the modification of the magnetic shear on the dominant insta-

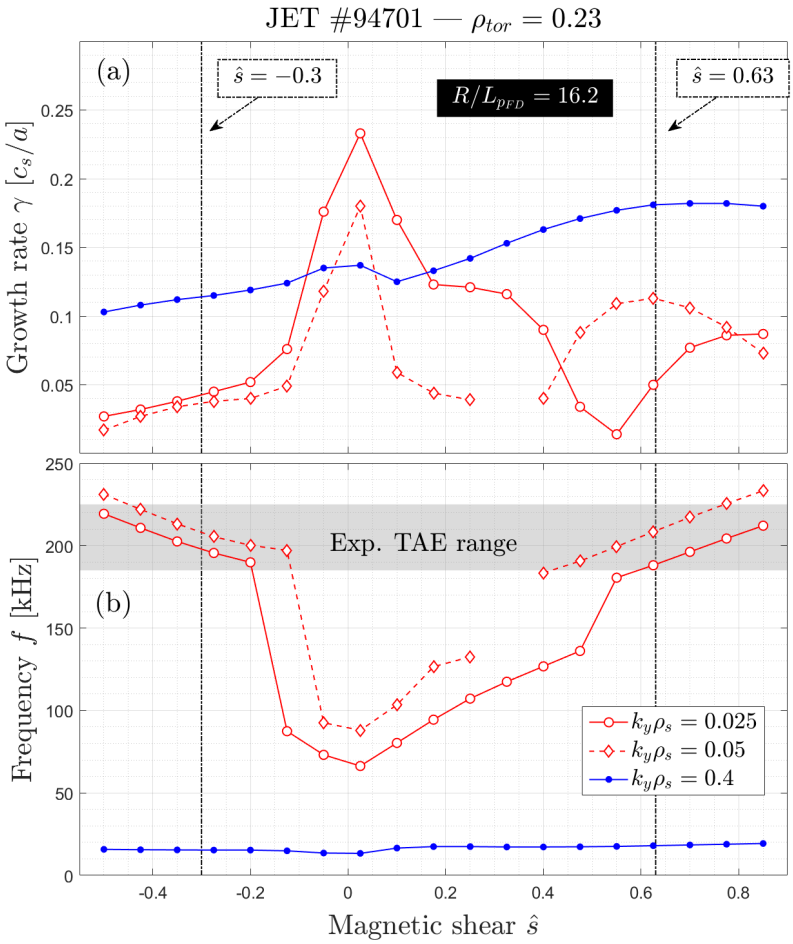

Figure 3.35: *Linear growth rates (a) and frequencies (b) computed by the* GENE *code for the JET pulse #94701 at $\rho_{tor} = 0.23$ are plotted as a function of the magnetic shear for three different binormal wavenumbers in the configuration with $R/L_{p_{FD}} = 16.2$. The three wavenumbers correspond to the TAE scale (in red curves) and to the ITG scale (in blue curve). The gray shaded area in the frequency spectra displays the range at which the TAEs are experimentally detected by the Mirnov coils. The vertical dotted-dashed lines indicate the values of the magnetic shear selected for the comparison in the nonlinear regime.*

bilities at two different spatial scales, i.e. for the TAE and the ITG range of $k_y\rho_s$. The simulations are performed always at $\rho_{tor} = 0.23$ with exactly the same setup configuration used for the positive magnetic shear case, except of course for the value of the magnetic shear. The linear results are shown in Figure 3.35, where in panel (a) and (b) the growth rate and the mode frequency as a function of the magnetic shear $\hat{s}$ are respectively illustrated for $k_y\rho_s = 0.025$, 0.05 and 0.4 in the configuration with $R/L_{p_{FD}} = 16.2$. The vertical dashed lines represent the two magnetic shear configurations that are also compared in the nonlinear regime. It

can be observed that the growth rate of the ITG mode (blue curve) is not strongly affected by the magnetic shear value, reporting a larger rate for positive magnetic shear values with respect to negative ones. The almost constant mode frequency for the wide range of $\hat{s}$ indicates that the ITG instability nature is almost unaffected. The TAEs are indeed not always dominant for the range of analyzed magnetic shear values. As it is demonstrated by the sharp modification of the mode frequency in panel (b), the range $-0.15 \lesssim \hat{s} \lesssim 0.48$ is dominated by a different instability. An identification of such unstable with much larger growth rate in the vicinity of $\hat{s} = 0$ is still elusive, although the frequency range may suggest that they are RSAEs. Nevertheless, it can be observed that also for the low-k_y range, the growth rate is decreased moving from positive to negative magnetic shear values, especially for the $k_y\rho_s = 0.05$ mode. Eventually, the transition to negative magnetic shear regimes may strongly affect the nonlinear resulting fluxes, mainly for what concerns the large-scale instabilities. It must be however noted that although the growth rate is decreased, the TAEs are still destabilized at negative magnetic shear, consistently with the experimental findings.

The stabilizing effect of the negative magnetic shear on the ballooning-type instabilities has been widely discussed in the literature. The main effect of negative $\hat{s}$ values is a local twisting of the magnetic field lines, leading to a strong modifications of the flux surface orientation during a toroidal turn. This results in a unfavorable situation for the ballooning-type instabilities, which are therefore strongly stabilized [149, 150, 151]. The growth rate decrease of the ITG modes observed in Figure 3.35 is thus explained. The TAEs also benefit from the local twisting of the field lines, but an additional result reported in Ref. [149] could also affect the stability of the TAEs in the present work. In fact, it is worth reminding that the main contribution to the TAE excitation is given by the trapped fast ions in the positive magnetic shear system, as illustrated by Figure 3.15. Kadomtsev and Pogutse in [149] found a negative critical value of magnetic shear for which the instabilities driven by trapped particles are stabilized, because of the increased time spent by trapped particles in the favorable region of the poloidal plane in which the toroidal magnetic drift is concordant with the gradient of the magnetic field (the high field side). Later experiments and related modeling confirm these theoretical findings [152].

For this reason, in-depth analyses of the free energy exchange evaluated in the velocity space, similarly to the study described in section 3.3.4, have been performed. The contribution of the suprathermal species to the total time derivative of the potential energy at the outer mid-plane is shown in Figure 3.36 for the two wavenumbers also analyzed before, i.e. $k_y\rho_s = 0.025$ ($n = 4$) and $k_y\rho_s = 0.05$ ($n = 7$), respectively in panel (a) and (b). Comparing to Figure 3.15 with positive magnetic shear, the resonant structures are highly reduced in terms of their extension. For $k_y\rho_s = 0.025$, the resonant structure has even disappeared, being now the parallel particles to be the dominant driver of the TAE instability. In the case of $k_y\rho_s = 0.05$, indeed, the structure in the trapping cone is strongly shrinked and also shifted up slightly. Nevertheless, the strength of the contribution of the peak is almost unvaried with respect to the case with positive magnetic shear.

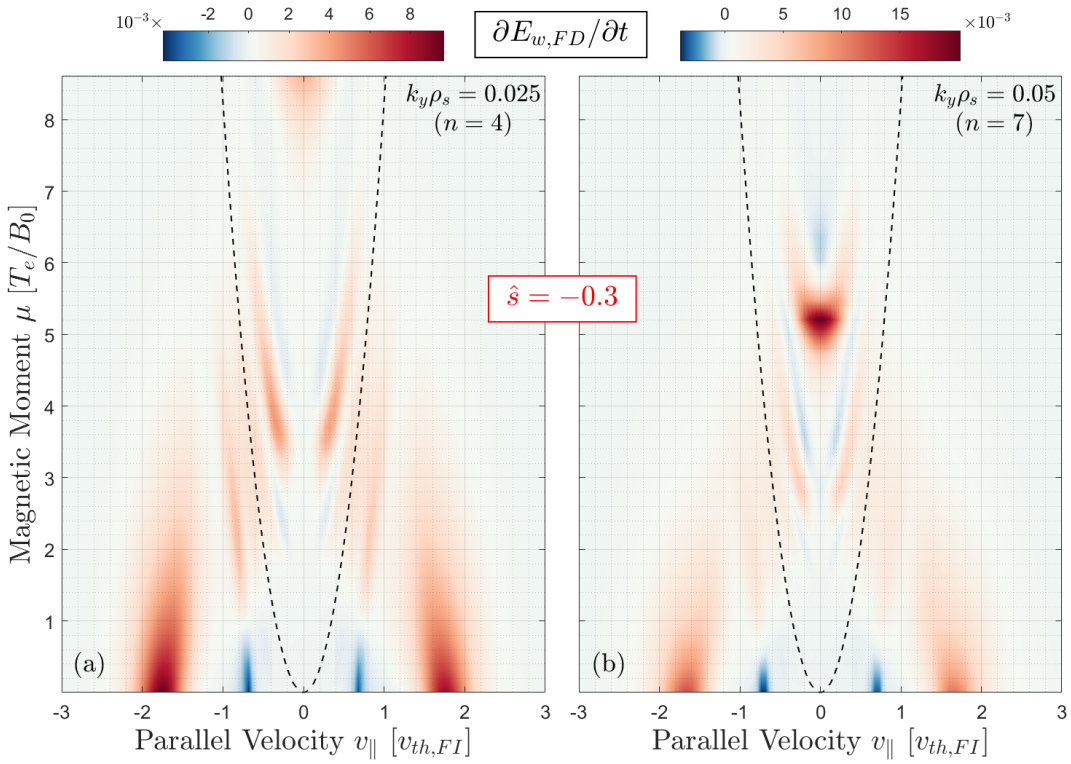

Figure 3.36: *The derivative in time of the potential energy of the fast ions $\partial E_{w,FD}/\partial t$ for $k_y\rho_s = 0.025$ and $k_y\rho_s = 0.05$ are plotted in the velocity space in panels (a) and (b), respectively, for the configuration with negative magnetic shear ($\hat{s} = -0.3$). Positive and negative values of $\partial E_{w,FD}/\partial t$ indicate a destabilizing and stabilizing effects on the modes, respectively.*

Eventually, the inclusion of a negative magnetic shear value in the linear stability analysis results in a less favorable situation for the development of the fast-ion-driven TAEs.

It is thus shown that a modification of the magnetic equilibrium, moving essentially from a non-monotonic to a reversed q-profile could lead to strong differences in the transport level. Essentially, the fast-ion-driven turbulence may be strongly quenched by the change in the q-profile slope. It must be also remembered that the TAEs are a key ingredient for the turbulence suppression via the complex mechanism described in the previous sections. Therefore, a complete quench of the TAE linear excitation process would likely lead to a less intense zonal flow activity, and to a different turbulence pattern in which the ITG-driven transport – although being decreased in strength by the effects of the negative magnetic shear – is not suppressed. However, in the Mirnov coil spectrogram shown as Figure 3.6, the coexistence of TAE and RSAE signal implies that the two instabilities may not be exclusive and therefore the turbulence suppression mechanism still active. Even more, the overall confinement may benefit from a suitable combination of the two beneficial effects, i.e. the zonal activity triggered

by the MeV-ion-driven TAEs and the reverse of the q-profile, and lead thereby to an optimum plasma state, similarly to what observed experimentally in the three-ion ($D - D_{NBI} - {}^3He$) scenario at JET.

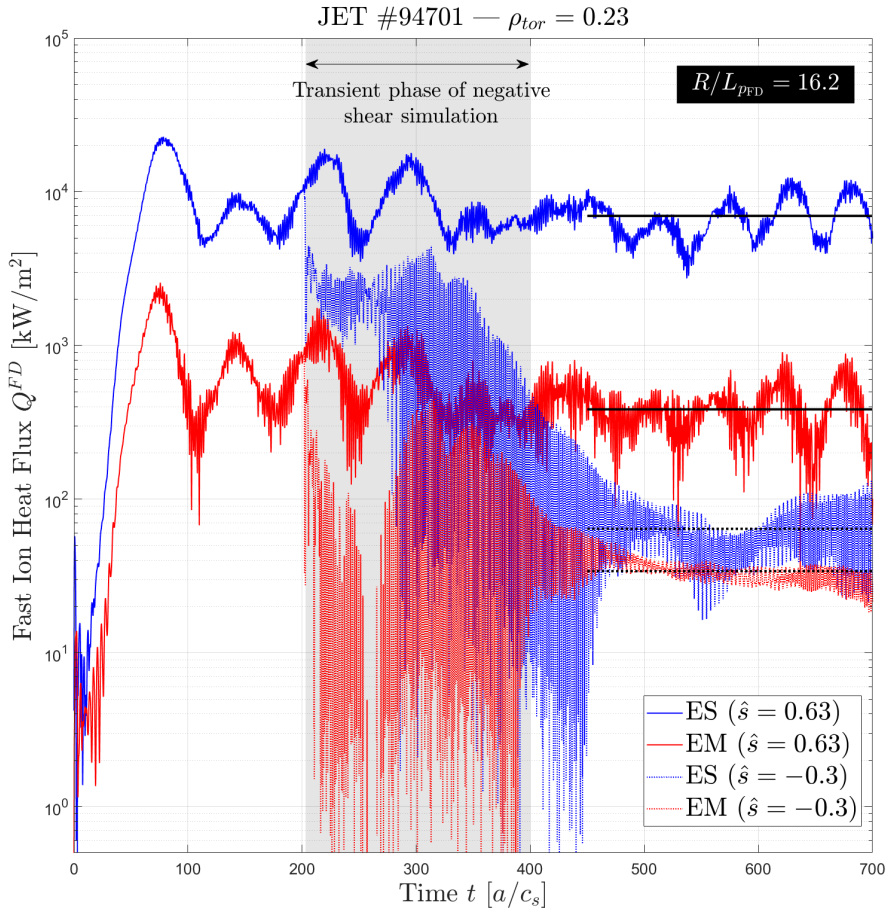

Figure 3.37: *The comparison of the time-traces of the fast-ion heat fluxes between the configuration with negative magnetic shear (dotted curves) and positive magnetic shear (solid curves) for the case with $R/L_{p_{FD}} = 16.2$ is shown. The gray shaded area approximately represents the transient phase after the introduction of the negative magnetic shear in the simulations.*

Additional nonlinear numerical simulations have been performed in order to address the effects of the negative magnetic shear on the fast-ion turbulent transport. For saving computational resources, the simulation with negative magnetic shear has been performed only for the case with $R/L_{p_{FD}} = 16.2$ and starting from a state of the positive magnetic shear simulation after the overshoot. In Figure 3.37, the time evolution of both electrostatic and electromagnetic heat fluxes of the fast ions is shown for the two magnetic shear configurations, namely for $\hat{s} = 0.63$ and $\hat{s} = -0.3$. As soon as the negative magnetic shear is set on in the simulation, the heat fluxes experience a sharp decrease already in the transient phase of the flux evolution with respect to the positive magnetic shear simulations (whose

fluxes are reported in solid lines). For the sake of clarity, the transient phase of the negative shear simulation is highlighted by the gray shaded area. Thus, after the transitory, the heat transport reaches a long-term quasi-stationary state, in which the measured level of the fast-ion fluxes are strongly reduced (note the logarithmic scale on the ordinates of Figure 3.37). Such a strong deviation from the positive magnetic shear case can be quantified by comparing the fast-ion heat diffusivities in the two cases. For the simulation with the $\hat{s} = 0.63$, the electrostatic and electromagnetic fast ion thermal diffusivities are respectively ${}^{+}\chi_{ES}^{FD} = 71.91$ m^2/s and ${}^{+}\chi_{EM}^{FD} = 4.15\ \mathrm{m}^2/s$. Instead, when the magnetic shear is set to $\hat{s} = -0.3$, those values abruptly decreased down to ${}^{-}\chi_{ES}^{FD} = 1.23\ \mathrm{m}^2/s$ and ${}^{-}\chi_{EM}^{FD} = 0.35$ m^2/s. A dramatic reduction of more than 98% is measured with the reversed shear geometry. This result implies a much better confinement for the fast ions in such conditions. The experimental relevance of such a result is confirmed by the regularly observed strong increase of the measured neutron rate concomitantly with the destabilization of the RSAEs in the three-ion scheme scenario at JET, and the subsequent neutron rate decrease when RSAEs are stabilized [113].

It must be also commented that the low levels of the thermal ion transport are almost unaffected by the $\hat{s}$ modification, still exhibiting thus a good agreement with the TRANSP integrated modelling predictions. This is an additional clue of the fact that the complex multi-scale mechanism leading to ion-scale turbulence suppression is still effective in the conditions of reversed q-profile.

As already stated, such a strong fast-ion transport reduction can be related to the weakening of the resonant structure in the velocity space which has been demonstrated to excite the fast-ion-driven TAEs. Moreover, as illustrated in Figures 3.35 and 3.36, the TAEs are still linearly unstable for $\hat{s} = -0.3$, although the growth rate is lowered. This condition is confirmed also in the nonlinear regime, as shown in Figure 3.38 where the frequency spectrum of the electrostatic potential $\hat{\phi}$ is shown for the quasi-stationary phase of the simulation with $\hat{s} = -0.3$. The TAEs are unstable and dominate the nonlinear perturbed electrostatic potential also with the negative magnetic shear configuration. This is essential for the complex multi-scale mechanism leading to the ion-scale turbulence suppression to be still active. The main peaks of the spectrum are within the experimentally detected TAE range ($f \approx 185 - 225$ kHz), as can be seen in panel (b). Furthermore, panel (a) clearly shows that the dominant structures are belonging to the low-k_y range. Therefore, it can be concluded that, despite the strong reduction of the fast-ion transport correlated with the stabilization of the excitation mechanism for the TAEs in negative magnetic shear regimes, the residual fast-ion heat fluxes are driven by the fast-ion-driven TAEs, consistently with the experimental observations.

It is now important to establish the effect of the reversed q-profile on the TAE excitation mechanism also in the nonlinear regime. To do so, the absolute value of the perturbed distribution function of the fast ion species averaged on the radial and binormal direction $\langle |F^{FD}| \rangle_{k_x, k_y^{1/2}}$ and evaluated at the outer mid-plane is shown in Figure 3.39 for both positive and negative magnetic shear configurations. As already been observed in section 3.3.4, the TAEs are excited through

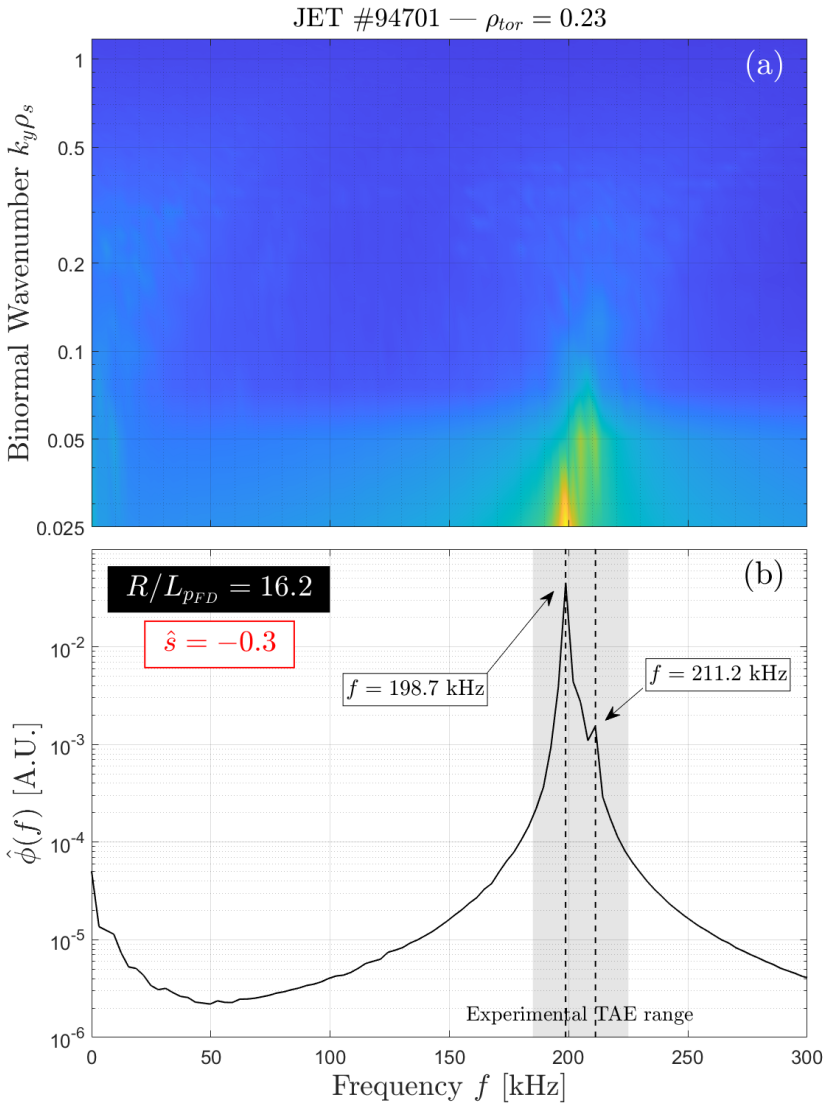

Figure 3.38: *In panel (a), the frequency spectrum computed from the nonlinear* GENE *simulations is shown as a function of the binormal wavenumber for the configuration with negative magnetic shear of the JET pulse #94701 at $\rho_{tor} = 0.23$. In (b), an additional average over the binormal wavenumbers helps in identifying the major peaks of the power spectrum. The gray shaded area represents the TAE experimental range of frequencies.*

a wave-particle interaction with trapped fast ions. Indeed, from the energy exchange it is possible to observe two dominant resonant structures in the trapping region of the velocity phase space (see Figure 3.15). Such structures can also be observed in the perturbed distribution function of the fast ions in panel (a) of Figure 3.39, corroborating the results previously discussed. It is also observed that the distribution function is strongly affected at $\mu = 4.96$, coinciding with the resonance at the $k_y\rho_s = 0.05$ wavelength. Although weaker, the resonant structure at higher μ values corresponding to $k_y\rho_s = 0.025$ wavelength is also visible. On the

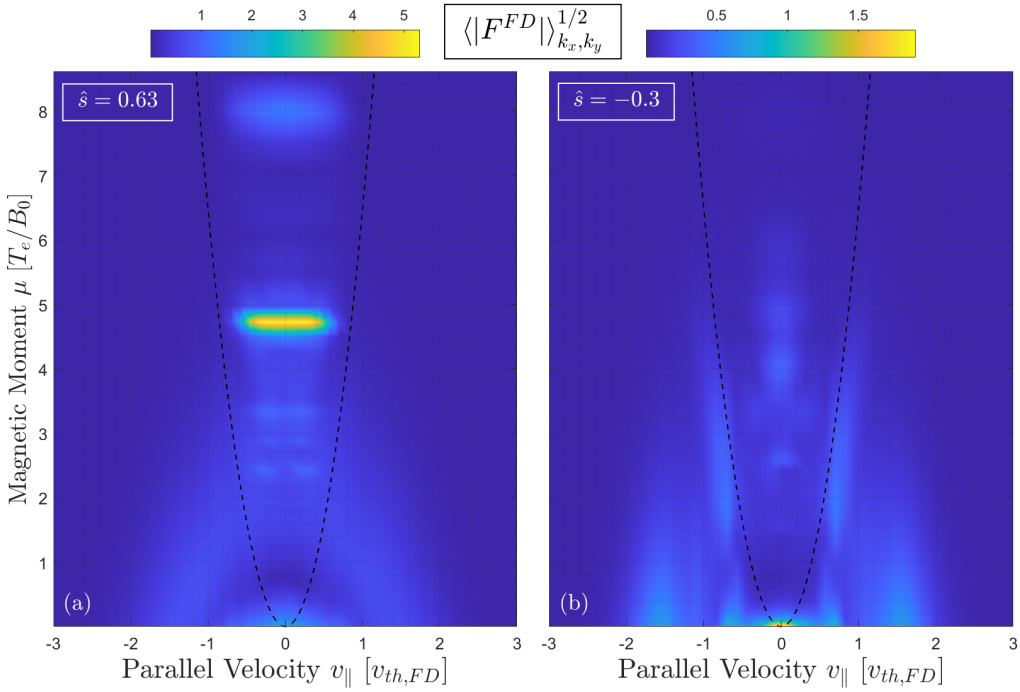

Figure 3.39: *The perturbed distribution of the fast ions is shown in the velocity phase space for the configurations with positive magnetic shear (panel (a)) and negative magnetic shear (panel (b)).*

other hand, when the negative magnetic shear is set on in the simulations, the resonant structures almost disappears, as can be appreciated in panel (b). The main perturbation is now present in the passing particle region, consistently with the linear picture. It should be also noted the strong difference in the perturbation amplitude of F^{FD} between the two magnetic shear configurations, highlighted by the colorbars in Figure 3.39. This is a another clear evidence of the strict relation between the reduction of the fast-ion transport and the stabilizing effect of the reversed magnetic shear on the TAEs.

Moreover, the stabilization of the TAE instability leads also to the additional effect on the amplitude of the magnetic potential fluctuations, which were observed in the case with $R/L_{p_{FD}} = 16.2$ and positive magnetic shear to largely increase the electron electromagnetic transport (see section 3.5 and Figure 3.28). Indeed, the large-amplitude oscillations of the magnetic potential are strongly weakened, and hence the electromagnetic transport is reduced. Eventually, the total electron heat diffusivity is reduced from $\chi^{el} = 3.43\ \mathrm{m}^2/\mathrm{s}$ down to $\chi^{el} = 0.50\ \mathrm{m}^2/\mathrm{s}$ when $\hat{s} = -0.3$, also matching the TRANSP estimation of $\chi^{el} = 0.43\ \mathrm{m}^2/\mathrm{s}$ reported in Figure 3.28.

Chapter 4

Impact of fast ions on different turbulent regimes: TEM

Contents

The reduction of turbulence through the already described complex mechanism, induced by the presence of – relatively high or low energetic – fast ions, is thereby demonstrated for ITG-dominated tokamak plasmas. In addition, the impact of nonlinearly triggered zonal flows has been proved to play a determinant role for such a beneficial effect. However, different turbulent regimes may not benefit from the shearing effect of zonal flows, and so the favorable process may be undermined. This could be the case of the TEM-induced turbulence. Indeed, the dominant saturation mechanism for the TEM instability, although still debated, is proved mainly not to be the zonal flows [153, 154, 155]. This is especially true for temperature-gradient-driven TEM – basically, when $R/L_{T_e} > R/L_{n_e}$ – likewise the case studied in the following.

For this purpose, the core of a JT-60U TEM-dominated hybrid scenario with a large population of NBI fast ions (in the order of 100 keV) [156] is used as test-bed case to analyze the impact of fast ions on an alternative turbulent regime. As the investigating numerical tool, the flux-tube version of the GENE code is again employed. In-depth analyses show that the NBI fast ions in this specific JT-60U hybrid scenario do not affect the thermal transport for a wide range of parameters. The fast ion pressure rather destabilizes large scale instabilities which lead to a severe increase of all the transport channels.

4.1 JT-60U hybrid scenario

As already stated, in the following sections the results of the gyrokinetic analyses of a JT-60U pulse are reported. This particular pulse is the JT-60U pulse #48158, which is embedded in the long-pulse advanced hybrid scenario performed at high β_N. This scenario has been developed to demonstrate the possibility of achieving high-β plasmas without reversed q-profile in the plasma core, which may lead to detrimental MHD instabilities and to poor confinement performance. Thus, the main purpose of this scenario was to obtain a good confinement, possibly leading to peaked profiles in the plasma core and the onset of a transport barrier, with high-β conditions to be exploited in future fusion devices, such as ITER. The long pulse time is provided by the efficient heating of the NBI systems in JT-60U, with both perpendicular and parallel injections. Such a heating scheme effectively generates a substantial population of suprathermal particles in the plasma core, where a flattish q-profile is also present. Thus, the magnetic shear $\hat{s}$ in the plasma core is very low. A detailed overview of the JT-60U developed scenario, and in particular of the pulse here analyzed, can be consulted in Ref. [156].

CRONOS integrated modeling [157] has been carried out for the JT-60U pulse #48158. In Figure 4.1, the radial profiles of some relevant physical parameters are shown. It can be seen that $T_i > T_e$, due to the efficient NBI heating, and that the q-profile is almost flat in the plasma core.

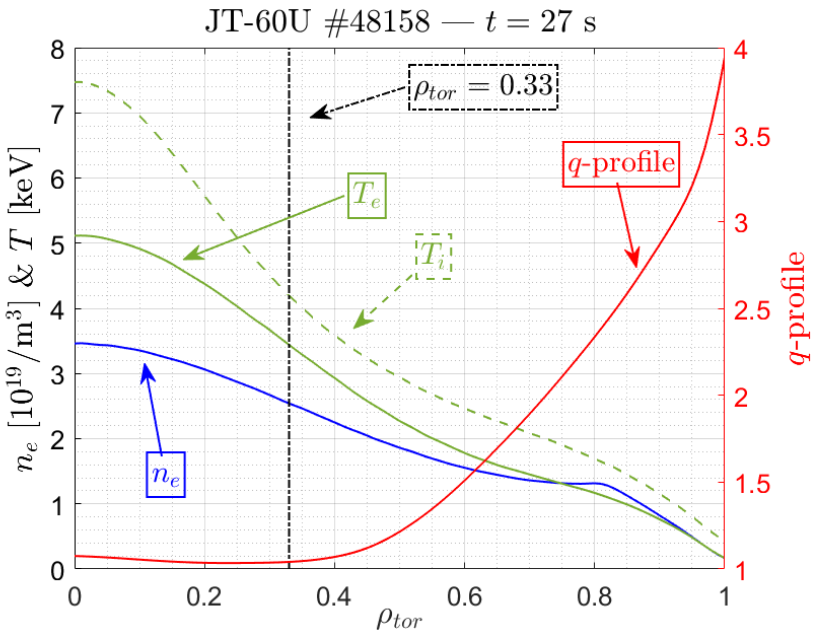

Figure 4.1: *Some relevant radial profiles computed with the CRONOS integrated suite for JT-60U pulse #48158 at $t = 27$ s are plotted. The black vertical dashed-dotted line represents the radial position $\rho_{tor} = 0.33$, at which the local gyrokinetic simulations have been performed.*

4.2 Numerical setup

The following results have been obtained by means of the gyrokinetic GENE code [57], applied in the flux-tube version to the JT-60U pulse #48158 at $\rho_{tor} = 0.33$ and $t = 27.0$ s. The use of the local approach is justified by the small ratio of the Larmor radius over the minor radius of JT-60U $\rho_s/a = \rho_s^*$ for both thermal ($\rho_i^* \approx 1/200$) and fast deuterium ($\rho_{fD}^* \approx 1/100$). Due to the very demanding numerical conditions of low magnetic shear, which may also impair the ballooning representation, additional check on the validity of the flux-tube approximation has been performed and will be presented in the dedicated paragraph 4.3.3 of this section.

The realistic magnetic equilibria, as well as the profiles, have been provided by the integrated modelling simulations with CRONOS [157] based on the experimental outcomes of JT-60U pulse #48158, as already stated. Table 4.1 summarizes the relevant input parameters for the gyrokinetic modeling which have remained fixed throughout all the analyses. Table 4.2 displays, indeed, the previously not specified parameters which are subject of more detailed studies in the following. Moreover, depending on the presence of the fast ions in the simulated system, the magnetic equilibria have been calculated consistently in the HELENA code [158] embedded in CRONOS. Although the complete slowing down fast-ion distribution was available thanks to calculation by means of the OMFC MonteCarlo code [159], the fast-ion distribution has been approximated with an equivalent

Table 4.1: *Employed plasma parameters in* GENE *simulations modeling JT-60U pulse #48158 at* $\rho_{tor} = 0.33$ *and* $t = 27.0$ *s, regardless the different configurations described in the next section 4.5.2. Here,* ϵ *represents the inverse aspect ratio,* n *the species density normalized to the electron density,* $R/L_{n,T}$ *the normalized logarithmic density and temperature gradient, and* $\nu^* \equiv (an_e/4|e|^2 n_i)\nu_{ei}$ *the normalized collision frequency, where* a *is the minor radius,* e *the electron charge and* nu_{ei} *the Hinton-Hazeltine electron-ion collision rate [27]. Eventually, the normalization factors in standard units are also reported, i.e. the on-axis magnetic field strength* B_0*, the local (*$\rho = 0.33$*) electron temperature* T_e *and density* n_e*, and the major radius* R_0*. The reported input parameters are common to all the numerical* GENE *simulation cases. For the remaining input parameters, see Table 4.2*

ϵ	q	$\hat{s}$	T_i/T_e	R/L_{n_e}	R/L_{T_e}
0.30	1.06	0.05	1.20	5.28	7.40
T_{FI}/T_e	ν^*	B_0 [T]	T_e [keV]	n_e [m^{-3}]	R_0 [m]
8.62	8.5×10^{-5}	1.46	3.44	2.54×10^{19}	3.50

Maxwellian in the GENE simulations. Carbon impurities have also been considered throughout the whole analysis. The toroidal rotation and the subsequent external $E \times B$ shearing rate have been neglected because of the relatively low torque induced by NBI in the experiment.

The numerical box discretization is $(n_x, n_y, n_z, n_{v_\parallel}, n_\mu) = (864, 32, 32, 48, 16)$ for a perpendicular box size of $[L_x, L_y] = [812, 125]$ in units of ρ_s. When the suprathermal species has been neglected, the simulation box size in the radial direction has been decreased down to $L_x = 622$, always in units of ρ_s, justified by the smaller thermal ion Larmor radius. However, in this latter case, the number of radial points has been increased up to $n_x = 1152$. These values for the numerical setup have been chosen and validated after extensive convergence tests also in the nonlinear phase. With respect to the numerical analyses explained in chapter 3, the resolution in the perpendicular velocity direction (μ direction) is lower. Besides the linear convergence tests, no signs of nonlinear resonant structures are observed in the velocity space for this JT-60U case. Therefore, stressing that the discretization for the μ direction in GENE is sparser with increasing values of μ, the chosen resolution is thought to be reasonable to capture the possibly occurring wave-particle interactions at low energy. The high-energy interactions should not be expected for this kind of analyses. The employed large values for the box discretization in the radial direction are basically due to the low magnetic shear ($\hat{s} = 0.05$) equilibria achieved in the JT-60U hybrid scenario. Indeed, in the ballooning approximation employed in the flux-tube approach, the value of the magnetic shear is inversely proportional to the distance between consecutive rational surfaces, defined as $\delta r = x/(q\hat{s}n)$, where x is the radial coordinate, q the value of the safety factor profile at the corresponding flux-tube and n the toroidal wavenumber.

4.3 Linear stability studies

In this section the linear analyses performed with the GENE code are detailed. The linear growth rate and mode frequency are intended in normalized c_s/a units and the binormal k_y and radial k_x wavenumbers in ρ_s units, if not otherwise defined.

4.3.1 Analysis of the linear spectrum without fast ions

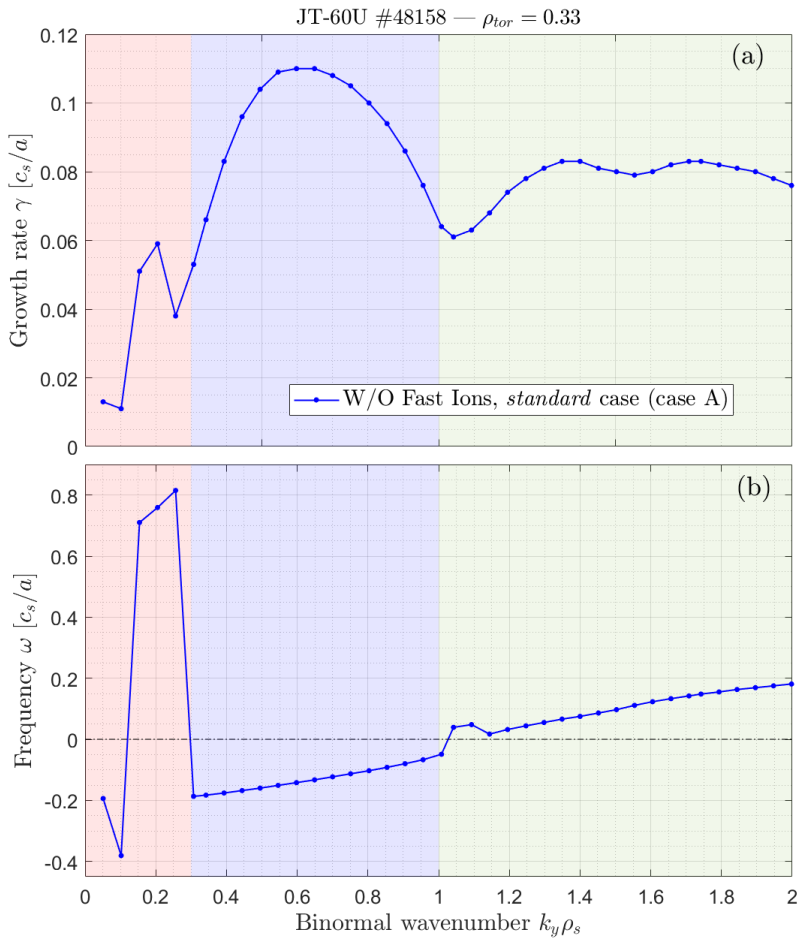

Figure 4.2: *The linear growth rate (b) and the mode frequency (b) computed with the* GENE *code for JT-60U pulse #48158 at* $\rho_{tor} = 0.33$ *without retaining the fast ions are plotted as a function of the binormal wavenumber. Three different regions of the linear spectrum can be identified, dominated by different instabilities and thus highlighted with different colors.*

The linear spectra are displayed in Figure 4.2. A clear peak of the growth rate can be distinguished around $k_y\rho_s = 0.6$, to which corresponds a negative frequency. This means that, in GENE convention, the mode is rotating in the elec-

tron diamagnetic direction. Therefore, due to this latter consideration and to the localization of the peak in the ion-scale region, the instability is identified as TEM [29]. In the following, further analyses prove the identification. This result is consistent with previous numerical studies performed on this particular JT-60U scenario in a different framework [160], where TEMs were found to be the dominant ion-scale instability. Other modes are found unstable in different regions of the spectrum, as it is illustrated in Figure 4.2. For the sake of simplicity, the displayed range of binormal wavenumbers will be subdivide in three different regions:

- $k_y\rho_s < 0.3$: this is the large scale region of the spectrum, and hence it will be often named as low-k_y region in the remainder;
- $0.3 \leq k_y\rho_s \leq 1$: it is the ion-scale region, where TEMs are dominant;
- $k_y\rho_s > 1$: the small scale instabilities arises here, in the large-k_y region.

In Figure 4.2 the three regions are highlighted with shaded areas of different colors. It must be noted that this subdivision is not strict, as for different configurations of the input parameters, which will be investigate in the following, the three regions could span diverse ranges of $k_y\rho_s$. This classification is thereby meant only for the sake of convenience and could be somehow relaxed or modified. Eventually, beyond $k_y\rho_s \approx 5$, where the non-global dominant mode of the third region stabilizes, no signs of unstable electron-driven modes such as ETGs are found up to $k_y\rho_s = 70$.

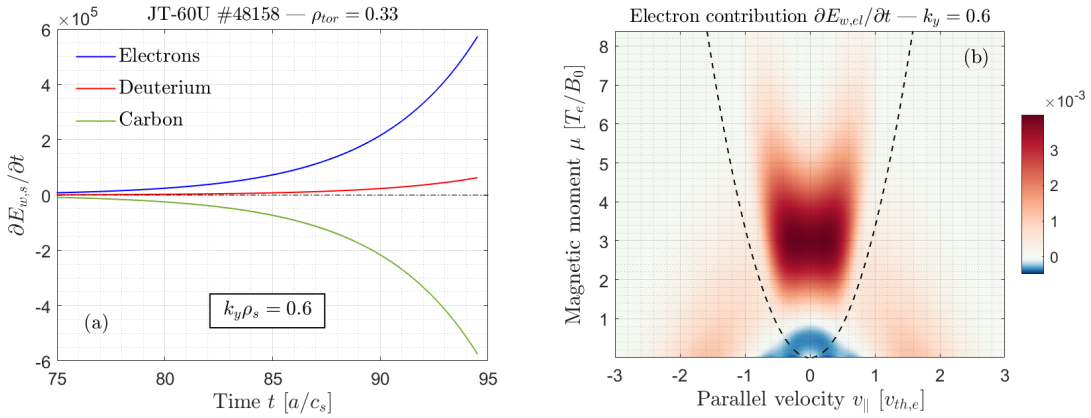

Figure 4.3: *In (a) the time-dependent contribution of each species to the total free energy exchange and in (b) the free energy exchange of the electrons in the velocity phase space are plotted for the binormal wavenumber $k_y\rho_s = 0.6$ in the case without fast ions.*

The broad maximum of the growth rate spectrum displayed in Figure 4.2(a), which peaks in the ion-scale region, has been identified as a TEM instability. Characterizing the unstable modes in the linear spectra is essential for understanding the impact of the fast ions on both the linear stability of the system and on the nonlinearly developed regimes. Thus, a specific analysis on the energy

exchange of each considered species in the system is shown in Figure 4.3. Such an analysis shows basically the decomposition of the species contributions to the total growth rate, as already reported in previous section 3.3.4.

In Figure 4.3(a), the time evolution of the contribution to the perturbed distribution function of each species, flux-surface averaged at $k_y\rho_s = 0.6$, is shown. The subsequent contribution to the total growth rate of the unstable mode can be thereby inferred from this plot. It is clear that the main drive for the mode comes from the electron species. Nonetheless, although with a minor strength than the electrons, deuterium is also giving energy to the instability, whereas the carbon impurity species is strongly damping it. The positive contribution of the deuterium is an indication that the analyzed unstable mode is not a pure TEM, but some contributions also come from the main ion species. Indeed, the damping mechanism of the carbon impurity is likely linked to the detrapping of the electrons, which leads to the reduction of energy reservoir to drive the TEMs. Focusing on the dependence of electron contribution term to the total potential energy rate in the velocity space, it clearly appears that the main response is located within the trapping cone. This is shown in Figure 4.3(b), where the dashed parabola curve delimits the passing and the trapping particle region. This additional evidence clearly proves that the dominant unstable mode of the considered linear system is the TEM, fully consistent with the negative sign of the mode frequency in the linear spectrum of Figure 4.2(b) as already discussed.

Moving to the small scale region of the spectrum, a mode rotating in the ion diamagnetic direction is found unstable up to $k_y\rho_s \approx 3.5$, peaking around $k_y\rho_s = 1.5$. Performing the same analysis on the species contribution to the potential energy balance as above, the main drive of the mode comes from the carbon species. This is shown in Figure 4.4(b). This non-global dominant instability

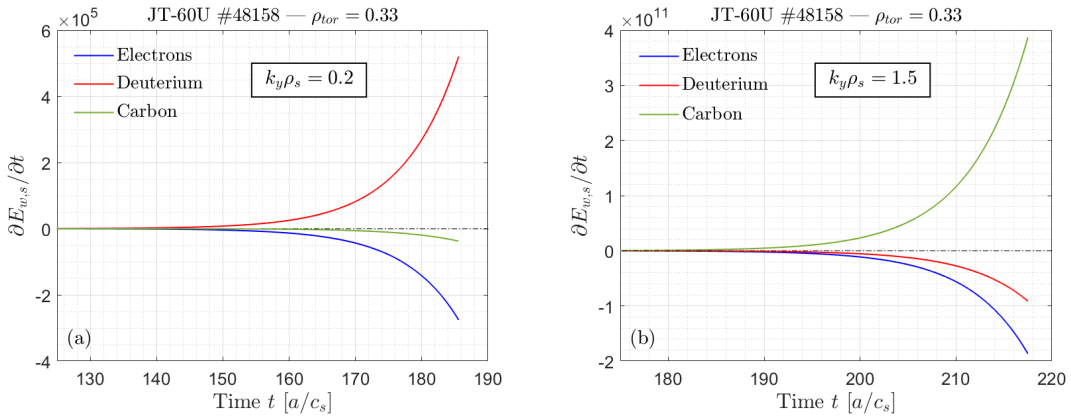

Figure 4.4: *The time-dependent contribution of each species to the total free energy exchange is shown for the binormal wavenumbers $k_y\rho_s = 0.2$ (a) and $k_y\rho_s = 1.5$ (b) in the case without fast ions.*

can be therefore identified as a carbon-driven-ITG (C-ITG), driven unstable by the large temperature gradient. Such an instability can be associated to the sub-

stantial presence of the carbon impurity computed by the CRONOS integrated modeling consistently with the experimental measurements. Generally, the ITG instability driven by the main ion species is excited at lower $k_y\rho_s$ [32]. Nevertheless, being this C-ITG driven by the carbon impurity, whose greater mass with respect to the deuterium leads to a slower normalizing thermal velocity and subsequently to a smaller gyroradius, a shift to higher wavenumbers is measured in this numerical study. Additional analyses corroborate this identification by inspecting the dependence of the growth rate on the β parameter. The well established electromagnetic stabilizing effect on the ITG linear growth rate [161, 162] is found for a wide range of binormal wavenumbers in the C-ITG-dominated region of the spectrum (see Figure 4.5 which illustrates, as an example wavelength, the dependence of the C-ITG mode on the β_e at $k_y\rho_s = 1.5$).

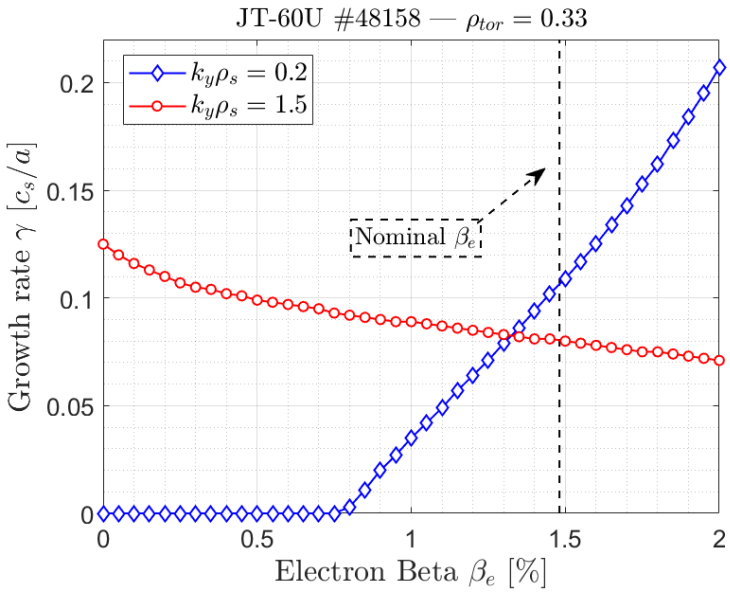

Figure 4.5: *The linear growth rates for the binormal wavenumbers $k_y\rho_s = 0.2$ and $k_y\rho_s = 1.5$ are shown as a function of β_e. The vertical dashed line represents the nominal value of $\beta_e = 1.48\%$.*

The main focus is now moving to the low-k_y region of the spectrum, i.e. for $k_y\rho_s \leq 0.25$ in Figure 4.2. Such a region is of particular relevance in this kind of studies as the direct fast ion effects on the spectra are measured at larger scales with respect to the bulk instabilities, due to the larger thermal velocity of the suprathermal species. In essence, the modes driven by the fast ions are likely measured in this range of wavenumbers. In Figure 4.2, an high-frequency instability is excited in this range. The mode frequency is rotating in the ion diamagnetic direction, hence the mode is likely driven unstable by the thermal ions. It must be stressed that in the simulations illustrated in Figure 4.2 the fast ions are not retained, and therefore the thermal ions are responsible of this high-frequency mode. As it is shown in Figure 4.5, the instability is mainly electromagnetic, as it is stabilized in the electrostatic limit (cf. the blue curve dependence on the β_e pa-

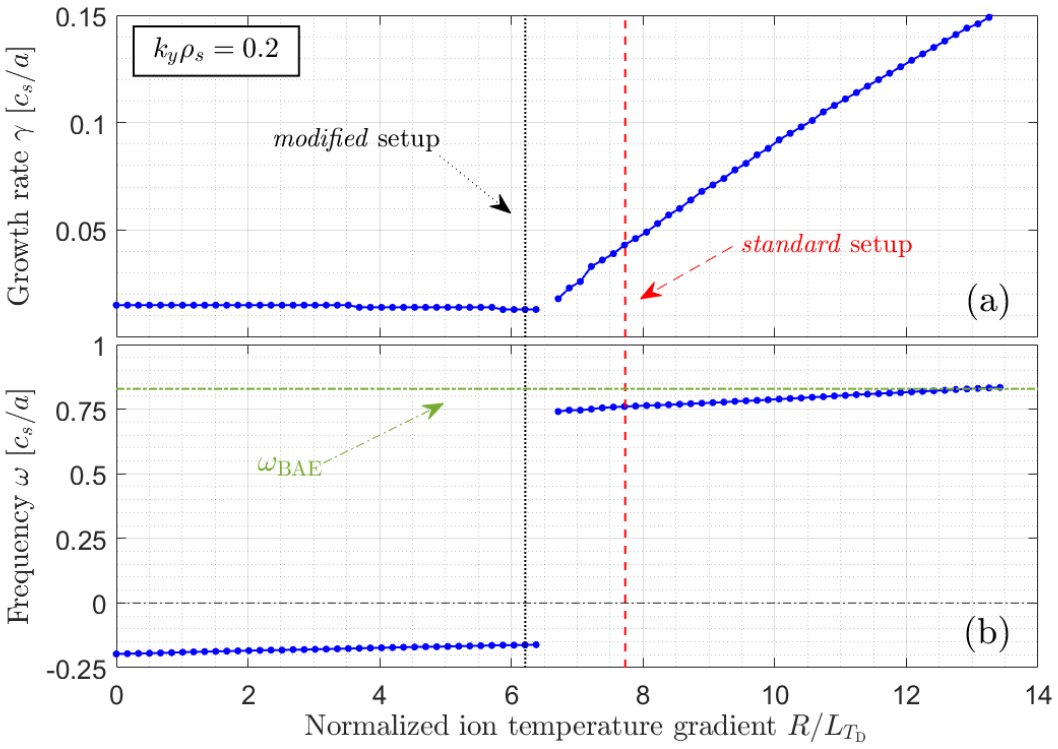

Figure 4.6: *The linear growth rate (a) and mode frequency (b) for the binormal wavenumber $k_y\rho_s = 0.2$ are plotted as a function of the normalized temperature gradient of the thermal ions R/L_{T_i}. The red and black vertical curves represent, respectively, the nominal value of R/L_{T_i} for the standard and modified configurations (an explanation of the difference between these two setups will be given in section 4.4). The horizontal green line in (b) represent the BAE center gap, computed as reported in Relation 4.1.*

rameter). Although the growth rate it is not dominant over the entire spectrum, such a mode may have a strong effect in the nonlinear phase by nonlinear coupling with other unstable modes. Therefore, its identification is essential. Analyzing the various contributions of the species to the high-frequency mode growth rate in Figure 4.4(a), as it has been done for the other regions of the spectrum, reveals that the mode is mainly driven by the bulk ions. For this reason, a scan over the thermal ion temperature gradient, which is the most probable candidate for the reservoir of the free energy for the mode destabilization, is performed for $k_y\rho_s = 0.2$ and reported in Figure 4.6. The vertical dashed line represents the value of the normalized ion temperature gradient $R/L_{T_i} = 7.73$ prescribed by the CRONOS integrated modelling and employed in the numerical analysis shown in Figure 4.2. A transition from an electron-driven to a thermal-ion-driven mode occurs at $R/L_{T_i} \approx 6.5$. Beyond the critical threshold, the growth rate of the instability driven by the bulk ions shows a sharp increase, whereas the mode frequency, which turns to the ion diamagnetic direction, remains almost constant. In Figure 4.6(b), the frequency at the center of the beta-induced gap [52, 163] in the Alfvén continuum is reported in GENE units for comparison, revealing a good

agreement with the computed mode frequency beyond the critical R/L_{T_i} threshold. The frequency of the BAE gap in the Alfvén continuum has been already reported in Relation 1.54, but is further illustrated in the following for the sake of simplicity:

$$\omega_{BAE}/[c_s/a] = \sqrt{\left(\frac{2}{\tau} + \frac{7}{2} + \frac{1}{\tau q^2}\right)} \tag{4.1}$$

with $\tau = T_i/T_e$. It must be stressed that Equation 4.1 is physically correct only in the limit of $k_\parallel = 0$, where the mode frequency of the BAE accumulation point collapses into the one of the Geodesic Acoustic mode (GAM) [55]. A demonstration of $k_\parallel = 0$ for the considered mode is shown in Figure 4.10(d), and will be treated in the following section 4.3.3. The high-frequency mode has been found unstable in the present numerical analysis from the toroidal number $n = 5$ to $n = 11$ (corresponding to the range $0.15 < k_y\rho_s < 0.25$), and therefore the GAM instability is excluded, being destabilized only at $n = 0$. For the reasons presented above, the high-frequency mode destabilized in the low-k_y region has been identified as a shear-Alfvénic ion temperature gradient mode (AITG) [164, 165]. AITG modes are localized electromagnetic instabilities which are driven at low toroidal numbers by the temperature gradient of the bulk ions, and have been already observed in global electromagnetic simulations [166] as well as in recent experiments performed at the Chinese tokamak HL-2A [167]. AITG modes can be destabilized when the plasma is close to the ideal MHD threshold or even below, and for this reason it is found to connect the unstable branches of the KBM [168] and of the BAE [48]. The conventional wisdom is to consider indiscriminately the AITG and the KBM instabilities, nonetheless a clear distinction can be made on the basis of the fundamental wave-particle interactions. Whereas the KBMs are excited through a fluid destabilizing mechanism, the AITG modes present a kinetic resonant interaction as destabilizing mechanism mainly driven by the thermal ion temperature gradient [43].

The linear stability of the AITG modes is strongly affected by the magnetic shear and by the total pressure gradient. This is shown in the aforementioned experiments [167], where AITGs are found unstable at low-n in weak magnetic shear and low pressure gradient radial locations of the considered plasma. Numerical computations show that the AITG modes are already destabilized for $\alpha \approx 0.1$, where $\alpha = -R_0 q^2 \mathrm{d}\beta/\mathrm{d}r$, in the HL-2A plasma [167], for a narrow range of magnetic shear values around zero. This range is further broadened when larger radial pressure gradients are considered, also implying that AITGs are destabilized easily at larger α as the computed growth rates increase with the increasing pressure gradient. This latter observation is consistent with previous theoretical studies [165]. The present JT-60U Hybrid scenario, at the considered radial location of $\rho_{tor} = 0.33$, has a flat q-profile with $\hat{s} = 0.05$, within the range studied in Ref. [167], whereas the parameter $\alpha = 0.9$ (for the configuration illustrated in Figure 4.2). An additional evidence of such an identification is given by the eigenmode structure of the electrostatic potential for the unstable AITG modes

from the numerical calculations of the AITG/KBM dispersion relation (e.g., Figure 7 of Ref. [167]). The eigenmode structure is indeed largely extended along the magnetic field lines, which is consistent with the structure computed by the GENE code in the present study and reported in Figure 4.10(a).

4.3.2 Analysis of the linear spectrum with fast ions

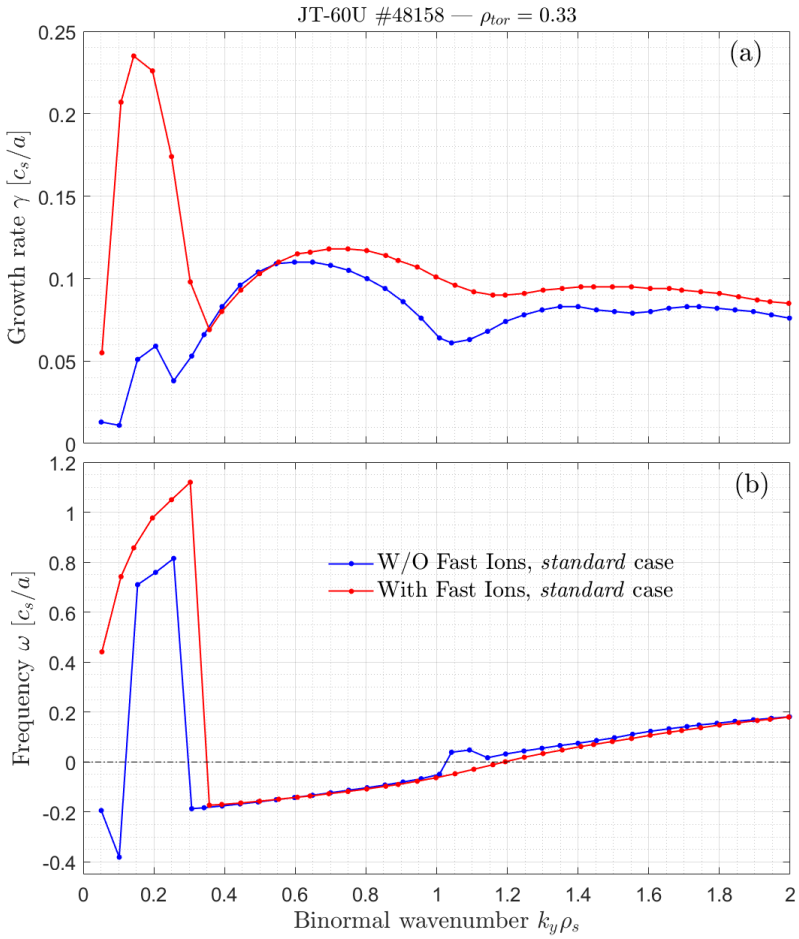

Figure 4.7: *The linear growth rate (b) and the mode frequency (b) computed with the* GENE *code for JT-60U pulse #48158 at* $\rho_{tor} = 0.33$ *with (red) and without (blue) fast ions are plotted as a function of the binormal wavenumber.*

The suprathermal ions introduced as a kinetic species in the simulations represent the fast deuterium introduced by the multiple NBI systems in the considered JT-60U pulse. As it has already been said, the fast ion distribution function has been calculated with the OMFC Monte Carlo code [159], and then approximated in the GENE code by an equivalent Maxwellian to the slowing down distribution. Moreover, when the fast ions have been retained in the system, the magnetic equilibrium has been recalculated considering also the fast ion pressure.

The spectrum partition presented above still holds in the case with fast ions, and therefore it will be employed also in the following for the sake of convenience. Here, we will analyze the low-k_y region, since the main effects of the steep fast ion pressure gradient are expected to take place at this spatial scale, leaving the description of the fast-ion impact on the linear spectrum for a following section (cf. 4.3.4). As shown in Figure 4.7, the growth rate spectrum is strongly modified when fast ions are retained in the narrow region $k_y\rho_s < 0.3$. The global-dominant mode is now peaking at $k_y\rho_s = 0.15$, with the frequency rotating in the ion diamagnetic direction and roughly spanning the same range of the identified AITG modes in the case without fast ions. The mode, similarly to the AITG modes, is destabilized only when the fluctuations of the magnetic potential are taken into account, as shown in Figure 4.9(a). In the electrostatic limit ($\beta_e = 0$), the mode is indeed completely stabilized. In Figure 4.8(a), the

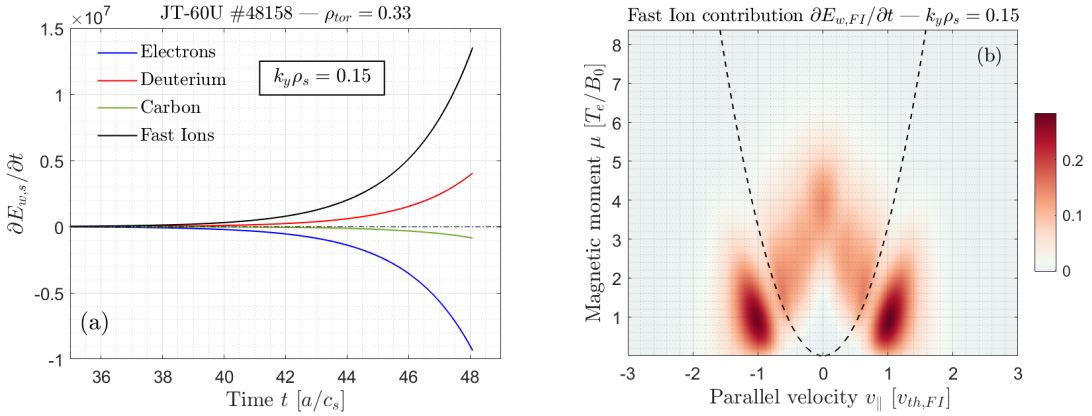

Figure 4.8: *In (a) the time-dependent contribution of each species to the total free energy exchange and in (b) the free energy exchange of the fast ions in the velocity phase space are plotted for the binormal wavenumber $k_y\rho_s = 0.15$ in the case with including fast ions.*

contributions of the various species to the time derivative of the potential energy are illustrated. It is thus clear that the fast ions are driving unstable the mode at $k_y\rho_s = 0.15$, likely due to the free energy contained in the large fast ion pressure gradient, leading to a strong increase of the growth rate with respect to the case without fast ions. It can still be seen a positive contribution coming from the bulk ions, whereas the electrons and the carbon impurity are damping the instability. Inspecting the contributions of the only fast ions in the velocity space in Figure 4.8(b), it can be seen that it mainly comes from passing particles, as expected due to the tangential injection of fast deuterium through NBI in JT-60U pulse #48158. Although the response partly comes from the trapped fast ions, the potential energy exchanged has been integrated in the passing and trapped domains of Figure 4.8(b), verifying that almost 80% of the driving contribution is related to the passing fast ions. The mode frequency remains very close to the BAE gap in the Alfvén continuum especially for the wavenumbers where the mode peaks, as shown in Figure 4.7(b). Yet, a transition from the temperature gradient of the

thermal ions to the fast ion pressure gradient instability driver occurs. For these reasons, such a fast-ion mode has been identified as fast-ion-pressure-gradient-driven BAE (FI-BAE), and it is referred in this way for the remainder of the study. As an additional demonstration of the fast-ion pressure gradient as the main instability driver, Figure 4.9(b) is shown. The strong dependence of the FI-BAE growth rate on the normalized fast-ion temperature gradient $R/L_{T_{FI}}$ is thus illustrated. Furthermore, although not shown here, increasing the density gradient of the fast ions leads to an enhancement of the FI-BAE destabilization. Therefore, it is concluded that the fast ion pressure gradient is the main driver of the FI-BAE instability in these numerical analyses. An essential ingredient for the destabilization of FI-BAE, as hinted previously, is a significant strength of the magnetic fluctuations, represented by the β_e parameter in Figure 4.9(a). It is shown indeed that for the half of the nominal value of β_e (0.74%, brown curve), the growth rate of FI-BAE is extremely low. The critical threshold for the FI-BAE destabilization (with the nominal fast-ion characteristics) has been found around $\beta_e \approx 0.6\%$.

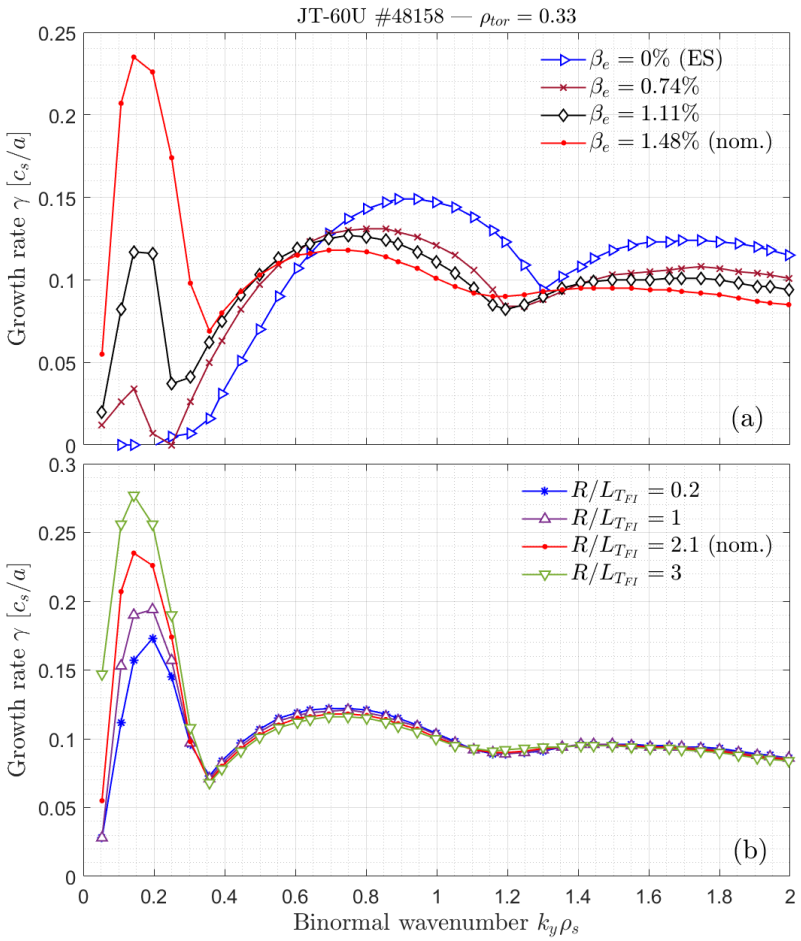

Figure 4.9: *The linear growth rate computed with the* GENE *code for JT-60U pulse #48158 at $\rho_{tor} = 0.33$ with fast ions is plotted as a function of the binormal wavenumber for various values of β_e (a) and $R/L_{T_{FI}}$ (b).*

As a final remark on the low-k_y region, however, it must be noted that for a fully correct and quantitative comparison of the AITG and FI-BAE modes with experimental measurements, a global treatment should be employed. Indeed, in the present GENE local analyses, the q-profile at $\rho_{tor} = 0.33$ is $q = 1.06$, whereas in the experiments performed at HL-2A, where the AITG modes were measured, the flux surface $q = 1$ was present close to the radial localization of this instability. Linear global analyses, performed with the LIGKA code [169] by Philipp Lauber in order to validate the results obtained with the local version of GENE, were inconclusive: for $q = 1.06$ at $\rho_{tor} = 0.33$ the accumulation point of the BAE gap in the Alfvén continuum was not matching the frequency computed by linear simulations with the GENE code.

4.3.3 Validity of the flux-tube approximation

Before analyzing the impact of the suprathermal ions on the linear stability of the system, it is crucial to determine the validity and the full consistency of the local approach employed in this study. To do so, the structure of the eigenmodes at the different regions of the linear spectrum is studied carefully both in the ballooning and in the real space (for the difference between ballooning and real space refer to section 2.1). For the sake of simplicity, only one eigenmode for each of the three regions described in section 4.3.1 is studied, since the analysis of the remaining wavevectors would lead to the same conclusions. Hence in Figure 4.10, the electrostatic potential of the wavenumbers $k_y\rho_s = 0.15$ (AITG/FI-BAE), $k_y\rho_s = 0.6$ (TEM) and $k_y\rho_s = 1.5$ (C-ITG) is plotted against the ballooning angle χ in the first row (panels (a)-(c)) and against the radial coordinate $n[q_0 - q(r)]$ in real space (panels (d)-(f)).

The first column of Figure 4.10 refers to the low-k_y region of the spectrum, where the AITG modes and the FI-BAEs, respectively in the cases without and with considering fast ions, are dominant. Although it is not shown, the AITG and FI-BAE have very similar structures of the electrostatic potential, and can be thereby analyzed together. In the specific instance of Figures 4.10(a) and (d), the structures correspond to the case with fast ions, and therefore represents the structures of the FI-BAE found unstable in the GENE linear analyses. The eigenmode is extended in the ballooning angle χ, whereas after being Fourier-transformed in the real space presents a radially localized structure. The dominant peak of the eigenmode is sitting at the rational surface $n[q_0 - q(r)] = 0$, whereas only relatively small peaks are measured at the adjacent rational surfaces . For this reason, the AITG/FI-BAE modes can be considered with the parallel wavenumber $k_\parallel = nq - m = 0$, and more importantly the employed local approximation is thereby valid for this instability.

For what concerns the TEM-dominated region of the spectrum, the structure of ϕ is typical of TEMs: the amplitude of the central k_x mode is comparable to the contiguous sidebands in the ballooning space, as it is shown in panel (b) of Figure 4.10. This structure reflects in the real space to a coupling between the neighboring rational surfaces, as is visible in panel (e), since the dominant peaks of ϕ are

localized at $n[q_0 - q(r)] = \pm 0.5$. However, the validity of the local approximation for the computed TEMs is ensured by the small value of the ratio between the sideband and the dominant peaks (in this case $< 20\%$), as well as by the large values of the considered toroidal wavenumbers. As a further consideration, sitting the peaks in the middle of rational surfaces, the parallel wavenumbers of such TEMs are finite.

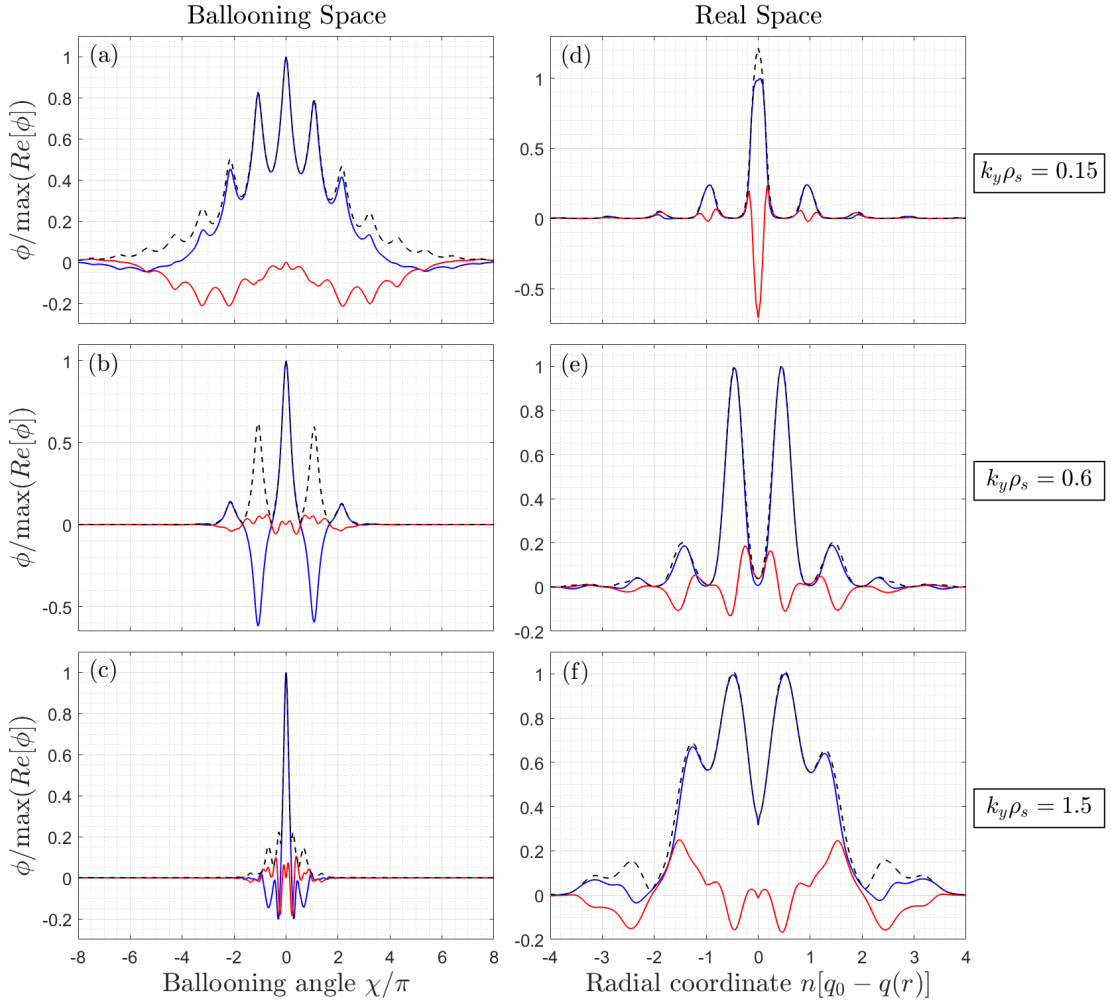

Figure 4.10: *The normalized electrostatic potential eigenmode structures of the main instabilities found in* GENE *linear stability analyses are plotted in the ballooning (left column) and in the real (right column) spaces.*

Similarly, and even more obviously, to what occurs for the TEM-dominated region, the local approximation for the unstable modes at the scale $k_y\rho_s > 1.3$ is inherently valid. In fact, the translational invariance assumption of having a negligible variation of the plasma parameters and the safety factor between consecutive rational surfaces, which reflects to have $n \gg 1$, is fulfilled. For this reason, inspecting the structures of the electrostatic potential in both the ballooning and

real spaces for the unstable C-ITG is not strictly necessary. However, they are shown in Figure 4.10 for completeness.

This reported analysis ensures that the local approximation employed in this study is valid. Nevertheless, such a consideration only guarantees that the unstable modes computed by the GENE code are consistent with the assumptions of the flux-tube approach, but it does not mean that the present study is absolutely sufficient for establishing the quantitative comparison with the reconstructed experimental data of the JT-60U Hybrid scenario [156]. For such a comparison a global approach would be desirable, as it has already been said above.

4.3.4 Linear effects of fast ions on TEM

The main focus of this paragraph is to analyze the effects of the suprathermal species on the TEMs in the JT-60U hybrid scenario by comparing the TEM characteristics in the cases with and without fast ions. If one excludes the low-k_y region, in which as it has already described the growth rate of the unstable modes is highly enhanced, the effect of the fast ions on the remaining wavenumbers is unimportant. The TEM growth rate, as well as for the C-ITG, is mildly increased, whereas the peak of the TEM region is slightly shifted to larger wavenumbers, from $k_y\rho_s = 0.6$ to 0.75. The latter change is likely due to the modification of the thermal deuterium input parameters in order to accommodate for the fast ions and still fulfill the quasi-neutrality relation. Indeed, the introduction of the fast ions in the system requires the modification of the density and density gradient of a thermal ion species. It has been decided to modify the thermal deuterium parameters, since higher values of uncertainties are present on this measurements in the plasma core. As it has already been underlined in Figure 4.3(a), the contribution of the thermal deuterium to the TEM growth rate is small but not null. Such a not-pure TEM seems to be stabilized by the thermal deuterium density and density gradient, similarly to what occurs for the ITG instability. Therefore, the decreasing of those two parameters when moving to the configuration with fast ions is likely responsible for the mild changes in the TEM region of Figure 4.7. This slight increasing and shifting of TEM peak is obtained also in the electrostatic limit. Additionally, the contribution of the suprathermal species to the derivative of the potential energy at $k_y\rho_s = 0.6$, where the TEM dominates, is negligible as it is illustrated in Figure 4.11(a). As a further piece of evidence, modifying the fast ion temperature gradient $R/L_{T_{FI}}$ does not lead to any significant change in the TEM growth rate. This is shown in Figure 4.9(b), in which the TEM growth rate is only mildly affected by the $R/L_{T_{FI}}$ spanning a wide range of values.

Negligible impact of the different magnetic equilibria is measured when moving from the case without fast ions to the one with fast ions. This latter consideration has been verified by performing a linear simulation including the suprathermal species but using the magnetic equilibrium calculated with only the thermal pressure and comparing the outcomes with the red curve in Figure 4.7. Such a negligible difference may be expected as in the deep core at $\rho_{tor} = 0.33$, where the GENE analyses are carried out, the impact of the suprathermal species, although

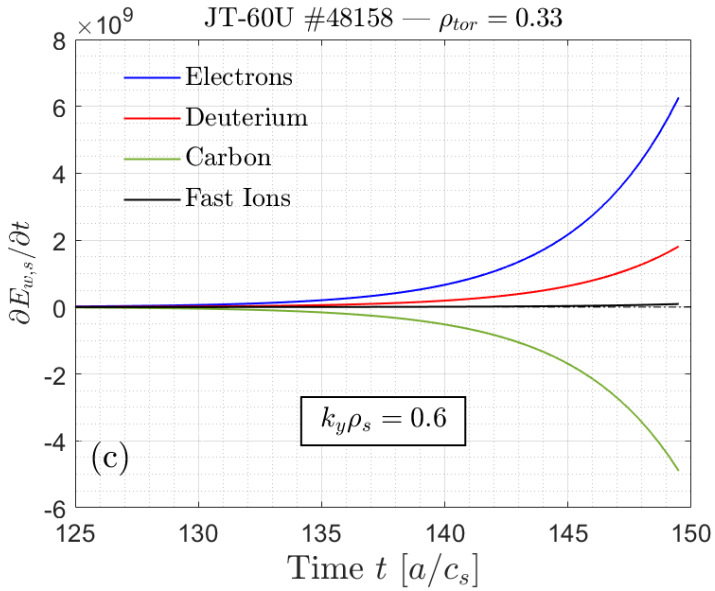

Figure 4.11: *The time-dependent contribution of each species to the total free energy exchange is shown for the binormal wavenumber $k_y\rho_s = 0.6$ in the case with fast ions.*

strongly populated, is not significant.

The absence of fast ion effect on TEMs is in counter-trend with previous results about the fast ion linear stabilization of ITG in JET hybrid scenarios [76, 77]. It has been shown indeed that the linear growth rate of ITG was significantly reduced when the suprathermal species was retained in the simulations. Extensive analyses demonstrated that such an ITG growth rate reduction is due to a wave-particle resonance between the fast-ion magnetic drift frequency and the ITG linear frequency in a favorable region of the phase space [72]. This stabilization is not present in the reported study of the fast-ion impact on TEMs. Yet, such an absence of the fast-ion effect on TEM is still elusive, and deeper analyses are required. Moreover, the lack of TEM stabilization due to fast ions can also be related to the fast-ion parameter configurations employed in this study. Indeed, it has been demonstrated that the linear resonant effect between the fast-ion magnetic frequency and the ITG linear eigenfrequency occurs more positively when $R/L_{T_{FI}} \gg R/L_{n_{FI}}$ [72, 73, 75]. This condition is usually obtained for ICRH plasmas, whereas the here studied JT-60U hybrid scenario is mainly heated through NBI [156]. Nevertheless, as already been said, the fast ion pressure gradient has been largely scanned in Figure 4.9(b), but only a mild impact is measured. So, it is not expected that the TEM growth rate would be strongly decreased also for an ICRH-like fast-ion parametrization. In this framework, other studies have been performed by investigating analytically the impact of the fast ions on the density-gradient-driven collisionless TEM instability [170]. It has been shown that the collisionless TEM can be further destabilized in the presence of fast ions due to the downshift of the electron diamagnetic frequency originated by flattening of the thermal ion gradients. The results here presented may be also related

to such an effect, but in-depth comparative analyses are needed.

4.4 Preliminary nonlinear analyses: Need for setup modification

This section will be dedicated to study the complex regime of the system already presented by means of nonlinear simulations with the GENE code. As it has already been said, studying the nonlinear phase is crucial in order to assess the complex and turbulent behavior of the considered plasma and thereby understand the fine structures of the interaction between fast ions and microturbulence. In the following, the preliminary analyses by extending the linear setup described in the previous section 4.3 to the nonlinear regime will be examined. As it will be clear, in order to disentangle the effects of the low-k_y instabilities on the transport, the numerical input configuration requires to be modified. Tuning the input parameters within the typical 20% of experimental error bars for the bulk plasma characteristics reveals sufficient to the stabilization of the AITG modes, whereas a more intense variation is needed for the FI-BAE driven by the suprathermal component. As it will be reported, such a stabilization is required because no high frequency modes have been experimentally detected in the core of the JT-60U pulse #48158. Indeed, the low-frequency mode measured by magnetic coils in this pulse [156] have been identified as an energetic particle driven wall mode (EWM) with fishbone-like characteristics [171], but it has been radially localized closer to the $q = 2$ surface and so outer than the $\rho_{tor} = 0.33$ surface studied in the present context. Eventually, the linear stabilization of both low-k_y modes allows to study the impact of the fast ions on the dominant TEM instability in a validating framework for the JT-60U hybrid scenario.

4.4.1 Effects of high-frequency instability on the heat transport

The first nonlinear simulations performed using the setup without fast ions (also employed, for instance, to obtain the linear spectrum of Figure 4.2) resulted in transport regimes extremely far from the experimental outcomes. Indeed, the GENE computed heat diffusivity for the thermal ions is more than one order of magnitude higher than what reported in Ref. [156], namely $\chi^{\mathrm{D}} \approx 1\ \mathrm{m}^2/\mathrm{s}$ at $\rho_{tor} = 0.33$ for $t = 27$ s. Even worse results are obtained when fast ions are retained in the system: the simulations could not reach the quasi-stationary phase, since the heat transport exploded up to levels unacceptably high during the overshoot phase, and so it was stopped to save computational resources.

As a first tentative, the fast ion pressure gradient was significantly lowered down to only 20% and 37% of the nominal value computed by the OMFC Monte-Carlo code [159]. The strong reduction of the steepness of the fast ion pressure profile can be appreciated in Figure 4.12. It is to be noted that the reduction of the fast ion pressure gradient has already been found necessary in similar studies, for instance in Refs. [76, 77], in order to stabilize the fast-ion-driven instabilities and

reconcile the experimental power balances with the gyrokinetic modeling outcomes. After reducing the fast ion pressure gradient, a scan over the system total

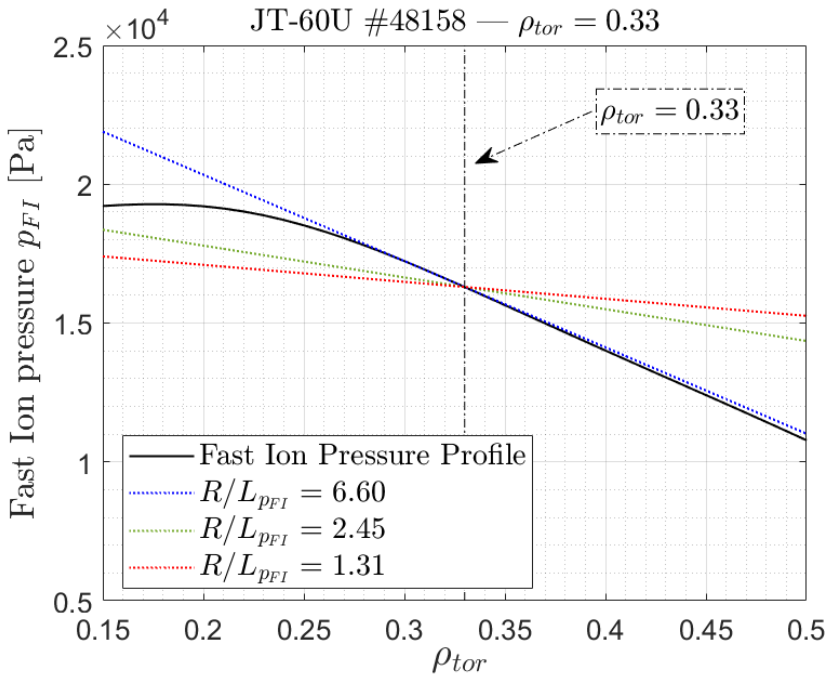

Figure 4.12: *The local gradients at $\rho_{tor} = .33$ are shown for the various numerical setups analyzed in this study.*

pressure, represented by the β_e parameter, has been performed for both configurations. As it has already been pointed out more in detail in the previous chapter 2, the reconstruction of the fast ion distribution function, and so the radial profiles, are carried out by means of numerical calculations based on experimental measurements. In this case, the OMFC code does not take into account any fast-ion transport due to both thermal- and fast-ion-driven turbulence. For this reason, the computed distribution function may be overestimated – and usually is. Hence, the fast-ion parametrization for the gyrokinetic analyses is generally affected by a much larger uncertainty with respect to the thermal part of the plasma, and thereby allows for more room to tuning it. This latter consideration, again, explains the reason of the large setup modification that has been operated.

The linear results are illustrated in Figure 4.13(a), where the low-k_y wavevectors for the two configurations are compared to the nominal fast-ion pressure gradient case. The linear β-scan reveals that the growth rate increases beyond the threshold value $\beta_e \approx 1.4\%$ for the two reduced configurations $R/L_{p_{FI}} = 1.31$ and 2.45, and at the nominal value of $\beta_e = 1.48\%$ (represented by the black vertical dashed line) the FI-BAEs are unstable. It must be noted that the threshold value $\beta_e = 1.3\%$ is actually within the experimental uncertainty of the electron β, which is assumed to be $\pm 20\%$.

Differently, the case with the nominal fast ion pressure gradient (the black curves in Figure 4.13(a)) presents the destabilization of the FI-BAE instability al-

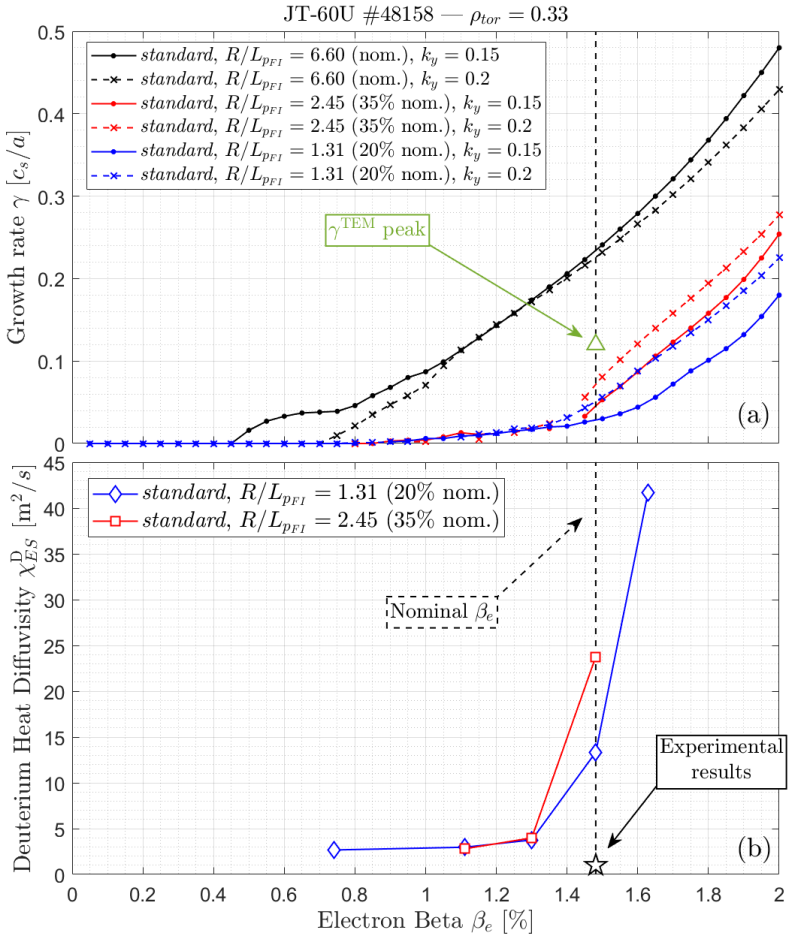

Figure 4.13: *In panel (a), the linear growth rates for two different low-k_y wavenumbers, $k_y\rho_s = 0.15$ and $k_y\rho_s = 0.2$, at three different values of the fast ion pressure gradient are plotted as a function of the electron beta. The green triangle represents the peak of the TEMs at the nominal β_e for comparison. In panel (b), the deuterium electrostatic heat diffusivity is plotted in a nonlinear scan over the β_e for two different configurations of the fast ions pressure gradient. The black star symbol represents the thermal ion diffusivity from experimental power balances [156] for comparison.*

ready at $\beta_e = 0.75\%$, reaching very intense growth rates at the nominal value of β_e. For this reason, the performed nonlinear simulations with the nominal setup could not even reach the saturated phase, as the FI-BAE strongly dominates the overall turbulent transport leading to measureless levels of heat fluxes. For what concerns the cases with reduced fast ion pressure gradient, the β-scan reveals that at the nominal value of β_e the FI-BAEs are unstable, but not dominant over the TEM instability growth rate. For comparison, the peak of the TEM spectrum region that can be seen in Figure 4.7(a), settled around $\gamma^{\mathrm{TEM}} \approx 0.12\ c_s/a$, has been reported in Figure 4.13(a) as a green triangle. Nevertheless, as it has already been detailed in the literature (for instance see Refs. [124, 76, 77, 90]), a linearly sub-

dominant high-frequency fast-ion driven mode is likely to dominate the whole nonlinear spectrum by coupling to small scales modes. Indeed, as can be seen in panel (b) of Figure 4.13, the electrostatic heat diffusivity of the thermal deuterium χ^{D}_{ES} is strongly increased also at the nominal β_e value, although the FI-BAE is not the dominant instability. Such an increase, consistently with the linear results, is essentially due to the nonlinear synergy between the dominant TEM and the FI-BAE instabilities. As a matter of fact, the stiffness of the transport in the β-scan is enhanced when the fast-ion pressure gradient is increased, underlying the important role of the FI-BAEs in driving the transport. As another piece of evidence, the diffusivities at $\beta_e = 1.11\%$ for the two fast-ion pressure gradient configurations are very similar. This demonstrates that, since the TEM instabilities are shown not be dependent on the $R/L_{T_{FI}}$ in this system (see Figure 4.9(b)), when the FI-BAEs are stable before the threshold the transport is not affected by the fast ion presence. Furthermore, an additional analysis on the heat flux spectra has been performed for the case with $R/L_{p_{FI}} = 1.31$ and the results are illustrated in Figure 4.14. It is thus shown that with increasing β_e – the parameter representative of the total plasma pressure – the deuterium heat flux spectra shift toward the low-k_y region ($k_y\rho_s \sim 0.2$) where the FI-BAE are linearly destabilized. A very similar behaviour is observed also for the electrostatic heat flux of the electrons (for the sake of simplicity the figure is not reported).

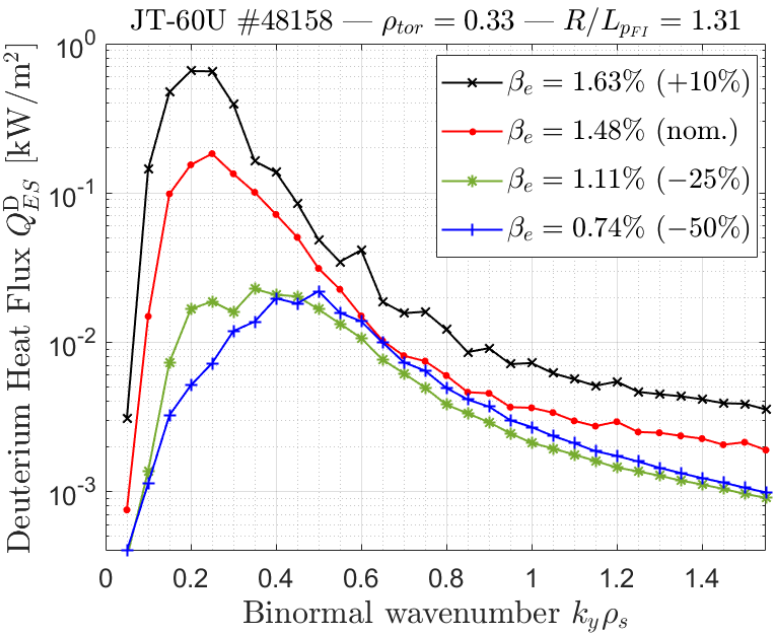

Figure 4.14: *The electrostatic heat flux spectra of the thermal ions as a function of the binormal wavenumbers are shown in a scan over β_e for the standard configuration with $R/L_{p_{FI}} = 1.31$.*

In Figure 4.13(b), only the electrostatic heat diffusivities are reported, as the electromagnetic counterparts are almost irrelevant before the β_e threshold and

small after for the thermal ion transport. This is understandable as the electromagnetic transport is only driven by the FI-BAE, since the TEM instability, which is the dominant instability for $\beta_e < 1.3\%$, is basically electrostatic. In this context, it must be noted that the electromagnetic electron transport reveals to be negligible with respect to the electrostatic transport also at $\beta_e = 1.63\%$, when the FI-BAEs are destabilized.

Therefore, it is clear that the strong increase of the thermal ion heat fluxes is essentially due to the destabilization of the FI-BAE modes, which carry the most part of the overall bulk transport although not dominant in the linear regime. Such a destabilization and nonlinearly synergy between the unstable modes are further enhanced by the electromagnetic effects, as well as by the fast-ion pressure gradient, which has been demonstrated to be the main FI-BAE driver.

It could be also interesting to look at the effects of the high-frequency FI-BAE instability on the transport of the suprathermal and carbon impurity species. This is done, consistently with the previous analyses, by measuring the heat diffusivities of both species in the scan over the β_e parameter for both fast-ion configurations, i.e. with $R/L_{p_{FI}} = 1.31$ and 2.45. The results are reported in Figure 4.15. In panel (a), the electrostatic (ES) and electromagnetic (EM) fast ion diffusivity shows the destabilization of the FI-BAE for the case with $R/L_{p_{FI}} = 2.45$ already at $\beta_e = 1.3\%$. This is demonstrated by the increase of the heat diffusivities, with the transport being mainly electrostatic. It must be noted that χ_{ES}^{FI} reaches very large values with respect to the thermal transport at the nominal β_e ($\chi_{ES}^{FI} = 150.7$ m^2/s vs. $\chi_{ES}^{\mathrm{D}} = 23.8\,\mathrm{m}^2/\mathrm{s}$ at $\beta_e = 1.48\%$). As already stated before, the electromagnetic heat flux is strongly enhanced when the β_e is increased, which is consistent with the enhancement of the magnetic potential fluctuation amplitude. More complex is the behavior for the setup with $R/L_{p_{FI}} = 1.31$. The electrostatic diffusivity presents a well at the nominal β_e, which seems to suggest an improvement of the fast ion confinement. However, the electromagnetic transport is indeed increased approaching the nominal β_e. This complex behaviour can be better analyzed by checking the fast ion heat flux spectra. In Figure 4.16, the electrostatic heat fluxes for the case with $R/L_{p_{FI}} = 1.31$ are shown in the binormal wavenumber domain. It can be observed that when the FI-BAEs are destabilized, i.e. for $\beta_e \geq 1.48\%$, the low-k_y region presents negative values for the heat flux, meaning that an inward fast-ion electrostatic transport is ongoing. At the nominal β_e, such inward transport dominates over the small residual outward transport, whereas for $\beta_e = 1.63\%$ the outward electrostatic heat fluxes mainly developing at $k_y\rho_s = 0.25$ is much larger and therefore strongly contributes to the total transport. Such a complex behaviour is still elusive, but it must be related to particular nonlinear mode-mode coupling occurring at the onset of the FI-BAE destabilization.

For what concerns the carbon impurity transport, in panel (b) of Figure 4.15 the electrostatic heat diffusivities are plotted. The electromagnetic transport for carbon is always negligible with respect to the electrostatic counterpart. The trend shown is interesting, considering that the carbon transport is mainly induced by the C-ITG instability, which peaks around $k_y\rho_s = 1.5$ in the linear spec-

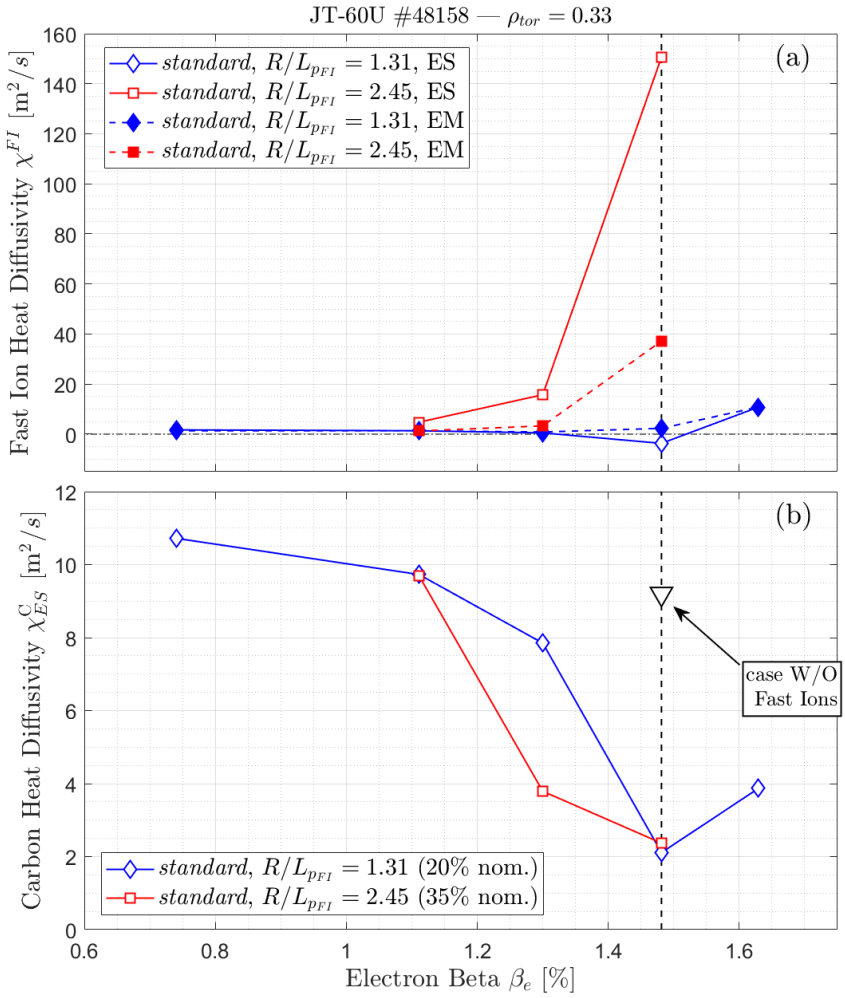

Figure 4.15: *In panel (a), the electrostatic and electromagnetic fast ion heat diffusivities are plotted as a function of β_e for two different configurations of the fast-ion pressure gradient in the standard setup. In panel (b), indeed, the electrostatic carbon diffusivities are reported for the same configurations. The black symbol represents the electrostatic carbon heat diffusivity for the case without including fast ions.*

trum, but is likely subdominant for a large range of wavelengths. Indeed, although the nonlinear simulation box extends only up to $k_y\rho_s = 1.55$ in the binormal direction, and therefore cuts out a considerable part of the C-ITG-dominated spectrum, the shape of the growth rate spectrum of such modes suggests that C-ITG is also unstable at lower k_y (see for instance Figure 4.7(a)). Therefore, consistently with the well-known ITG stabilization by increasing the total pressure of the system [12], the carbon diffusivity is diminished by increasing β_e. It is also worthy to note that a clear reduction of the transport is measured at the nominal β_e when fast ions are introduced in the simulation setup with respect to the case without including them (black triangle in panel (b) of Figure 4.15). It is hard to relate such a reduction to a fast-ion effect only on the magnetic geometry. A more

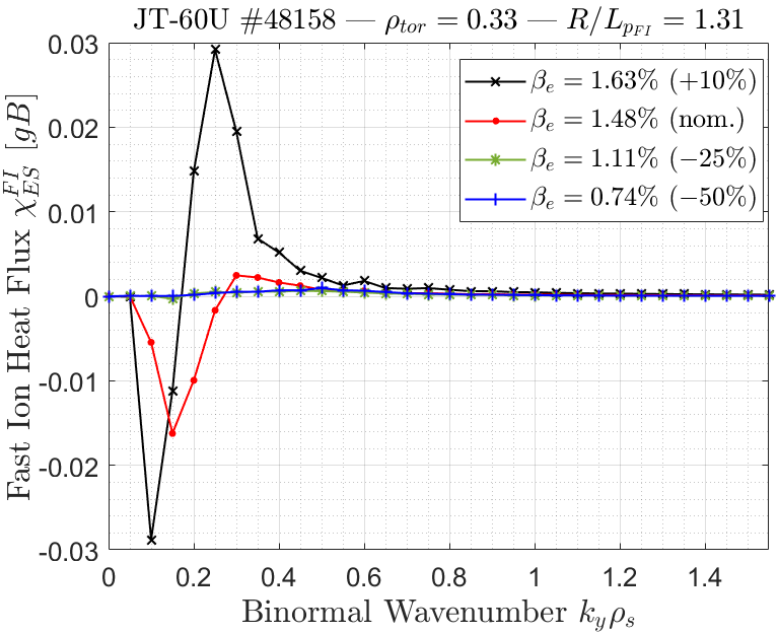

Figure 4.16: *The electrostatic heat flux spectra of fast ions, plotted as a function of the binormal wavenumbers, are shown for different values of β_e for the standard configuration with $R/L_{p_{FI}} = 1.31$.*

complex mechanism, which can likely be linked to what observed in the previous Chapter 3 and in the previously published studies on the ITG stabilization in the presence of suprathermal species [71, 77, 73, 90], may be underlying.

As a final remark to conclude this section, the results here reported demonstrate the large overestimation of the heat fluxes with respect to the experimental power balances, which is reported to be $\chi^{\mathrm{D}} \approx 1\ \mathrm{m}^2/\mathrm{s}$ at $\rho_{tor} = 0.33$ for $t = 27\ \mathrm{s}$ (represented by the black star in Figure 4.13(b)). For this reason, it has been established necessary to modify the modeling parameter setup, since this study is embedded in a validating framework for the JT-60U hybrid scenario. It has been shown that such a large overestimation of the heat transport can be essentially attributed to the destabilization of the low-k_y AITG and FI-BAE instabilities, mainly driven by the large thermal ion temperature gradient and by the total plasma pressure and fast-ion pressure gradient, respectively. AITG/FI-BAE modes dominate the nonlinear regimes by coupling to the other unstable modes, although their growth rates are not the largest in the linear spectra. As an additional argument, the high-frequency modes AITG and FI-BAE were not found unstable in the JT-60U pulse #48158 [156]. Indeed, the magnetic coils during this experiment detected only a low-frequency MHD instability sitting around $2 \sim 3\ \mathrm{kHz}$ during the stationary phase. Such modes have been identified as a fishbone-like instability and termed as energetic particle driven wall mode (EWM), generally observed in the high-β_{N} JT-60U plasmas. Radially localized around the $q = 2$ rational surface, with a toroidal mode number $n = 1$, its main drivers are the trapped fast ions injected from the perpendicular NBIs. All these characteristics have been

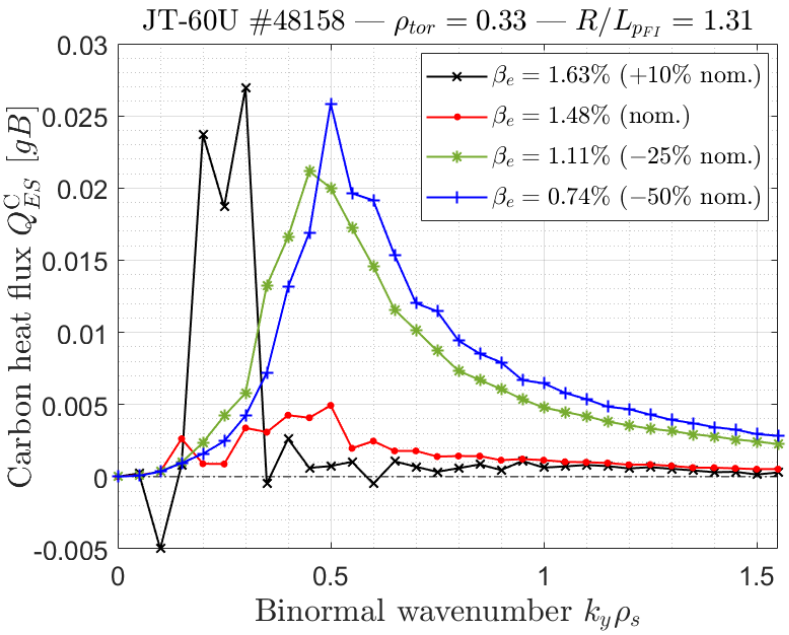

Figure 4.17: *The electrostatic heat flux spectra of the carbon species, plotted as a function of the binormal wavenumbers, are shown for different values of β_e for the standard configuration with $R/L_{p_{FI}} = 1.31$.*

shown throughout this chapter not to be attributable to the AITG and FI-BAE instabilities in the GENE modeling. In conclusion, the simulation parameter setup must be modified in order to stabilize the low-k_y high-frequency instabilities, thus validating the results against the experimental outcomes and, more importantly, determining the impact of the fast ions on the TEM-dominated transport. Nevertheless, it must be noted that a global approach would have been desirable, since the possible radial redistribution of the fast ions and the subsequent relaxation of the fast-ion pressure profile could have had an impact on the destabilization of the AITG and FI-BAE modes. This study was indeed conceived with a local approach, given the large uncertainties on the plasma parameters and thereby the need of diverse scan to be performed. Therefore, global simulations would have been too expensive and will be left for a future assessment.

4.5 Fast ion impact on TEM-dominated transport

In this section, the setup modification is firstly introduced and its main effects on the system stability examined. In a second place, the complex impact of the fast ions on this *modified* setup is analyzed by means of nonlinear simulations, followed by interpretations on the modeling results also in the context of the pursued validation study.

4.5.1 Description of the simulation setup modifications

As it has been established, a modification of the simulation setup needs to be done in order to stabilize the high-frequency instabilities driven by the large thermal and fast-ion pressure gradient, and thus to disentangle the possible effects of such instabilities on the transport in this study about the fast ion impact on TEM turbulent transport. The changes mainly concern the bulk plasma parameters, namely the thermal ion temperature gradient, the impurity content, and the total plasma pressure β_e. All these modifications are within the generally considered experimental uncertainty of $\pm 20\%$. Yet, as it has already been explained in the previous section 4.4.1, also the suprathermal components are altered. Those latter modifications are indeed concerning the fast-ion pressure gradient, which has been strongly reduced down to 80% of the nominal value as the maximum reduction, as well as the fast-ion density. The strong reduction of the steepness of the fast ion pressure profile which has been established necessary is visible in Figure 4.12. A summary of the variations of the simulation setup for the thermal

Table 4.2: *Parameters of the* GENE *simulations performed for the JT-60U pulse #48158 at $\rho_{tor} = 0.23$ and $t = 27$ s. In this table, the main differences between the standard and the modified cases are reported.*

Case	R/L_{T_D}	R/L_{n_D}	n_D	R/L_{n_C}	n_C	$\beta_e[\%]$
standard - W/O Fast Ions	7.73	5.28	0.44	5.32	0.09	1.48
modified - W/O Fast Ions	6.21	5.28	0.34	5.32	0.11	1.2
standard - With Fast Ions	7.73	7.16	0.3	5.32	0.09	1.48
modified - With Fast Ions	6.21	7.16	0.23	5.32	0.11	1.2

species is reported in Table 4.2. As a reminder, the simulation setup which has been analyzed in the previous sections – based on the nominal plasma parameters computed by the integrated modeling – is labeled as *standard* setup. On the other hand, the configuration which considers the modification made necessary for the stabilization of the low-k_y spectrum region is labeled *modified* setup.

The 20% reduction of the bulk ion temperature gradient leads to the stabilization of the AITG modes in the case without fast ions, as it was already clear in Figure 4.6, where the *standard* setup is represented by the vertical dashed red line well beyond the critical R/L_{T_D} and the *modified* setup by the vertical dotted black line just before the threshold. It was also observed that an increase of the carbon impurity density, which subsequently leads to the decrease of the bulk deuterium density for the quasi-neutrality relation, is beneficial for the stabilization of the low-k_y instabilities. Hence, the carbon density n_C is increased by less than 20%. Eventually, also the total plasma pressure has been slightly decreased from $\beta_e = 1.48\%$ to 1.2% for the same reason.

Concerning the modifications to the suprathermal parameters, it must be noted again that those affect the fast ion pressure gradient and the fast ion normalized

density. Both modifications are made in order to fully stabilize the FI-BAE instabilities, so that also in the nonlinear regime any possible coupling to other unstable modes was avoided. The change in fast ion density is still within the 20% uncertainty on the fast ion profile reconstruction, moving from $n_{FI}/n_e = 0.135$ to 0.11. On the other hand, the normalized fast ion pressure gradient $R/L_{T_{FI}}$ must be strongly decreased. Three different configurations have been explored in the *modified* setup, i.e. $R/L_{p_{FI}} = 3.51$ ($\sim 50\%$ of the nominal value), $R/L_{p_{FI}} = 2.45$ ($\sim 35\%$ of the nominal value) and $R/L_{p_{FI}} = 1.31$ ($\sim 20\%$ of the nominal value). In order to obtain those values of $R/L_{p_{FI}}$, it is possible to modify either the density gradient $R/L_{n_{FI}}$, the temperature gradient $R/L_{T_{FI}}$, or both at the same time. A table with the modifications of the two parameters is reported (see Table 4.3).

Table 4.3: *Values of the normalized fast ion pressure gradients $R/L_{p_{FI}}$ employed as input parameters in the various* GENE *simulations of JT-60U pulse #48158 and corresponding values of the normalized fast ion temperature $R/L_{T_{FI}}$ and density gradients $R/L_{n_{FI}}$.*

$R/L_{p_{FI}}$	$R/L_{T_{FI}}$	$R/L_{n_{FI}}$
6.60	2.04	4.56
3.51	1.23	2.28
2.45	0.17	2.28
1.31	0.17	1.14

Thus, it can be seen that for each simulation setup the relation $R/L_{n_{FI}} > R/L_{T_{FI}}$ holds. This is done in order to stay much closer as possible to a NBI-like setup, since the JT-60U pulse #48158 is mainly heated by NBI. All these configurations lead to almost identical linear spectra, since the FI-BAE is already stable for $R/L_{p_{FI}} = 3.51$ and the effect of the fast ion pressure gradient on the other instabilities is negligible (see Figure 4.9(a)). It must be also noted that the FI-BAEs are found to be fully unstable in the *standard* setup with $R/L_{p_{FI}} = 3.51$, leading thus to very high level of transport. Hence, such configuration was not analyzed in the previous section 4.4.1.

4.5.2 Effects of the modified setup on the linear stability

The linear spectra obtained with the *modified* simulation setup are compared to those of the *standard* setup in Figure 4.18. As a striking observation, the high-frequency instabilities, namely the AITG and the FI-BAE modes, have been completely stabilized. In the low-k_y region, some modes with Micro-Tearing Modes (MTMs)-like characteristics are found unstable. Nevertheless, the growth rate of those MTMs is extremely low, and no effects are expected in the nonlinear regime. Further checks on the ballooning structure of specific k_y in the following nonlinear simulations ensure that the effect of the MTM on the transport is either limited or even negligible. It is to be noted that the red dashed curve with

empty symbols, representing the GENE simulation with the *modified* setup retaining the fast ions, is here computed for $R/L_{p_{\mathrm{FI}}} = 3.51$. As already said, the other two explored configurations result in almost identical linear spectra, without the destabilization of FI-BAEs and very similar TEM growth rates.

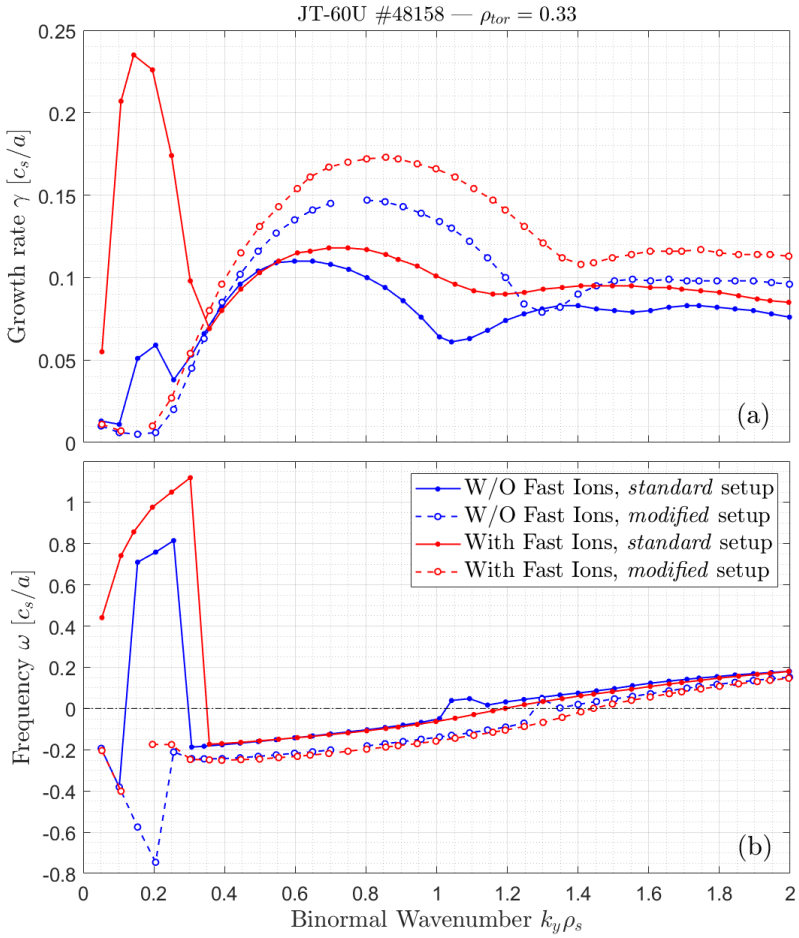

Figure 4.18: *The linear growth rate (b) and the mode frequency (b) computed with the* GENE *code for JT-60U pulse #48158 at* $\rho_{tor} = 0.33$ *with (red) and without (blue) fast ions are plotted as a function of the binormal wavenumber for both the standard (solid lines) and modified (dashed lines) numerical configurations.*

The thermal-ion scale region of the spectra also shows clear changes when the *modified* setup is considered. Essentially, the growth rate of the TEM is largely increased (by more than 30%) and the peak slightly shifted towards smaller scales. This increase is mainly due to the modification of the thermal ion density gradient, as it was already observed in section 4.3.4, when the introduction of the suprathermal species leads to a further destabilization of the TEMs. As an additional piece of evidence, in Figure 4.19, the thermal ion temperature gradient has been further decreased down to $R/L_{T_{\mathrm{D}}} = 5$ in the *standard* setup without retaining the fast ions. Such a decrease occurs in the stable AITG branch of the $R/L_{T_{\mathrm{D}}}$ (see

Figure 4.6) and leads to a very similar linear TEM growth rate values and shape with respect to the *modified* setup. This corroborates the idea that the increase of the TEM growth rate in the *modified* setup is essentially due to the modification of the thermal ion setup, and therefore such an instability is not a pure TEM. Beyond the direct impact of the thermal ion characteristics on the TEM growth rate, it must be considered also the side effects of the thermal deuterium pressure profile on the resonances taking place in the phase space. Indeed, the stabilizing or destabilizing regions of the phase space could be strongly affected by any modification of the pressure profiles. Since the TEM instability is excited when the bounce motion of the trapped electrons resonates with the wave frequency, TEMs could be strongly affected by the modifications of the resonant regions in the velocity space. This suggests that, in this particular system, TEM resonances are moving towards a destabilizing region of the phase space when the thermal deuterium temperature gradient is lowered.

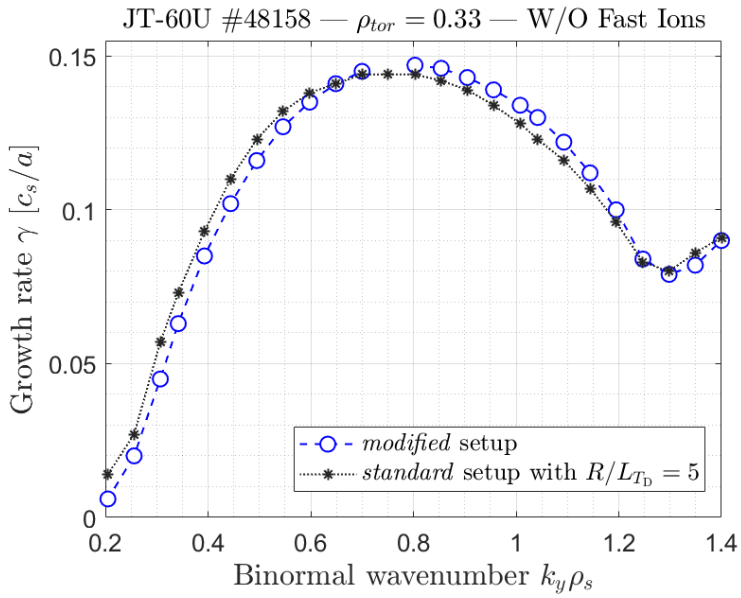

Figure 4.19: *The linear growth rates for the modified (dashed blue curve) and for the standard with modified R/L_{T_i} (dotted black curve) configurations are plotted as a function of the binormal wavenumber.*

For what concerns the small-scale instability, the growth rate of the C-ITG is enhanced for the *modified* setup with respect to the *standard* one. This is indeed mainly caused by the increase of the carbon density, as it is reported in Table 4.2, although a mild impact may be also related to the decrease of the β_e parameter, whose impact on the ITG instability is well known [12, 76, 172, 173].

4.5.3 Impact of fast ions on TEM-induced fluxes in the nonlinear regime

It is now analyzed the impact of the suprathermal species on the transport driven by TEMs. To do so, the *modified* setup is employed also in the nonlinear simulations. As it is shown in Figure 4.18 and discussed in the previous sections, the AITG/FI-BAE modes are stable for the *modified* input configuration, leading thus to a TEM-dominated turbulent transport. Hence, the fast ion impact on the TEM instability can be assessed, without forgetting the validation framework of this study. Indeed, as already stated in section 4.4.1 and illustrated in Figure 4.14, the low-k_y instabilities critically increase the heat fluxes of all the species, leading to a matchless comparison with the experimental outcomes. It must be noted, however, that the C-ITG modes are unstable even in the *modified* setup. For their complete stabilization, the modifications required in the simulation setup would be too far from the parameters computed in the integrated modeling. For this reason, as it has already been explained, it has been decided to only marginally include the C-ITG modes by limiting the nonlinear simulation box to $k_y\rho_s < 1.6$. The C-ITG may still be subdominant in the retained binormal range, but the smaller growth rate compared to the dominant TEMs suggests that only minor effects on the transport are expected.

In Figure 4.20, the electrostatic heat flux time-traces (panel (a)) and spectra (panel (b)) for both electrons and thermal ions are shown in a comparison between the case without fast ions and two setups with different fast ion pressure gradients. The electromagnetic fluxes are not directly shown here, since their relative value with respect to the electrostatic counterpart is not significant ($Q_{EM}/Q_{ES} < 5\%$). It is thus visible the impact of the fast ions on the transport dominated by the TEMs. Analyzing the time evolution of the heat fluxes, the two cases with $R/L_{p_{FD}} = 1.31$ and $R/L_{p_{FD}} = 3.51$ almost overlap the case without fast ions. It can also be observed that consistently with the linear stability analysis, the two cases including the suprathermal species have a steeper linear phase ($t \lesssim 30$ $[a/c_s]$), corresponding to a larger growth rate of the dominant instability (see Figure 4.18). The case without including fast ions, indeed, have a less steep linear phase, but saturates at a very similar level with respect to the case with fast ions. Such a finding is clearly visible for the electron fluxes in Figure 4.20(a), nonetheless an analogous dynamic is obtained for the thermal ion fluxes. This similarity on the time evolution of the fluxes suggests that the cases with and without fast ions have the same saturation mechanism. This observation is important to link the different impact of the fast ions on the ITG and TEM instability, and it will be discussed also in the following. For what concerns the spectra of the heat fluxes, these are shown in logarithmic scale in panel (b) of Figure 4.20. A small shift towards larger scales is observed when the fast ions are introduced in the simulation. This shift is reminiscent of the transition observed for the *standard* setup and illustrated in Figure 4.14. Therefore, this indicates that the fast-ion-driven instability could be easily recovered by further increasing the fast ion pressure gradient also in the *modified* setup.

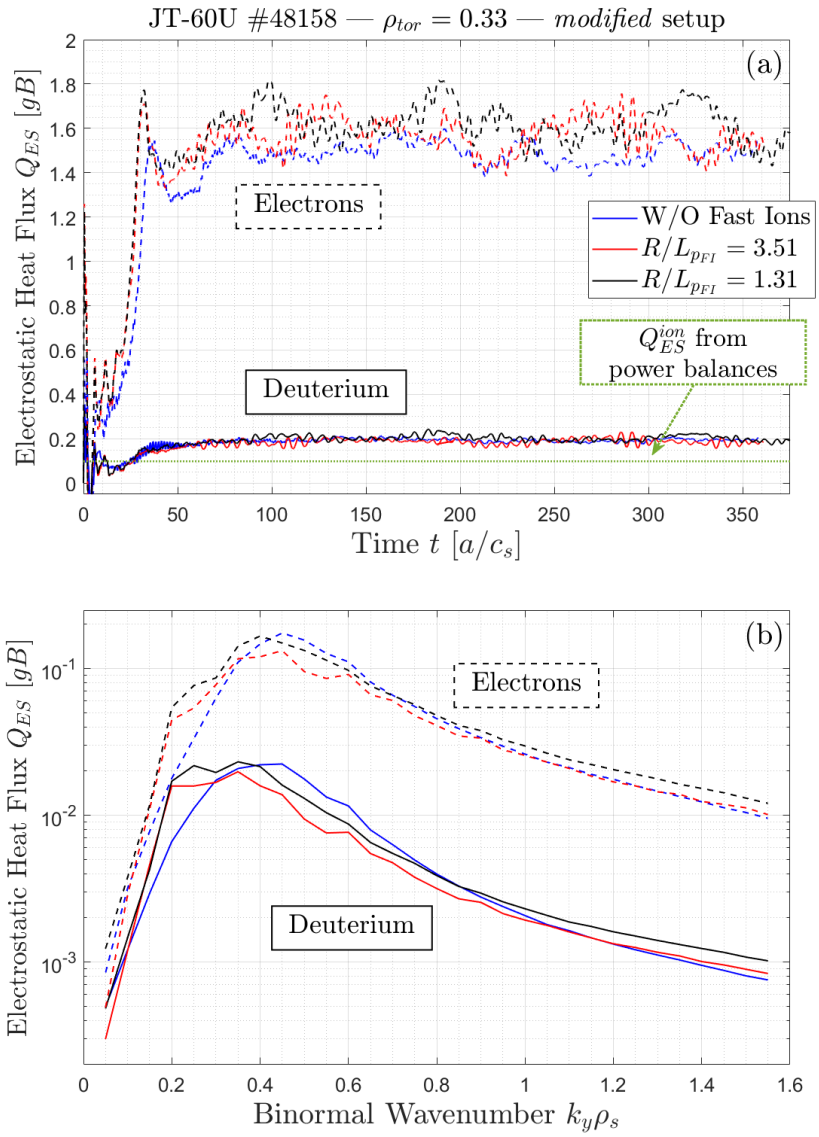

Figure 4.20: *In panel (a), the electrostatic heat flux time-traces of the electrons (dashed curves) and thermal ions (solid curves) are shown for the case without fast ions and for two different configurations of the fast ion pressure gradient in the modified numerical setup, which is TEM-dominated. The green horizontal dashed line represents the value of the thermal ion heat flux from the experimental power balances [156]. In panel (b), the heat flux spectra of the time-traces are shown for the same cases.*

A further analysis on the frequency of the electrostatic potential fluctuations has been carried out in order to certificate the dominant role of the TEMs in driving the transport. In Figure 4.21, the frequency spectra of the perturbed electrostatic potential without retaining the zonal components is shown for both the case without (panel (a)) and with fast ions (panel (b)). The case with fast ions illustrates the configuration with $R/L_{p_{FD}} = 3.51$. The dominant structures of

both spectra peak in the TEM frequency range, represented by the gray shaded area (consistently with the linear range of frequencies in Figure 4.18(b)). It is thus shown that the transport in the *modified* configuration is mainly induced by the TEM instability in both cases, with and without the suprathermal species. In Figure 4.21, also the frequency ranges of AITG and FI-BAE modes are reported as blue and red, respectively, shaded areas. Hence, it could be seen that in the case without retaining the fast ions, the structure in the AITG frequency range is very weak and hardly visible. On the other hand, for the case with $R/L_{p_{FD}} = 3.51$, an incipient structure in the FI-BAE region is clearly rising. Such a peak reveals that the FI-BAEs are weakly excited. This consideration could explained also the mild shift of the heat flux spectra toward lower binormal wavevectors displayed in Figure 4.20(b). These findings can be also related to the study of the highly energetic fast ion impact on the ITG-driven transport in the three-ion scenario at JET (Chapter 3), and even to the study reported in Ref. [90]. In fact, it has been definitely shown that the ITG turbulent transport is reduced when the high-frequency fast-ion-driven modes are subdominant, with a full suppression only when such modes are clearly destabilized. Yet, in this JT-60U plasma, this complex mechanism is not active, as the case with $R/L_{p_{FD}} = 3.51$, where a notable subdominant destabilization of the FI-BAEs is present, do not lead to any TEM turbulence reduction/suppression. Thus, once more, the TEM-dominated plasma here analyzed evidently is not beneficially affected by the presence of the suprathermal ions. Further explanations will be provided in the following section 4.5.4.

Since these studies are embedded in a validating framework, it is relevant to compare the thermal ion heat diffusivity in the *modified* setup including the fast ions computed by GENE with the experimental power balance. This latter information can be easily derived from Figure 3 of Ref. [156], in which the heat diffusivity radial profile for the thermal ions at $t = 27$ s is reported. As it is also pointed out in section 4.1, the thermal-ion heat diffusivity computed by the integrated modeling for JT-60U pulse #48158 at $\rho_{tor} = 0.33$ is $\chi^{ions} \approx 1.3\ \mathrm{m}^2/\mathrm{s}$. The total (electrostatic plus magnetic contributions) heat diffusivity for the thermal deuterium computed by GENE is indeed $\chi^{\mathrm{D}} = 2.5\ \mathrm{m}^2/\mathrm{s}$. For the sake of clarity, a green horizontal dotted line representing the integrated modeling result is reported also in Figure 4.20(a). Thus, only a rough agreement between the integrated modeling and the gyrokinetic analysis is achieved. Such an agreement is however much more remarkable with respect to the *standard* configuration, which overestimates the thermal ion transport by more than one order of magnitude (see Figure 4.14(b)). Nevertheless, this result should also be evaluated in light of the various approximation and uncertainties that have been employed or taken into account. As a matter of fact, the magnetic equilibrium, and in particular the shape of the q-profile and subsequently the magnetic shear, are affected by a strong experimental uncertainty especially in the plasma core; the integrated modeling can only qualitatively assess those values, whose impact on the heat fluxes computed by GENE could also be substantial. Moreover, these experimental uncertainties on the magnetic equilibrium reflect also into the shape of the ion pressure profile.

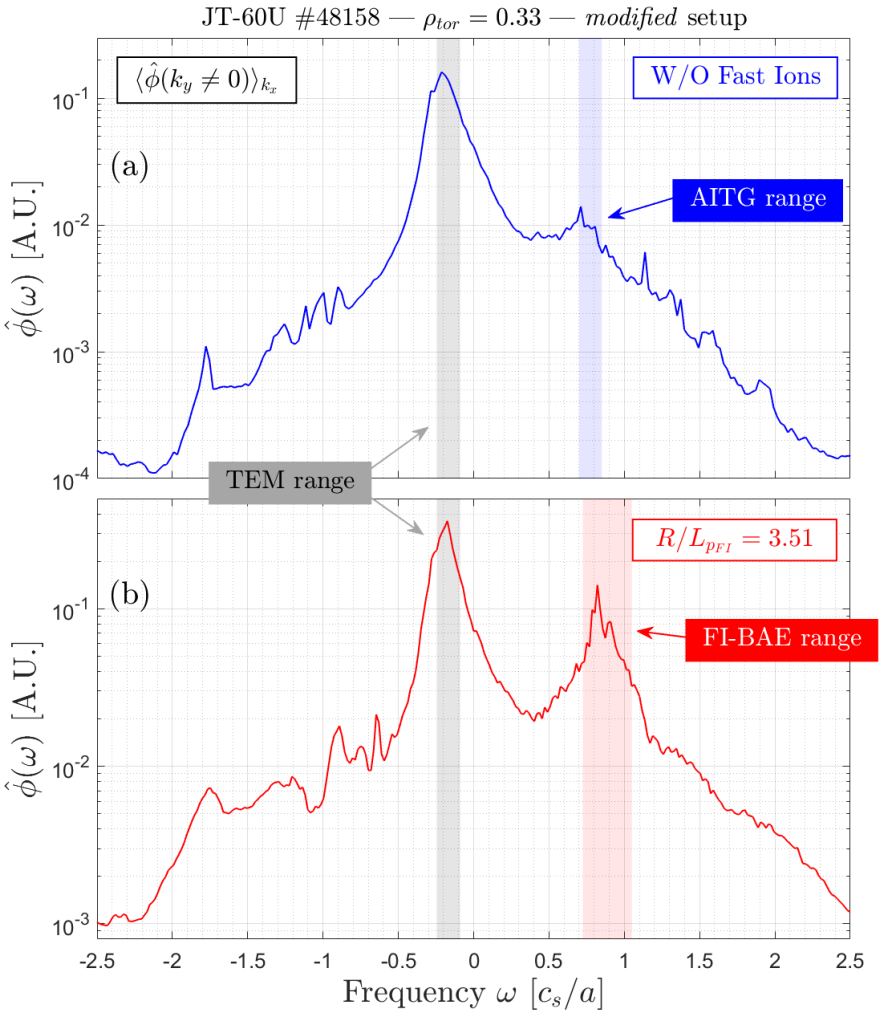

Figure 4.21: *The frequency spectra averaged over all the finite binormal wavenumbers ($k_y \neq 0$) and radial wavenumbers (k_x) in the nonlinear regime for the modified cases without fast ions (a) and with $R/L_{p_{FI}} = 3.51$ (b). The gray shaded areas represent the TEM linear range of frequencies. Indeed, the blue and the red one represent respectively the AITG and FI-BAE range of frequencies computed in the linear stability analyses.*

Hence, a flatter temperature profile and thereby lower temperature gradient for the thermal species could lead to lower transport levels. Eventually, those results are obtained in the local approximation. A gradient-driven global simulation is still to be performed, and it could be desirable to shed light on the quantitative assessment of the results produced with the local approximation in this validating study. Nevertheless, although the achieved agreement could be ameliorated, those results are noteworthy and enforce the evaluation about the impact of fast ions on TEM-driven turbulent transport.

It is thus shown that the fast ions have a mild impact on the TEM-dominated heat fluxes in the analyzed JT-60U hybrid scenario #48158. Such a result confirms the outcomes of the linear stability analysis, which indeed reports a moderate

destabilizing effect of the fast ions on the TEM growth rate. This is somehow in counter-tendency with respect to the ITG-dominated case, which has been discussed in the previous Chapter 3 and widely studied in the last decade (see e.g. Refs. [71, 77, 87, 93, 72, 90]). In the following section, a possible explanation about the different impact of fast ions on diverse turbulence regimes will be investigated.

4.5.4 Role of zonal flows as saturation mechanism of TEM turbulence

As it has been shown in the previous sections, the effect of the fast ions on the TEM-dominated transport is observed to be negligible, unlike what occurs for the ITG turbulence regime. Denoting the crucial role of the zonal shearing on the ITG turbulence suppression in the presence of fast ions, this path is likely to give interesting insights on the different behavior between ITG and TEM turbulence regimes. For this reason, as a first assessment, the impact of the zonal flow is evaluated by the well-established rule of thumb $\gamma_{E\times B,\mathrm{zonal}}/\gamma_{max}$ [174], where $\gamma_{E\times B,\mathrm{zonal}} = |k_x^2\phi(k_x,0)|$ is the zonal shearing rate and γ_{max} the maximum of the linear growth rate at the ion-scale. In this JT-60U plasma, the maximum of the growth rate at the ion-scale is always related to the TEM instability. Such an analysis has been shown to be valid for the wavelength region $k_y\rho_i \lesssim 2$ [175], where ρ_i is the thermal ion gyroradius. In the present study, the long-wavelength region – usually dominated by the ETG instability – is not considered, and therefore the approximation of the role of thumb is still applicable. It has been shown indeed that when the large-k_y spectrum is considered, such an approximation is not anymore valid, and another saturation mechanism, which is the zonal flow mixing rate, plays a comparable – sometimes even dominant – role [175].

In Table 4.4, the ratio $\gamma_{E\times B,\mathrm{zonal}}/\gamma_{max}$ is reported for the different cases discussed in this chapter. As can be seen, the ratio is strongly increased when the fast ion species is introduced in the simulation setup but only for the *standard* cases, namely when the fast-ion drive is large enough to excite FI-BAEs. On the other hand, in the *modified* configuration, where the FI-BAEs are linearly stable, the ratio $\gamma_{E\times B,\mathrm{zonal}}/\gamma_{max}$ is reduced. This suggests that the zonal flow shearing rate is increased when the FI-BAEs are destabilized, similarly to what observed in the previous Chapter 3, and more importantly that in the TEM-dominated regime the zonal flows are not expected to play a determinant role. Essentially, the reduced strength of the zonal flow activity on the TEM-induced turbulent transport may prevent the fast ions from providing the beneficial effect observed in the ITG-dominated cases. Indeed, the complex mechanism leading to the ion-scale turbulence reduction does not take place due to the missing nonlinear interaction between the large-scale instabilities and the zonal components of the electrostatic potential fluctuations. Reminding what observed in section 4.5.2, the modification of the numerical setup from the *standard* to the *modified* configuration leads to an increase of the TEM linear growth rate (see Figure 4.18(a)). This certainly affects the ratio $\gamma_{E\times B,\mathrm{zonal}}/\gamma_{max}$. Therefore, in order to properly account for the

Table 4.4: *Zonal flow shearing rates computed by* GENE *for different configurations of JT-60U plasma at* $\rho_{tor} = 0.33$ *and* $t = 27$ *s.*

Case	$\gamma_{E\times B,\text{zonal}}\,[c_s/a]$	$\gamma_{E\times B,\text{zonal}}/\gamma_{max}$
W/O Fast Ions		
standard - $\beta_e = 1.48\%$	0.43	1.87
modified - $\beta_e = 1.20\%$	0.18	1.23
With Fast Ions - $R/L_{p_{FI}} = 1.31$		
standard - $\beta_e = 0.74\%$	0.17	1.33
standard - $\beta_e = 1.11\%$	0.19	1.47
standard - $\beta_e = 1.30\%$	0.23	1.78
standard - $\beta_e = 1.48\%$	0.43	2.92
standard - $\beta_e = 1.63\%$	0.52	3.99
modified - $\beta_e = 1.20\%$	0.18	1.04
With Fast Ions - $R/L_{p_{FI}} = 2.45$		
standard - $\beta_e = 1.11\%$	0.19	1.47
standard - $\beta_e = 1.30\%$	0.35	2.71
standard - $\beta_e = 1.48\%$	0.46	3.29
With Fast Ions - $R/L_{p_{FI}} = 3.51$		
modified - $\beta_e = 1.20\%$	0.17	1.03

strength of the zonal perturbations of the electrostatic potential, Table 4.4 reports also the value of the zonal flow shearing rate for the different cases. The shearing rate presents thus an increment proportional to the FI-BAE/AITG drive. In fact, increasing either the fast ion pressure gradient or β_e leads to an enhancement of the zonal flow shearing rate. Essentially, this result underlines again the strong correlation that may occur between the large-scale modes and the zonal flows.

It must be also observed that for the *modified* cases, independently from the value of the fast ion pressure gradient, the shearing rate remains almost constant. This clearly highlights that the introduction of the fast ion species in the JT-60U TEM-dominated turbulence regime does not provide any beneficial effect, differently to what observed in the ITG turbulence pattern.

A preliminary conclusion that can be drawn from such considerations is that the turbulence regime strongly dominated by the TEM instability may preclude the increase of the zonal flow activity triggered by the fast-ion-driven modes. Such a preliminary conclusion can be further elaborated by inspecting the pos-

sible nonlinear interactions occurring in the various cases. This is done by an extensive bispectral analysis, whose results are summarized in the following. For a detailed explanation of the wavelet bispectral analysis see the previous section 3.4.4.

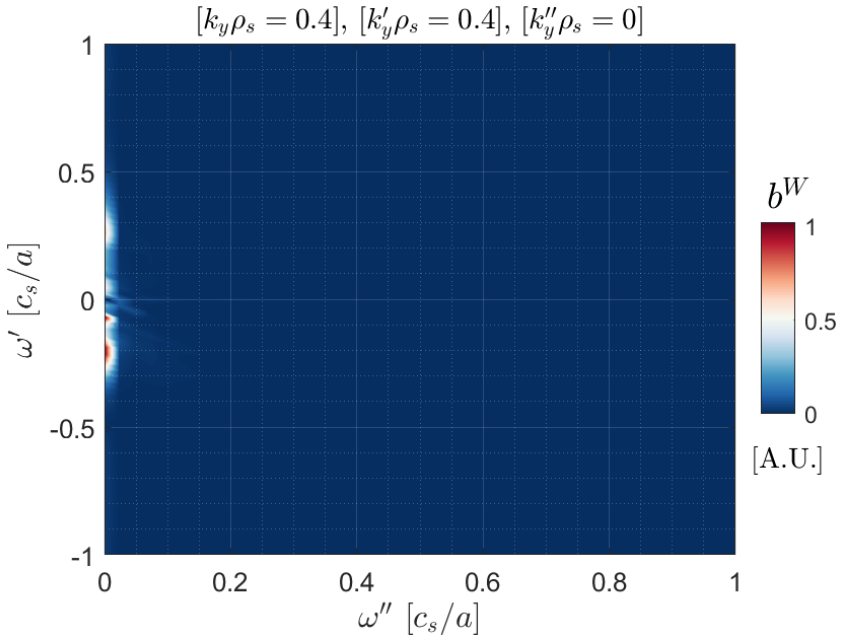

Figure 4.22: *Wavelet bispectrum for the electrostatic potential fluctuations highlighting the spatio-temporal coupling between the TEMs and the zonal components is shown for the selected triads:* $k_y = 0.4$, $k'_y = 0.4$ *and* $k''_y = 0$ *in the standard numerical setup.*

In Figure 4.22, the bispectrum b^W for the triads composed by $(k_x, k_y) = (0, 0.4)$, the zonal components of the field $(k''_x, k''_y) = (a, 0)$ and the modes completing the triplets $(k'_x, k'_y) = (-a, 0.4)$, with $a \in [-k_{x,max}, k_{x,max}]$ is shown for the case without fast ions in the *modified* setup. The mode $(k_x, k_y) = (0, 0.4)$ has been selected being the most destabilized TEM wavevector. The bispectrum shows dominant structures in the TEM frequency range, determining thereby a nonlinear coupling between the TEM and the zonal spatio-temporal scales. It is worthy to remind that the bispectral analysis could only identify the mode-mode couplings, without defining the possible nonlinear transfer of energy among the involved modes. Thus, although it has been shown that the TEM perturbations are coupled to the zonal components of the electrostatic potential, any conclusion on the transfer of energy from the TEMs to the zonal flows cannot be drawn.

Now inspecting the bispectrum *modified* configuration with fast ions (and with $R/L_{p_{FD}} = 3.51$) delineates a more complex situation. Indeed, the bispectral analysis performed over a significant amount of triads coupled to the zonal components does not allow to define any dominant nonlinear coupling, although the spatio-temporal interactions between the TEM and zonal flow range of frequencies is always present. For the sake of simplicity, the figures are not reported

here. It is important to stress that, even if Figure 4.21(b) clearly shows a subdominant destabilization of the FI-BAEs, such a low-k_y instability is not coupled to the zonal perturbations of the electrostatic potential. This lack of nonlinear interaction is likely preventing the increase of the zonal flow shearing rate and thereby the reduction of the ion-scale turbulent transport in the JT-60U plasma that has been analyzed.

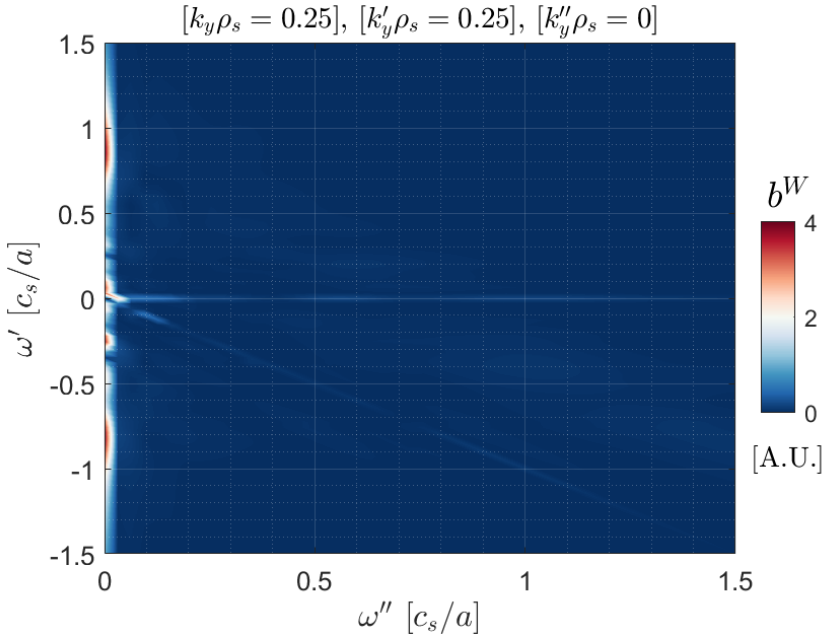

Figure 4.23: *Wavelet bispectrum for the electrostatic potential fluctuations highlighting the spatio-temporal coupling between the FI-BAEs and the zonal components is shown for the selected triads:* $k_y = 0.25$, $k'_y = 0.25$ *and* $k''_y = 0$, *for the standard setup.*

Concerning the *standard* setup, in which the low-k_y instabilities are dominant when the electron beta approaches the nominal value (or goes beyond that), the bispectral analysis reveals a correlation between the FI-BAEs and the zonal perturbations of ϕ. This is shown in Figure 4.23, where the triads composed by the wavevectors $(k_x, k_y) = (0, 0.25)$, $(k''_x, k''_y) = (a, 0)$ and $(k'_x, k'_y) = (-a, 0.25)$ are analyzed. A clear detection of the nonlinear coupling between the FI-BAE and the zonal flow scales is thus evidenced (at $\omega' \approx 0.7 - 1\ c_s/a$ and $\omega'' = 0\ c_s/a$). Very similar structures are also present for the triads corresponding to the contiguous binormal wavenumbers, such as $k_y\rho_s = 0.2$ and 0.3. Similarly to what occurs for the study reported in Chapter 3, the strong increase of the zonal flow shearing rate in the presence of the destabilization of the fast-ion-driven modes can be highlighted by this bispectral analysis, which also suggests a net energy transfer from the low-k_y modes to the zonal flows.

Eventually, despite the strong increase of the zonal flow shearing rate, related to an increased zonal flow activity, the ion-scale turbulent transport, in this case mostly driven by the TEM instability, is not reduced. Vice-versa, the overall trans-

port is strongly enhanced when the fast-ion-driven modes are destabilized, contrarily to what observed in the ITG-dominated regime.

4.6 Partial conclusions

This brief section is dedicated to summarize the main results obtained in the study of the plasma core of JT-60U pulse #48158. The plasma core conditions have been described, with a high-β TEM-dominated turbulent regime. Flattish q-profile is also present in the core, leading to low magnetic shear values. Thus, very demanding numerical analyses, with the gyrokinetic code GENE in its flux-tube version, are carried out to investigate on the interaction between the substantial population of externally generated fast ions and the TEM-driven microturbulence. Linear stability studies show that the high value of β_e facilitates the excitation of high-frequency low-k_y modes. Indeed, even in the numerical setup without fast ions AITG modes are unstable, although TEMs dominate the linear spectrum. The introduction of the suprathermal species in the setup further destabilizes the low-k_y region of the spectrum, leading to strongly unstable fast-ion-driven BAEs, now dominant also over the TEMs. It must be stressed at this point that the high-frequency unstable modes have not been detected during the experimental sessions. In this linear phase, TEMs are only mildly affected by the presence of the fast ions. After having established the validity of the flux-tube approximation with dedicated studies, nonlinear simulations are performed. In the *standard* numerical configuration, the low-k_y modes strongly impair the turbulent fluxes, by increasing the transport levels one order of magnitude higher than the one obtained through experimental power balance evaluations. The increase of the turbulent heat fluxes has been measured for all the species, both thermal species and fast ions. It has, thus, been revealed necessary a modification of the numerical setup in order to recover the transport levels observed experimentally. Whereas the input parameters for the thermal species have been changed within the assumed 20% error bar, the fast-ion characteristics needed a more important modification. Basically, the main purpose of these modifications was to stabilize the experimentally non-observed high-frequency modes. In this *modified* configuration, the TEMs are the dominant instability, also in the nonlinear regime. It has thus been possible to evaluate the impact of the fast ions on the TEM-dominated turbulent transport, in a validated framework. The results demonstrate the absence of interaction between the TEM-driven heat fluxes and the fast ions. The role of the zonal flows has then been investigated, showing that the zonal flow shearing rate is not affected by the presence of the fast ions. The missing impact of the zonal flows on the TEM-induced transport can also be related to the absence of the fast-ion-driven modes, which have been shown to strongly couple to the zonal components of the electrostatic potential. Thus, unlike the outcomes of the ITG turbulent transport reduction in the presence of highly energetic ions reported in Chapter 3, the TEM-induced heat fluxes are not affected by the fast ions in this JT-60U hybrid scenario.

4.7 Numerical experiment: TEM transport reduced with highly energetic ions and low-β conditions

In this section, the numerical experiment on a tailored TEM-dominated system, with a population of highly energetic ions, is carried out in the same fashion of the previous analyses, i.e. by means of the gyrokinetic code GENE in its flux-tube version. This analysis has the purpose to further investigate on the TEM-dominated turbulent transport, whose elusive interaction with zonal flows make prohibitive any generalization. It must be however highlighted that those results are preliminary, and more in-depth analyses are required to draw any general conclusion.

Table 4.5: *Employed plasma parameters in* GENE *simulations inspired by TCV pulse #58375 at* $\rho_{tor} = 0.33$ *and* $t = 1.4$ *s. Here,* ϵ *represents the inverse aspect ratio,* n *the species density normalized to the electron density,* $R/L_{n,T}$ *the normalized logarithmic density and temperature gradient,* β_e *the electron-beta, and* $\nu^* \equiv (an_e/4|e|^2 n_i)\nu_{ei}$ *the normalized collision frequency, where* a *is the minor radius,* e *the electron charge and* nu_{ei} *the Hinton-Hazeltine electron-ion collision rate [27]. Eventually, the normalization factors in standard units are also reported, i.e. the on-axis magnetic field strength* B_0*, the local (*$\rho = 0.33$*) electron temperature* T_e *and density* n_e*, and the major radius* R_0*. The reported input parameters are common to all the following numerical* GENE *simulation cases.*

ϵ	q	$\hat{s}$	T_i/T_e	R/L_{n_e}	R/L_{T_e}
0.34	1.53	0.59	0.09	2.63	7.03
n_{D}/n_e	$R/L_{n_{\mathrm{D}}}$	$R/L_{T_{\mathrm{D}}}$	n_{FD}/n_e	T_{FD}/T_e	$R/L_{n_{FI}}$
0.91	2.60	1.47	0.09	23.50	2.93
β_e [%]	ν^*	B_0 [T]	T_e [keV]	n_e [m^{-3}]	R_0 [m]
0.57	1.95×10^{-4}	1.36	1.15	2.29×10^{19}	0.92

The numerical setup of this study takes inspiration from the experimental outcomes of the TCV pulse #58375 [176]. As already stated in the introduction of this thesis, recent developments of the external heating system at TCV could more efficiently provide a substantial population of suprathermal particles. In particular, a second tangential NBI system with nominal power of 1 MW, injecting particles at $50 - 60$ keV of energy, has been installed [177]. Such an improvement would effectively generate the experimental conditions to study the fast-ion effects reported in this thesis even in the TCV tokamak. Therefore, the numerical transport study of the experimental scenario reported in Ref. [176] is justified as a preparation to future experimental campaigns at TCV making use of both NBI systems. Nevertheless, a substantial modification of the parameters at the radial location $\rho_{tor} = 0.33$ has been done in order to stabilize possible subdominant ITG modes and to have thereby an almost pure dominant TEM instability

in the linear spectrum. In Table 4.5, the principal input parameters are reported. As already said, the numerical configuration leads to a TEM-dominated system

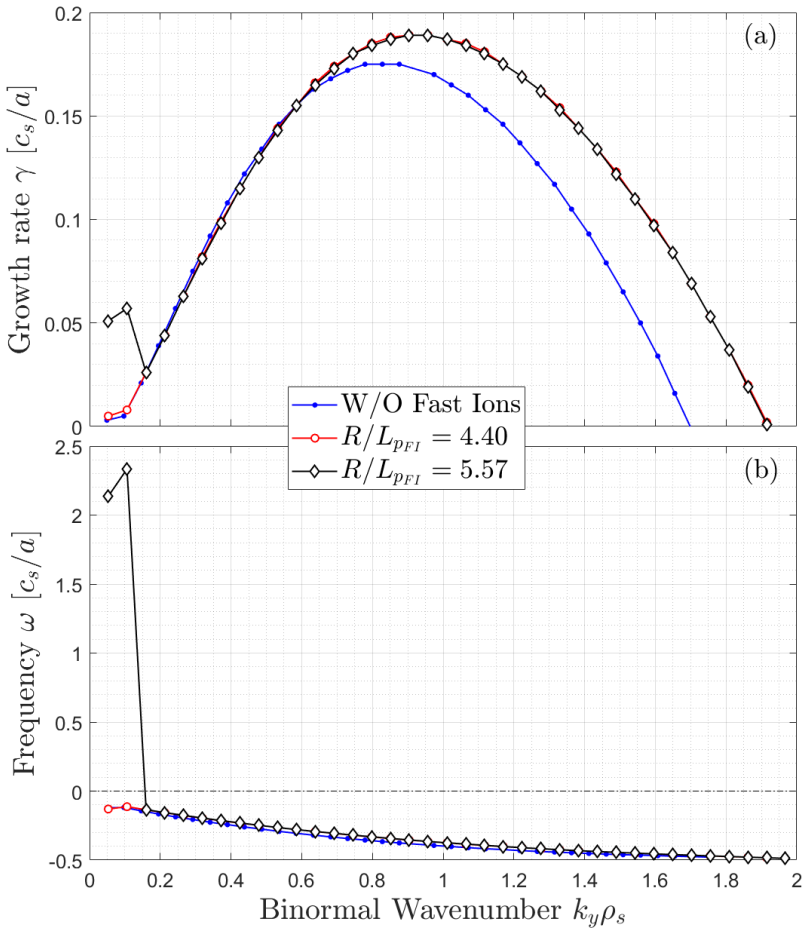

Figure 4.24: *The linear growth rate and the mode frequency computed by the* GENE *code simulating the TCV pulse #58375 at $\rho_{tor} = 0.33$ are plotted against the binormal wavenumber $k_y\rho_s$ respectively in panel (a) and (b). Three different numerical setup are reported.*

when the suprathermal species is not retained. This is confirmed both by the linear spectrum in Figure 4.24 and by the time derivative of the electron potential energy displayed in the velocity space in Figure 4.25. As can be seen, indeed, the peak of the growth rate is at the ion-scale (at $k_y\rho_s = 0.8$) with the mode rotating in the electron diamagnetic direction. Moreover, the instability excited at $k_y\rho_s = 0.8$ is driven by the trapped electron particles, clearly identifying the dominant instability as TEM. The thermal ion temperature gradient has been lowered to $R/L_{T_i} = 1.47$ in order to avoid the destabilization of the ITG modes. Further analyses show that no subdominant ITG modes are present in this configuration.

Another relevant investigation is illustrated in Figure 4.26. A scan over the

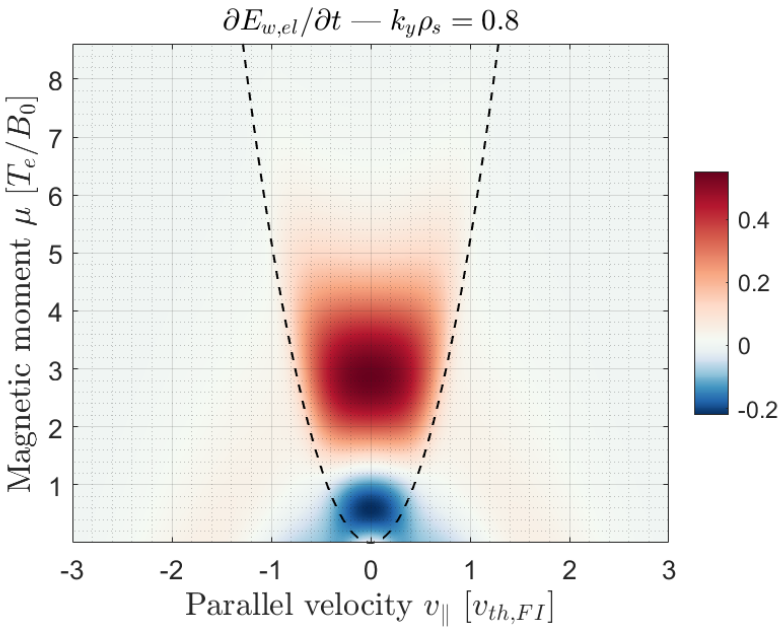

Figure 4.25: *The free energy exchange is plotted in the velocity space for the wavenumber $k_y\rho_s = 0.8$, demonstrating that the wave-particle interaction with the trapped electrons is the excitation mechanism for this particular wavenumber.*

normalized fast ion temperature gradient is performed for three different wavelengths in the low-k_y region, namely $k_y\rho_s = 0.05, 0.1, 0.15$ (corresponding to the toroidal numbers $n = 1, 2, 3$ respectively). The growth rate curves displays a sharp transition, for the wavevectors $k_y\rho_s = 0.05$ and $k_y\rho_s = 0.1$. The dominant modes within the low-k_y range transit from a TEM to a high-frequency fast-ion-driven mode. Therefore, such a tailored configuration allows clearly to define three different setups: far from the fast-ion mode destabilization, within the marginal stability region and in the fully destabilized fast-ion mode region of the phase space. The three particular input setups, that will be analyzed also in the nonlinear regime in the following, are represented by the vertical lines. This is useful to link this particular numerical exercises with the validating framework of the study described in Chapter 3. Moreover, the role of the fast-ion-driven modes in the complex mechanism is thereby definitely highlighted.

In Figure 4.26, the wavenumber $k_y\rho_s = 0.15$ remains TEM-dominated throughout the entire scan over $R/L_{T_{FI}}$. As it is also suggested by the linear spectra in Figure 4.24(a), the fast ion pressure gradient modification does not affect the TEM growth rate. It must be noted, however, that in this scan, as well as in the two curves in Figure 4.24(a), the fast ion density gradient has been fixed to $R/L_{n_{FI}} = 2.93$ and not further modified. This is because of the quasi-neutrality relation that must be fulfilled, which does not allow a simple change in the density gradients, as instead it could be done for the temperature gradients. For the sake of simplicity, therefore, the scan over the fast-ion mode drive has been performed varying $R/L_{T_{FI}}$ only.

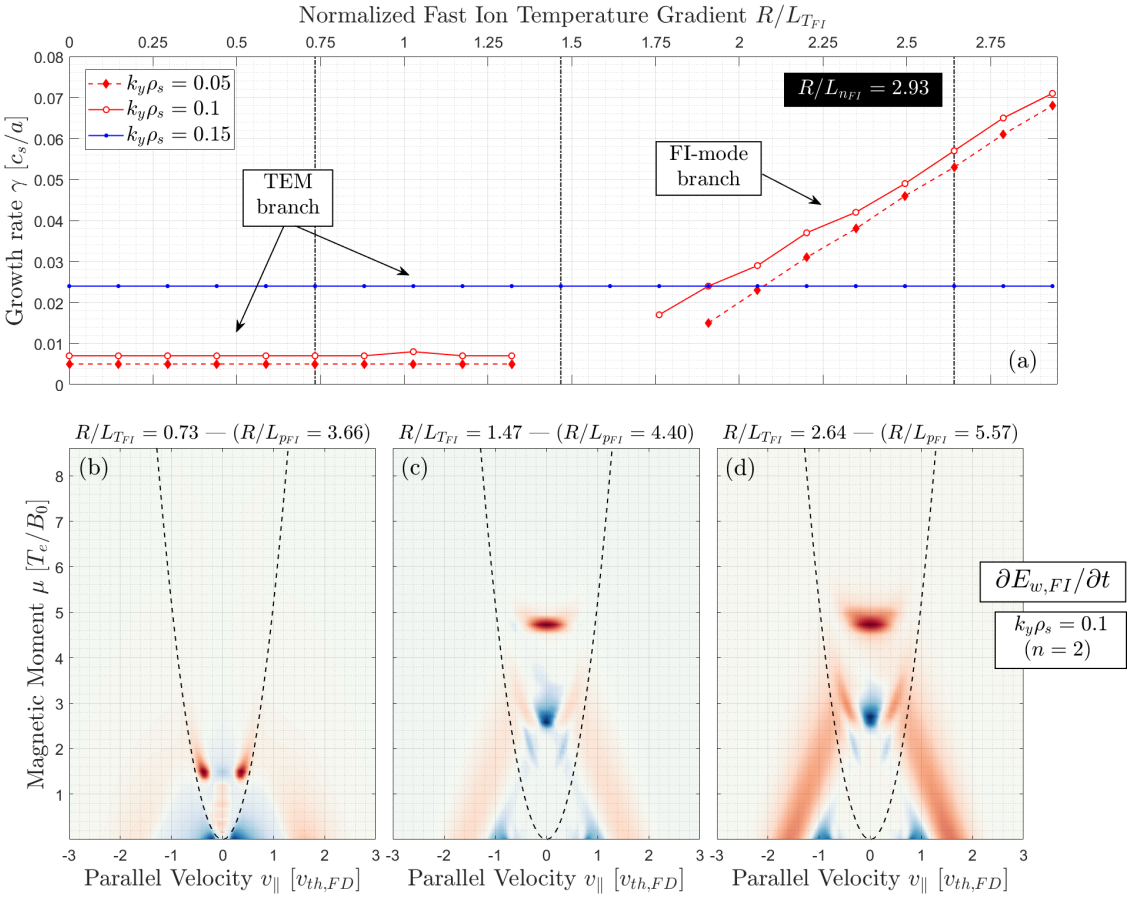

Figure 4.26: *In panel (a), the linear growth rates for three different binormal wavenumbers are plotted as a function of the normalized fast ion pressure gradient. The vertical dotted-dashed lines refer to three particular values of $R/L_{p_{FD}}$ (indicated in the title of panels (b-d)), representing three different fast-ion-driven mode stability statuses. In panles (b-d), the free energy exchange is plotted in the velocity space for $k_y\rho_s = 0.1$ $(n = 2)$.*

As already stated, the principal effect of the increase of the fast ion pressure gradient is the destabilization of the high-frequency modes in the low-k_y range. An accurate identification of these instabilities has not been carried out yet, nonetheless in the corresponding experiment, i.e. TCV pulse #58375, no high-frequency MHD activity has been observed [176]. This latter consideration would suggest that the fast ion drive (i.e. $R/L_{p_{FI}}$) must be below the critical value for the destabilization of the high-frequency mode. However, the focus of this study is the demonstration of the beneficial effect of fast ions also on the TEM instability. Hence, also the configuration with unstable fast-ion-driven modes is considered. In the second row of Figure 4.26, panels (b-d) illustrate the time derivative of the fast-ion potential energy exchanged at the binormal wavenumber $k_y\rho_s = 0.01$ in the velocity space for three different values of $R/L_{T_{FI}}$ described above. It can be clearly seen that increasing the fast-ion drive leads to the appearance of a well-localized resonant structure within the trapping cone. For the marginal

stability case ($R/L_{T_{FI}} = 1.47$), the structure is already visible although weaker with respect to the case with $R/L_{T_{FI}} = 2.64$. It is also worthy to note the clear link between this TEM-dominated case and the ITG-dominated case of the three-ion scenario at JET reported in great details in Chapter 3. Even the structures related to the excitation of the fast-ion-driven mode within the trapping cone presents strong similarities. Furthermore, the AITG/FI-BAE modes are not excited through the wave-particle resonance with the trapped particles, but instead with passing fast ions (see Figure 4.8). This consideration may open the possibility to clearly identify the trapped fast particles as a key factor of the beneficial complex mechanism. Yet, more in-depth analyses are required to draw any conclusion on that.

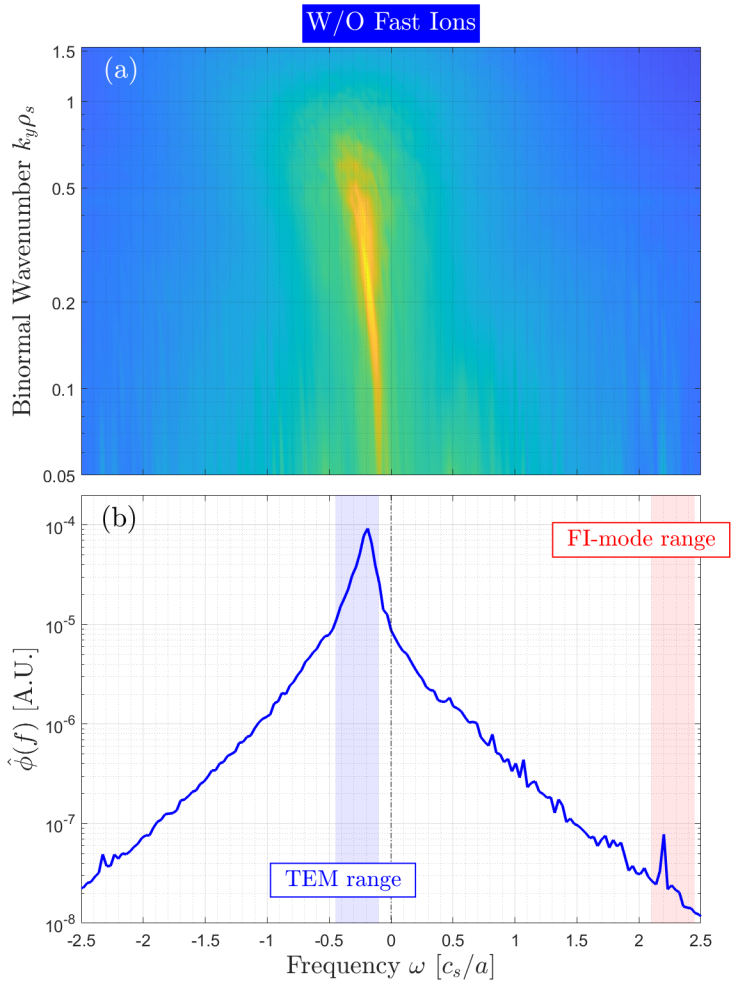

Figure 4.27: *In panel (a), the frequency spectrum computed from the nonlinear* GENE *simulations is shown as a function of the binormal wavenumber for the configuration without retaining fast ions. In (b), an additional average over the binormal wavenumbers helps in identifying the major peaks of the power spectrum. The blue and red shaded areas represent, respectively, the TEM and the fast-ion-driven mode range of frequencies computed in the linear stability analysis.*

In the following, the nonlinear effects of the highly energetic fast ions on the TEM-dominated fluxes will be presented. Nevertheless, it is also useful to have a look at the frequency power spectrum in the case without fast ions, in order to clearly demonstrate the dominant role of the TEMs in this numerical configuration. This is shown in Figure 4.27, where in panel (a) the frequency is shown also in function of the binormal wavenumbers, and in panel (b) the additional average over k_y helps in identifying the global and local dominant peaks in the spectrum. It can thus been seen that the global dominant structure occurs around $k_y\rho_s = 0.2 - 0.35$, in the TEM linear measured frequency (cf. the linear spectrum in Figure 4.24(b)). Surprisingly, a local dominant spike is also measured at low-k_y in the range of frequency where the FI-modes are excited in the configuration including fast ions. This latter range of frequency is highlighted with the red shaded area in panel (b) of Figure 4.27. Although this may signify that a precursor for the destabilization of the fast-ion-driven modes is also present in the simulation without suprathermal particles, it must be also noted that this peak is more than four orders of magnitude weaker than that of the TEMs. The picture is indeed totally different when the fast ions are included in the simulation with a pressure gradient large enough to drive the low-k_y high-frequency modes unstable. This is illustrated Figure 4.28, in which it is clear the dominance of the fast-ion-driven modes in the frequency power spectrum.

It is now shown in Figure 4.29 the effect of these low-k_y modes driven by the wave-particle resonance with the highly energetic ions. Consistently with the framework reported in Chapter 3, a strong reduction of the electrostatic heat fluxes is measured only when the fast-ion-driven modes are destabilized. It should also be stressed that, contrarily to the ITG-dominated case, the electron transport is not fully suppressed. Indeed, the reduction can be quantified by $\sim$60% in the configuration with $R/L_{p_{FI}} = 5.57$. In this TEM-dominated numerical experiment, the thermal ion transport can be neglected, since it contributes by less than 3% of the total transport. The electron electromagnetic transport, on the other hand, can be neglected only when the fast-ion-driven modes are linearly stable or marginally stable. In fact, in the fully destabilized configuration, the electromagnetic electron flux is strongly increased and reaches more than one third of the electrostatic counterpart, thereby far from being negligible. Figure 4.29 has been split in two panels to facilitate the illustration. In fact, when the fast-ion modes are fully destabilized, i.e. with $R/L_{p_{FI}} = 5.57$, the oscillations of the fluxes are almost one order of magnitude larger than the average value. This is interesting because, although being very large, the amplitude is not comparable to the dramatic ones reported in Ref. [78]. Such a difference may be due to the electron β range, but also to the fast-ion energy with respect to the bulk plasma. Despite being a very attractive question to be addressed, the answer still remains elusive.

Another important point of such an analysis on the TEM-dominated numerical experiment is about the causes of such a turbulence reduction, which are explained in the following. Consistently with what observed for the JET ITG-dominated three-ion scenario, the destabilized fast-ion-driven modes determine a nonlinear coupling between their scales to the zonal ones. The nonlinear inter-

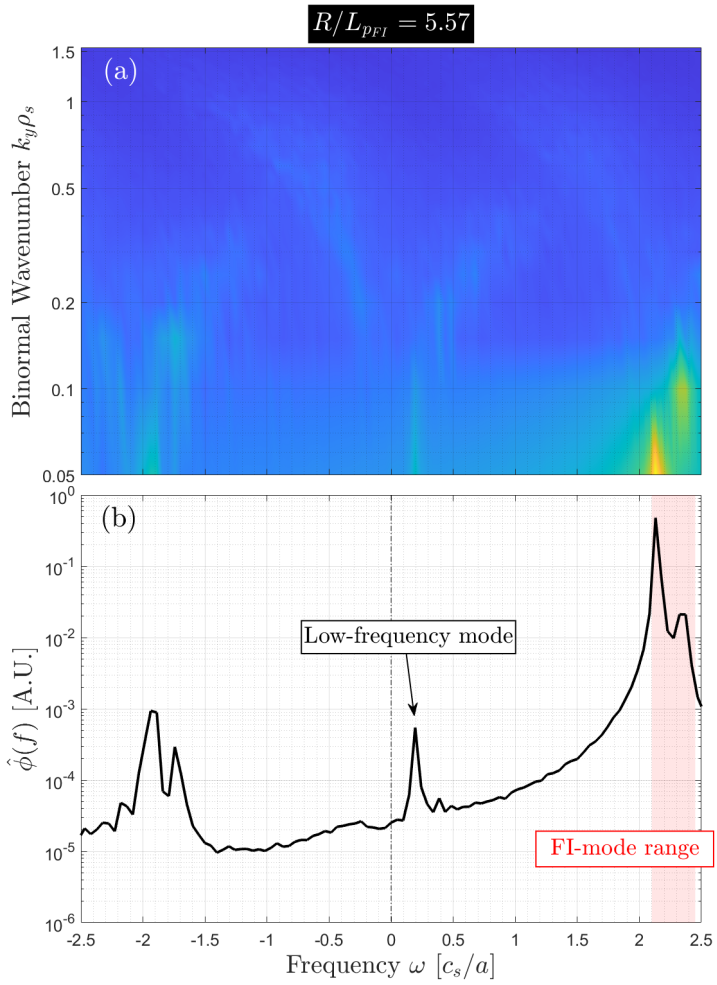

Figure 4.28: *In panel (a), the frequency spectrum computed from the nonlinear* GENE *simulations is shown as a function of the binormal wavenumber for the configuration with $R/L_{p_{FI}} = 5.57$. In (b), an additional average over the binormal wavenumbers helps in identifying the major peaks of the power spectrum. The red shaded area represents the fast-ion-driven mode range of frequencies computed in the linear stability analysis. The low-frequency mode peak is also highlighted in panel (b).*

action is reported in Figure 4.31, similarly to what observed in the ITG-dominated case reported in Chapter 3. The consequences of such mode-mode coupling can be appreciated in Figure 4.30, where the zonal flow shearing rate $\gamma_{E\times B,\text{zonal}}$ is plotted for the different configurations in function of the zonal radial wavenumbers k_x, after being averaged over a sufficiently large time window. The increase in the case with $R/L_{p_{FI}} = 5.57$ occurs mainly in the low-k_x region of the spectrum. Moreover, the effect on the cross phase is present also in this case, similarly to what seen in Chapter 3. In fact, concomitantly with the increase of the zonal flow shearing rate, the phase angle of the electron physical parameters n^{el}, $T_{\parallel}^{el}$ and $T_{\perp}^{el}$ with the electrostatic potential ϕ is strongly shifted from around $\pi/2$ to almost π

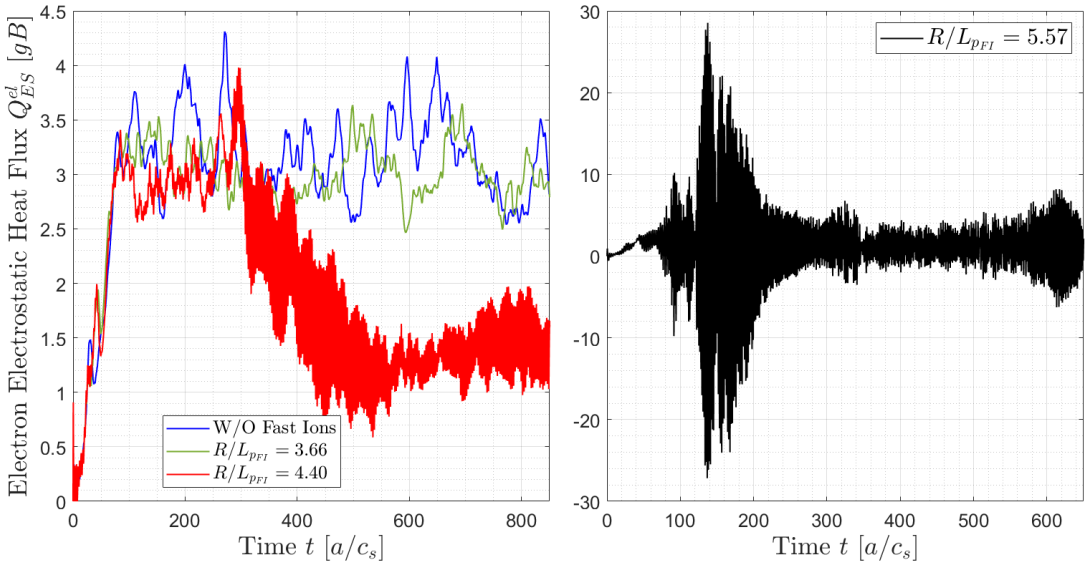

Figure 4.29: *Time evolution of the electron electrostatic heat flux at different values of the fast ion pressure gradient in the* GENE *simulations of a TEM-dominated system. The figure is split in two panels to facilitate the comparison, due to the large-amplitude fluctuations of the heat flux time trace in the case with* $R/L_{p_{FI}} = 5.57$.

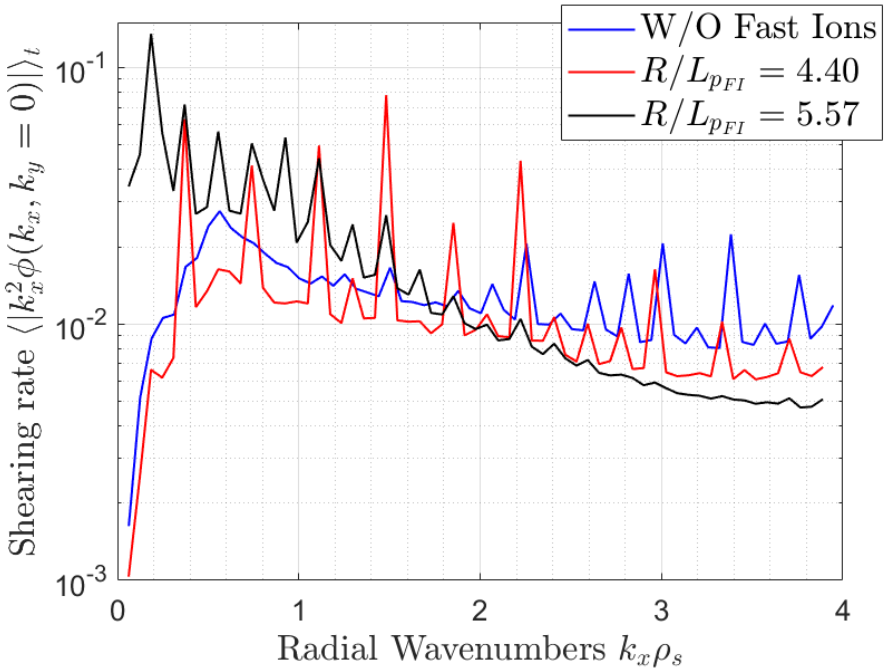

Figure 4.30: *The magnetic shear fluctuation rate* $\bar{s}_{fluc}$ *is plotted as a function of the radial wavenumber* $k_x \rho_s$ *for various configurations.*

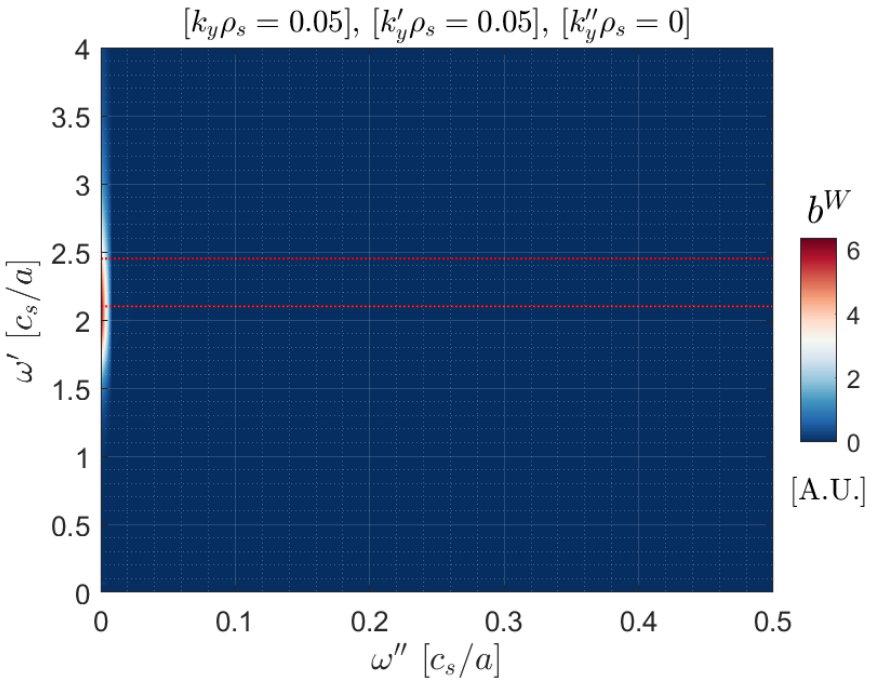

Figure 4.31: *Wavelet bispectrum for the electrostatic potential fluctuations highlighting the spatio-temporal coupling between the TAEs and the zonal components is shown for the selected triads:* $k_y = 0.05$, $k'_y = 0.05$ *and* $k''_y = 0$, *for the case with* $R/L_{p_{FD}} = 5.57$.

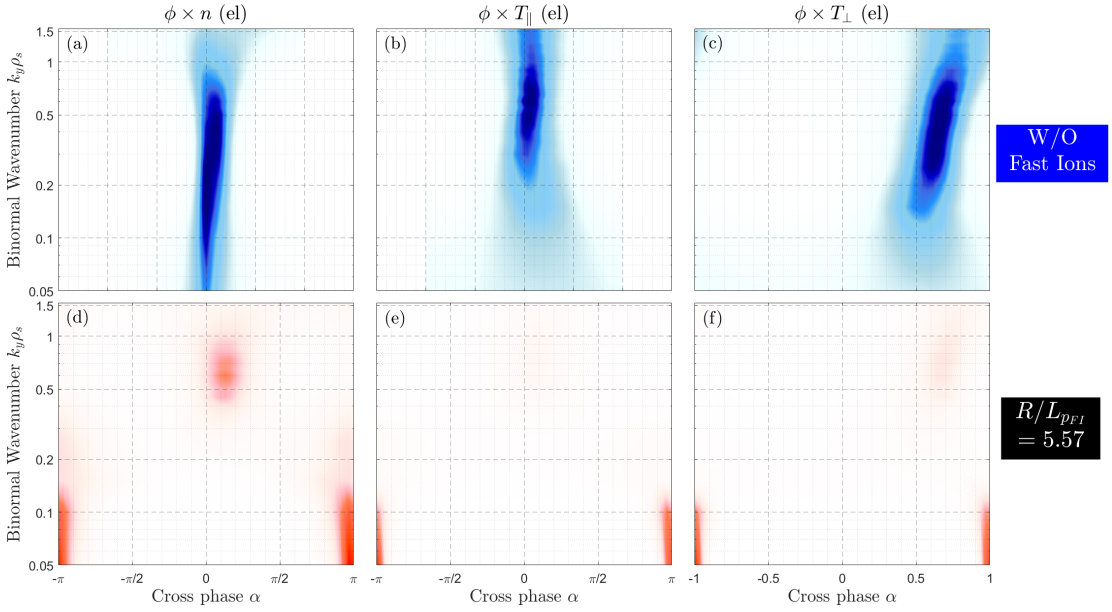

Figure 4.32: *The cross-phase* $\alpha(\phi \times n^{^3\mathrm{He}})$, $\alpha(\phi \times T_\parallel^{^3\mathrm{He}})$ *and* $\alpha(\phi \times T_\perp^{^3\mathrm{He}})$ *histograms are shown in the first row (panels (a-c)) for the case without fast ions, while in the second row (panels (d-f)) for the case with* $R/L_{p_{FI}} = 5.57$.

when the fast-ion-driven modes are destabilized. This means that the phase angle is shifted from a out-of-phase, which suggests a non-null flux, to a in-phase situation, in which the transport is thus strongly reduced. Moreover, the destabilized fast-ion-driven modes have also an effect on the main transport length scale, which is shifted from the thermal ion scales (around $k_y\rho_s = 0.2$) to the large scales dominated by the fast ion dynamics ($k_y\rho_s = 0.05$ and 0.1). This is shown in Figure 4.32, where the upper row represents the case without fast ions, and the lower one represents the simulation with fully destabilized fast-ion-driven modes (namely $R/L_{p_{FI}} = 5.57$).

To conclude this chapter, a very striking observation is made clearer. In fact, in Figure 4.28, besides the dominant structure at the fast-ion-driven mode frequency range, a spike is observed at lower frequencies in the positive side of the power spectrum. Such a feature has also been detected in the numerical studies on the three-ion scenario at JET (reported in Section 3.4.4), corroborating once more the accuracy of such an analysis. Additionally, again in Figure 4.28, also the high-frequency electron-driven modes are detected in the electrostatic potential frequency spectrum. Hence, the similarity observed between these two numerical studies is quite impressive. It must be said that, consistently with the results reported in Chapter 3, the low-frequency unstable mode is only detected after the saturation of the fast-ion-driven instabilities. In fact, Figure 4.28 illus-

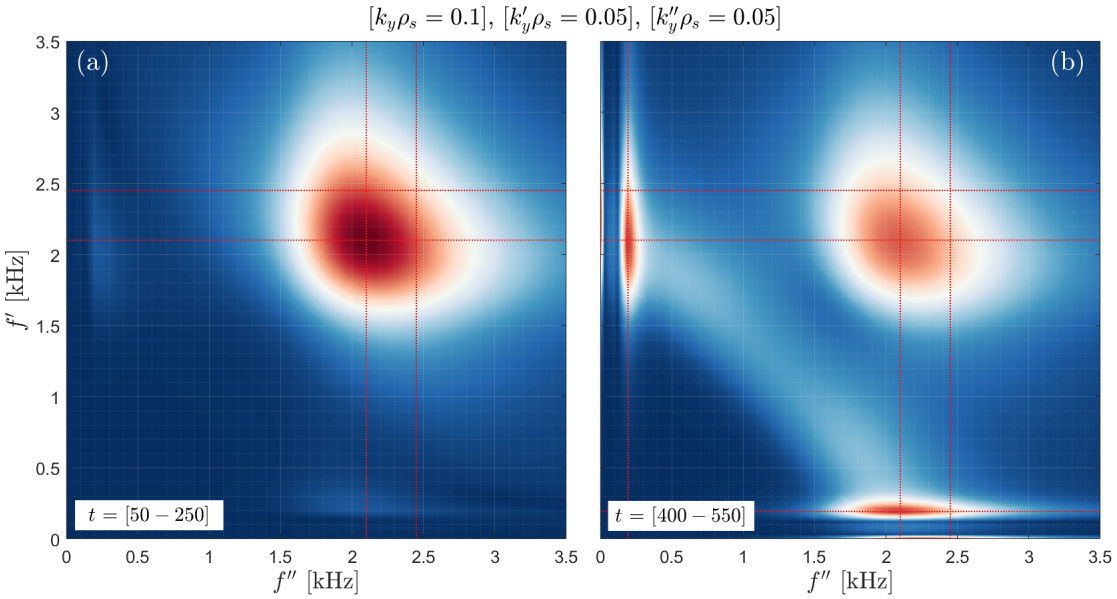

Figure 4.33: *Wavelet bispectrum for the electrostatic potential fluctuations highlighting the spatio-temporal coupling between the TAEs and the low frequency modes is shown for the selected triads: $k'_y = 0.1$ and the low-frequency mode range $k''_y = 0.025$, for the case with $R/L_{p_{FD}} = 5.57$. In panel (a), the first TAE growing phase [50-250] a/c_s, and in panel(b) the TAE saturated phase [400-550] a/c_s.*

trates the power spectrum computed in the time window when a quasi-stationary phase of the flux evolution is reached, specifically $t = [400 - 575]\ a/c_s$. The same

Fourier transform of ϕ performed in the earlier phase of the simulation is not conclusive about the low-frequency mode. To confirm such results, a bispectral analysis is performed on the nonlinear interactions occurring among the triplets $(k_y\rho_s, k_x\rho_s) = (0.1, 0)$, $(k_y\rho'_s, k_x\rho'_s) = (0.05, a)$ and $(k_y\rho''_s, k_x\rho''_s) = (0.05, -a)$. The modulus of the bispectrum is shown in Figure 4.33 for two different time windows: $t = [50 - 250]\ a/c_s$ (panel (a)) and $t = [400 - 550]\ a/c_s$ (panel (b)), representing respectively the phase before and after the saturation of the fluxes induced by the fast-ion instability. In the first phase of the simulation, the main resonance occurs at the fast-ion-driven mode range of frequencies, and suggests a dominant coupling among the fast-ion-driven modes. It must be also noted that weak structures in the low-frequency range are already visible, likely related to the final stage of the analyzed time window. Indeed, in panel (b), the dominant structures are occurring at the intersection between the fast-ion-driven mode frequency range and the low-frequency mode, as the red dashed lines illustrate. As already observed before, this is perfectly aligned to earlier studies on the interaction between TAEs and EPMs, published in Ref. [142]. Furthermore, this result may suggest that the low-frequency mode is an hallmark of the ion-scale turbulence reduction/suppression in the presence of fully destabilized fast-ion-driven modes.

Chapter 5

Conclusions and future directions

The main purpose of this thesis has dealt with deeper investigating unexplored regions of this rapidly evolving subject of research, that is the impact of fast ions on the microturbulent transport in tokamak plasmas. Attractive insights for the efficient exploitation of the present and, even more importantly, future devices have thus been provided.

In the last two decades, a passionate commitment has grown in order to understand some striking observations, which can be firstly traced back to the first D-T experimental campaigns in the '90s, where it was conjectured a possible correlation between the alpha particles and the *anomalous* ion heating. Following these observations, some further multi-device experiments evidenced that the turbulence reduction mechanism of ion confinement improvement played a role in the presence of the externally generated fast ions. Pioneering studies then demonstrated the beneficial impact of the NBI and/or ICRH fast ions on the ITG turbulence transport through different mechanisms, such as a linear wave-wave resonance reducing the ITG growth rate, and a nonlinear interactions involving subdominant fast-ion-driven TAEs and electrostatic zonal flows. Although great steps have been made to the comprehension of such a complex field, still some elusive points are missing to complete the frame. In this thesis, two crucial points have been analyzed in great detail by means of extensive gyrokinetic numerical analyses in validated frameworks, in order to extend the knowledge on the impact of suprathermal ions on the microturbulent transport. After providing the reader with the physical background and mathematical descriptions essential for the topic, Chapter 3 and 4 are devoted to address the two still unexplored paths.

5.1 Main conclusions

One of the main concern of the first D-T experimental campaign at ITER, planned to take place in 2035 [178], is about the effects of the alpha particles on the global confinement of the plasma, and in particular their interactions with the turbulent transport. In order to have some insights about this, the development of ITER-relevant scenarios must be pursued and then examined with great attention. In Chapter 3, the recent three-ion scheme scenario at JET is briefly analyzed from

the experimental point of view, focusing mainly on the striking observation of improved thermal ion confinement in the presence of MeV-range ions. Such MeV-range ions can mimic the alpha particle energy and can thereby be a good proxy for predicting future burning scenarios. In fact, both experimental diagnostics and integrated modeling calculations confirm the presence in the plasma core of a substantial population of efficiently generated fast ions in the range of MeV energies, and a concomitantly improved ion thermal confinement. It must be stressed however that the MeV-ions are mainly generated as co-passing particles, differently from the isotropic distribution of the fusion-born alpha particles. This scenario is therefore a suitable test-bed case for exploring the impact of highly energetic ions on the turbulent transport.

Linear stability analyses at the radial position $\rho_{tor} = 0.23$ have been carried out using the gyrokinetic code GENE, revealing that transport in the core is dominated by ITG modes. It should be also stressed that the novelty of this work does not rely only on the characteristics of the suprathermal species, for which the energy is higher than in the previous studies about this topic and both density and temperature are much closer to the ITER predicted scenario, but also on the systematic experimentally observations of unstable AEs. Such modes play a determinant role in the mechanism for the ITG turbulence reduction, but they were never detected in the previous related studies. In the present work, the linear stability analyses already showed the destabilization of fast-ion-driven TAEs, in good agreement with the experimental measurements, in the low-k_y region beyond a critical fast ion pressure gradient. The excitation mechanism of the TAEs in the numerical simulations involved the trapped fast particles, with a clear resonance occurring at high perpendicular velocities. Due to the large inaccuracy of the fast-ion characteristic computation by the integrated modeling, the adopted strategy was to scan the system $-$ even nonlinearly $-$ over a wide range of $R/L_{p_{FD}}$ values to assess the turbulence patterns thereby developing. It has thus been established that the electrostatic heat fluxes of the thermal ions, both the D majority and ^{3}He minority species, are suppressed only when the fast-ion-driven TAEs are nonlinearly destabilized. These results, also in agreement with the power balances determined by the integrated modeling, highlight the paramount importance of the high-frequency electromagnetic instabilities in achieving the suppression of the ion-scale transport, with respect to only a partial reduction in the case of subdominant TAEs. In fact, together with the observation of the quenching of the ITG-induced fluxes, an enhanced zonal flow activity has been detected, whose beneficial impact on the saturation and further reduction of the radial turbulent transport is well-known [63]. It has been demonstrated with multi-mode bispectral analysis that a strong correlation between the zonal flow and the TAE spatio-temporal scales occurs, thereby suggesting a net transfer of energy flowing from the high-frequency fast-ion-driven modes to the zonal component of the electrostatic potential. A noteworthy study has been performed on the effect of this complex mechanism on the cross-phase of the heat-flux-relevant fluctuating parameters, corroborating thus the clear effects of such mechanism on the ion-scale transport reduction. Although the main purpose of this study was to

analyze the impact of this highly energetic ions on the thermal ion confinement, some insights have been given also about the electron and fast-ion transport in the presence of fully destabilized TAEs. Indeed, the fast-ion-driven TAEs induce a strong fast-ion transport, larger with increasing $R/L_{p_{FD}}$, suggesting that if the evolution of the radial distribution of the suprathermal particles had been taken into account, a flattening of the profile would have been observed. A balance could thus be found at lower $R/L_{p_{FD}}$, where the fast-ion transport is significantly lower. Furthermore, the electron electrostatic transport follows the trend of the thermal ion fluxes, being totally suppressed in the conditions of unstable TAEs and enhanced zonal flow activity. The electromagnetic contribution, on the other hand, increases at higher $R/L_{p_{FI}}$ values, due to the large-amplitude fluctuations of the vector potential induced by the destabilized fast-ion-driven modes. However, it must be reported that the electron electromagnetic fluxes do not show an explosion, as it was expected in the conditions of strong electron heating and unstable Alfvénic modes. Together with this observation, an enhanced zonal field activity is also measured in the simulations with fully destabilized TAEs.

Eventually, the systematic appearance of RSAEs in the three-ion scenario at JET indicates a non-monotonic behaviour of the safety factor profile which may influence the global plasma confinement. Thus, additional numerical simulations, were performed with negative magnetic shear ($\hat{s} = -0.3$), without changing the other input parameters, in order to conduct a preliminary study. It has been shown that the direct effect of the negative shear is to quench the linear excitation of the fast-ion-driven TAEs, whose consequences are also observed in the nonlinear regime with a dramatic decrease of the fast-ion transport. This finding may also explain the increase of the experimentally measured neutron rate in the presence of destabilized RSAEs, which is likely related to an improved confinement of the externally generated fast ions.

Whereas Chapter 3 is dedicated to extend the beneficial fast-ion effect on the ITG turbulent transport beyond the critical threshold for the destabilization of the fast-ion-driven modes, such effect remains elusive in a differently dominated turbulence regime. Chapter 4 of this thesis focuses on exploring the impact of externally generated fast ions on the TEM-induced turbulent transport in a JT-60U hybrid scenario. Following the same workflow adopted in the previous study, the linear stability analyses are carried out with the GENE code simulating only a flux tube centered at $\rho_{tor} = 0.33$. Preliminary analyses indicate that TEMs are the dominant unstable modes. In the nonlinear regime, unstable AITG modes at low-k_y are destabilized leading to a different turbulent pattern. The introduction of the NBI-generated fast ions, for the same parameter configuration, further destabilizes the low-k_y modes $-$ now identified as FI-BAE $-$ which become thereby dominant in the whole linear spectrum. This leads to unrealistic thermal fluxes in the nonlinear regime. Therefore, the input parameters, especially the normalized temperature gradients of electrons and bulk ions and the β_e (both being drivers of the low-k_y instability), have been modified within the error bars. The fast-ion characteristics, instead, are strongly changed, with a reduction of more than 50% in order to linearly stabilize the FI-BAE. In this *modified* configuration, the TEMs

are established to be the dominant drive of the ion-scale turbulent transport, and thus the impact of the suprathermal particles on TEMs can be evaluated. Extensive numerical analyses demonstrate that the TEM-induced fluxes are not affected by the fast ions in the core of JT-60U hybrid scenario, clearly indicating a difference with the well-established ITG-dominated case. The underlying mechanism of the increasing of the zonal flow activity in the presence of high-frequency instabilities is hypothesized not to be effective on the TEM-induced transport. Indeed, although an increase of the parameter of merit $\gamma_{E\times B,zonal}$ because of the nonlinear coupling to the large-scale fast-ion-driven instability, the heat fluxes of the thermal species are dramatically enhanced, as well as the fast-ion transport. In fact, the numerical investigation, carried out to evaluate the impact of the fast-ion-driven instability in comparison with the previous ITG-dominated case, highlights that a very steep trend of the nonlinear fluxes is achieved beyond the critical β_e leading to a large transport. Therefore, in this validation framework, the modification of the parameter setup for the stabilization of the low-k_y modes is found to be necessary to match the experimental power balance, corroborating thus the very weak or absent impact of fast ions on the TEM-induced turbulent fluxes.

In this context, an additional numerical analysis about the impact of externally generated fast ions has been performed on a pure TEM-dominated system, suitably tailored from a TCV NBI-heated L-mode pulse. The results of such an analysis recover the complex mechanism observed in the ITG-dominated case, with the strong increase of the zonal flow activity in the presence of fully destabilized fast-ion-driven modes leading to a significant reduction of the thermal fluxes, in this case induced by the TEMs. Manifest similarities are observed between the two systems, suggesting that the beneficial fast-ion effect is not only limited to ITG-dominated regime, but also to other turbulence patterns, such as the TEM regimes. Nevertheless, even in this numerical experiments the fast ions lead to a only partial reduction of the TEM-turbulent transport, not equivalently to the clear suppression of the thermal fluxes in the ITG-dominated case. Eventually this consideration, together with the outcomes of the aforementioned study on the TEM-dominated JT-60U plasma core, highlight that the ITG and the TEM turbulence regimes present also evident differences regarding the exploitation of such a beneficial mechanism triggered by the presence of the suprathermal ions in present and future fusion devices.

5.2 Future work

Appearing as inevitable, the closer one gets to the full comprehension of a subject, the larger is the number of open questions that the study leads to. Therefore, this thesis, although clearly indicating new relevant directions, has disseminated along the path of this topic some unsolved points which should require additional efforts.

The studies reported in this work of thesis have made use of the gyrokinetic code GENE in its flux-tube version, simulating therefore only a small portion of

the entire plasma volume and neglecting the global effects. As it has been stated in Chapters 3 and 4, the dynamics of the large-scale instabilities excited by the fast ions and the radial structure of the sheared zonal flows push the local approximation and thereby the code capability to the limit. For further validation and verification of these results, global analyses are necessary. Although pioneering works have been recently pursued to describe this effect in extremely demanding global gradient-driven simulations [75], the large number of parameter uncertainties still force the use of scans, somehow unaffordable in global frameworks to date. Further developments of the exa-scale high performance computing resources and the fully exploitation of the GPU capabilities may alleviate such a requirement in the near future. Thus, although qualitative insights can be gained from the local simulations, for an accurate quantitative evaluation of the gyrokinetic analyses the global approach must be pursued. In addition, because of the substantial fast-ion transport induced by the large-amplitude fluctuations of the electromagnetic fields induced by the fast-ion-driven modes, the definitive evaluation of the global confinement needs a self-consistent evolution of the profiles in the radial and velocity phase space, which can be assessed only in flux-driven global electromagnetic numerical studies. Yet, such a numerical tool is still prohibitive, and further efforts are thereby required. Promising results have been obtained with the flux-driven, full-F, global code GYSELA [81], which has been recently upgraded to account for the magnetic fluctuations [179].

However, a stronger connection between the experimental outcomes and the numerical gyrokinetic analyses must be built, making use of advanced techniques. Pioneering studies with dedicated experimental (e.g., Refs. [180, 181]) and synthetic (e.g., Refs. [182, 183]) diagnostics showed the possibility of further validating the results of the turbulence numerical analyses against actual plasma behaviour. This must be necessarily pursued in ITER-relevant regimes – e.g. with the presence of AEs destabilized by MeV-ions, low plasma rotation and ratio $T_i/T_e \sim 1$ – in order to gain more insights on the impact of the suprathermal ions on the turbulent transport.

A relevant point that has been uncovered in this thesis is the importance of the kinetic resonances occurring in the velocity phase space for the excitation of the fast-ion-driven instabilities. Although the sensitivity of the system to the modification of those resonant dynamics has not been fully investigated, it is shown that the appearing or disappearing of such structures could seriously change the described picture. For this reason, accounting for the realistic distribution function in the velocity space, especially for the highly energetic ions, instead of the here employed equivalent Maxwellian, should be required for the analyses performed in this thesis. This is an additional work that could be carried out in the near future, similarly to what was already reported in earlier studies [104, 74, 100]. In fact, the effects of the anisotropic distribution function must be taken into account in a validation framework to have an accurate quantitative comparison with the experiments.

A future direction that can be also explored is the inclusion of the small-scale effects on the ion-scale confinement, basically by extending the simulating do-

main down to the electron scales. This is because it has already been shown in some previous studies that the electron-driven turbulent structures may also influence the behaviour of the turbulent transport developing at the ion-scale [184, 147]. Therefore, although the rule of thumb employed in this work suggested that ETGs should not play an important role in the thermal ion transport, a further clarification on this point could be proposed in the future by performing multi-scale analyses in the presence of highly energetic ions and turbulent transport suppression, following what was already done in the past for moderately fast ions [127].

In both ITG- and TEM-dominated cases, the study of the cross phase angle between the heat-flux relevant fluctuating physical parameters shows that additional mechanisms can exist on top of the zonal-flow-induced shearing. The modification of the phase angle could indeed have a notable effect on the transport reduction. Yet, more efforts must be spent to obtain with great confidence a full comprehension of such results. Additionally, these studies on the cross-phase can also be exploitable in a validating framework. Indeed, as already reported in earlier studies (see, e.g., Refs. [185, 186]), the cross phase computed by the gyrokinetic analyses can be compared to experimental measured outcomes.

Inspecting the different behaviour observed in the present studies, in which the reduction of the turbulent transport is achieved also beyond the critical threshold of the fast-ion mode destabilization, with respect to the earlier studies, the relevance of pressure regime should be highlighted. Indeed, the exorbitant increase of the electron electromagnetic transport [79, 76], as well as the unreliable fluctuations of the ion fluxes [78], may be related to the large β_e values. The experimental observations and numerical assessments of the improved ion confinement reported in this work are related to relatively low-β L-mode plasmas. Reaching advanced pressure regimes, denotated by higher β values, may hence be deleterious for such complex mechanism to be effective, because of the increased amplitude of the electromagnetic fluctuations induced by the destabilized fast-ion-driven modes. At this regard, firstly as a numerical investigation and successively as an experimental design, the different pressure regimes should be deeper investigated.

Finally, it is important to determine the main ingredients of the mechanisms underlying the turbulence suppression. In this way it will be possible to tailor with enough confidence the scenarios in present and future fusion devices for a better confinement. For instance, it has been observed that trapped fast ions may play an important role in destabilizing high-frequency modes which are the first and principal ingredient to trigger the complex interaction between fast ions and turbulence suppression. Gyrokinetic simulations performed during this thesis show that a relevant difference, between the systems where turbulence is reduced and those where it is not, relies on the excitation of fast-ion-driven modes. This implies that there are instabilities that might be beneficial for the global confinement and there are other instabilities that might be deleterious. Another fingerprint, which however has been shown to be only a consequences of the unstable high-frequency modes, is the low-frequency mode systematically observed in the

plasmas core of the three-ion scenario at JET, captured by the gyrokinetic analyses about such a JET scenario in Chapter 3, and surprisingly present in the numerical experiment performed for the TEM-dominated case and reported at the end of Chapter 4. Although a clear identification of this mode in the present studies is still elusive, previous analyses already displayed a clear relation with the unstable TAEs in a DIII-D scenario [142]. Therefore, gaining more insight on this particular mode could open the way to the design of new experiments potentially exhibiting a turbulence suppression and hence a better plasma confinement.

Bibliography

[1] J. D. Lawson. Some criteria for a power producing thermonuclear reactor. *Proceedings of the Physical Society. Section B*, 70:6, 1957.

[2] R. Betti and O. A. Hurricane. Inertial-confinement fusion with lasers. *Nature Physics*, 12(5):435–448, 2016.

[3] J. Ongena, R. Koch, R. Wolf, and H. Zohm. Magnetic-confinement fusion. *Nature Physics*, 12(5):398–410, 2016.

[4] P. Xanthopoulos, S. A. Bozhenkov, M. N. Beurskens, H. M. Smith, G. G. Plunk, P. Helander, C. D. Beidler, J. A. Alcusón, A. Alonso, A. Dinklage, et al. Turbulence mechanisms of enhanced performance stellarator plasmas. *Physical Review Letters*, 125(7):075001, 2020.

[5] C. D. Beidler, H. M. Smith, A. Alonso, T. Andreeva, J. Baldzuhn, M. N. A. Beurskens, M. Borchardt, S. A. Bozhenkov, K. J. Brunner, H. Damm, et al. Demonstration of reduced neoclassical energy transport in Wendelstein 7-X. *Nature*, 596(7871):221–226, 2021.

[6] J. Abiteboul. *Turbulent and neoclassical toroidal momentum transport in tokamak plasmas*. PhD thesis, Aix-Marseille Université, 2012.

[7] M. Keilhacker, A. Gibson, C. Gormezano, P. J. Lomas, P. R. Thomas, M. L. Watkins, P. Andrew, B. Balet, D. Borba, C. D. Challis, et al. High fusion performance from deuterium-tritium plasmas in JET. *Nuclear Fusion*, 39(2):209, 1999.

[8] J. Wesson. *Tokamaks*, volume 149. Oxford university press, 2011.

[9] T. J. M. Boyd and J. J. Sanderson. *The Physics of Plasmas*. Cambridge University Press, 2003.

[10] F. F. Chen. *Introduction to Plasma Physics*. Springer Science & Business Media, 2012.

[11] J. P. Freidberg. *Plasma Physics and Fusion Energy*. Cambridge University Press, 2008.

[12] E. J. Doyle et al. Chapter 2: Plasma confinement and transport. *Nuclear Fusion*, 47(6):S18, 2007.

[13] Y. Camenen, A. Pochelon, R. Behn, A. Bottino, A. Bortolon, S. Coda, A. Karpushov, O. Sauter, G. Zhuang, et al. Impact of plasma triangularity and collisionality on electron heat transport in TCV L-mode plasmas. *Nuclear Fusion*, 47(7):510, 2007.

[14] A. Pochelon, P. Angelino, R. Behn, S. Brunner, S. Coda, N. Kirneva, S. Y. Medvedev, H. Reimerdes, J. Rossel, O. Sauter, et al. Recent TCV results-innovative plasma shaping to improve plasma properties and insight. *Plasma and Fusion Research*, 7:2502148–2502148, 2012.

[15] M. E. Austin, A. Marinoni, M. L. Walker, M. W. Brookman, J. S. DeGrassie, A. W. Hyatt, G. R. McKee, C. C. Petty, T. L. Rhodes, S. P. Smith, et al. Achievement of reactor-relevant performance in negative triangularity shape in the DIII-D tokamak. *Physical Review Letters*, 122(11):115001, 2019.

[16] R. L. Miller, M.-S. Chu, J. M. Greene, Y. R. Lin-Liu, and R. E. Waltz. Noncircular, finite aspect ratio, local equilibrium model. *Physics of Plasmas*, 5(4):973–978, 1998.

[17] J. C. Maxwell. *A treatise on electricity and magnetism*, volume 1. Clarendon Press, 1873.

[18] T. H. Stix. Fast-wave heating of a two-component plasma. *Nuclear Fusion*, 15:737, 1975.

[19] W. Dorland, F. Jenko, M. Kotschenreuther, and B. N. Rogers. Electron temperature gradient turbulence. *Physical Review Letters*, 85(26):5579, 2000.

[20] J. Candy and R. E. Waltz. An eulerian gyrokinetic-maxwell solver. *Journal of Computational Physics*, 186(2):545–581, 2003.

[21] F. Merz. *Gyrokinetic simulation of multimode plasma turbulence*. PhD thesis, Universität Münster, 2008.

[22] A. G. Peeters, Y. Camenen, F. J. Casson, W. A. Hornsby, A. P. Snodin, D. Strintzi, and G. Szepesi. The nonlinear gyro-kinetic flux tube code GKW. *Computer Physics Communications*, 180(12):2650–2672, 2009.

[23] A. J. Brizard and T. S. Hahm. Foundations of nonlinear gyrokinetic theory. *Reviews of Modern Physics*, 79(2):421, 2007.

[24] A. Dvornova, G. T. A. Huijsmans, S. Sharapov, F. J. Artola Such, P. Puglia, M. Hoelzl, S. Pamela, A. Fasoli, and D. Testa. Modeling of TAE mode excitation with an antenna in realistic X-point geometry. *Physics of Plasmas*, 27(1):012507, 2020.

[25] A. Dvornova. *Hybrid fluid-kinetic MHD simulations of the excitation of toroidal Alfvén eigenmodes by fast particles and external antenna*. PhD thesis, Eindhoven University of Technology, 2021.

[26] M. Hoelzl, G. T. A. Huysmans, S. J. P. Pamela, M. Becoulet, E. Nardon, F. J. Artola, B. Nkonga, C. V. Atanasiu, V. Bandaru, A. Bhole, et al. The JOREK non-linear extended MHD code and applications to large-scale instabilities and their control in magnetically confined fusion plasmas. *Nuclear Fusion*, 61(6):065001, 2021.

[27] F. L. Hinton and R. D. Hazeltine. Theory of plasma transport in toroidal confinement systems. *Reviews of Modern Physics*, 48(2):239, 1976.

[28] P. Liewer. Measurements of microturbulence in tokamaks and comparisons with theories of turbulence and anomalous transport. *Nuclear Fusion*, 25(5):543, 1985.

[29] W. Horton. Drift waves and transport. *Reviews of Modern Physics*, 71(3):735–778, 1999.

[30] Y. Sarazin. Interactions multi-échelles en turbulence des plasmas de fusion. *Habilitation dissertation, University of Provence (Aix-Marseille I), France*, 2008.

[31] D. Zarzoso. *Kinetic description of interaction between energetic particles and waves in fusion plasmas*. PhD thesis, Ecole Polytechnique X, 2012.

[32] F. Romanelli. Ion temperature-gradient-driven modes and anomalous ion transport in tokamaks. *Physics of Fluids B: Plasma Physics*, 1(5):1018–1025, 1989.

[33] P. N. Guzdar, C. S. Liu, J. Q. Dong, and Y. C. Lee. Model for thermal transport in tokamaks. *Physical Review Letters*, 57(22):2818, 1986.

[34] Y. C. Lee, J. Q. Dong, P. N. Guzdar, and C. S. Liu. Collisionless electron temperature gradient instability. *The Physics of Fluids*, 30(5):1331–1339, 1987.

[35] W. Horton, B. G. Hong, and W. M. Tang. Toroidal electron temperature gradient driven drift modes. *The Physics of Fluids*, 31(10):2971–2983, 1988.

[36] S. C. Prager, A. K. Sen, and T. C. Marshall. Dissipative trapped-electron instability in cylindrical geometry. *Physical Review Letters*, 33(12):692, 1974.

[37] M. Nakata, M. Nunami, H. Sugama, and T.-H. Watanabe. Isotope effects on trapped-electron-mode driven turbulence and zonal flows in helical and tokamak plasmas. *Physical Review Letters*, 118(16):165002, 2017.

[38] J. Candy. Beta scaling of transport in microturbulence simulations. *Physics of Plasmas*, 12(7):072307, 2005.

[39] W. Heidbrink and G. Sadler. The behaviour of fast ions in tokamak experiments. *Nuclear Fusion*, 34(4):535, 1994.

[40] A. Fasoli, C. Gormenzano, H. Berk, B. Breizman, S. Briguglio, D. Darrow, N. Gorelenkov, W. Heidbrink, A. Jaun, S. Konovalov, et al. Physics of energetic ions. *Nuclear Fusion*, 47:S264, 2007.

[41] B. N. Breizman and S. E. Sharapov. Major minority: Energetic particles in fusion plasmas. *Plasma Physics and Controlled Fusion*, 53(5):054001, 2011.

[42] P. Lauber. Super-thermal particles in hot plasmas—kinetic models, numerical solution strategies, and comparison to tokamak experiments. *Physics Reports*, 533(2):33–68, 2013.

[43] L. Chen and F. Zonca. Physics of Alfvén waves and energetic particles in burning plasmas. *Reviews of Modern Physics*, 88(1):015008, 2016.

[44] H. Alfvén. Existence of electromagnetic-hydrodynamic waves. *Nature*, 150(3805):405–406, 1942.

[45] F. Zonca. *Continuum damping of toroidal Alfvén eigenmodes in finite-beta tokamak equilibria*. PhD thesis, Princeton University, 1993.

[46] J. Tataronis and W. Grossmann. Decay of MHD waves by phase mixing. *Zeitschrift für Physik A Hadrons and nuclei*, 261(3):203–216, 1973.

[47] A. Hasegawa and L. Chen. Plasma heating by Alfvén-wave phase mixing. *Physical Review Letters*, 32(9):454, 1974.

[48] W. Heidbrink. Basic physics of alfvén instabilities driven by energetic particles in toroidally confined plasmas. *Physics of Plasmas*, 15(5):055501, 2008.

[49] G. Y. Fu and J. W. Van Dam. Excitation of the toroidicity-induced shear Alfvén eigenmode by fusion alpha particles in an ignited tokamak. *Physics of Fluids B: Plasma Physics*, 1(10):1949–1952, 1989.

[50] C. Z. Cheng, L. Chen, and M. S. Chance. High-n ideal and resistive shear Alfvén waves in tokamaks. *Annals of Physics*, 161(1):21–47, 1985.

[51] C. Z. Cheng and M. S. Chance. Low-n shear Alfvén spectra in axisymmetric toroidal plasmas. *Physics of Fluids*, 29:3695, 1986.

[52] W. W. Heidbrink, E. J. Strait, M. S. Chu, and A. D. Turnbull. Observation of beta-induced Alfvén eigenmodes in the DIII-D tokamak. *Physical Review Letters*, 71(6):855–858, 1993.

[53] M.-S. Chu, J. M. Greene, L. L. Lao, A. D. Turnbull, and M. S. Chance. A numerical study of the high-n shear Alfvén spectrum gap and the high-n gap mode. *Physics of Fluids B: Plasma Physics*, 4(11):3713–3721, 1992.

[54] A. D. Turnbull, E. J. Strait, W. W. Heidbrink, M. S. Chu, H. H. Duong, J. M. Greene, L. L. Lao, T. S. Taylor, and S. J. Thompson. Global Alfvén modes: Theory and experiment. *Physics of Fluids B: Plasma Physics*, 5(7):2546–2553, 1993.

[55] F. Zonca, L. Chen, and R. Santoro. Kinetic theory of low-frequency Alfvén modes in tokamaks. *Plasma Physics and Controlled Fusion*, 38(11):2011, 1996.

[56] L. Chen. Theory of magnetohydrodynamic instabilities excited by energetic particles in tokamaks. *Physics of Plasmas*, 1(5):1519–1522, 1994.

[57] F. Jenko, W. Dorland, M. Kotschenreuther, and B. N. Rogers. Electron temperature gradient driven turbulence. *Physics of Plasmas*, 7(5):1904–1910, 2000.

[58] P. A. Davidson. *Turbulence: An introduction for scientists and engineers*. Oxford university press, 2015.

[59] D. Zarzoso, D. del Castillo-Negrete, D. Escande, Y. Sarazin, X. Garbet, V. Grandgirard, C. Passeron, G. Latu, and S. Benkadda. Particle transport due to energetic-particle-driven geodesic acoustic modes. *Nuclear Fusion*, 58(10):106030, 2018.

[60] H. L. Berk, B. N. Breizman, and H. Ye. Scenarios for the nonlinear evolution of alpha-particle-induced Alfvén wave instability. *Physical Review Letters*, 68(24):3563–3566, 1992.

[61] B. N. Breizman, H. L. Berk, and H. Ye. Collective transport of alpha particles due to Alfvén wave instability. *Physics of Fluids B: Plasma Physics*, 5(9):3217–3226, 1993.

[62] H. Biglari, P. Diamond, and P. Terry. Influence of sheared poloidal rotation on edge turbulence. *Physics of Fluids B: Plasma Physics*, 2:1, 1990.

[63] P. Diamond, S. Itoh, K. Itoh, and T. Hahm. Zonal flows in plasmas - a review. *Plasma Physics and Controlled Fusion*, 47:R35, 2005.

[64] M. N. Rosenbluth and F. L. Hinton. Poloidal flow driven by ion-temperature-gradient turbulence in tokamaks. *Physical Review Letters*, 80(4):724–727, 1998.

[65] P. R. Thomas, P. Andrew, B. Balet, D. Bartlett, J. Bull, B. De Esch, A. Gibson, C. Gowers, H. Guo, G. Huysmans, et al. Observation of alpha heating in JET DT plasmas. *Physical Review Letters*, 80(25):5548, 1998.

[66] P. Mantica, D. Strintzi, T. Tala, C. Giroud, T. Johnson, H. Leggate, E. Lerche, T. Loarer, A. Peeters, A. Salmi, et al. Experimental study of the ion critical-gradient length and stiffness level and the impact of rotation in the JET tokamak. *Physical Review Letters*, 102(17):175002, 2009.

[67] P. Mantica, C. Angioni, C. Challis, G. Colyer, L. Frassinetti, N. Hawkes, T. Johnson, M. Tsalas, J. Weiland, B. Baiocchi, et al. A key to improved ion core confinement in the jet tokamak: ion stiffness mitigation due to combined plasma rotation and low magnetic shear. *Physical review letters*, 107(13):135004, 2011.

[68] M. Romanelli, A. Zocco, and F. Crisanti. Fast ion stabilization of the ion temperature gradient driven modes in the Joint European Torus hybrid-scenario plasmas: a trigger mechanism for internal transport barrier formation. *Plasma Physics and Controlled Fusion*, 52(4):045007, 2010.

[69] G. Tardini, J. Hobirk, V. Igochine, C. Maggi, P. Martin, D. McCune, A. Peeters, A. Sips, A. Stabler, J. Stober, et al. Thermal ions dilution and ITG suppression in ASDEX Upgrade ion ITBs. *Nuclear fusion*, 47(4):280, 2007.

[70] J. Garcia and G. Giruzzi. Critical behavior of magnetically confined plasma regimes. *Physical Review Letters*, 104(20):205003, 2010.

[71] J. Citrin, F. Jenko, P. Mantica, D. Told, C. Bourdelle, J. Garcia, J. W. Haverkort, G. M. D. Hogeweij, T. Johnson, and M. J. Pueschel. Nonlinear stabilization of tokamak microturbulence by fast ions. *Physical Review Letters*, 111(15):155001, 2013.

[72] A. Di Siena, T. Görler, H. Dörk, E. Poli, and R. Bilato. Fast-ion stabilization of tokamak plasma turbulence. *Nuclear Fusion*, 58(5):054002, 2018.

[73] A. Di Siena, T. Görler, E. Poli, R. Bilato, H. Dörk, and A. Zocco. Resonant interaction of energetic ions with bulk-ion plasma micro-turbulence. *Physics of Plasmas*, 26(5):052504, 2019.

[74] N. Bonanomi, P. Mantica, A. Di Siena, E. Delabie, C. Giroud, T. Johnson, E. Lerche, S. Menmuir, M. Tsalas, D. Van Eester, et al. Turbulent transport stabilization by ICRH minority fast ions in low rotating JET ILW L-mode plasmas. *Nuclear Fusion*, 58(5):056025, 2018.

[75] A. Di Siena, R. Bilato, T. Görler, A. Bañón Navarro, E. Poli, V. Bobkov, D. Jarema, E. Fable, C. Angioni, Y. O. Kazakov, et al. New high-confinement regime with fast ions in the core of fusion plasmas. *Physical Review Letters*, 127(2):025002, 2021.

[76] J. Citrin, J. Garcia, T. Görler, F. Jenko, P. Mantica, D. Told, C. Bourdelle, D. Hatch, G. Hogeweij, T. Johnson, et al. Electromagnetic stabilization of tokamak microturbulence in a high-β regime. *Plasma Physics and Controlled Fusion*, 57(1):014032, 2014.

[77] J. Garcia, C. Challis, J. Citrin, H. Dörk, G. Giruzzi, T. Görler, F. Jenko, P. Maget, and J. Contributors. Key impact of finite-beta and fast ions in core and edge tokamak regions for the transition to advanced scenarios. *Nuclear Fusion*, 55(5):053007, 2015.

[78] A. Di Siena, T. Görler, E. Poli, A. Bañón Navarro, A. Biancalani, R. Bilato, N. Bonanomi, I. Novikau, F. Vannini, and F. Jenko. Nonlinear electromagnetic interplay between fast ions and ion-temperature-gradient plasma turbulence. *Journal of Plasma Physics*, 87(2), 2021.

[79] N. N. Gorelenkov, D. Stutman, K. Tritz, A. Boozer, L. Delgado-Aparicio, E. Fredrickson, S. Kaye, and R. White. Anomalous electron transport due to multiple high frequency beam ion driven Alfvén eigenmodes. *Nuclear Fusion*, 50(8):084012, 2010.

[80] D. Zarzoso, Y. Sarazin, X. Garbet, R. Dumont, A. Strugarek, J. Abiteboul, T. Cartier-Michaud, G. Dif-Pradalier, P. Ghendrih, V. Grandgirard, et al. Impact of Energetic-Particle-Driven Geodesic Acoustic Modes on Turbulence. *Physical Review Letters*, 110(12):125002, 2013.

[81] V. Grandgirard, J. Abiteboul, J. Bigot, T. Cartier-Michaud, N. Crouseilles, G. Dif-Pradalier, C. Ehrlacher, D. Esteve, X. Garbet, P. Ghendrih, et al. A 5D gyrokinetic full-f global semi-Lagrangian code for flux-driven ion turbulence simulations. *Computer Physics Communications*, 207:35–68, 2016.

[82] N. Winsor, J. Johnson, and J. Dawson. Geodesic acoustic waves in hydromagnetic systems. *Physics of Fluids*, 11:2448, 1968.

[83] D. Zarzoso, X. Garbet, Y. Sarazin, R. Dumont, and V. Grandgirard. *Physics of Plasmas*, 19(2):022102–022102, 2012.

[84] G. Y. Fu. Energetic-particle-induced geodesic acoustic mode. *Physical Review Letters*, 101(18):185002, 2008.

[85] M. Sasaki, K. Itoh, K. Hallatschek, N. Kasuya, M. Lesur, Y. Kosuga, and S.-I. Itoh. Enhancement and suppression of turbulence by energetic-particle-driven geodesic acoustic modes. *Scientific Reports*, 7(1):1–7, 2017.

[86] D. Zarzoso, P. Migliano, V. Grandgirard, G. Latu, and C. Passeron. Nonlinear interaction between energetic particles and turbulence in gyrokinetic simulations and impact on turbulence properties. *Nuclear Fusion*, 57(7):072011, 2017.

[87] H. Dörk, A. Bock, A. Di Siena, E. Fable, T. Görler, F. Jenko, J. Stober, et al. Turbulence in high-beta ASDEX Upgrade advanced scenarios. *Nuclear Fusion*, 58(1):016044, 2017.

[88] C. Holland, C. C. Petty, L. Schmitz, K. H. Burrell, G. R. McKee, T. L. Rhodes, and J. Candy. Progress in GYRO validation studies of DIII-D H-mode plasmas. *Nuclear Fusion*, 52(11):114007, 2012.

[89] C. Holland, T. C. Luce, B. A. Grierson, S. P. Smith, A. Marinoni, K. H. Burrell, C. C. Petty, and E. M. Bass. Examination of stiff ion temperature gradient mode physics in simulations of DIII-D H-mode transport. *Nuclear Fusion*, 61(6):066033, 2021.

[90] A. Di Siena, T. Görler, E. Poli, A. Bañon-Navarro, A. Biancalani, and F. Jenko. Electromagnetic turbulence suppression by energetic particle driven modes. *Nuclear Fusion*, 59(12):124001, 2019.

[91] D. Testa and M. Albergante. Evidence for a new path to the self-sustainment of thermonuclear fusion in magnetically confined plasmas. *EPL (Europhysics Letters)*, 97(3):35003, 2012.

[92] D. Testa and M. Albergante. A phenomenological explanation for the anomalous ion heating observed in the JET alpha-heating experiment of 1997. *Nuclear Fusion*, 52(8):083010, 2012.

[93] J. Garcia, T. Görler, and F. Jenko. Isotope and fast ions turbulence suppression effects: Consequences for high-β ITER plasmas. *Physics of Plasmas*, 25(5):055902, 2018.

[94] K. Besseghir, J. Garcia, J.-F. Artaud, F. Imbeaux, R. R. Khayrutdinov, J. B. Lister, V. E. Lukash, and P. Maget. Achieving and sustaining advanced scenarios in ITER modelled by CRONOS and DINA-CH. *Plasma Physics and Controlled Fusion*, 55(12):125012, 2013.

[95] S. J. Zweben and S. S. Medley. Visible imaging of edge fluctuations in the TFTR tokamak. *Physics of Fluids B: Plasma Physics*, 1(10):2058–2065, 1989.

[96] B. Scott. Global consistency for thin flux tube treatments of toroidal geometry. *Physics of Plasmas*, 5(6):2334–2339, 1998.

[97] J. W. Connor, R. J. Hastie, and J. B. Taylor. Shear, periodicity, and plasma ballooning modes. *Physical Review Letters*, 40(6):396, 1978.

[98] GENE Development Team. Dedicated website: www.genecode.org.

[99] T. Görler. *Multiscale effects in plasma microturbulence*. PhD thesis, Universität Ulm, 2009.

[100] A. Di Siena. *Implementation and investigation of the impact of different background distributions in gyrokinetic plasma turbulence studies*. PhD thesis, Universität Ulm, 2020.

[101] J. Candy, R. E. Waltz, S. E. Parker, and Y. Chen. Relevance of the parallel nonlinearity in gyrokinetic simulations of tokamak plasmas. *Physics of Plasmas*, 13(7):074501, 2006.

[102] Y. Idomura, M. Ida, S. Tokuda, and L. Villard. New conservative gyrokinetic full-f Vlasov code and its comparison to gyrokinetic δf particle-in-cell code. *Journal of Computational Physics*, 226(1):244–262, 2007.

[103] S. Jolliet. *Gyrokinetic particle-in-cell global simulations of ion-temperature-gradient and collisionless-trapped-electron-mode turbulence in tokamaks*. PhD thesis, EPFL, 2009.

[104] A. Di Siena, T. Görler, H. Dörk, R. Bilato, J. Citrin, T. Johnson, M. Schneider, E. Poli, and J. Contributors. Non-maxwellian fast particle effects in gyrokinetic GENE simulations. *Physics of Plasmas*, 25(4):042304, 2018.

[105] Z. Lin, T. S. Hahm, W. W. Lee, W. M. Tang, and P. H. Diamond. Effects of collisional zonal flow damping on turbulent transport. *Physical Review Letters*, 83(18):3645–3648, 1999.

[106] H. Dörk. *Gyrokinetic simulation of microtearing turbulence*. PhD thesis, Universität Ulm, 2013.

[107] R. A. Tinguely, P. G. Puglia, N. Fil, S. Dowson, M. Porkolab, A. Dvornova, A. Fasoli, M. Fitzgerald, V. Guillemot, G. T. A. Huysmans, et al. Experimental studies of plasma-antenna coupling with the JET Alfvén Eigenmode Active Diagnostic. *Nuclear Fusion*, 61(2):026003, 2020.

[108] Y. O. Kazakov, D. Van Eester, R. Dumont, and J. Ongena. On resonant ICRF absorption in three-ion component plasmas: a new promising tool for fast ion generation. *Nuclear Fusion*, 55(3):032001, 2015.

[109] J. Ongena, Y. O. Kazakov, Y. Baranov, C. Hellesen, J. Eriksson, T. Johnson, V. G. Kiptily, M. J. Mantsinen, M. Nocente, R. Bilato, et al. Synergetic heating of D-NBI ions in the vicinity of the mode conversion layer in H-D plasmas in JET with the ITER like wall. In *EPJ Web of Conferences*, volume 157, page 02006. EDP Sciences, 2017.

[110] Y. O. Kazakov, J. Ongena, J. C. Wright, S. J. Wukitch, E. Lerche, M. J. Mantsinen, D. Van Eester, T. Craciunescu, V. G. Kiptily, Y. Lin, et al. Efficient generation of energetic ions in multi-ion plasmas by radio-frequency heating. *Nature Physics*, 13(10):973–978, 2017.

[111] M. Nocente, Y. O. Kazakov, J. Garcia, V. G. Kiptily, J. Ongena, M. Dreval, M. Fitzgerald, S. E. Sharapov, Z. Stancar, H. Weisen, et al. Generation and observation of fast deuterium ions and fusion-born alpha particles in JET plasmas with the 3-ion radio-frequency heating scenario. *Nuclear Fusion*, 60(12):124006, 2020.

[112] Y. O. Kazakov, M. Nocente, M. Mantsinen, J. Ongena, Y. Baranov, T. Craciunescu, M. Dreval, R. Dumont, J. Eriksson, J. Garcia, et al. Plasma heating and generation of energetic D ions with the 3-ion ICRF + NBI scheme in mixed H-D plasmas at JET-ILW. *Nuclear Fusion*, 60(11):112013, 2020.

[113] Y. O. Kazakov, J. Ongena, J. C. Wright, S. J. Wukitch, V. Bobkov, J. Garcia, V. G. Kiptily, M. J. Mantsinen, M. Nocente, M. Schneider, et al. Physics and applications of three-ion ICRF scenarios for fusion research. *Physics of Plasmas*, 28(2):020501, 2021.

[114] M. Riva, B. Esposito, D. Marocco, F. Belli, B. Syme, J. Contributors, et al. The new digital electronics for the JET neutron profile monitor: Performances and first experimental results. *Fusion Engineering and Design*, 86(6-8):1191–1195, 2011.

[115] A. Sahlberg, J. Eriksson, S. Conroy, G. Ericsson, M. Nocente, Y. O. Kazakov, and J. Contributors. Spatially resolved measurements of RF accelerated deuterons at JET. *Nuclear Fusion*, 61(3):036025, 2021.

[116] M. Gatu Johnson, L. Giacomelli, A. Hjalmarsson, J. Källne, M. Weiszflog, E. A. Sundén, S. Conroy, G. Ericsson, C. Hellesen, E. Ronchi, et al. The 2.5-MeV neutron time-of-flight spectrometer TOFOR for experiments at JET. *Nuclear Instruments and Methods in Physics Research Section A: Accelerators, Spectrometers, Detectors and Associated Equipment*, 591(2):417–430, 2008.

[117] J. Eriksson, C. Hellesen, F. Binda, M. Cecconello, S. Conroy, G. Ericsson, L. Giacomelli, G. Gorini, A. Hjalmarsson, V. G. Kiptily, et al. Measuring fast ions in fusion plasmas with neutron diagnostics at JET. *Plasma Physics and Controlled Fusion*, 61(1):014027, 2018.

[118] Y. Kusama, H. Kimura, T. Ozeki, M. Saigusa, G. J. Kramer, T. Oikawa, S. Moriyama, M. Nemoto, T. Fujita, K. Tobita, et al. Toroidal Alfvén eigenmodes driven with ICRF accelerated protons in JT-60U negative shear discharges. *Nuclear fusion*, 38(8):1215, 1998.

[119] R. B. White, P. H. Rutherford, P. Colestock, and M. N. Bussac. Sawtooth stabilization by energetic trapped particles. *Physical Review Letters*, 60(20):2038, 1988.

[120] D. J. Campbell, D. F. H. Start, J. A. Wesson, D. V. Bartlett, V. P. Bhatnagar, M. Bures, J. G. Cordey, G. A. Cottrell, P. A. Dupperex, A. W. Edwards, et al. Stabilization of sawteeth with additional heating in the JET tokamak. *Physical Review Letters*, 60(21):2148, 1988.

[121] S. Hacquin, S. E. Sharapov, B. Alper, C. D. Challis, A. Fonseca, E. Mazzucato, A. Meigs, L. Meneses, I. Nunes, S. D. Pinches, et al. Localized X-mode reflectometry measurements of Alfvén eigenmodes on the JET tokamak. *Plasma Physics and Controlled Fusion*, 49(9):1371, 2007.

[122] L. Meneses, L. Cupido, and M. E. Manso. A novel approach to correlation reflectometry. *Fusion Engineering and Design*, 86(6-8):552–555, 2011.

[123] S. Mazzi et al. Towards enhanced performance in fusion plasmas via turbulence suppression by MeV ions. *Submitted to Nature Physics*, 2020.

[124] E. M. Bass and R. E. Waltz. Gyrokinetic simulations of mesoscale energetic particle-driven Alfvénic turbulent transport embedded in microturbulence. *Physics of Plasmas*, 17(11):112319, 2010.

[125] S. Mazzi, D. Zarzoso, J. Garcia, T. Görler, A. Di Siena, Y. Camenen, S. Benkadda, M. Yoshida, N. Hayashi, and K. Shinohara. Impact of fast ions on a trapped-electron-mode dominated plasma in a JT-60U hybrid scenario. *Nuclear Fusion*, 60(4):046026, 2020.

[126] R. J. Hawryluk. An empirical approach to tokamak transport. In *Physics of Plasmas Close to Thermonuclear Conditions*, pages 19–46. Elsevier, 1981.

[127] N. Bonanomi, P. Mantica, J. Citrin, T. G orler, B. Teaca, and J. Contributors. Impact of electron-scale turbulence and multi-scale interactions in the JET tokamak. *Nuclear Fusion*, 58(12):124003, 2018.

[128] J. Citrin, C. Angioni, N. Bonanomi, F. J. Casson, T. Görler, S. Maeyama, P. Mantica, A. Mariani, G. Staebler, T. H. Watanabe, et al. Validating reduced turbulence model predictions of Electron Temperature Gradient transport on a JET improved-confinement scenario. In *47th EPS Conference on Plasma Physics*, 2021.

[129] A. Mariani, N. Bonanomi, P. Mantica, C. Angioni, T. Görler, O. Sauter, and G. M. Staebler. Experimental investigation and gyrokinetic simulations of multi-scale electron heat transport in JET, AUG, TCV. *Nuclear Fusion*, 2021.

[130] G. M. Staebler, N. T. Howard, J. Candy, and C. Holland. A model of the saturation of coupled electron and ion scale gyrokinetic turbulence. *Nuclear Fusion*, 57(6):066046, 2017.

[131] M. A. Beer, S. C. Cowley, and G. W. Hammett. Field-aligned coordinates for nonlinear simulations of tokamak turbulence. *Physics of Plasmas*, 2(7):2687–2700, 1995.

[132] J. Dominski, S. Brunner, T. Görler, F. Jenko, D. Told, and L. Villard. How non-adiabatic passing electron layers of linear microinstabilities affect turbulent transport. *Physics of Plasmas*, 22(6):062303, 2015.

[133] H. Sheng, R. E. Waltz, and G. M. Staebler. Alfvén eigenmode stability and critical gradient energetic particle transport using the Trapped-Gyro-Landau-Fluid model. *Physics of Plasmas*, 24(7):072305, 2017.

[134] A. Bañon Navarro, P. Morel, M. Albrecht-Marc, D. Carati, F. Merz, T. Görler, and F. Jenko. Free energy balance in gyrokinetic turbulence. *Physics of plasmas*, 18(9):092303, 2011.

[135] D. Zarzoso and D. Del-Castillo-Negrete. Anomalous losses of energetic particles in the presence of an oscillating radial electric field in fusion plasmas. *Journal of Plasma Physics*, 86(2):795860201, 2020.

[136] H. Dörk, C. Challis, J. Citrin, J. Garcia, T. Görler, F. Jenko, and J. Contributors. Gyrokinetic study of turbulence suppression in a JET-ILW power scan. *Plasma Physics and Controlled Fusion*, 58(11):115005, 2016.

[137] F. N. de Oliveira Lopes. Nonlinear electromagnetic stabilization of microturbulence by fast ions. Master's thesis, Universitat Politècnica de Catalunya, 2017.

[138] G. Arfken. Mathematical methods for physicists. 3rd edn academic press, 1985.

[139] Z. Qiu, L. Chen, and F. Zonca. Effects of energetic particles on zonal flow generation by toroidal Alfvén eigenmode. *Physics of Plasmas*, 23(9):090702, 2016.

[140] Y. Todo and T. Sato. Linear and nonlinear particle-magnetohydrodynamic simulations of the toroidal Alfvén eigenmode. *Physics of Plasmas*, 5(5):1321–1327, 1998.

[141] Y. Todo, H. L. Berk, and B. N. Breizman. Nonlinear magnetohydrodynamic effects on Alfvén eigenmode evolution and zonal flow generation. *Nuclear Fusion*, 50(8):084016, 2010.

[142] N. A. Crocker, W. A. Peebles, S. Kubota, E. D. Fredrickson, S. M. Kaye, B. P. LeBlanc, and J. E. Menard. Three-wave interactions between fast-ion modes in the national spherical torus experiment. *Physical Review Letters*, 97(4):045002, 2006.

[143] D. Told, F. Jenko, T. Görler, F. J. Casson, E. Fable, and A. U. Team. Characterizing turbulent transport in ASDEX Upgrade L-mode plasmas via nonlinear gyrokinetic simulations. *Physics of Plasmas*, 20(12):122312, 2013.

[144] B. D. Scott. Drift wave versus interchange turbulence in tokamak geometry: Linear versus nonlinear mode structure. *Physics of Plasmas*, 12(6):062314, 2005.

[145] P. W. Terry, D. E. Newman, and A. S. Ware. Suppression of transport cross phase by strongly sheared flow. *Physical Review Letters*, 87(18):185001, 2001.

[146] G. Birkenmeier, M. Ramisch, B. Schmid, and U. Stroth. Experimental evidence of turbulent transport regulation by zonal flows. *Physical Review Letters*, 110(14):145004, 2013.

[147] N. T. Howard, C. Holland, A. E. White, M. Greenwald, J. Candy, and A. J. Creely. Multi-scale gyrokinetic simulations: Comparison with experiment and implications for predicting turbulence and transport. *Physics of Plasmas*, 23(5):056109, 2016.

[148] L. Chen and F. Zonca. Nonlinear excitations of zonal structures by toroidal Alfvén eigenmodes. *Physical Review Letters*, 109(14):145002, 2012.

[149] B. B. Kadomtsev and O. Pogutse. Plasma instability due to particle trapping in a toroidal geometry. *Sov. Phys. JETP*, 24:1172–1179, 1967.

[150] T. M. Antonsen Jr., J. F. Drake, P. N. Guzdar, A. B. Hassam, Y. T. Lau, C. S. Liu, and S. V. Novakovskii. Physical mechanism of enhanced stability from negative shear in tokamaks: Implications for edge transport and the L-H transition. *Physics of Plasmas*, 3(6):2221–2223, 1996.

[151] O. Beeke, M. Barnes, M. Romanelli, M. Nakata, and M. Yoshida. Impact of shaping on microstability in high-performance tokamak plasmas. *Nuclear Fusion*, 61(6):066020, 2021.

[152] C. Kessel, J. Manickam, G. Rewoldt, and W. M. Tang. Improved plasma performance in tokamaks with negative magnetic shear. *Physical Review Letters*, 72(8):1212, 1994.

[153] T. Dannert and F. Jenko. Gyrokinetic simulation of collisionless trapped-electron mode turbulence. *Physics of Plasmas*, 12(7):072309, 2005.

[154] F. Merz and F. Jenko. Nonlinear saturation of trapped electron modes via perpendicular particle diffusion. *Physical review letters*, 100(3):035005, 2008.

[155] D. Ernst, K. Burrell, W. Guttenfelder, T. Rhodes, A. Dimits, R. Bravenec, B. Grierson, C. Holland, J. Lohr, A. Marinoni, et al. Role of density gradient driven trapped electron mode turbulence in the H-mode inner core with electron heating. *Physics of Plasmas*, 23(5):056112, 2016.

[156] N. Oyama, A. Isayama, G. Matsunaga, T. Suzuki, H. Takenaga, Y. Sakamoto, T. Nakano, Y. Kamada, S. Ide, et al. Long-pulse hybrid scenario development in JT-60U. *Nuclear Fusion*, 49(6):065026, 2009.

[157] J. F. Artaud, V. Basiuk, F. Imbeaux, M. Schneider, J. Garcia, G. Giruzzi, P. Huynh, T. Aniel, F. Albajar, J. Ané, et al. The CRONOS suite of codes for integrated tokamak modelling. *Nuclear Fusion*, 50(4):043001, 2010.

[158] G. Huysmans, J. Goedbloed, and W. Kerner. Cp90 conf. on computational physics, 1991.

[159] K. Tani, M. Azumi, H. Kishimoto, and S. Tamura. Effect of toroidal field ripple on fast ion behavior in a tokamak. *Journal of the Physical Society of Japan*, 50(5):1726–1737, 1981.

[160] J. Garcia, N. Hayashi, B. Baiocchi, G. Giruzzi, M. Honda, S. Ide, P. Maget, E. Narita, M. Schneider, H. Urano, et al. Physics comparison and modelling of the JET and JT-60U core and edge: towards JT-60SA predictions. *Nuclear Fusion*, 54(9):093010, 2014.

[161] J. Weiland and A. Hirose. Electromagnetic and kinetic effects on the ion temperature gradient mode. *Nuclear Fusion*, 32(1):151, 1992.

[162] A. Hirose. On finite β stabilization of the toroidal ion temperature gradient mode. *Physics of Plasmas*, 7(2):433–436, 2000.

[163] W. W. Heidbrink, E. Ruskov, E. M. Carolipio, J. Fang, M. A. Van Zeeland, and R. A. James. What is the beta-induced Alfvén eigenmode? *Physics of Plasmas*, 6(4):1147–1161, 1999.

[164] F. Zonca, L. Chen, J. Dong, and R. Santoro. Existence of ion temperature gradient driven shear Alfvén instabilities in tokamaks. *Physics of Plasmas*, 6(5):1917–1924, 1999.

[165] J. Dong, L. Chen, and F. Zonca. Study of kinetic shear alfvén modes driven by ion temperature gradient in tokamak plasmas. *Nuclear Fusion*, 39(8):1041, 1999.

[166] G. Falchetto, J. Vaclavik, and L. Villard. Global-gyrokinetic study of finite β effects on linear microinstabilities. *Physics of Plasmas*, 10(5):1424–1436, 2003.

[167] W. Chen, R. Ma, Y. Li, Z. Shi, H. Du, M. Jiang, L. Yu, B. Yuan, Y. Li, Z. Yang, et al. Alfvénic ion temperature gradient activities in a weak magnetic shear plasma. *EPL (Europhysics Letters)*, 116(4):45003, 2017.

[168] C. Z. Cheng. Kinetic theory of collisionless ballooning modes. *The Physics of Fluids*, 25(6):1020–1026, 1982.

[169] P. Lauber, S. Günter, A. Könies, and S. D. Pinches. LIGKA: A linear gyrokinetic code for the description of background kinetic and fast particle effects on the MHD stability in tokamaks. *Journal of Computational Physics*, 226(1):447–465, 2007.

[170] M. S. Hussain, W. Guo, and L. Wang. Effects of energetic particles on the density gradient driven collisionless trapped electron mode instability in tokamak plasmas. *Plasma Physics and Controlled Fusion*, 2021.

[171] G. Matsunaga, K. Shinohara, N. Aiba, Y. Sakamoto, A. Isayama, N. Asakura, T. Suzuki, M. Takechi, N. Oyama, H. Urano, et al. Energetic particle driven instability in wall-stabilized high-β plasmas. *Nuclear Fusion*, 50(8):084003, 2010.

[172] G. G. Whelan, M. J. Pueschel, and P. W. Terry. Nonlinear electromagnetic stabilization of plasma microturbulence. *Physical Review Letters*, 120(17):175002, 2018.

[173] G. G. Whelan, M. J. Pueschel, P. W. Terry, J. Citrin, I. J. McKinney, W. Guttenfelder, and H. Dörk. Saturation and nonlinear electromagnetic stabilization of ITG turbulence. *Physics of Plasmas*, 26(8):082302, 2019.

[174] R. Waltz, G. Kerbel, and J. Milovich. Toroidal gyro-landau fluid model turbulence simulations in a nonlinear ballooning mode representation with radial modes. *Physics of Plasmas*, 1(7):2229–2244, 1994.

[175] G. M. Staebler, J. Candy, N. T. Howard, and C. Holland. The role of zonal flows in the saturation of multi-scale gyrokinetic turbulence. *Physics of Plasmas*, 23(6):062518, 2016.

[176] C. Piron, J. Garcia, M. Agostini, M. Fontana, G. Giruzzi, M. Gobbin, T. P. Goodman, A. N. Karpushov, M. Kong, A. Merle, et al. Extension of the operating space of high-β_n fully non-inductive scenarios on TCV using neutral beam injection. *Nuclear Fusion*, 59(9):096012, 2019.

[177] A. Fasoli, H. Reimerdes, S. Alberti, M. Baquero-Ruiz, B. P. Duval, E. Havlikova, A. Karpushov, J.-M. Moret, M. Toussaint, H. Elaian, et al. TCV heating and divertor upgrades. *Nuclear Fusion*, 60(1):016019, 2019.

[178] ITER Organization. ITER research plan within the staged approach (2018).

[179] C. Gillot. *Model reduction for tokamak plasma turbulence: beyond fluid and quasilinear descriptions*. PhD thesis, Aix-Marseille Université, 2020.

[180] B. P. van Milligen, B. A. Carreras, I. Voldiner, U. Losada, C. Hidalgo, and T.-I. Team. Causality, intermittence, and crossphase evolution during confinement transitions in the TJ-II stellarator. *Physics of Plasmas*, 28(9):092302, 2021.

[181] J. Ruiz Ruiz, F. Parra, V. Hall-Chen, N. Christen, M. Barnes, J. Candy, J. Garcia, C. Giroud, W. Guttenfelder, J. Hillesheim, et al. Gyrokinetic modelling and experimental comparisons of radial correlation and time delay Doppler backscattering measurements in JET. *Bulletin of the American Physical Society*, 2021.

[182] J. Ruiz Ruiz, W. Guttenfelder, A. E. White, N. T. Howard, J. Candy, Y. Ren, D. R. Smith, N. F. Loureiro, C. Holland, and C. W. Domier. Validation of gyrokinetic simulations in NSTX and projections for high-k turbulence measurements in NSTX-U. *Physics of Plasmas*, 27(12):122505, 2020.

[183] S. Coda, A. Iantchenko, S. Brunner, M. Toussaint, and K. Tanaka. A phase-contrast-imaging core fluctuation diagnostic and first-principles turbulence modeling for JT-60SA. *Nuclear Fusion*, 2021.

[184] S. Maeyama, Y. Idomura, T.-H. Watanabe, M. Nakata, M. Yagi, N. Miyato, A. Ishizawa, and M. Nunami. Cross-scale interactions between electron and ion scale turbulence in a tokamak plasma. *Physical Review Letters*, 114(25):255002, 2015.

[185] A. E. White, W. A. Peebles, T. L. Rhodes, C. H. Holland, G. Wang, L. Schmitz, T. A. Carter, J. C. Hillesheim, E. J. Doyle, L. Zeng, et al. Measurements of the cross-phase angle between density and electron temperature fluctuations and comparison with gyrokinetic simulations. *Physics of Plasmas*, 17(5):056103, 2010.

[186] T. Görler, A. E. White, D. Told, F. Jenko, C. Holland, and T. L. Rhodes. A flux-matched gyrokinetic analysis of DIII-D L-mode turbulence. *Physics of Plasmas*, 21(12):122307, 2014.